DEVELOPMENT OF A SIMULATION-BASED METHODOLOGY FOR MOLD DESIGN OPTIMIZATION AND RELIABILITY ASSESSMENT OF CAST PARTS

BY

MUHAMMAD AZHAR ALI KHAN

A Dissertation Presented to the
DEANSHIP OF GRADUATE STUDIES

KING FAHD UNIVERSITY OF PETROLEUM & MINERALS
DHAHRAN, SAUDI ARABIA

In Partial Fulfillment of the
Requirements for the Degree of

DOCTOR OF PHILOSOPHY
In

MECHANICAL ENGINEERING

MAY 2018

KING FAHD UNIVERSITY OF PETROLEUM & MINERALS
DHAHRAN- 31261, SAUDI ARABIA
DEANSHIP OF GRADUATE STUDIES

This thesis, written by **MUHAMMAD AZHAR ALI KHAN** under the direction his thesis advisor and approved by his thesis committee, has been presented and accepted by the Dean of Graduate Studies, in partial fulfillment of the requirements for the degree of **DOCTOR OF PHILOSOPHY IN MECHANICAL ENGINEERING.**

Anwar Khalil Sheikh

Dr. Anwar Khalil Sheikh
(Advisor)

Dr. Zafarullah Khan
(Member)

Dr. Zuhair Mattoug Gasem
(Member)

Dr. Syed Sohail Akhtar
(Member)

Dr. Anwar Ul-Hamid
(Member)

Dr. Zuhair Mattoug Gasem
Department Chairman

Dr. Salam A. Zummo
Dean of Graduate Studies

3/6/18
Date

Dedicated to my family,

for their unconditional support, trust and encouragement.

ACKNOWLEDGMENTS

First and foremost, I am extremely thankful to ***Allah (SWT)*** who blessed me with aptitude, courage, strength, and patience to achieve this milestone.

I offer my sincerest gratitude to my supervisor, *Dr. Anwar Khalil Sheikh*, who has supported me throughout this work with his patience and knowledge whilst providing me the room to work in my own way. I attribute the level of my PhD degree to his advice, encouragement and efforts.

Besides my advisor, I would like to thank the rest of my thesis committee: *Dr. Zafarullah Khan, Dr. Zuhair Gasem, Dr. Syed Sohail Akhtar,* and *Dr. Anwar-ul-Hamid*, for their insightful comments and suggestions throughout the research and reviewing process. I am immensely thankful to *Dr. Sulaiman Pasha* for his guidance and support.

Special thanks to *Mr. Marc Kothen*, and *Mr. Tamer Said* from *MAGMA* for their continuous support during this research. I am also grateful to *Dr. Bilal Sulaiman Al-Shaer, Mr. Sunil Kumar Jondhale, Mr. Abdulqadir,* and *Mr. Wilfredo Tagorio* in facilitating the casting runs at MASABIK foundry.

This work is supported by *The National Science, Technology and Innovation Plan* (NSTIP), Saudi Arabia, under grant number 14-ADV890-04-R.

Finally, I thank my fellow postgraduate students in Mechanical Engineering Department at King Fahd University of Petroleum and Minerals for stimulating discussions and the friendly environment they provided throughout my research.

TABLE OF CONTENTS

LIST OF TABLES

LIST OF FIGURES

LIST OF ABBREVIATIONS

AFS : American Foundry Society

ASTM : American Society for Testing and Materials

CA : Cellular Automation Method

CAD : Computer Aided Drawing

CAFE : Cellular Automation Finite Element

CAM : Computer Aided Manufacturing

CHTC : Constant Heat Transfer Coefficient

DOE : Design of Experiments

EPS : Expanded Polystyrene

FDM : Finite Difference Method

FEM : Finite Element Method

FVM : Finite Volume Method

JICA : Japan International Cooperation Agency

LEFM : Linear Elastic Fracture Mechanics

SAE : Society of Automotive Engineering

VEM : Vector Element Method

VHTC	:	Variable Heat Transfer Coefficient
WCB	:	Wrought Carbon with Grade B

ABSTRACT

Full Name	:	Muhammad Azhar Ali Khan
Thesis Title	:	Development of a Simulation-Based Methodology for Mold Design Optimization and Reliability Assessment of Cast Parts
Major Field	:	Mechanical Engineering
Date of Degree	:	May 2018

Casting simulation software are increasingly being used in modern foundries and metal casting industries. Software simulate the casting process in a virtual domain and provide insight into mold filling, solidification and cooling, and casting defects. Casting simulations allow designers to model, verify and validate the process, iteratively leading to optimized design and process parameters before actually producing the cast parts. These cast parts are supposed to have no porosity or defect, however, in reality due to complexity of metal solidification under different boundary conditions there may be some minimal porosity or defects still exist. Thus it is essential to evaluate the mechanical performance and reliability of cast products with defects predicted by casting simulations. This research focuses on the development of a strategy for cradle to grave analysis of castings in a virtual domain by utilizing advanced metal casting and FEM simulation tools. The materials under consideration are ASTM A216 WCB cast steel and GGG-40 ductile cast iron due to their widespread use in modern foundries for a range of cast products. A methodology for cradle to grave analysis of cast products is developed and validated for standard tensile and fatigue test specimens produced as castings made in MAGMASoft based optimized mold. The specimens are considered as simple cast products for which the initial mold designs are based on standards and expertise of foundrymen. Initial mold design is simulated in MAGMASoft to predict defects, to reduce these defects (primarily porosity) to minimum or none, and to optimize the design using the software. The optimized mold designs are used to cast specimens in a foundry. Simulated porosity, which is minimized through mold design optimization, is then mapped to finite element simulations to evaluate the mechanical performance of the cast components in ABAQUS. Fatigue damage models are used to estimate the life (time to failure) of cast products using fe-safe. The reliability of the cast products is determined through probabilistic methods using fatigue strength-stress interference model. The reliability is computed for different scenarios such as deterministic, Weibull and Normal distributed load induced stresses, zero and some percent variability in load-induced stresses, and variability in material's strength. Next, moderately complex cast product(s) in service are selected and analyzed from mold design to reliability assessment based on the developed and validated methodology for cradle to grave analysis. The results of the study provide measures which should be taken to reduce failure of cast products by developing a near optimal mold in virtual reality before making it in a foundry, a systematic methodology for cradle to grave analysis of cast products by integrating casting simulation and finite element interfaces, and a stringent acceptance criteria for critical high value cast parts based on the reliability assessment during service life.

ملخص الرسالة

الاسم الكامل: محمد ازهر علي خان

عنوان الرسالة: تطوير منهجية تحسين تصميم القوالب المبنية على المحاكاة وتقييم موثوقية الأجسام المصبوبة

التخصص: الهندسة الميكانيكية

تاريخ الدرجة العلمية: مايو ٢٠١٨

بشكل متزايد يتم استخدام برامج المحاكاة في مصانع سبك وصب المعادن الحديثة. تحاكي البرامج عملية الصب بطريقة افتراضية وتقدم نظرة دقيقة لِطريقة ملء القالب والتجمد والتبريد وكذلك لعيوب الصب. تُمكّن عمليات المحاكاة المصممين من نمذجة عملية الصب والتحقق منها والتحقق من صحتها. إن تكرار عمليات المحاكاة يقود إلى تحسين معايير التصميم والمعالجة قبل القيام بتصنيع القطع. هذه القطع من المفترض أن تكون خالية من المسامية والعيوب التصنيعية ولكن في الواقع ونتيجة لتعقيد عملية تجمد المواد تحت ظروف مختلفة لابد من وجود حد أدنى من المسامية والعيوب التصنيعية. لذلك من الضروري تقييم الأداء الميكانيكي ودقة منتجات عمليات الصب بما تحتويه من العيوب المتوقعة من عمليات المحاكاة. يركز هذا البحث على تطوير استراتيجية لتحليل شامل لعمليات الصب في مجال افتراضي بالاستفادة من أدوات صب المعادن والمحاكاة بواسطة طريقة العناصر المنتهية FEM المتقدمة. المواد قيد الدراسة هي الفولاذ المصبوب ASTM A216 WCB والحديد المصبوب المرن GGG-40 وذلك لاستخدامهما على نطاق واسع في مصانع السبك الحديثة لمجموعة من منتجات الصب. تم تطوير واختبار منهجية للتحليل الشامل من المهد إلى اللحد لعينات قياسية لاختباري الشد والإجهاد المُصنعة كمصبوب في القالب الأمثل المُنتج بواسطة برنامج MAGMASOFT. تُعتبر العينات منتجات صب بسيطة تعتمد عليها تصاميم القوالب المبدئية وفقاً للمعايير القياسية وخبرات العاملين في مصانع السبك. تتم محاكاة تصميم القالب الأولي من خلال MAGMASOFT للتنبؤ بالعيوب المصنعية ولتقليل هذه العيوب -خاصةَ المسامية- للحد الأدنى أو بحيث تخلو من العيوب وكذلك لتحسين التصميم. تستخدم تصميمات القوالب المُحسنة في صب العينات في مسبك. بعد محاكاة المسامية والتي تم تقليلها من خلال تحسين تصميم القالب يتم رسمها لمحاكاتها بواسطة طريقة العناصر المنتهية لتقييم الأداء الميكانيكي لعناصر الصب من خلال برنامج

ABAQUS. يتم استخدام نماذج تلف اختبار الإجهاد لتقدير حياة (الوقت المستغرق حتى التلف) منتجات الصب بواسطة برنامج fe-safe. يتم تحديد موثوقية المنتجات المصبوبة من خلال طرق إحصائية باستخدام نموذج تداخل قوة الإجهاد-الضغط. تم حساب الموثوقية لافتراضيات مختلفة مثل التوزيع الحتمي وتوزيع ايبول Weibull والتوزيع الطبيعي للحمل الناتج عن الضغط المستحث. كما تم افتراض نسب متفاوتة من الحمل الناتج عن الضغط المستحث والتفاوت في قوة المادة. بعد ذلك تم اختيار وتحليل مجموعة منتجات مصبوبة قيد التشغيل ومتوسطة التعقيد ابتداءً من تصميم القالب إلى تقييم الأداء بناءً على المنهجية المطورة والمختبرة للتحليل الشامل. تعطي نتائج الدراسة مقاييس ينبغي اتخاذها للتقليل من تلف المنتجات المصبوبة بواسطة تطوير قالب شبه مثالي في الواقع الافتراضي قبل تصنيعه في مسبك، منهجية متناسقة لتحليل شامل للمنتجات المصبوبة بواسطة دمج محاكاة الصب وطريقة العناصر المنتهية، ومعايير قبول صارمة لقطع صب عالية الجودة بناءً على تقييم الموثوقية خلال التشغيل.

CHAPTER 1

INTRODUCTION

1.1 MOTIVATION AND SIGNIFICANCE

The use of computational methods and numerical simulations in metal casting has become a powerful tool to analyze mold filling, solidification and cooling, and to predict the location and type of internal defects [1]. These simulation methods allow modern foundries to shift from conventional "trial-and-error" to "proof-of-concept" approach in cast product development. The shift from heuristic know-how and experimental means to more scientific simulations enabled researchers and foundrymen to analyze entire casting process and the dynamic behavior of a casting system during working conditions [2]. Increased market demands for higher casting yield, minimum design and production lead times, high dimensional accuracy, modern and difficult to cast designs, and improved product quality brings about a need to computationally design a casting process which can eradicate all bottlenecks as observed in a conventional cast product development. Computer aided design and manufacturing (CAD/CAM) together with casting industry standards partially remove these bottlenecks by reducing time and cost in product development. However, CAD/CAM does not address issues such as prediction and minimization of defects (microporosity, misruns, cold shuts etc.) by quickly comparing alternative mold designs with the initial mold design. Casting simulations, on the other hand, not only allow researchers to model, verify and validate the process but also to optimize the design and process parameters before they actually put into practice in a foundry. With such capabilities, these simulations are now viewed as most technologically efficient and economical method to analyze a complete casting process with the prediction of quality and defects of cast products.

The continuous development in casting simulation tools have led them to be utilized in a range of stages of product development such as casting design, process determination, flow pattern, design of tooling, quality control and product stress analysis to name a few. Casting design is important as it influences all subsequent stages of product development. Computer aided casting design allows for optimum casting geometries and features, which can be confirmed by filling simulation, solidification analysis, and stress distribution within the cast product. From process determination perspective, the flow characteristics in a mold are revealed and subsequent solidification behavior can be analyzed, which confirms the optimum mold design, appropriate process routing and process parameters. Defect minimization and quality improvements are also possible by simulating and viewing the filling and solidification behavior and understanding the underlying factors affecting product quality and mechanisms of defect formations. Nevertheless, the critical question remains whether the mechanical performance of the cast product during its service life can be evaluated in the presence of defects already predicted by the casting simulation software.

The work presented here adopts an integrated approach to develop a methodology for cradle to grave analysis of castings in a virtual domain. Casting simulation and mechanical performance simulation softwares are used simultaneously to minimize the casting defects and to predict the life of cast products in the presence of defects respectively. The developed methodology is validated for simple casting geometries through experiments conducted in the laboratory. Probabilistic methods are used for reliability assessment of cast parts under different loading scenarios. The developed simulation-based methodology is then applied to analyze two high valued cast parts from mold design to failure together with their reliability assessment.

1.2 CASTING METHODS AND PROCESSES

Metal casting process is considered to be one of the simplest and direct method of producing a near net shape product. The process essentially needs a mold cavity (made up of sand, ceramic or even steel) of the desired shape where molten metal is poured to get the cast product. In its most usual form, the molten metal is supplied to the mold cavity through pouring basin followed by runner and gating system which allows adequate flow of molten metal within the cavity. During solidification, most metals experience shrinkage and the additional amount of molten metal is supplied through risers or feeders. These additional features are added to casting systems in order to produce sound (pore free) products with minimum defects (sand inclusions, slag, cracks, etc.). The conventional metal casting process begins with designing a mold based on industrial standards such as JICA, ASTM, and SAE etc. and expertise of the foundrymen. Developing an acceptable final mold design is iterative owing to a repetitive cycle of activities such as using a master pattern, gating and riser system design, use of cores and chills if needed, preparation of a mold, melting of metal ,pouring, shakeup of mold , post-processing ,inspection and quality checks. The cast products with the final mold design are reasonably defect free, however, some of the defects remain undetected until the product fails during its service life. Figure 1.1 shows the schematic diagram of a typical metal casting process.

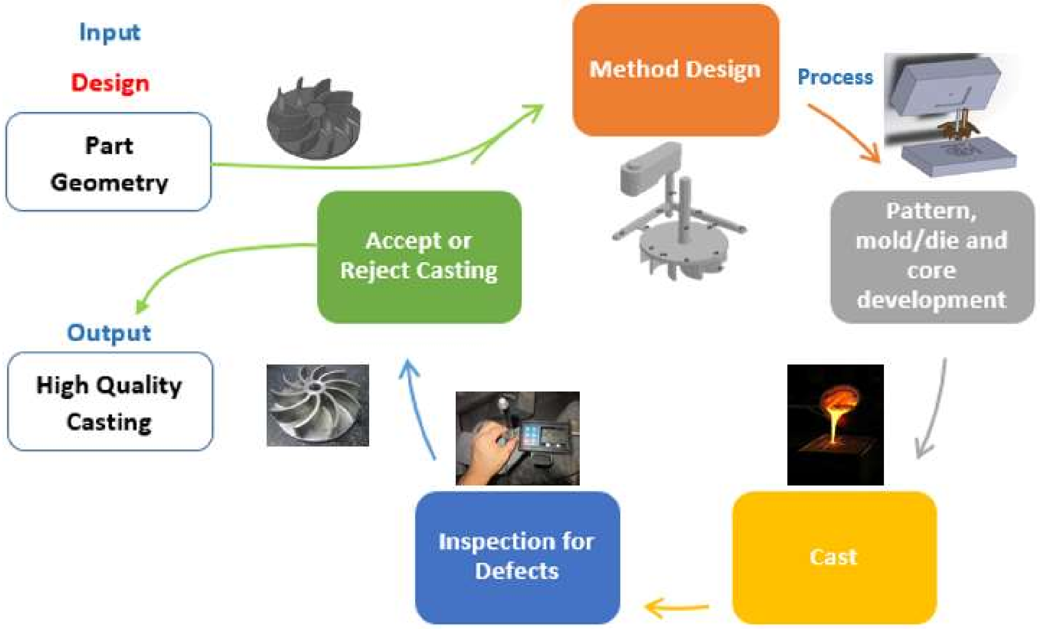

Figure 1.1 Schematic diagram of a typical metal casting process

Modern metal casting is classified based on a variety of parameters. In fact the casting processes can be distinguished based on (a) the type of mold such as sand, permanent, etc., (b) the flow of molten metal in mold cavity under the action of gravity, vacuum, pressure, (c) state of the metal i.e. fraction of metal which is liquid, (d) the state of the mold cavity itself such as solid, gas, air or vacuum. In general, two or more of these processes are combined together. For example, use of green-sand molds and chemically bonded sand molds, semi-permanent molds where mold contains sand and metal components, high pressure or low pressure die casting etc. Figure 1.2 shows a detailed hierarchical classification of various casting processes. A summary of general characteristics of various casting processes is presented in Table 1.1.

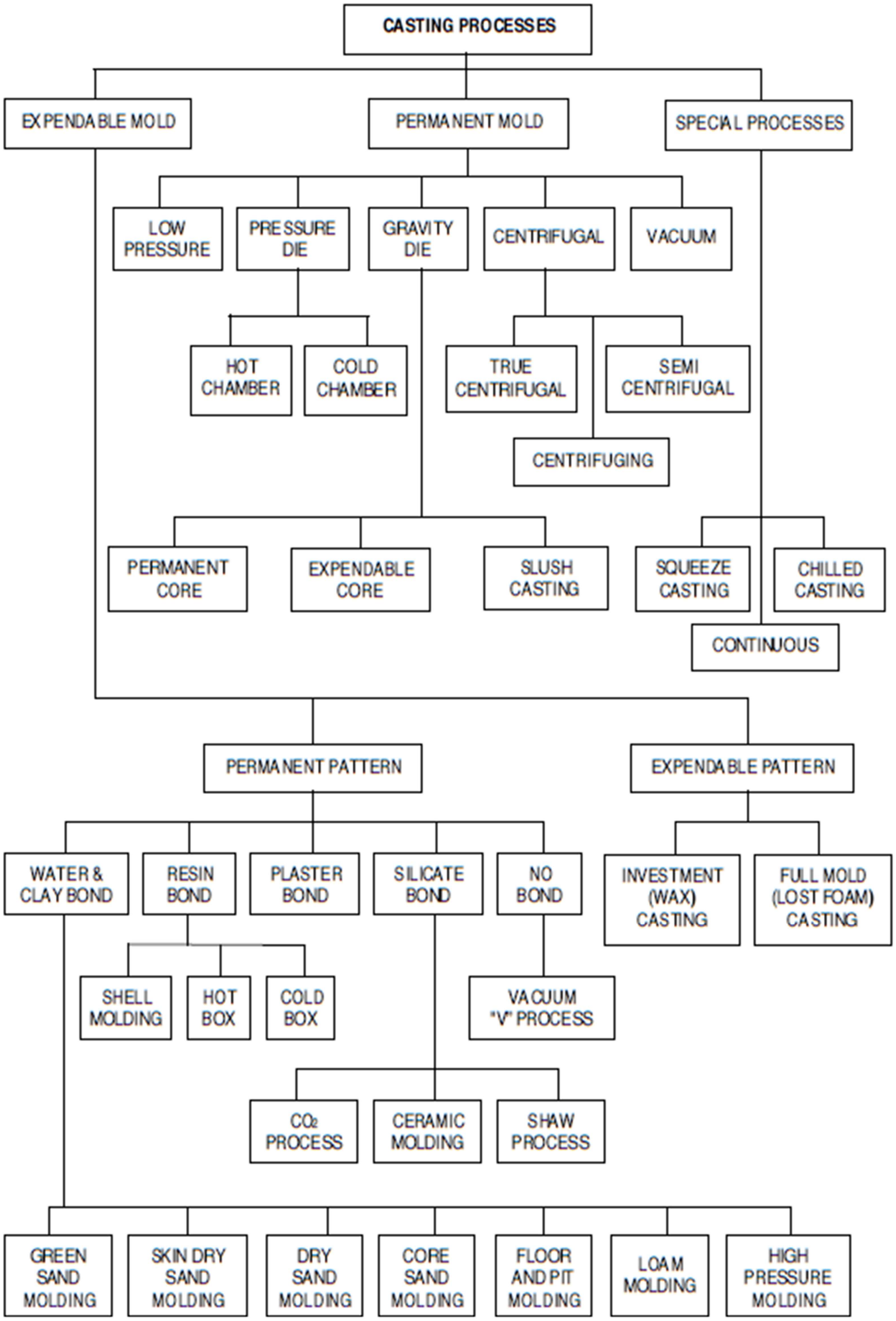

Figure 1.2 Hierarchical classification of various casting processes [3]

Table 1.1 General characteristics of casting processes [4]

	Sand	Shell	Evaporative Pattern	Plaster	Investment	Permanent Mold	Die	Centrifugal
Cast Materials	All	All	All	Nonferrous (Al, Mg, Zn, Cu)	All	All	Nonferrous (Al, Mg, Zn, Cu)	All
Weight (kg)								
Minimum	0.01	0.01	0.01	0.01	0.001	0.1	<0.01	0.01
Maximum	No limit	100+	100+	50+	100+	300	50	5000+
Typical surface finish (R_a in µm)	5-25	1-3	5-25	1-2	0.3-2	2-6	1-2	2-10
Porosity[1]	3-5	4-5	3-5	4-5	5	2-3	3-4	3-4
Shape complexity[1]	1-2	2-3	1-2	1-2	1	2-3	3-4	3-4
Dimensional accuracy[1]	3	2	3	2	1	1	1	3
Section thickness (mm)								
Minimum	3	2	2	1	1	2	0.5	2
Maximum	No limit	-	-	-	75	50	12	100
Typical dimensional tolerance (mm)	1.6-4	±0.003		+0.005-0.010	+0.005	±0.015	±0.001-0.005	0.015
Equipment	3-5	3	2-3	3-5	3-5	2	1	1
Pattern/Die	3-5	2-3	2-3	3-5	2-3	2	1	1
Labor	1-3	3	3	1-2	1-2	3	5	5
Typical lead time[2]	Days	Weeks	Weeks	Days	Weeks	Weeks	Weeks to months	Months
Typical production rate[2] (parts/mold-hour)	1-20	5-50	1-20	1-10	1-1000	5-50	2-200	1-1000
Minimum quantity[2]	1	100	500	10	10	1000	10,000	10-10,000

[1] Relative rating from 1 (best) to 5 (worst)

[2] Approximate values without rapid prototyping technologies. Minimum quantity is 1 with the use of rapid prototyping

1.3 FOUNDRY PRACTICES

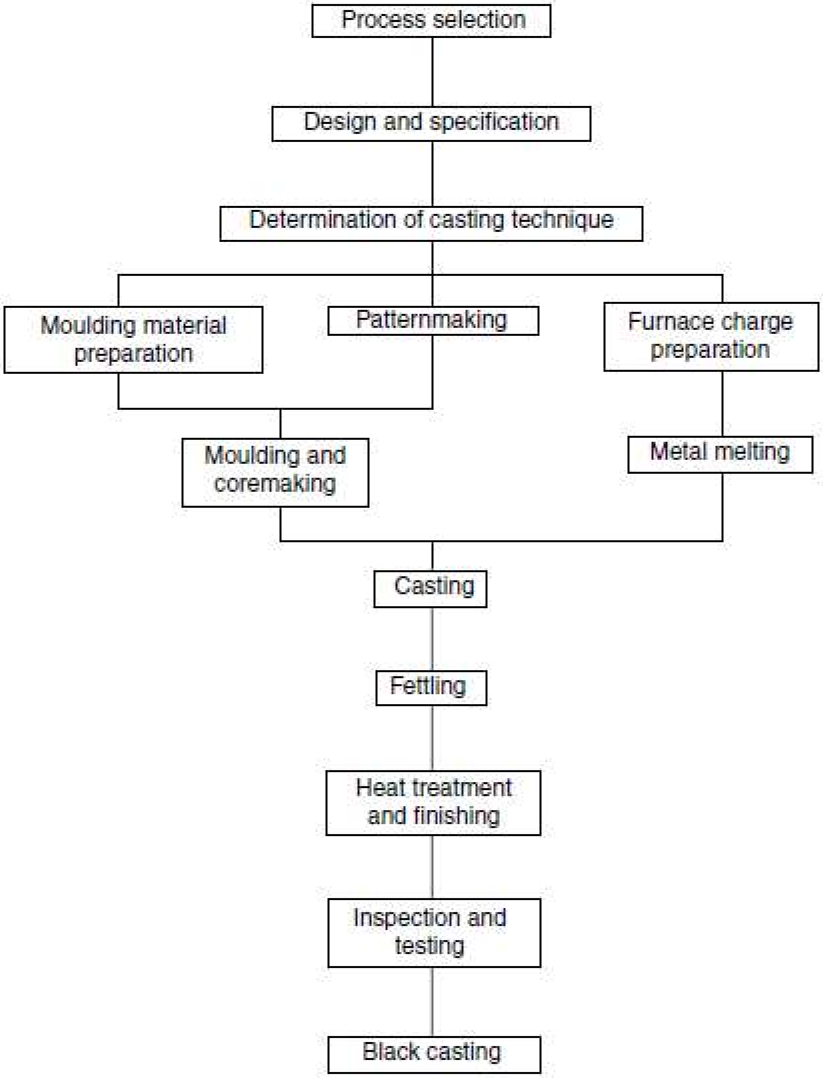

Figure 1.3 Casting process flow diagram in a foundry [5]

As discussed above, casting processes differ from each other in terms of molding technique (expendable or permanent), pattern (expendable or permanent), flow of the melt (pressurized or non-pressurized) etc. However, the general characteristics of a typical foundry process can be fairly explained with respect to a central theme, production of sand castings through conventional molding. The essential steps which follows the sequence from casting design to finished product are presented in Figure 1.3. Most of the casting processes follow the same sequence with slight modifications in the process. This section is mainly focused on important practices in a foundry setup such as molding techniques, pattern making, casting alloys, furnaces for melt preparation, pouring cleaning, and heat treatment etc.

1.3.1 MOLD MATERIALS AND MOLDING TECHNIQUES

Mold materials and molding techniques are exposed to high temperature melt during any casting process. It is of utmost importance to carefully select the appropriate mold material and molding technique in order to obtain high quality cast products. The selection criteria includes but not limited to the type of melt, type of casting, availability of molding materials, mold and core preparation capabilities in foundry, and quality requirements of the consumers. Molds are generally made up of sands, clay and binders (thermoplastic or thermosetting resins) as shown in Figure 1.4. The use of sand molds in metal casting industry is quite prevalent owing to its low cost in comparison to that of a permanent mold, making it the most suitable choice for low and medium production runs [6]. A variety of sands are available, however, all of them should possess some general properties which are as follows.

1. High temperature thermal and dimensional stability
2. Chemically inert with the melt
3. Suitable size and shape of particles
4. Not readily wetted by the melt
5. Economical availability

6. Free from chemicals which produce gases upon heating
7. Consistent in terms of cleanliness, composition, and pH
8. Compatibility with binding agents

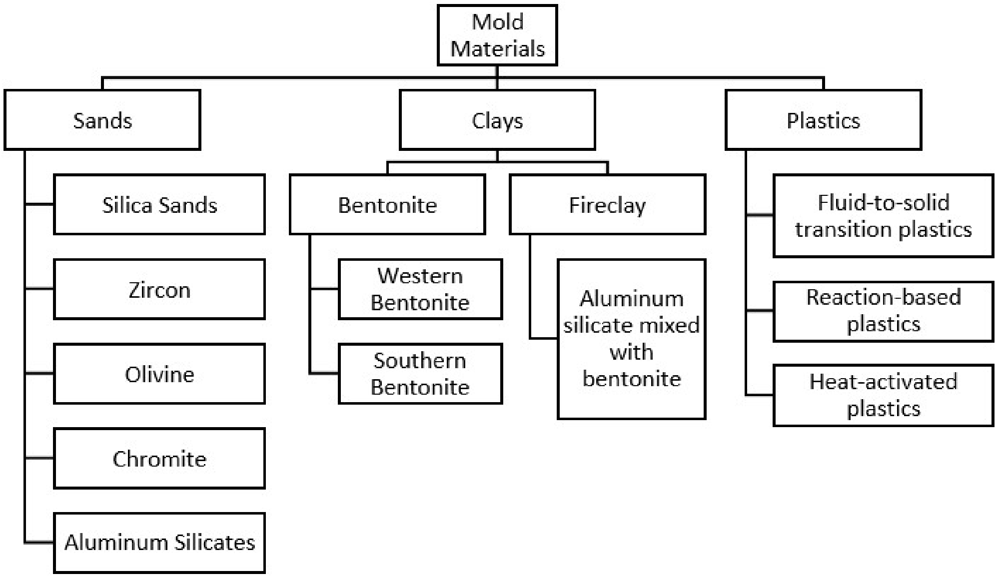

Figure 1.4 Mold material used in a foundry

1.3.2 PATTERNS

Pattern making is one of the crucial steps towards a *"good"* casting. Patterns are an integral component of a casting process as molding material (usually prepared sand) is formed around it to shape the casting cavity. Patterns are prepared using plastics, wood, or even metal depending on the complexity of the part to be cast and the number of cast products required in a batch. Some of the important considerations in pattern design are as follows.

1. Pattern should have an allowance for solid state shrinkage which is an inherent feature of any casting during solidification from melting temperature to room temperature.

2. A draft angle should be provided such that the pattern can be removed smoothly from the mold without destroying it.
3. Inclusion of enough extra stock to take into account the variations that might arise in casting dimensions due to mold preparation, pattern wear etc.

Patterns are design in a number of ways to meet the process requirements and economic considerations [7]. Selection of a particular pattern type is based on number of cast products required, molding and casting technique employed, pattern size, and casting tolerances needed. Some patterns are reusable over a large number of production cycles of sand castings such as solid pattern, split pattern, matchplate pattern, and cope-and-drag patterns. Figure 1.5 shows various pattern types used in sand casting. Besides these commonly used patterns for sand castings, there are special patterns made up of metals and/or low melting temperature substances for various other casting processes.

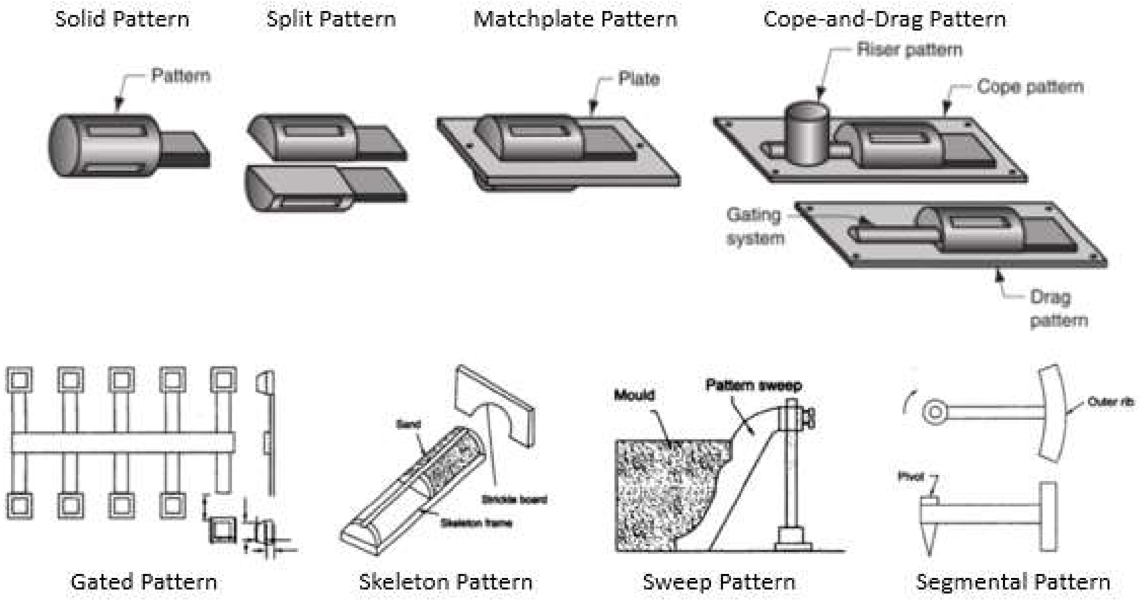

Figure 1.5 Pattern types for sand casting process [8], [9]

1.3.3 CORES

The external shape of the casting can be defined using a pattern as discussed in the section above. If the casting is hollow or it has an inner surface profile, then it requires a core. A core is a full scale model of the interior surface of the cast part [7], [8]. It is an integral part of molds for casting hollow products. During pouring, the molten metal flows between the mold cavity and the core, resulting in the desired hollow casting. The cores are usually prepared with chemically bonded sands and includes shrinkage and machining allowances similar to a pattern. A core can be easily placed inside the mold assembly without any support, however if needed, chaplets (made up of a metal with higher melting temperature as compared to cast metal) are used to hold the core at appropriate position within the mold. Figure 1.6 shows a mold assembly with a core that is supported by chaplets. Any portion of chaplet that protrudes on the final casting is removed during finishing operations.

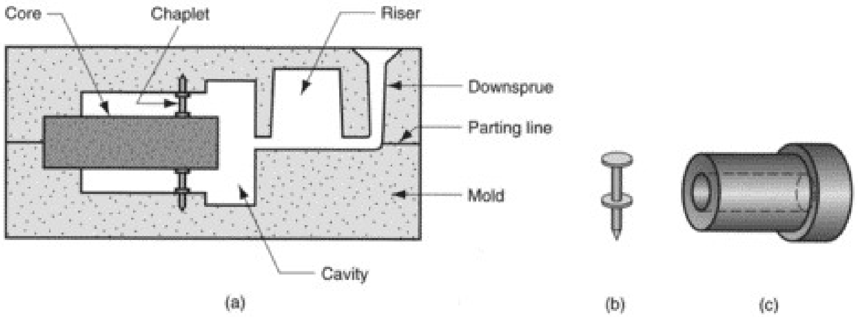

Figure 1.6 (a) Core in a mold supported by chaplets (b) A chaplet design (c) Hollow cast product [7]

1.3.4 PATTERN-LESS CASTING TECHNOLOGY

In more recent years a new technology of additive manufacturing has been developed in order to reduce the casting time and cost. Such techniques are often termed as "Rapid

Casting” processes [10], where no pattern or die is needed. Instead, the mold is prepared by milling in one time. During molding, sand molds and cores can be integrated to reduce the number of sand cores, resulting in a simplified design and reduced allowance of machining [11]. Casting dimension are easy to control in this method. The mold cavity and cores can be synchronously shaped which improves the accuracy of sand mold and casting. Since, no pattern draft is needed, the final castings are found to be less in weight compared to conventional castings. Castings of intricate designs became possible with this method, especially the accuracy of curved surfaces can be maintained and controlled to a great extent.

One of the most promising technologies in pattern-less casting is three dimensional printing, often known as 3D-printig. Three-dimensional (3D) printing is the process of joining material, layer-by-layer, to make objects from 3D model data (usually created by a computer-aided design software or a scan of an existing object)[12]. Figure 1.7 (a) and (b) depicts 3D-printing process and its process flow diagram respectively. This technique has gained popularity in recent past and has resulted in significant improvements in processing speed and minimizing cost [13]. The 3D printed prototypes can be used to directly produce the molds for casting or used as a pattern to produce mold indirectly. Another improvement in the pattern less casting technology is ZCast process where the complex cavities and cores are 3D-printed using a ceramic material. ZCast process is limited to cast only non-ferrous alloys. In contrast to conventional metal casting which is constrained in dimensional accuracy by pattern extractability, the layer by layer construction allows creating complex objects, without restricting the undercuts provided that the unconsolidated powder can be removed from the cavity [14]. This method simply eliminates the pattern creation phase in conventional casting and thus reduces production time from weeks to days [15].

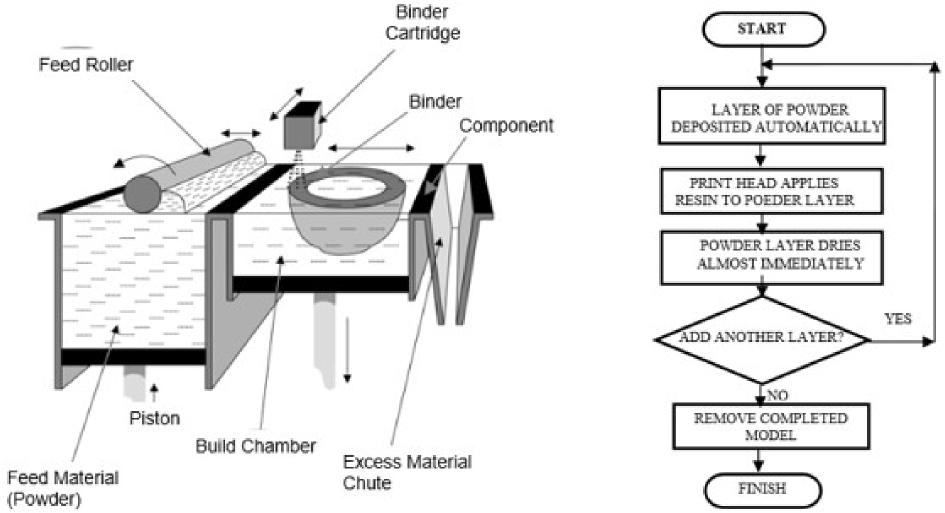

(a) (b)

Figure 1.7 (a) 3D printing process (b) Process flow diagram of 3D printing [10],[16]

1.3.5 CASTING ALLOYS

The development in casting techniques enable to cast many alloy compositions. These alloys can be broadly categorized in two categories: Nonferrous Alloys and Ferrous Alloys as shown in Figure 1.8.

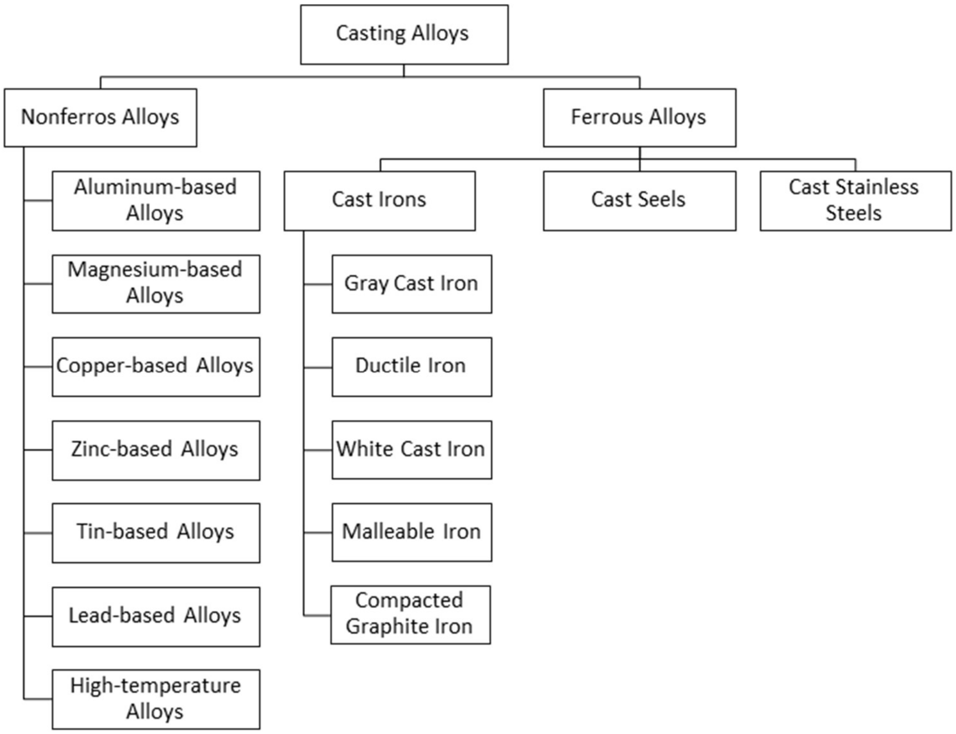

Figure 1.8 Classification of Casting Alloys

1.3.6 FURNACES AND MELTING PRACTICE

The melting of cast metals is an essential step in any casting process. This requires heat input which is supplied through a furnace. These furnaces are charged with melting stock which consists of metal, alloying elements, and other materials such as flux and slag-forming products. The function of fluxes is to remove impurities and dissolved gases from the melt to be poured in mold cavity. Some of the commonly used furnaces in a foundry are *Electric Arc Furnaces (cast iron and steel)*, *Induction Furnaces (cast iron, steel, and aluminum), Crucible Furnaces (aluminum and other non-ferrous),* and *Cupola Furnace (cast iron).*

Electric arc furnaces heat directly using an arc between the graphite electrodes and the charge. Induction furnace heats and melts the charge by inducing eddy currents into it with a high power, high frequency alternating current. Gas fired crucible furnaces do not have a direct contact of molten metal and burning fuel mixture, instead, the combustion of natural gas is performed immediately outside a crucible carrying the charge. A cupola furnace utilizes the metallurgical coke as the fuel.

1.3.7 POURING, CLEANING AND HEAT TREATMENT

The movement of molten metal from furnace to the mold is a critical step in a casting foundry due to very higher temperatures of the melt. This is usually done by ladles, a common name for containers that contain melts after taking it out from the furnace. Different type of ladles are available in a foundry most common of which are crane ladle and a two-man ladle. A problem faced during pouring is the introduction of oxides into the mold cavity which results in casting defects. In order to avoid such occurrences either fluxes are used to avoid oxidation or filters are used to catch the oxides during pouring. An alternative solution to this problem is to allow flow of molten metal in the mold from bottom of the ladle since the top surface is usually accumulated with the oxides.

Once the molten metal is poured and solidified in the mold cavity, a number of additional operations have to be done to obtain a finished cast product. These additional operations often referred to as *Cleaning* in a foundry include trimming, removal of cores (if added in mold), cleaning of cast surface, inspection for quality check, and repair if needed. The removal of all other components attached to cast parts such as sprue, runners, risers, parting line flash, fins, chaplets etc. is called trimming. Trimming may require hammering, shearing, hack-sawing, band-sawing, abrasive wheel cutting or any other torch cutting methods. If final casting contains cores, they are removed either by manual or mechanical shaking or in some instances the bonding agent in core is dissolved chemically.

Surface cleaning of the final cast product is important, the extent of which depends on the process used for casting. Sand castings need more cleaning whereas castings from permanent mold processes requires minimal or even no cleaning at all. Some cleaning methods for sand castings include wire brushing, buffing, air-blasting with metal shot or coarse sand grits, tumbling, and chemical pickling etc. The quality of casting is then evaluated during inspection through various techniques during which all casting defects are identified and repaired if required. Last of all, castings are often subjected to heat treatment either to improve properties for subsequent machining operations or to obtain required properties for application of cast parts.

1.4 CASTING DEFECTS

The process of casting involves a host of parameters which increases the probability of having defects in the final cast product. These defects may arise due to cast material, product geometry, and process techniques. While some of the casting defects are visual which affect the appearance of product, others can have adverse effects on the performance of castings in service. It is, therefore, important to analyze these defects together with their root causes and possible remedies. Casting defects can be classified into four categories as (a) filling related defects (b) shape related defects (c) thermal defects and (d) defects by appearance. Figure 1.9 shows various types of defects under each of these categories. Possible causes are remedies for different defects are listed in Table 1.2.

Table 1.2 Casting defects, causes and remedies[17]

Casting Defect		Definition	Causes	Remedies
Filling related defects	Blowhole	Cavity defect formed by gases entrapped during solidification	1) Inadequate venting 2) Low gas permeability of sand	1) Improve venting 2) Use coarse sands for improved gas permeability
	Sand burning	Sticking sand to the casting at higher temperatures	1) Uneven mold compaction 2) Very high melt temperature 3) Uneven distribution of inflowing metal	1) Ensure uniform compaction 2) Even out incoming metal flow 3) Reduce pouring rate
	Sand inclusion	Slag inside of metal castings	1) Uneven mold compaction 2) Pouring rate too high 3) Ladle too far above pouring basin 4) Pouring time too long	1) Ensure uniform compaction 2 Avoid high pouring rates 3) Shorten pouring time 4) Improve distribution of gates
	Cold shut	When two metal streams do not fuse together properly due to poor gating system	1) Lack of fluidity in melt 2) Faulty design 3) Faulty gating	1) Adjust proper pouring temperature 2) Modify design 3) Modify gating system
	Misrun	Incomplete casting defect when metal is unable to fill complete mold cavity	1) Lack of fluidity in melt 2) Faulty design 3) Faulty gating	1) Adjust proper pouring temperature 2) Modify design 3) Modify gating system
	Porosity	Defect arises due to air entrapment within the mold	1) Low metal pouring temperature 2) Lack of fluidity in melt 3) Pouring too slow 4) Interrupted pouring	1) Increase metal pouring temperature 2) Improved melt fluidity 3) Fast pouring 4) Adequate venting of molds and cores
Shape related defects	Mismatch defect	Defect due to shifting molding flashes. It causes the dislocation at parting line	1) Improper positioning of cope and drag 2) Loose box pins, inaccurate pattern dowel pins	1) Check pattern mounting on match plate rectify, correct dowels 2) Proper molding box and closing pins
	Distortion or warp	Distortion due to warpage	Residual stresses in casting	Heat treatment

	Flash defect	Unwanted, excess material which forms at parting surfaces	1) Bending, crowning or stretching of dies 2) Insufficient machine clamp-up 3) Cavities offset from center of plate	Weight down the mold
Thermal defect	Cracks or tears	Lines on the surface of castings which separates it without breaking	1) Shrinkage of casting 2) Uneven or excessive ejection forces 3) Insufficient draft 4) Excessive porosity	1) Reduce pouring temperature 2) Avoid superheating of melt 3) Use chills and proper feeders 4) Avoid early knockout 5) Reduce sharp corners
	Shrinkage	When feed metal is not available to compensate for shrinkage during solidification	Difference in alloy density in molten and solid state	Ensure liquid metal under pressure continues to flow into the voids as they form
Defects by appearance	Metallic projection	Joint flash or fins	1) Clearance between two elements of the mold 2) Poorly fit mold joint	Care in core setting and mold assembly
	Cavities	Blowholes, pinholes, smooth-walled cavities	Gas entrapment during solidification	1) Appropriate venting 2)Increased gas permeability of mold and cores
	Discontinuities	Hot cracking	1) Rough handling 2) Excessive temperature at shakeout	1) Care in shakeout 2) Proper handling 3) Sufficient cooling in mold
	Incorrect dimension or shape	Distorted castings due to improper ramming of mold	Insufficient rigidity of pattern or pattern plate to withstand the ramming pressure applied to the sand	Assure adequate rigidity of patterns and pattern plate
	Defective surface	Flow marks	Oxide films which lodge at the surface	1) Increased mold temperature 2) Lower pouring temperature 3) Modify gating system

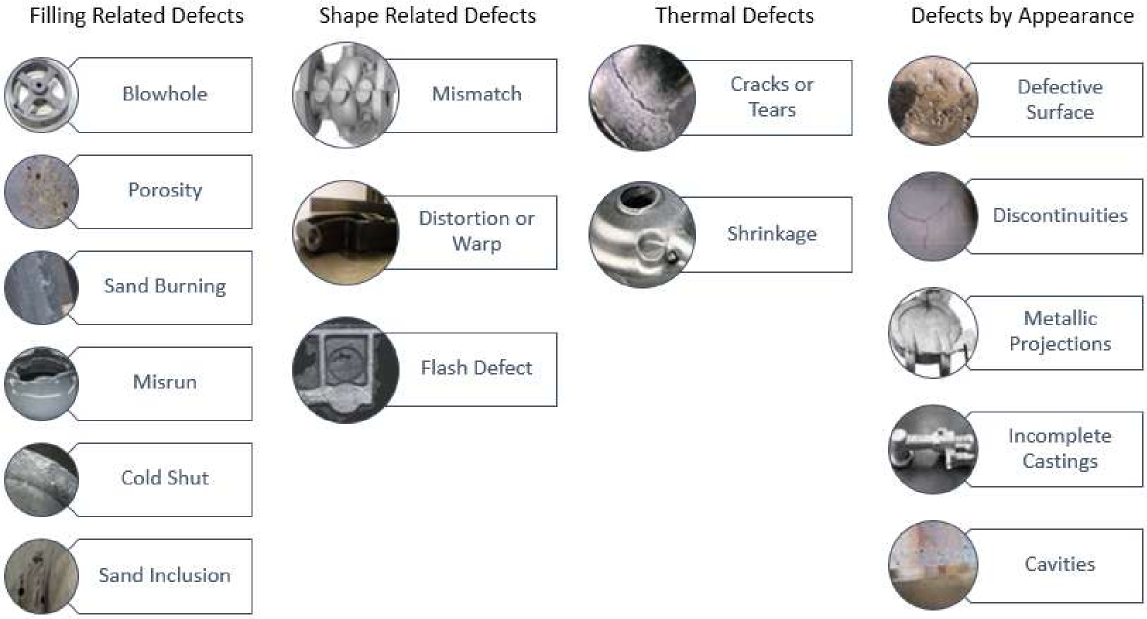

Figure 1.9 Types of casting defects [17]

1.5 DESIGN CONSIDERATIONS IN METAL CASTING

A good casting design often results in sound cast products free from defects. The casting design comprises of six steps [18] which are as follows.

1. Physical designing of the parts to be cast: size, shape, tolerances, dimensional changes during the process and others.
2. Material selection: mechanical and physical properties, castability, fluid flow characteristics, section size sensitivity.
3. Pattern making for mold and cores: gating and risers design, fluid flow and heat transfer
4. Casting process selection: casting size, metal casting limitations, dimensional requirements, and production costs.
5. Post casting procedures: Machining, heat treatment etc.

6. Casting product evaluation and quality control

Owing to the iterative nature of the process, it requires excellent communication between the personnel involved throughout the process. Figure 1.10 demonstrates a complete casting design process envelop where the needed communication is represented by the arrows. It is important for a casting designer to analyze the material for its properties and limitations, process capabilities and possible obstacles to produce that casting. The key considerations by a casting designer include but not limited to minimal changes in section size, minimization/elimination of sharp corners, understanding of mechanical properties desired in the cast product, tolerancing, locating and handling requirements, process limitations, machining requirements, and use of statistical methods for process control [18]. During casting design, the conventional way of making a part must be questioned and knowledge of new technologies should be employed to stretch the design envelop as much as possible.

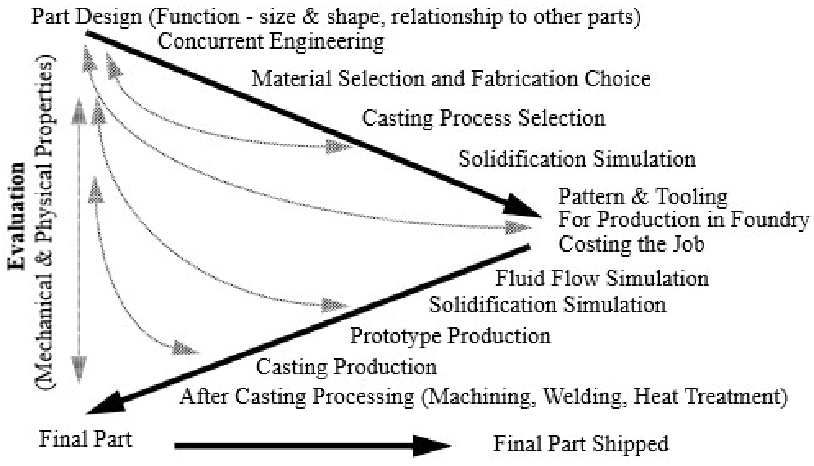

Figure 1.10 Casting process design envelop [18]

The next phase is to decide upon if the part can be produced using the selected material and the casting process in an economical manner. Pattern makers and method engineers utilize the knowledge of fluid flow and heat transfer to design the mold and cores (if necessary) for the part to be cast. It is important at this stage to computationally analyze the filling and solidification sequence of the casting process for which various casting simulation softwares are available. These simulations not only provide the insight of the process but also reduces the time between the design and prototype castings by optimizing the gating and riser system. This whole process requires designer, pattern engineer and the method engineer to be well communicated as shown by the dashed lines in Figure 1.10. The final estimates of cost are provided by planning people in foundry after careful economic consideration. If the cost is within the realm of reality, it leads to the production of pattern for casting the final product. However, if the cost is too high, the design has to be modified critically from scratch. Some of the important considerations by a casting engineer during the process are evaluation of dimensional accuracy, quantification of microstructural integrity (presence of required micro-constituents, casting defects etc.), understanding of response to machining, heat treatment or welding, determination of mechanical properties in critical sections etc.

In more recent years, rapid prototyping is being utilized to minimize production time for cast products. Fast pattern production is accomplished through technologies such as stereolithography, selective laser sintering, fused deposition modeling, laminated object manufacturing, direct shell production etc. Casting engineer must also aware of the dimensional tolerances and understand the effect of different casting processes on the dimensional accuracy of the cast products. Certainly, each process (green sand vs. lost foam vs. investment) provides a different attainable dimensional accuracy which must be understood prior to select the process for any particular product. It is evident from

Figure 1.10 the design improvements can be suggested at this stage to maximize production and minimize cost and difficulty of the process simultaneously.

The design considerations discussed above are documented in the form of industrial standards which are followed by foundrymen. Some of the well-known organizations for developing casting standards are American Society for Testing and Materials (ASTM), American Foundry Society (AFS), Society of Automotive Engineers (SAE), and Japan International Cooperation Agency (JICA). These standards are developed for proper utilization of different cast materials and casting processes to produce castings used in various engineering applications such as valves, flanges, fittings, and other pressure containing parts for high- and low-temperature applications.

1.6 OBJECTIVES OF THE WORK

The objectives of the current work are as follows.

1. Deployment of modern casting simulation tools backed by intensive material properties (mold material and casting material) to develop an almost defect-free mold and thus eliminate several trial-and-error attempts as currently practiced in most traditional foundries.

2. Development of an integrated approach of utilizing casting simulation results and defects obtained in the products, then incorporate this knowledge in FEM through an interface software. Expected loading conditions in service are used to predict the life of simple and moderately complex parts.

3. Validation of methodology by comparing the experimental results with the simulated results. Experimental program will be limited to simple parts in this case for which the testing equipment are available.
4. Reliability assessment of cast parts using probabilistic methods to determine the survival/failure of components during service life.
5. Recommendations to improve the entire casting process by a validated simulation-based approach leading to defect minimization and improved service life.

1.7 APPROACH AND OUTLINE OF WORK

The current work involves the formulation of a methodology for mold design optimization and reliability assessment of cast parts and the application of this methodology to some moderately complex castings. Based on the objectives, the work has been divided into three main parts. In the first part, the development of initial mold design for casting standard test specimens using standard practices and its simulation based optimization is presented. The second part is focused on experimental work which includes casting of test specimens using optimized mold design and mechanical testing. The third part of the study covers the finite element simulations of mechanical testing, life prediction, and reliability assessment of cast parts. The applications of developed methodology to a valve body and a spring flap is also presented. A graphical summary of all works carried out in the dissertation is presented in Figure 1.11.

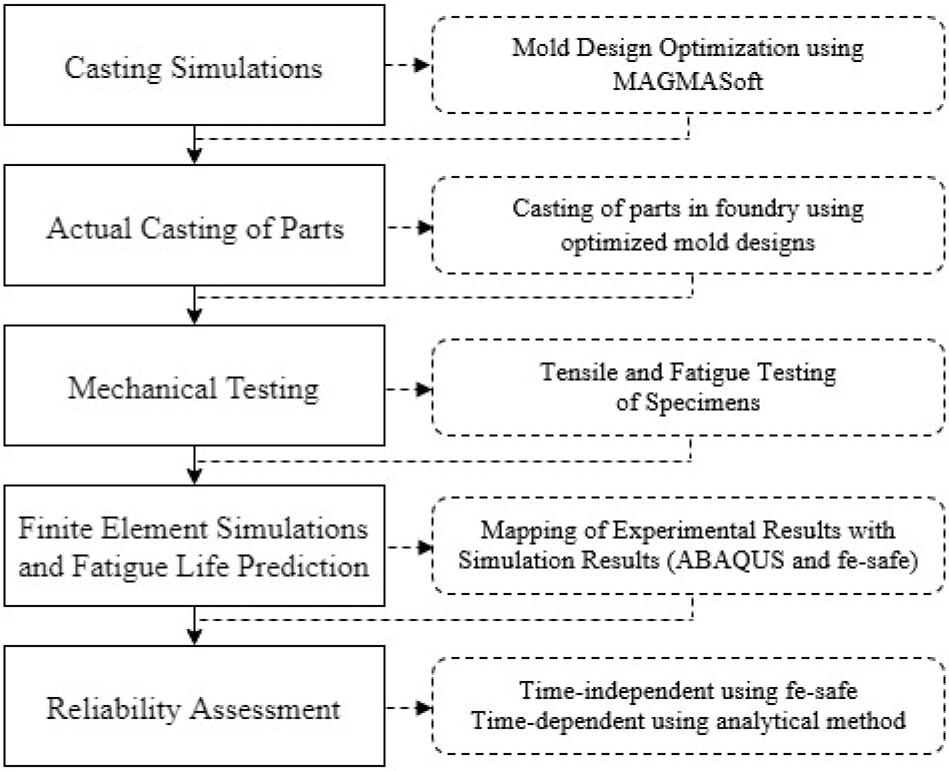

Figure 1.11 Graphical summary of work done as part of dissertation

The dissertation consists of 9 chapters. Chapter 2 presents mathematical background of various aspects in a metal casting process. Chapter 3 presents a literature review of casting simulation softwares and use of these softwares in simulation-based casting. In Chapter 4, the casting simulations for different mold designs are presented. The details of initial mold designs using standards and experience, and optimized mold designs using MAGMASoft are included. Simulation results for filling and solidification sequence, residual stress distribution, and defects prediction are presented. The experimental work including casting using optimized mold designs and mechanical testing are presented in Chapter 5. Chapter 6 reflects on the finite element simulations of mechanical testing and fatigue life prediction of cast specimens. The process of porosity integration in finite element simulations is also discussed in the same chapter. Chapter 7 presents the reliability assessment of cast parts using concepts of probability and strength-stress interference model for reliability computations. Various scenarios are considered in reliability estimation such as time-independent and time dependent load-induced stresses, zero percent and some percent variability in the load-induced stresses, and variability in materials strength. The applications of developed methodology from Chapter 4 to Chapter 7 are presented in Chapter 8. Two moderately complex parts i.e. steel spring flap used in automotive suspension system and a ductile iron valve body are considered for which casting simulations, FE simulations, fatigue lives prediction, and reliability assessments are done and presented. Finally, conclusions and recommendations for future work are summarized in Chapter 9.

CHAPTER 2

MATHEMATICAL BACKGROUND

This chapter presents the mathematical background of various aspects in a metal casting process and is aimed to understand the mathematical underpinnings of melting, pouring, cooling and solidification, casting yield etc. These mathematical relationships are building blocks in the development of a casting simulation software and thus should be carefully implemented for accurate representation of the actual phenomena taking place during a casting process.

2.1 MELTING

The molten metal for metal casting processes is derived from melting the raw material, often called *charge*. Melting is practiced in metal casting industries either by combustion of fossil fuels or by using electrical energy. The heat energy required to melt is the sum of

1. The heat to raise the temperature to the melting point
2. The heat of fusion to convert it from solid to liquid
3. The heat to raise the molten metal to the desired pouring temperature (superheat temperature)

Mathematically,

$$H = \rho V\left[C_s(T_m - T_o) + H_f + C_l\left(T_p - T_m\right)\right] \tag{2.1}$$

where, H is the heat energy required to melt the metal (Joules), ρ is the density (kg/m^3), V is the volume (m^3), C_s is the specific heat for solid metal (J/g - °C), C_l is the specific heat for liquid metal (J/g - °C), T_m is the melting temperature (°C), T_o is the starting temperature (°C), T_p is the pouring temperature (°C), and H_f is the heat of fusion (J/g).

The melting time (in seconds) is estimated by

$$Time = \frac{Energy}{Power} \tag{2.2}$$

The efficiency of furnace is taken into consideration while estimating melting time. A range of losses are incurred during melting which are due to undesired heat transfer by conduction, convection and radiation, stack loss, and metal loss. These losses can be quantified based on design of furnace, the fuel used, and the means of supplying heat to the metals. It is reported that typical metal furnaces are thermally efficient from 7 percent to 76 percent, together with a range of metal loss between 0.75 percent to 6 percent [19]. Although electric melting furnaces are 3 times more efficient than gas-fired furnaces, the cost of electricity is also 3 times that of natural gas when compared based on the energy content of electricity (Btu/kWh) and natural gas (Btu/ft^3). However, in terms of dross, electric furnaces generate ~1% dross which is less than gas-fired furnaces with ~3% dross generation.

2.2 POURING ANALYSIS

Pouring refers to transfer of molten metal from ladle to the mold cavity. In order to produce a good casting, it must be ensured that the melt flows into all parts of the mold, especially in the main cavity for casting, before solidification. Pouring is influenced by some factors such as pouring temperature, pouring rate and turbulence. Certainly pouring temperature is higher than the solidification temperature of the metal, and the difference between the pouring temperature and solidification temperature of the metal is termed as *superheat* as shown in Figure 2.1. Pouring rate also plays an important role on the quality of casting and it must be carefully controlled during pouring [20], [21]. A faster pouring rate may result in turbulence whereas a slower pouring rate may cause molten metal to solidify even before the mold is completely filled. Moreover, turbulence can accelerate oxide and void formation together with mold erosion.

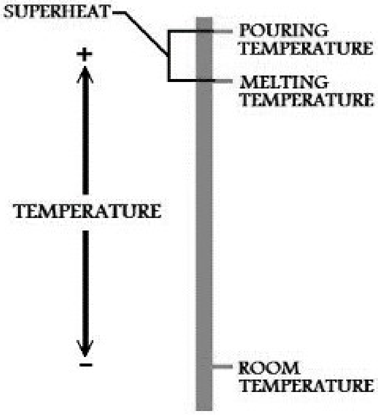

Figure 2.1 Superheat (the difference between pouring and solidification temperature)

It is important to understand the basic principles of fluid flow for effective pouring. Figure 2.2 represents the schematic diagram of a typical casting system. The top of the pouring basin is considered as *reference* and termed as point 0. The locations where pouring basin and sprue end are considered as point 1 and 2 respectively. Any location between point 1 and point 2 is considered as x.

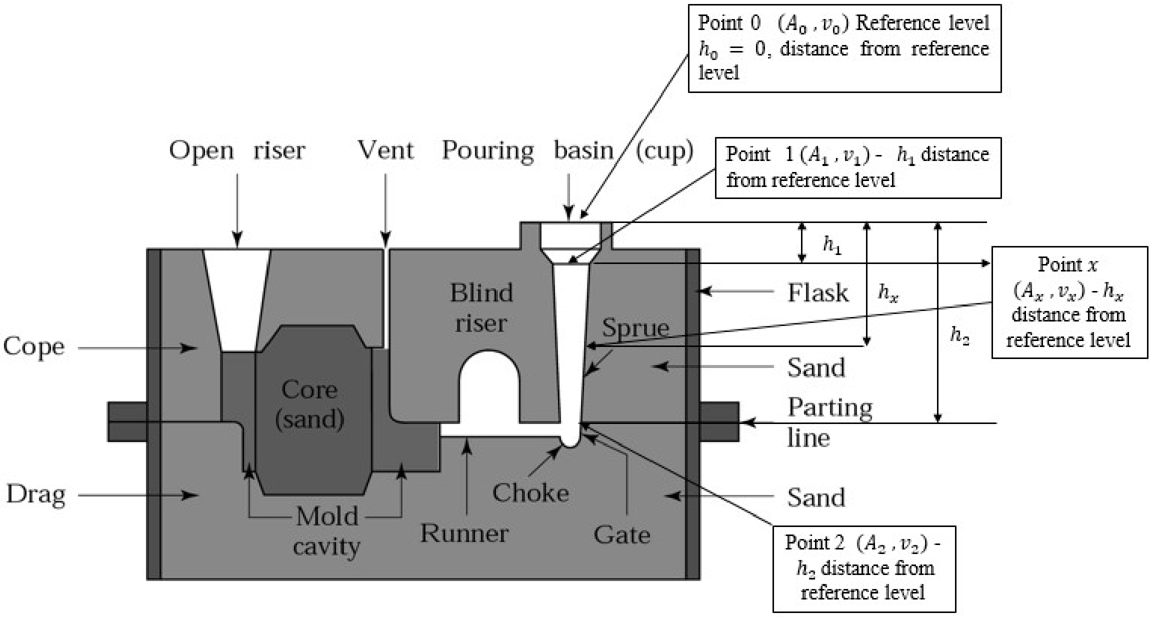

Figure 2.2 Schematic diagram for mathematical analysis of a typical casting system

2.2.1 BERNOULLI'S THEOREM

Assuming steady state, incompressible, and inviscid flow, the application of Bernoulli's theorem between two points 1 and 2 leads to

$$P_1 + \frac{\rho {v_1}^2}{2} + \rho g h_1 = P_2 + \frac{\rho {v_2}^2}{2} + \rho g h_2 + f \tag{2.3}$$

or

$$\frac{P_1}{\rho g} + \frac{{v_1}^2}{2g} + h_1 = \frac{P_2}{\rho g} + \frac{{v_2}^2}{2g} + h_2 + f \tag{2.4}$$

Where, P is the pressure (N/mm^2), g is the acceleration due to gravity (m/s^2), ρ is the density (kg/m^3), h is the height (m), v is the velocity (m/s), and f represents the losses due to friction. By applying Bernoulli's theorem at points 0 and 1

$$\frac{P_0}{\rho g}+\frac{{v_0}^2}{2g}+h_0=\frac{P_1}{\rho g}+\frac{{v_1}^2}{2g}+h_1+f \tag{2.5}$$

Since point 0 is reference, assuming no frictional loss and same pressure $P_0 = P_1$,$v_0 = 0$ and $h_0 = 0$, the Bernoulli's Law reduces for points 0 and 1 to

$$h_1=\frac{{v_1}^2}{2g} \tag{2.6}$$

$$v_1=\sqrt{2gh_1} \tag{2.7}$$

Similarly, by applying Bernoulli's theorem between points 0 and 2

$$\frac{P_0}{\rho g}+\frac{{v_0}^2}{2g}+h_0=\frac{P_2}{\rho g}+\frac{{v_2}^2}{2g}+h_2+f \tag{2.8}$$

and with the same assumptions i.e. no frictional loss and same pressure $P_0 = P_2$,$v_0 = 0$ and $h_0 = 0$,

$$h_2=\frac{{v_2}^2}{2g} \tag{2.9}$$

$$v_2=\sqrt{2gh_2} \tag{2.10}$$

2.2.2 CONTINUITY EQUATION

Since the mass is conserved along a line of flow, by using continuity,

$$Q=A_1v_1=A_2v_2 \tag{2.11}$$

where, A_1 and A_2 are the cross-sectional areas (m^2) and v_1 and v_2 are the velocities (m/s) at points 1 and 2 respectively.

Similarly, applying Bernoulli's theorem and continuity equation at point 0 and x with the same assumption that no frictional loss and same pressure at all points within the mold $P_0 = P_x$,$v_0 = 0$ and $h_0 = 0$,

$$h_x = \frac{{v_x}^2}{2g} \tag{2.12}$$

$$v_x = \sqrt{2gh_x} \tag{2.13}$$

and

$$Q = A_1 v_1 = A_x v_x \tag{2.14}$$

$$Q = A_1\sqrt{2gh_1} = A_x\sqrt{2gh_x} \tag{2.15}$$

Or

$$A_x = A_1\sqrt{\frac{h_1}{h_x}} \tag{2.16}$$

If $h_x = h_2$, then

$$\frac{A_2}{A_1} = \sqrt{\frac{h_1}{h_2}} \tag{2.17}$$

2.2.3 MOLD FILLING TIME

The mold filling time can be computed as follows.

$$t_f = \frac{V}{Q} \tag{2.18}$$

where, t_f is the mold filling time (sec), V is the volume of the mold (m^3), and Q is the volume

2.2.4 REYNOLD'S NUMBER

The nature of flow (laminar or turbulent) of molten metal within the mold can be determined using Reynold's number (Re) as follows.

$$Re = \frac{\rho v D}{\eta} \tag{2.19}$$

where, ρ is the density (kg/m^3), v is the velocity (m/s), D is the characteristic length (m), and η is the viscosity ($N\ s/m^2$). The flow is laminar if $Re \leq 2000$, turbulent if $Re \geq 20{,}000$, and mixture of laminar and turbulent if Re is in between 2,000 and 20,000.

2.2.5 GATING DESIGN

Gating design plays an important role in overcoming the difficulties during pouring such as appropriate pouring rate, turbulence, excessive temperature loss, gas entrapment and dross formation. Gating system is design based on both metal and mold compositions. For example, for low melting point metals and alloys, a detailed gating design is needed to avoid dross such as oxides. On the other hand, for cast iron, short metal paths are designed to avoid a high pouring temperature. Also, gating design for ceramic mold is not similar to normally used for a permeable sand mold [22].

In general, gating designs are classified into three categories: (i) vertical gating, (ii) bottom gating, and (iii) horizontal gating. Vertical gating works with the gravity driven flow where molten metal is poured into the mold with atmospheric pressure at the base. However, a bottom gating design fills the mold from bottom to top thereby avoids the splashing and oxidation which otherwise observed in a vertical gating design. Horizontal gating design is not unique except providing additional horizontal channels for proper distribution of the melt in the mold with minimum turbulence. Figure 2.3 (a) and (b) represents a vertical and horizontal gating design respectively.

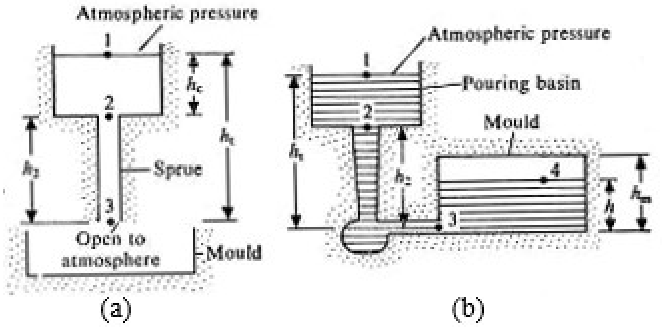

Figure 2.3 Types of gating system (a) vertical and (b) horizontal [22]

As discussed earlier, the principles of fluid flow can be used to analyze the two gating designs presented in Figure 2.3. In Figure 2.3(a) with vertical gating design, by applying Bernoulli's theorem between points 1 and 3 assuming that $P_1 = P_3, v_1 = 0$ and no frictional losses,

$$gh_t = \frac{{v_3}^2}{2} \tag{2.20}$$

$$v_3 = \sqrt{2gh_t} \tag{2.21}$$

where, g is the acceleration due to gravity (m/s^2) and v_3 is the velocity (m/s) of the melt at the gate and can be represented as v_g. The mold filling time in this gating design can be computed using Equation (2.18) as

$$t_f = \frac{V}{A_g v_3} = \frac{V}{A_g v_g} \tag{2.22}$$

where, A_g is the cross-sectional area of the gate (m^2) and V is the volume of the mold (m^3).

Similarly, for bottom gating design in Figure 2.3(b), energy balance between points 1 and 3 leads to

$$gh_t = \frac{P_3}{\rho} + \frac{{v_3}^2}{2} \tag{2.23}$$

where, ρ is the density (kg/m^3) of liquid metal, P_3 is the pressure at point 3, and h_t is constant. Next, by applying Bernoulli's theorem between point 3 and 4 with the assumptions that v_4 is very small and all the kinetic energy is lost after the liquid metal enters the mold, the equation will be

$$gh = \frac{P_3}{\rho} \tag{2.24}$$

From Equations (2.23) and (2.24), the velocity of the melt at gate can be obtained as

$$v_g = v_3 = \sqrt{2g(h_t - h)} \tag{2.25}$$

Equation (2.25) represents the velocity of a jet discharging against a static head h making the effective head as $(h_t - h)$. Let the height of metal in mold increases by dh in time interval dt, A_m and A_g are the cross-sectional areas of the mold and gate respectively. Using continuity

$$A_m dh = A_g V_g dt \tag{2.26}$$

From Equations (2.25) and (2.26)

$$\frac{1}{\sqrt{2g}}\frac{dh}{\sqrt{h_t - h}} = \frac{A_g}{A_m}dt \tag{2.27}$$

At $t = 0$, $h = 0$, and at $t = t_f$, $h = h_m$, the integration of Equation (2.27) gives

$$\frac{1}{\sqrt{2g}}\int_0^{h_m}\frac{dh}{\sqrt{h_t - h}} = \frac{A_g}{A_m}\int_0^{t_f}dt$$

or

$$t_f = \frac{A_m}{A_g}\frac{1}{\sqrt{2g}}2(\sqrt{h_t} - \sqrt{h_t - h_m}) \tag{2.28}$$

If a riser is added to compensate the shrinkage from pouring temperature then the time to fill up the riser should also be considered in mold filling time. Generally, open risers are filled up to the level of pouring sprue, thus, the time to fill up the riser is estimated by replacing A_m with A_r (cross-sectional area of the riser) and h_m with h_t in Equation (2.28).

2.2.6 FLUIDITY

The fluidity is defined as the ability of molten metal to flow easily before being stopped by solidification [23]. Primarily, fluidity is a function of freezing range of the alloy (ΔT) and the degree of superheat (pouring temperature – liquidus temperature). Besides, these two temperatures, fluidity also depends on mold design and dimensions, mold material and surface characteristics, pouring rate, and the associated heat transfer mechanisms. Moreover, the characteristics of molten metal also influence fluidity. For example high viscosity and surface tension reduces fluidity, small amount of alloy additions to pure metals decreases fluidity, inclusions (insoluble particles) affects fluidity, and higher heat of fusion increases fluidity etc. [24]. Figure 2.4 depicts the fluidity as a function of superheat and alloy content. It can be observed that fluidity of pure metals and eutectics, with a freezing range of zero, is the greatest. Large freezing range alloys often have reduced fluidities. However, all metals and alloys show high fluidity with increasing superheat.

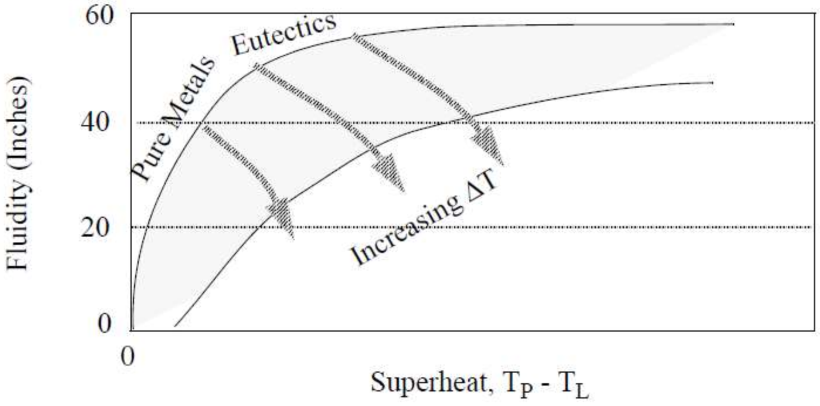

Figure 2.4 Fluidity as a function of superheat and alloy content

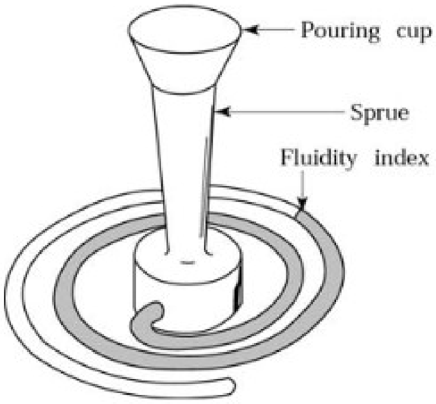

Figure 2.5 Schematic diagram of spiral test for fluidity measurement [23]

Since fluidity depends on a host of variables, it is not feasible to determine it theoretically, and therefore, empirical methods are used to do so. A common method to estimate fluidity of molten metal is spiral test as shown in Figure 2.5, where a spiral tube is cast and the length to which molten metal penetrates the spiral represents the fluidity index. The empirical relationship to determine fluidity could be obtained from many experiments done on a particular casting alloy. One such example is gray cast iron which is one of the most widely used metal in metal casting applications. Empirical fluidity spiral data from many experiments on gray cast iron yields

$$\text{Fluidity} = 14.9 \times CF + 0.05T - 155 \tag{2.29}$$

where, fluidity is measured in inches, T is the pouring temperature (°F), and CF is the composition of iron given by

$$CF = \%C + \frac{1}{4}\%Si + \frac{1}{2}\%P \tag{2.30}$$

It is obvious that the fluidity needs to successfully fill a mold depends upon the section size of cast part to be produced. Thin sections definitely requires higher fluidity and thus higher super heat for complete filling before solidification. On the other hand, thick sections and chunky cast products requires lower superheat and consequently less fluidity for effective filling.

2.2.7 BUOYANCY FORCE

Another important consideration during pouring is the buoyancy force due to the pressure of the liquid metal. This problem occurs if the weight of the cope is less than the buoyancy force. If the weight of the cope is greater than the buoyancy force then no additional force is required to restrain the mold from moving up. The weight of the cope can be calculated as follows.

$$W_{cope} = (V_{cope} - V_{casting})\rho_{mold} \tag{2.31}$$

where, W_{cope} is the weight of cope (kg), V_{cope} is the volume of cope (m^3), $V_{casting}$ is the volume of casting (m^3), and ρ_{mold} is the density of mold (kg/m^3). Next, the buoyancy force for a horizontal cylindrical casting with parting line in the middle as shown in Figure 2.6 can be calculated as follows.

$$F_b = \rho h A \tag{2.32}$$

where, F_b is the buoyancy force (kg), ρ is the density of the metal (kg/m^3), h is the height of the liquid (m), and $A = w \times 2r_0$ is the projected area on the parting plane (m^2).

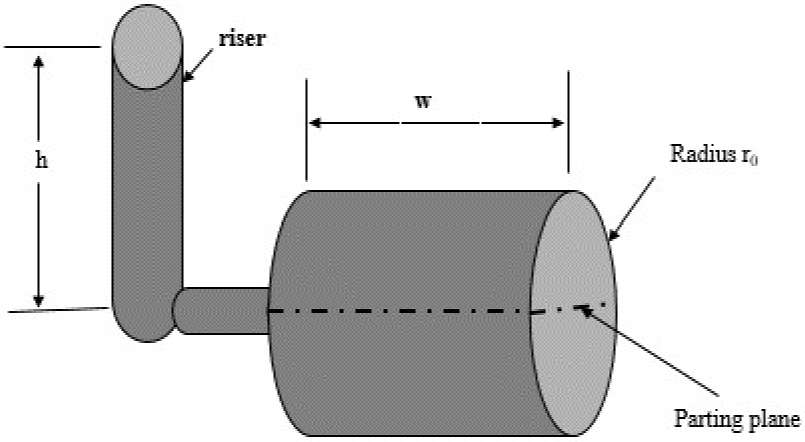

Figure 2.6 A horizontal cylindrical casting with parting line in the middle

2.3 COOLING AND SOLIDIFICATION

Solidification refers to the change of liquid to solid metal after pouring and it decides upon the performance of a metal casting during its serviceability period. The solidification process could be completed in seconds or may last for hours depending upon the size of casting and the casting process used. Both intrinsic and extrinsic factors influence the solidification mechanism. For example, chemical composition of the metal, cooling rate during solidification, and the subsequent heat and mechanical treatments are some of the intrinsic factors which determine the final microstructure and properties of the casting. On the other hand, cleanliness of metal, additives for microstructure control, casting design, gating and riser system design, solidification rate control, and temperature control subsequent to solidification are the extrinsic factors which are used to control the casting process so that the properties promised by intrinsic factors can be obtained.

2.3.1 HEAT TRANSFER MECHANISMS

During solidification and cooling, heat is transferred from metal to mold. It is essential to control the flow of this heat transfer to obtain high quality and defect free castings. Moreover, the cooling characteristics influence the grain size and microstructure, and thus the mechanical properties of cast products. If the heat transfer rates are too high, it can cause sharp thermal gradients and stresses due to which mold is distorted severely and poor cast shapes are produced.

a) Insulating Mold

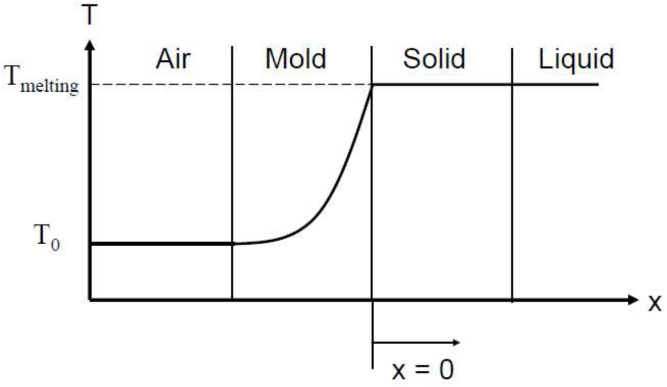

Figure 2.7 One-dimensional heat transfer model for insulating mold

In order to analyze the heat transfer during solidification, consider a one-dimensional model as shown in Figure 2.7. For simplicity, following assumptions have to be made in mathematical analysis of conductive heat transfer during solidification.

- Metals is solidified against a flat surface with uniform thickness of solid formed at all locations.
- No thermal resistance at mold-metal interface.
- No temperature gradient in liquid or solid metal.
- Mold is semi-infinite medium with uniform and invariant properties.

The heat flux at any distance x in the mold is proportional to the temperature gradient. Mathematically,

$$\frac{q}{A} = -k_{mold}\frac{\partial T}{\partial x} \tag{2.33}$$

where, $\frac{q}{A}$ is the heat flux (J/s or watt), k_{mold} is the thermal conductivity of the mold (W/m-K), and the minus sign shows that heat flows down the temperature gradient i.e. from hot to cold. Next, the Fourier equation for temperature distribution as a function of time and location is as follows.

$$\frac{\partial T}{\partial t} = \alpha\frac{\partial^2 T}{\partial x^2} \tag{2.34}$$

where, α is the thermal diffusivity (m^2/s) and is defined as

$$\alpha = \frac{k_{mold}}{\rho_{mold} c_{mold}} \tag{2.35}$$

where, ρ_{mold} is the density of the mold (kg/m^3) and c_{mold} is the heat capacity of the mold material (J/kg-K). The solution of differential equation (2.34) yields the following general form.

$$T(x) = A \int exp\left(\frac{-\lambda^2}{4\alpha}\right) d\lambda + B \tag{2.36}$$

where

$$\lambda = \frac{x}{\sqrt{t}}$$

There is no direct solution of integral in Equation (2.36) but it may be re-expressed using *Gaussian error function*. The convergence of the series is as follows.

$$erf(z) = \frac{2}{\sqrt{\pi}}\left(z - \frac{z^3}{3.1!} + \frac{z^5}{5.2!} + \frac{z^7}{7.3!} + \cdots\right) \tag{2.37}$$

or the integral

$$erf(z) = \frac{2}{\sqrt{\pi}} \int_0^x exp(-x^2).dx$$

The values of $erf\ (z)$ are provided in Table 2.1. The constants A and B in Equation (2.36) can be computed using boundary conditions,

$$\begin{aligned} T(x) &= T_m\ at\ x = 0 \\ T(x) &= T_0 \qquad at\ x = \infty \end{aligned} \tag{2.38}$$

With these boundary conditions, the solution to Equation (2.36) is

$$T(x,t) = T_{melting} + (T_0 - T_m).erf\left(\frac{x}{2\sqrt{\alpha_{mold}t}}\right) \tag{2.39}$$

where, T_0 is the initial mold temperature and T_m is the metal melting temperature. The temperature gradient in the mold can be obtained by differentiating Equation (2.39) as follows.

$$\frac{\partial T}{\partial x} = \frac{T_m - T_0}{\sqrt{\pi\alpha_{mold}t}} exp\left(\frac{-x^2}{4\alpha_{mold}t}\right) \tag{2.40}$$

Table 2.1 Gaussian error function [25]

z	erf(z)	z	erf(z)
0	0	1	0.843
0.025	0.028	1.1	0.88
0.05	0.056	1.2	0.91
0.1	0.113	1.3	0.934
0.15	0.168	1.4	0.952
0.2	0.223	1.5	0.966
0.3	0.329	1.6	0.976
0.4	0.428	1.8	0.989
0.5	0.521	2	0.995
0.6	0.604	2.2	0.998
0.7	0.678	2.4	0.999
0.8	0.742	∞	1
0.9	0.797		

The heat flux at mold-metal interface (or at $x = 0$) from Equation (2.33) is

$$\left(\frac{q}{A}\right)_{mold_{x=0}} = -k_{mold}\left.\frac{\partial T}{\partial x}\right|_{x=0} \tag{2.41}$$

Substituting Equations (2.35) and (2.40) in the above equation provides the heat flus across the mold-metal interface as

$$\left(\frac{q}{A}\right)_{mold_{x=0}} = -\sqrt{\frac{k_{mold}\rho_{mold}c_{mold}}{\pi t}}(T_m - T_0) \tag{2.42}$$

If the metal is cast at its melting temperature, then the heat input to the mold is the latent heat of fusion of the metal, which is

$$\frac{dQ}{dt} = \rho_{casting}\Delta H_f \frac{dV}{dt}$$

$$\frac{dQ}{dt} = \rho_{casting}\Delta H_f A \frac{dS}{dt} \tag{2.43}$$

where, $\frac{dQ}{dt}$ is the rate of heat transfer from metal to mold (J/s), $\rho_{casting}$ is the density of casting (kg/m^3), ΔH_f is the latent heat of fusion (J/kg), V is the volume of solidified metal (m^3), A is the area of mold-metal interface (m^2), and S is the thickness of solidified metal (m).

The heat flux corresponding to Equation (2.43) is as follows.

$$\left(\frac{q}{A}\right)_{casting} = \rho_{casting}\Delta H_f \frac{dS}{dt} \tag{2.44}$$

Since the heat flux away from the mold is equal to heat flux to the mold-metal interface, Equations (2.42) and (2.44) can be equated as given below.

$$\left(\frac{q}{A}\right)_{mold_{x=0}} = \left(\frac{q}{A}\right)_{casting}$$

Or

$$\sqrt{\frac{k_{mold}\rho_{mold}c_{mold}}{\pi t}}(T_m - T_0) = \rho_{casting}\Delta H_f \frac{dS}{dt}$$

The integration of above equation provides the solidification distance in terms of elapsed time since the metal was poured into the mold, which is

$$S = \frac{2}{\sqrt{\pi}}\left(\frac{T_m - T_0}{\rho_{casting}\Delta H_f}\right)\sqrt{k_{mold}\rho_{mold}c_{mold}t} \tag{2.45}$$

The characteristic heat transfer length S from Figure 20 is

$$S = \frac{V}{A} \tag{2.46}$$

By combining Equation (2.46) with (2.45) and rearranging the terms, the solidification time for an insulating mold is found to be

$$t = \left[\frac{\pi}{4}\left(\frac{\rho_{casting}\Delta H_f}{T_m - T_0}\right)^2 \frac{1}{k_{mold}\rho_{mold}c_{mold}}\right]\left(\frac{V}{A}\right)^2 \tag{2.47}$$

The values for constants in Equation (2.47) are listed in Table 2.2. If superheating is included into the analysis, Equation (2.47) will be modified as follows.

$$t = \left[\frac{\pi}{4}\left(\frac{\rho_{casting}(\Delta H_f + c_p\Delta T)}{T_m - T_0}\right)^2 \frac{1}{k_{mold}\rho_{mold}c_{mold}}\right]\left(\frac{V}{A}\right)^2 \tag{2.48}$$

Equations (2.47) and (2.48) can be re-written in a more simplified form as

$$t = C\left(\frac{V}{A}\right)^2 \tag{2.49}$$

where, C is a constant representing all constant terms in Equations (2.47) and (2.48). This well-known relations ship is known as *Chvorinov's Rule*, and can be used not only for simple shapes but also as a first approximation to analyze the solidification behaviors of intricate shapes. The mold constant C depends upon the mold material, thermal properties of casting metal, and pouring temperature relative to melting point. Value of C for a given casting operation can be based on experimental data from previous operations carried out using same mold material, metal, and pouring temperature, even though the shape of the part may be quite different.

Table 2.2 Thermal properties of casting materials [25]

(a) Mold and metal constants			
Material	Specific heat	Density	Thermal Conductivity
	C_p (J/g °C)	ρ (g/cm^3)	k (W/m.°C)
Sand	1.16	1.5	0.60
Plaster	0.90	1.1	0.34
Mullite	0.77	1.6	0.37
Iron	0.70	7.9	73
Aluminum	0.90	2.7	202
Copper	0.39	9.0	385
Magnesium	1.07	1.7	156
(b) Liquid metal constants			
Metal	Melting Point	Latent heat of Solidification	Specific heat
	T_m (°C)	H_f (J/g)	C_p (J/g °C)
Iron	1540	280	0.77
Aluminum	660	396	1.05
Copper	1083	220	0.52
Magnesium	650	384	1.38

b) Conducting Mold

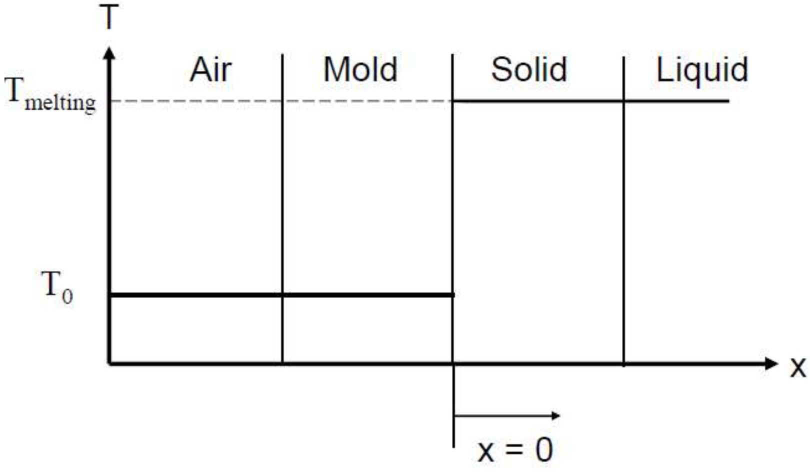

Figure 2.8 One-dimensional heat transfer model for conducting mold

A similar analysis could be done when the mold conducts in addition to the metal being cast, and the interface resistance dominates. For such a case, consider a one-dimensional model as shown in Figure 2.8. In this case the heat flux across the mold-metal interface into the mold is

$$\left(\frac{q}{A}\right)_{mold_{x=0}} = -h(T_m - T_0) \tag{2.50}$$

and, heat flux due to solidification of casting is

$$\left(\frac{q}{A}\right)_{casting} = \rho_{casting} \Delta H_f \frac{dS}{dt} \tag{2.51}$$

Once again, the heat flux away from the mold is equal to heat flux to the mold-metal interface, Equations (2.50) and (2.51) can be equated as follows.

$$\left(\frac{q}{A}\right)_{mold_{x=0}} = \left(\frac{q}{A}\right)_{casting} \tag{2.52}$$

or

$$h(T_m - T_0) = \rho_{casting}\Delta H_f \frac{dS}{dt} \tag{2.53}$$

The integration of above equation provides the solidification distance as

$$S = h\frac{T_m - T_0}{\rho_{casting}\Delta H_f}t \tag{2.54}$$

By combining Equation (2.46) with (2.54) and rearranging the terms, the solidification time for a conducting mold is found to be

$$t = \frac{\rho_{casting}\Delta H_f}{h(T_m - T_0)}\frac{V}{A} \tag{2.55}$$

If superheating is included into the analysis, Equation (2.55) will be modified as

$$t = \frac{\rho_{casting}(\Delta H_f + c_p\Delta T)}{h(T_m - T_0)}\frac{V}{A} \tag{2.56}$$

The Biot number is used to check if the mold is conducting or not.

$$Bi\# = \frac{h_{interface}l_{casting}}{k_{casting}} \ll 1 \tag{2.57}$$

or

$$h_{interface} \ll \frac{k_{casting}}{S} \tag{2.58}$$

Also, for a conducting mold,

$$k_{mold} \sim k_{casting}$$

$$\alpha_{mold} \sim \alpha_{casting}$$

If Biot number and insulating mold tests are not conclusive, mold may be relatively insulating and it must meet the following condition.

$$h_{interface}{}^{2} \ll \frac{k_m \rho_m c_m}{t} \tag{2.59}$$

2.3.2 RISER DESIGN

Shrinkage voids and macroporosity are unavoidable in the absence of a properly designed casting layout. Therefore, location and size of risers must be carefully designed to start solidification from the center of casting and proceed outwards, ending in risers. The risers should be the last part to solidify thereby contains all voids and macroporosity which eventually will be removed from the final cast product. This suggests that the time to solidify riser calculate from Equation (2.49) must be greater than time to solidify the casting. Mathematically,

$$t_{riser} > t_{casting}$$

or

$$\left(\frac{V}{A}\right)_{riser} > \left(\frac{V}{A}\right)_{casting} \tag{2.60}$$

The inequality in Equation (2.60) confirms no shrinkage in the cast product and the riser size can be calculated based on this equation. However, the riser size can be minimized by using insulators, chill or radiation shields since addition of these components alter the solidification time by changing the constant C in Equation (2.49).

2.4 CASTING YIELD

The metal which solidifies in sprue, runner, gates, and risers is removed from the actual cast product. Although it is not completely wasted, the solidified metal in the above mentioned regions requires treatment before it can be reused to cast another part. Besides high quality and integrity, it is also important taking into account the casting yield, which refers to the ratio of weight of the cast part to the weight of the total amount of metal poured in the mold. Casting yield is also viewed as the efficiency of a casting process. Mathematically

$$Casting\ Yield\ (\%) = \frac{Weight\ of\ trimmed\ casting}{Total\ weight\ of\ metal\ poured} \times 100 \tag{2.61}$$

2.5 SURFACE TENSION

Surface tension determines how well a material wets and flows into the mold. Surface tension becomes especially important while casting thin sections i.e. less than 5 mm. The effect of surface tension is similar to back pressure, often termed as capillary repulsion-the resistance experience by a metal while attempting to enter in a small hole or channel in the mold. However, if molten metal wetted the mold surface, it would experience capillary action which allows sucking of molten metal into the mold surface similar to sucking of water in a capillary tube. When the pressure in molten metal becomes too high, the surface tension fails to resist molten metal from penetrating into the spaces between sand grains of the mold. The resistance offered by surface tension can be quantified using Figure 2.9 as follows.

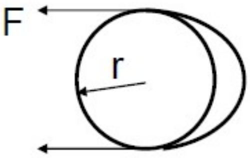

Figure 2.9 Schematic diagram for a hole between sand grains

$$P\pi r^2 = 2\pi r\gamma$$

or

$$P = \frac{2\gamma}{r} \tag{2.62}$$

where, P is the pressure (N/m^2), γ is the surface tension (Nm), and r is the average radius of the holes between the sand grains.

2.6 POROSITY

2.6.1 SHRINKAGE POROSITY

The solidification shrinkage defects are modeled using the well-known Niyama criterion [26]. It is defined as the ratio of local thermal gradient, G, to the square root of the local cooling rate, $\sqrt{\dot{T}}$. Mathematically

$$N_y = \frac{G}{\sqrt{\dot{T}}} \tag{2.63}$$

The common units for the Niyama criterion are $(\mathrm{C}-\mathrm{s})^{1/2}/\mathrm{mm}$, $(\mathrm{C}-\mathrm{min})^{1/2}/\mathrm{mm}$, and $(\mathrm{F}-\mathrm{min})^{1/2}/\mathrm{in}$, and the relationship between these units are $1\ (\mathrm{C}-\mathrm{s})^{1/2}/\mathrm{mm}$ = 1.29 $(\mathrm{C}-\mathrm{min})^{1/2}/\mathrm{mm}$ = 4.40 $(\mathrm{F}-\mathrm{min})^{1/2}/\mathrm{in}$. The Niyama criterion helps to identify porosities that develop due to solidification fronts approaching each other swiftly. These centerline cavities occur mainly in alloys with short saturations ranges such as steels. In those areas where solidification fronts approach each other with small gradients (for example bar geometries), there is often not enough time to feed the center, resulting in these defects. Consequently, the Niyama criterion is evaluated just before reaching the solidus temperature. It is important to note the Niyama evaluation temperature since it significantly influences the resulting Niyama values. Mathematically,

$$T_{Ny} = T_{sol} + X(T_{liq} - T_{sol}) \tag{2.64}$$

where, X is the % of the solidification range above the 100% solid (i.e., solidus) temperature.

The relationship between shrinkage porosity and the Niyama criterion is presented schematically in Figure 2.10. For sufficiently large Niyama values, no shrinkage porosity forms. When the Niyama value decreases below and critical value, Ny_{micro}, small amounts of micro-shrinkage begin to form. As the Niyama values decreases further (consider the log-scale on the x-axis), the amount of micro-shrinkage increases until it becomes detectable on a standard radiograph. This transition occurs at a second critical value, Ny_{macro}. The amount of shrinkage porosity continues to increase as the Niyama criterion decreases below Ny_{macro}. It is important to understand that the Niyama criterion only predict feeding-distance related shrinkage porosity, and it does not predict the hotspots in a casting, and it does not predict gas porosity. The Niyama criterion has been extended to alloys other than steel. Since, it is a prediction of directional solidification, a poor directional solidification is presented by a value of zero, and a good directional solidification by higher values. The range of critical values for steels and iron are 0 – 1 and 0 – 0.75 respectively.

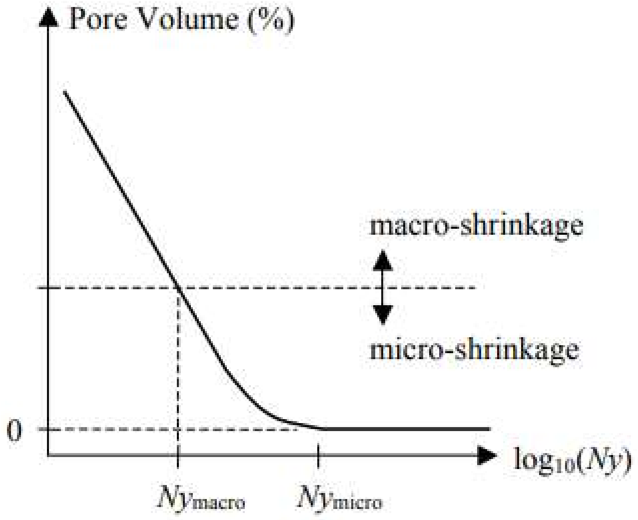

Figure 2.10 Relationship between shrinkage porosity volume and Niyama criterion [27]

2.6.2 GAS POROSITY

In addition to micro and macroporosity caused by shrinkage during solidification, there also exist a gas porosity which is caused by absorption of gases in the molten metal before it solidifies in the mold. Gas porosity affects the quality of casting by producing *blisters* due to expansion of entrapped gas during subsequent operations such as annealing or other heat treatments. Unlike irregular shaped micro and macroporosity, gas porosity is usually spherical in shape.

Hydrogen poses challenges in dealing with gas porosity. It diffuses into the molten metal from the moisture in atmosphere or as a result of combustion of fossil fuels during heating and melting. Besides hydrogen, other gases such as oxygen can also diffuse into the molten metal directly from the atmosphere. The equilibrium concentration of the gas in molten metal can be determined from *Sievert's law* as follows.

$$G = k\sqrt{P_g} \tag{2.65}$$

where, G is the equilibrium solubility of gas, k is an equilibrium constant, and P_g is the partial pressure of the gas at metal surface. Equation (2.65) can be used to calculate the volume of gas porosity in a casting.

CHAPTER 3

LITERATURE REVIEW

This chapter first explains how a casting simulation software works, associated mathematical models and solution methods, and the results obtained by simulation. Next, the current practices in metal casting simulations to minimize defect and improve casting quality are presented. Published case studies on gating, runner, and riser design, systematic and autonomous optimization, stress and strain simulations, and integration of casting simulations with mechanical performance simulations are reviewed to establish the state-of-the art in the simulation-based metal casting.

3.1 CASTING SIMULATION SOFTWARES

Modeling and simulation of casting processes is complicated due to a host of parameters involved such as fluid velocity, pressure, geometry of the mold, gating and runner system etc. A range of softwares that have been emerged over time are a result of understanding the physical phenomena during a casting process. The relevant mathematical models are either developed or modified and then implemented into computer programs to develop a software [28]. Some of the most commonly used casting simulation softwares which are currently available to researchers and foundrymen are ProCAST, Flow-3D Cast, MAGMASoft, Nova-Solid/Flow, AutoCAST, SOLIDCast, CastCAE, and CAPCAST etc. Figure 3.1 depicts the user interfaces of some of these softwares where the presentation of results is not much different from one to another simulation package.

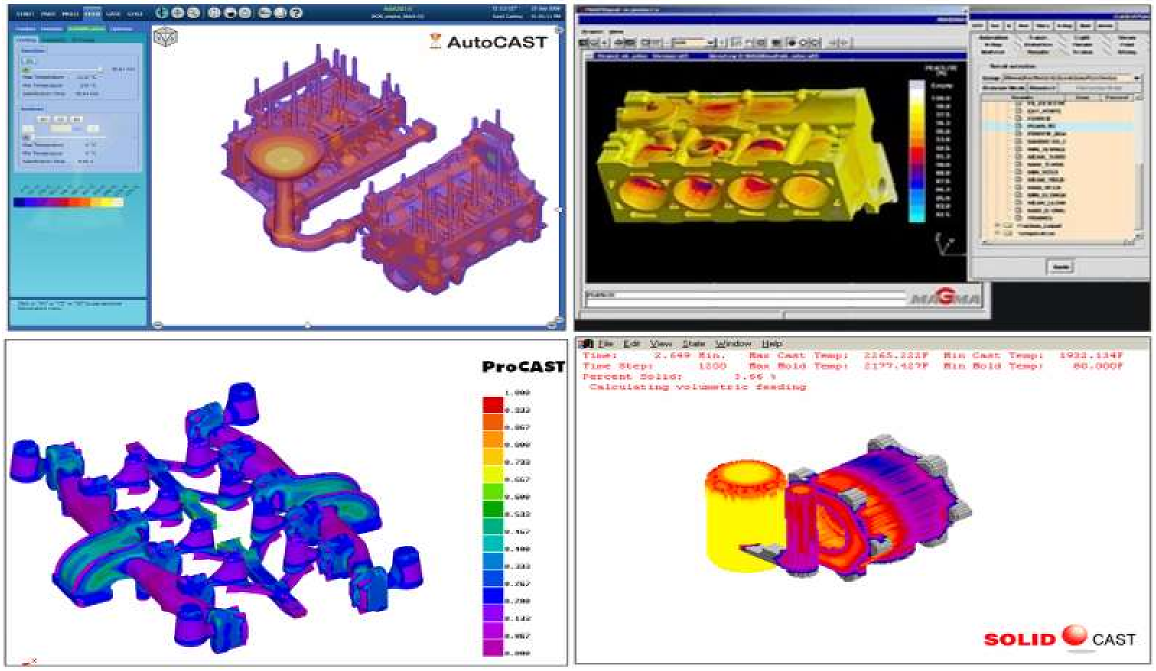

```
Time:       2.649 Min.   Max Cast Temp:  2165.222F  Min Cast Temp:  1932.134F
Time Step:        1200   Max Mold Temp:  2177.427F  Min Mold Temp:    80.000F
Percent Solid:       3.56 %
 Calculating volumetric feeding
```

Figure 3.1 User interface of common casting simulation softwares (AutoCAST, MAGMA, ProCAST and SolidCAST) [29]

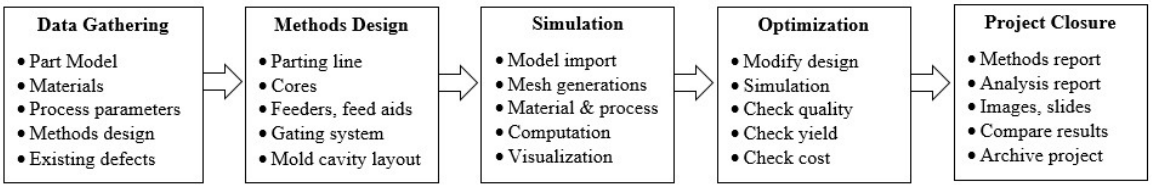

Figure 3.2 Casting simulation and optimization protocol [29]

A casting simulation project using commercial softwares generally comprised of five stages as shown in Figure 3.2 [29]. *Data gathering* refers to all information needed related to CAD model of casting, cast metal properties, mold properties and process parameters etc. *Methods design* and modeling primarily focuses on how to convert the as cast part model into a three dimensional mold which contains cavities, gating system, runners, risers, cores and feed-aids. Next, the *numerical simulation* is done after generating the optimum mesh and defining boundary conditions. Visualization of results is done by a post processing module in each simulation software. With the simulation results, it is often possible to identify defects such as hotspots, microporosity, shrinkage, cold shuts and others. Therefore, a step forward in simulation is *optimization* which includes modifications in gating and riser designs, process parameters and material properties, and even in part model to minimize the defects. The final stage which is termed as *project closure* includes complete documentation of results, generating methods and analysis reports, capturing images and animations for demonstration at the later stage.

3.2 MATHEMATICAL MODELING AND SOLUTION METHODS

Casting simulations begin with modeling the physical phenomena through mathematical equations. In a mathematical perspective, models are expressed as governing equations and boundary conditions. Owing to the non-linearity of models in terms of both geometry and material properties, numerical methods have to be used. The set of developed equations is then used to explain casting process in the form of action-behavior-property relationship [2]. For a metal casting process, the action is supplying molten material to the mold, the behavior is the flow of molten metal within the mold, and the behavior is further decided by properties of the molten metal. The physical and mathematical modeling perspective of this relationship is presented in Figure 3.3.

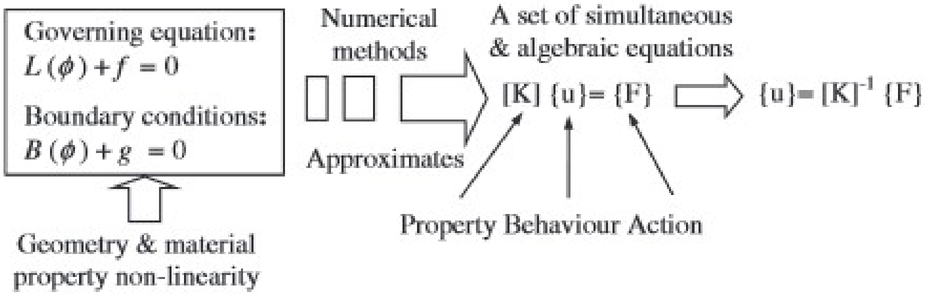

Figure 3.3 Action-behavior-property relationship from physical and mathematical perspective in a casting process [2]

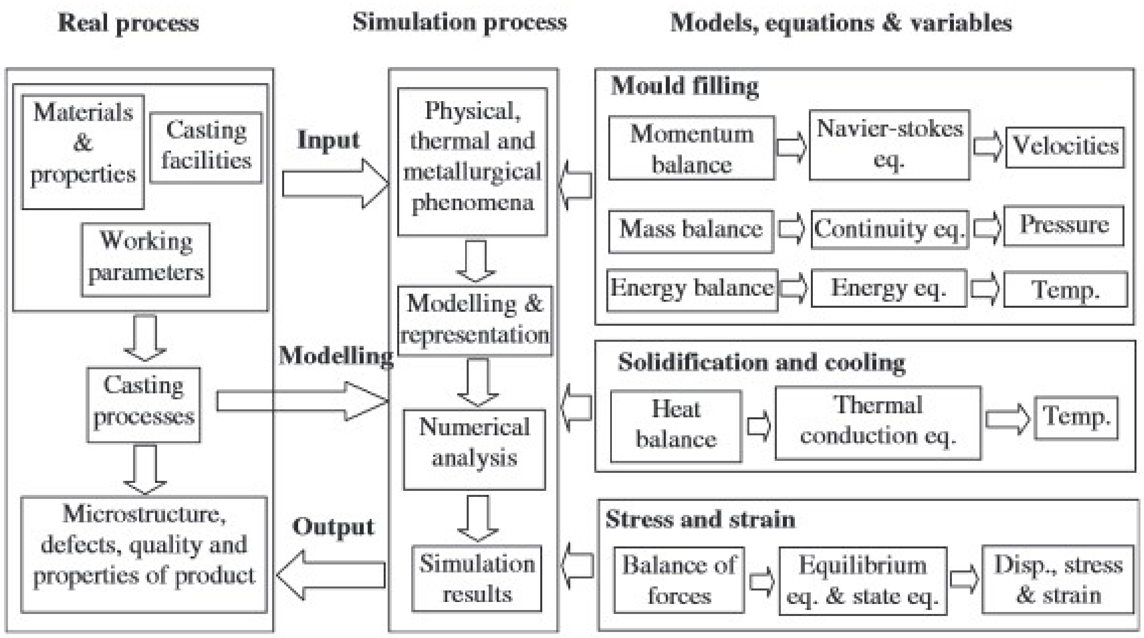

Figure 3.4 Relationship between the process, modeling, simulation and output variable

A relationship between an actual casting process, simulation procedure, modeling of physical phenomena, governing equations, and output variables is illustrated in Figure 3.4. Inputs require for a casting simulation are usually material, material properties and process parameters. Simulation results, however, demonstrates the physical behavior of the casting process and the final microstructure, defects, quality and properties of the cast products. From modeling point of view, three important phenomena in any casting process simulation are mold filling, solidification and cooling, and stress and strain profile of the cast parts. In each of these phenomenon a certain set of governing equations are employed. For example, mold filling is modeled by continuity equation, momentum equation (Navier-Stokes equation) and the energy equation [30]. Equations (3.1) to (3.3) represent the complete forms of continuity, momentum and energy equations respectively and thus modified accordingly if the density is assumed to be constant and/or the molten metal is a Newtonian fluid.

$$\frac{\partial \rho}{\partial t} + \frac{\partial}{\partial x_j}\left(\rho U_j\right) = 0 \tag{3.1}$$

$$\frac{\partial}{\partial t}\left(\rho U_i\right) + \frac{\partial}{\partial x_j}\left(\rho U_j U_i\right) = \frac{\partial \rho}{\partial x_i} + \frac{\partial}{\partial x_j}\left(\mu \frac{\partial U_i}{\partial X_j}\right) + \rho g_i \tag{3.2}$$

$$\frac{\partial}{\partial t}\left(\rho C_P T\right) + \frac{\partial}{\partial x_j}\left(\rho C_P U_j T\right) = \frac{\partial}{\partial x_j}\left(\lambda \frac{\partial T}{\partial x_j}\right) + Q \tag{3.3}$$

where:

t - Time

x - Space

ρ - density

μ - viscosity

g - gravity

C_P - heat capacity

λ - Conductivity

U - Velocity

T - temperature

Q - heat source

The non-linear nature of Equations (3.1) to (3.3) requires a numerical method to obtain a set of simultaneous and algebraic equations, the solution of which determines the velocity, pressure and temperature of the molten metal within the mold. The modeling of solidification is governed by Fourier's heat conduction equation taking into account the phase transformation enthalpies. The main objective of this modeling is to obtain temperature distribution in casting and to identify the solidification behavior. For stress-strain distribution in castings, equilibrium equations and Hooke's law are generally used to provide the relationship and thus the magnitude of displacement, stress and strain.

A variety of methods for solving mathematical equations are available, the most common of which are *finite difference method* (FDM), *finite volume method* (FVM), *finite element method* (FEM), *vector element method* (VEM), *cellular automation method* (CA) etc. [31].

Finite Difference Method: It is a numerical method where a complex problem is solved by discretizing the complete region of problem (also known as domain) into a finite number of small portions (also known as control volumes). Material properties are assumed to be constant throughout the volume. Therefore, for high accuracy of the results, the domain should be divided into maximum no. of control volumes possible taking into account the computational time. FDM is a differential scheme which is the approximation of Taylor series expansion. Calculations are iterative and done at a predetermined time-step. The results can be stored at the end of each time-step or after a pre-determined numbers of steps [30].

Finite Volume Method: Unlike FDM, FVM is an integral scheme. Although the idea of discretizing the domain into small control volumes remains the same, the use of integral formulations is advantageous in treating the Neumann boundary conditions as well as that of discontinuous source terms due to their reduced requirements on the regularity or smoothness of the solution.

Finite Element Method: FEM discretizes the complete domain of the problem into small pieces, however, they are now termed as elements. Each element is made up of nodes (corner points) and edges, which store material properties to be used in computation. Solution is done by using these values to determine a quantity for these specific points (also known as Gauss points) within the elements. The position of these points in elements is a function of the integration applied, initial coordinates of the nodes, and the element shape [30]. Values of variables, which are considered to be constant in FDM/FVM across the elements, are calculated using some interpolation function. However, the treatment of time in an iterative and step-wise manner is similar to FDM/FVM.

Vector Element Method: This approach to casting simulations is based on determining the largest thermal gradient at any point inside the casting, which is given by the vector sum of flux vectors in all directions from that point [32]. Vector element method is relatively simple when compared to other numerical techniques but provides reliable and robust results [33], [34].

In some instances a combination of two or more techniques may also be employed, the examples of which are cellular automation finite element (CAFE) method proposed by [35], and a hybrid method for casting process simulation by combining FDM and FEM [36]. The final simulation results, however, are representative of casting process and properties, qualities and defects of cast products irrespective of the type of solutions discussed above.

3.3 CASTING PROCESS SIMULATION

A complete framework of metal casting process simulation is presented in Figure 3.5. It must be clear at this stage that any casting design is completely based on what is required as an end product. Therefore, the product geometry is extremely important in determining the casting system design and process parameters. Besides the mathematical modeling as explained previously, a 3D model of casting system is developed in any CAD software AutoCAD, CATIA, I-DEAS, Pro-Engineer, SolidWorks, SolidEdge, and UG-NX. This 3D model consist of part cavities together with sprue, gating and runner system, cores etc. The process route and parameters are also needed to be determined in compliance with the casting design. While modeling a casting system, the physical models simplifies the engineering problems that might occur during a real casting process, mathematical models determines the initial and boundary conditions and process constraints, and the numerical models decides upon the element types, meshing and solution parameters. Since, the simulation process is iterative, solution parameters also details the iteration specifications and convergence criteria.

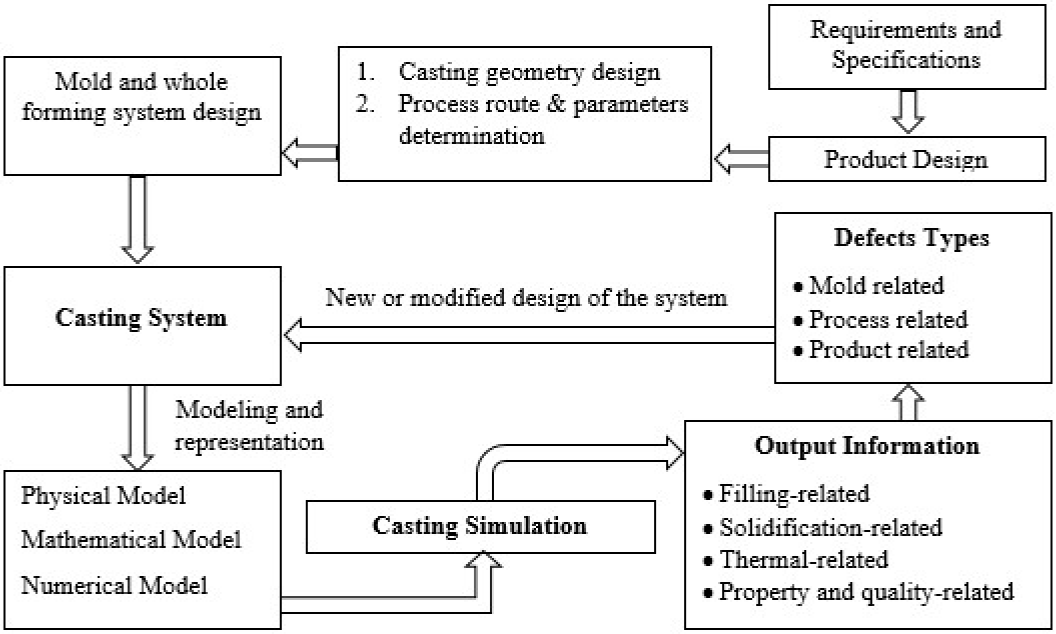

Figure 3.5 Casting simulation process for defects identification

Simulation results provides information about filling of molten metal in the mold, solidification behavior, quality and defects of the cast products. Nevertheless, the computer programs operate on GIGO: garbage in garbage out principle and the simulation results might be misleading. Hence, care must be taken in interpreting the results obtained from any casting simulation. Generally defects are attributed to improper mold design, irrational process parameters, and inappropriate product design, and thus referred to as mold-related, process related, and product related defects. Once, the defects and the mechanism by which they are produced are identified, necessary modifications are done wherever required. The new casting system is then re-simulated until a casting is obtained which is either free from defects or contain defects within the permissible limits set by the designer.

3.4 SIMULATION RESULTS

Casting simulations results in three major aspects: Filling, Solidification and Stress Analysis. Each of these three simulation types reveal sources and causes of casting defects and thus provides an opportunity to rectify any errors prior to a physical casting process in foundry.

Filling Process Simulation

Mathematical modeling and simulation of conservation of mass, momentum and energy in a filling process provides information about velocity of molten material within the mold cavity, the direction of flow, temperature and pressure at various instances within the mold. Physical and thermal characteristics of the filling process are derived from these results, some of which are

- Flow front progression, turbulence in flow, filling evenness
- Entrapment of air and gases within the mold so that proper venting can be designed
- Temperature profile within the mold
- Filling sequence and occurrences of over flowing
- Velocity profile of molten metal within the mold
- Odd behaviors, for example, splashing, misruns, cold shuts etc. during filling.

Solidification Process Simulation

Solidification in casting process is generally complex, where physical, thermal and metallurgical occurrences take place simultaneously. Solidification simulation provides information about how these phenomena are occurring in process conditions together with the defects that might arise during solidification phase. Some key findings of a solidification simulation include

- Cast area that solidifies last in a cast product
- Sequence of solidification and temperature profile within the mold
- Validation of cooling design
- Validation of runner design in a mold
- Identification of hotspots
- Defects due to shrinkage and microporosity and remedial actions to avoid such defects
- Appropriate riser geometry, size and location within the mold.

Stress and Strain Simulations

The stress and strain simulations demonstrates the state of cast parts after ejecting from the mold. The results of these simulations may include

- Identification of dimensional inaccuracies in cast part
- Residual stress generation and distribution in cast part

- Defects arises due to stress and strain
- Temperature profile in ejected cast part
- Design improvements in casting design such as modifications in riser design to reduce stresses etc.

3.5 CASE STUDIES IN SIMULATION-BASED METAL CASTING

Efforts have been made in past to obtain high quality defect free castings by developing an in-depth understanding of the areas such as (a) design of runner and gating systems [37]–[45] (b) design of feeding systems (locations and number of risers) [46]–[50], (c) filling and solidification during different casting processes [51]–[55], (d) casting process parameters (thermo-physical data, injection parameters etc.) [56]–[60], (e) stress distribution in cast products [61]–[65], and (f) quality control and assurance of the cast products [66]–[68]. Some of the case studies in these areas are discussed in forthcoming sub-sections.

3.5.1 GATING, RUNNER, AND RISER DESIGN OPTIMIZATION

Mi et al. [53] used casting simulations to modify gating and riser system of a valve block. The original design with two ingates and rounded-rectangular riser geometry as shown in Figure 3.6 (a) resulted in defects i.e. shrinkage and cold shut. The new casting design as shown in Figure 3.6 (b) comprised of a single ingate together with cylindrical risers as they allow more liquid metal during solidification. Chills were added to help solidification in the bottom region of casting and shrinkage was overcome via modified riser design. The final casting was reported to be free from surface cracks on the valve body.

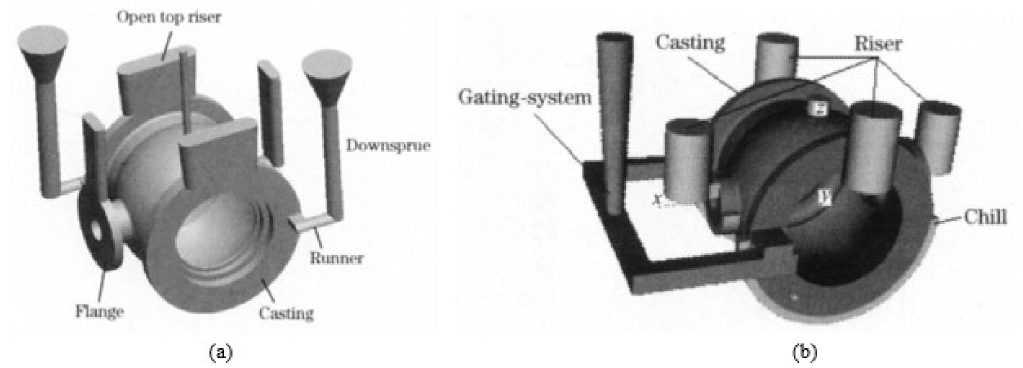

Figure 3.6 Casting design for a valve body (a) original and (b) modified [55]

Sun et al. [39] presented multiple objective optimization for gating system of a cylindrical magnesium alloy casting. The optimum gating system was selected by changing four parameters: ingate height, ingate width, runner height, and runner width as shown in Figure 3.7 (a). The main criteria for casting quality were filling velocity, shrinkage porosity and yield. Bottom filling approach was employed as shown in Figure 3.7 (b). It was concluded that runner with small height and large width is effective in reducing the metal velocity at the ingate which is consistent as reported by [37], [55].

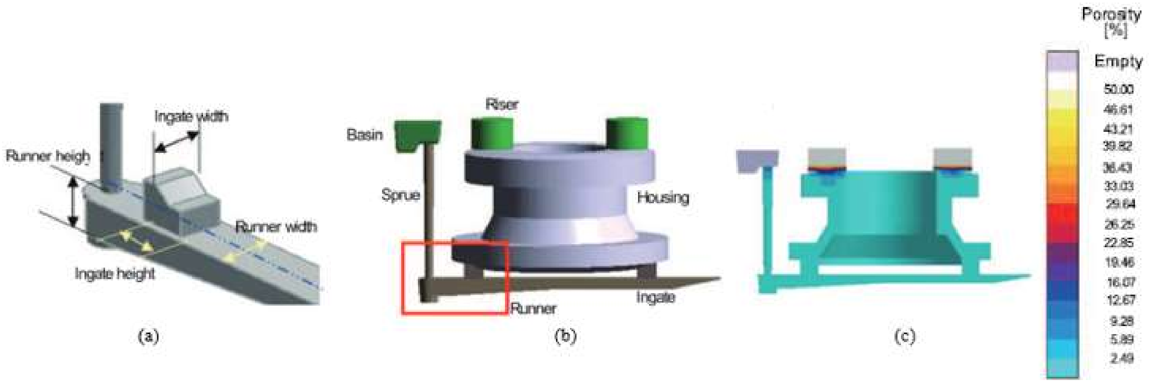

Figure 3.7 (a) Gating parameters (b) Gating system design and (c) Shrinkage porosity prediction in cylindrical magnesium casting [39]

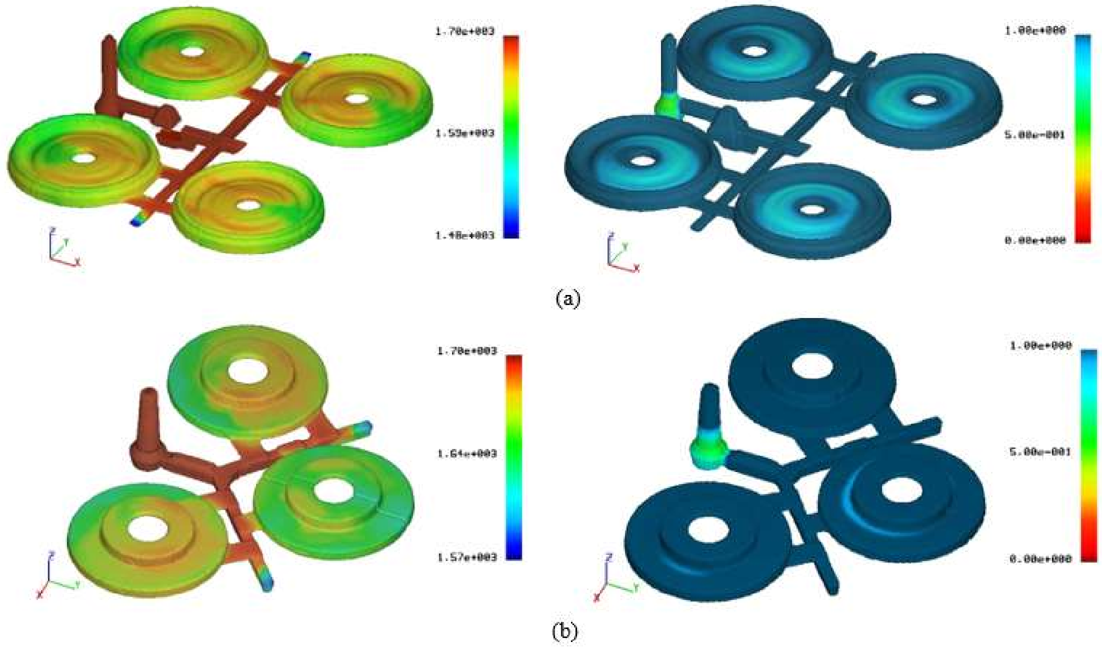

Figure 3.8 Final results of filling (left) and solidification (right) for (a) Flywheel and (b) Brake disc [53]

Kermanpur et al. [53] simulated the filling and solidification sequence of brake disc and flywheel in multi-cavity molds. It was reported that a symmetrical mold configuration for flywheel as shown in Figure 3.8(a) provides uniform filling contrary to the one for brake disc presented in Figure 3.8 (b). Simulated hotspot reflected as micro-shrinkage in brake disc for which lower superheat temperature was recommended. In another work by Choudhari et al. [48], the hotspot defect was eliminated by simulating an exothermic sleeve around the riser which delayed the solidification time as shown in Figure 3.9. Riser system design was simulated based on quality, feeding yield and feeding efficiency followed by experimental validation which also resulted in cast products free from shrinkage defect.

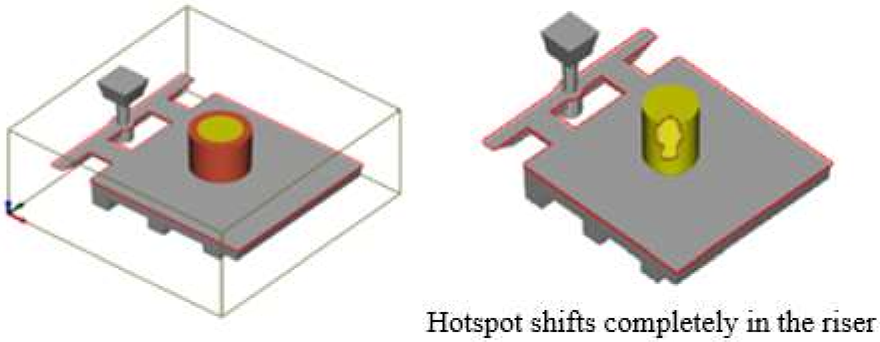

Figure 3.9 Effect of exothermic sleeve on the position of hotspot in stepped plate casting [48]

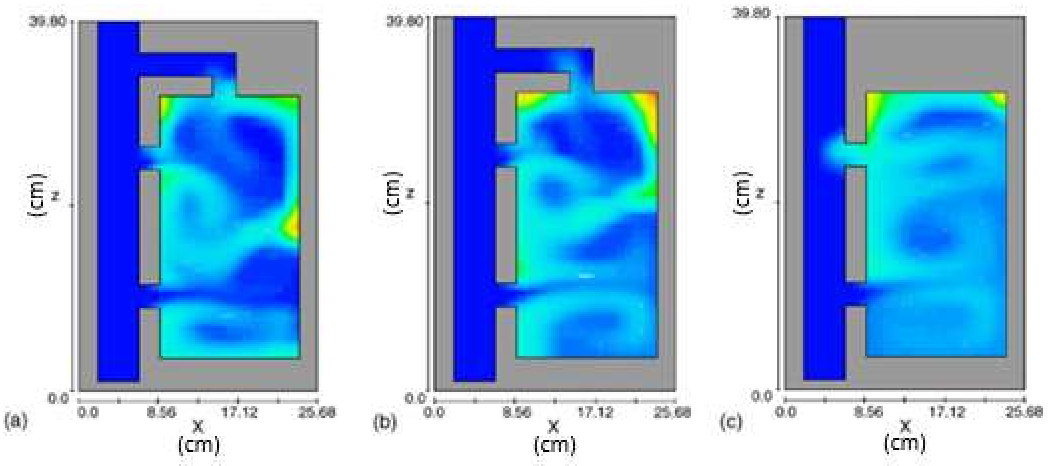

Figure 3.10 Formation of casting defects by (a) CHTC model; (b) VHTC model; and (c) modified model with two ingates (blue and red represents lowest and highest probability for defects respectively)[52]

Liu et al. [52] simulated the decomposition of expanded polystyrene (EPS) pattern in lost foam casting process using Flow 3D. The conventional constant heat transfer coefficient (CHTC) approach is modified by incorporating the variability in the heat transfer coefficient (VHTC), which resulted in a better agreement of simulation and experimental results. Effect of temperature on mold filling time was also studied and it was reported that mold filling time predicted by VHTC model were found close to the experimental results. Defects in castings are predicted via both CHTC and VHTC models where the main mechanism of defect formation was the meeting of metal fronts entering from different ingates. The results of defect predictions with three ingates and with a modified two ingates system are presented in Figure 3.10 which confirms reductions in casting defects with fewer ingates.

Nimbulkar et al. [69] optimized the gating and feeding system design for casting a wear plate using AUTOCAST. The original design for casting utilized a vertical gating system which resulted in casting defects. In this study, the vertical gating system was replaced by a horizontal gating system design. The existing and new casting design was simulated by AUTOCAST followed by their experimental validation. The final cast products were examined through ultrasonic inspection. It was found that vertical gating system was not suitable for thick casting components due to multiple casting defects observed during solidification. However, the horizontal gating system with symmetrical gates and risers enabled uniform flow of the melt together with minimized porosity in the final casting. In total the gating and feeding system related defects are found to be reduced by 30%.

3.5.2 SYSTEMATIC AND AUTONOMOUS OPTIMIZATION

A recent approach to improve simulation-based casting is systematic and autonomous optimization, where softwares are used as test field or virtual experimentation. Sikorski et al. [43] optimized the gating system of a simple casting layout using MAGMASoft which follows the sequence as shown in Figure 3.11 (a). Owing to a multi-cavity mold, it was aimed to reduce the filling time between the cavities to minimize defects due to air entrapment. The results of initial situation and final optimized solution using the filling time difference criterion are presented in Figure 3.11 (b) and (c) respectively. The final casting after autonomous optimization is found to be free from casting defects especially due to air entrapment and oxides.

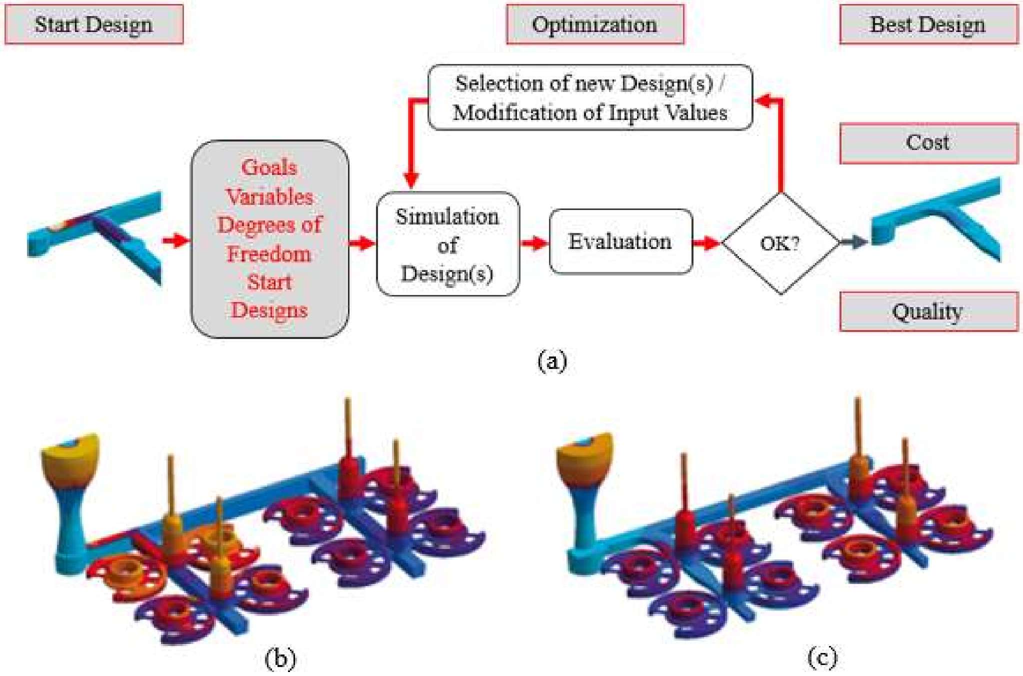

Figure 3.11 (a) Schematic sequence of optimization in MAGMASOFT (b) Initial situation and (c) Final optimized solution [43]

Figure 3.12 (a) Feeder and chills in cope (left) and drag (right) (b) Shrinkage distribution by autonomous optimization (left) and DOE (right) [40]

Hahn et al. [40] compared the design of experiments (DOE) with virtual autonomous optimization for steel casting. The number, location and dimension of the chills and feeders were investigated as shown in Figure 3.12 (a) to check their effect on the shrinkage distribution. The results as shown in Figure 3.12 (b) demonstrates that autonomous optimization led to further reduction in shrinkage by fine tuning the chill size. The autonomous optimization was also done for a ductile iron wind turbine hub to control shrinkage porosity. Moreover, the configuration of runners in a multi-cavity mold for casting six parts was also optimized in the same study [40].

Sturm et al. [70] performed autonomous optimization for casting a head cap in a multi-cavity mold. The actual mold design contained a single cavity where successful filling was achieved through specifically designed gate and a slightly slanted runner as shown in Figure 3.13 (a). A multi-cavity mold was designed and optimized to achieve similar melt velocities and directions as already obtained in single cavity mold. Moreover, minimization of air entrapment was also set as another criterion for optimization. In total, only 1 out of 106 designs for right-hand runner and 2 out of 97 designs for left-hand runner were qualified meeting all objectives of optimization. The flow patterns for single and multi-cavity molds are presented in Figure 3.13 (a) along with the actual head cap castings in Figure 3.13 (b).

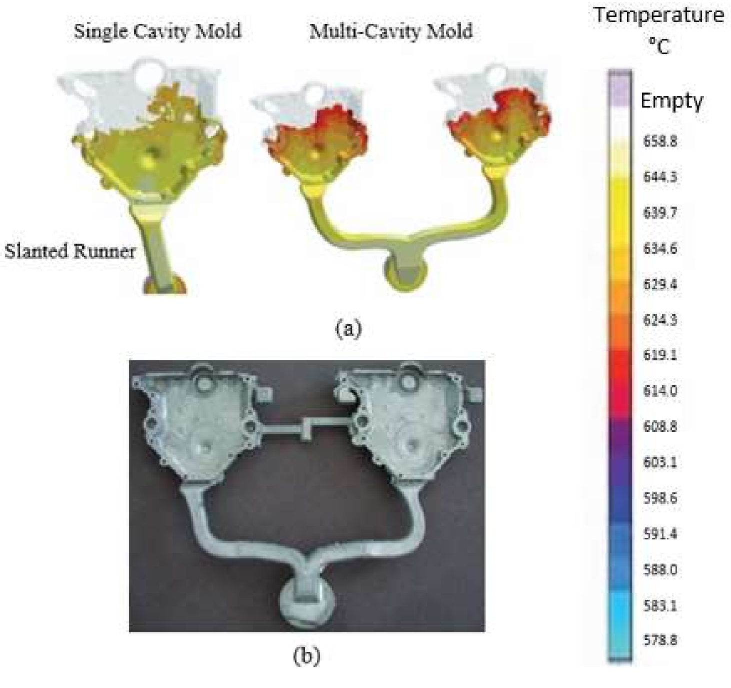

Figure 3.13 (a) Identical flow patterns in single and multi-cavity molds and (b) actual castings after autonomous optimization [70]

3.5.3 STRESS AND STRAIN SIMULATIONS

The application of numerical simulation to distortion and stress-related problem in casting was presented by [63]. The study first explained the formation of residual stresses and distortion in casting followed by simulation of die cast rear door lock panel for a passenger car. Figure 3.14 (a) represents the temperature field at ejection and it forms the basis for the formation of stresses and deformation during solidification and cooling to room temperature. The runner being hotter contracted more in the subsequent cooling phase and pulled the casting inwards toward it as shown in Figure 3.14 (b). The swan neck moved in an upward direction, as the upper side of the casting, which faced the shot slug, had a higher temperature than the lower side after ejection. Another problem of hot tears, especially important for high pressure die castings, was also investigated by [63] by simulating the hot tear criteria for a flywheel as shown in Figure 3.15. It was suggested that hot tears can be avoided by modifying process parameters and cooling conditions, or by minor changes in the geometry of casting.

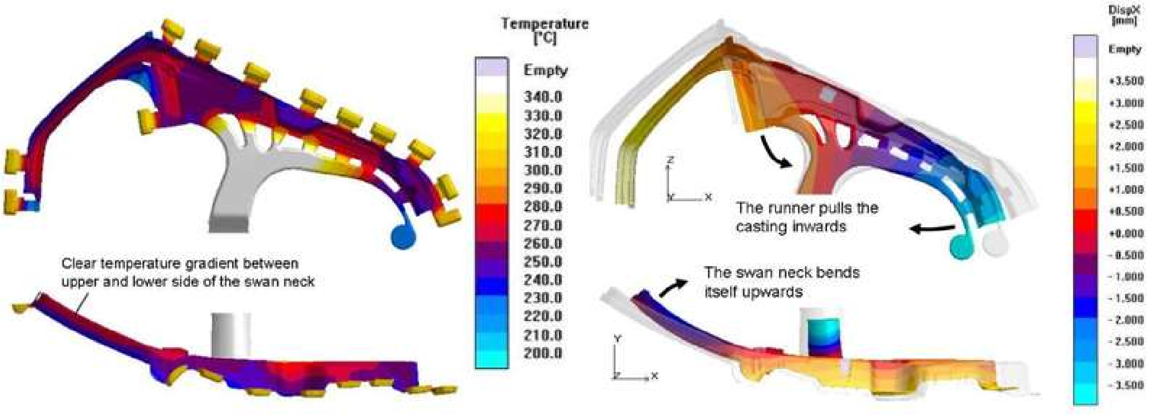

Figure 3.14 (a) Temperature distribution in casting and runner at ejection and (b) Deformation of the casting after cooling to room temperature: original geometry (semitransparent grey) and deformed geometry [63]

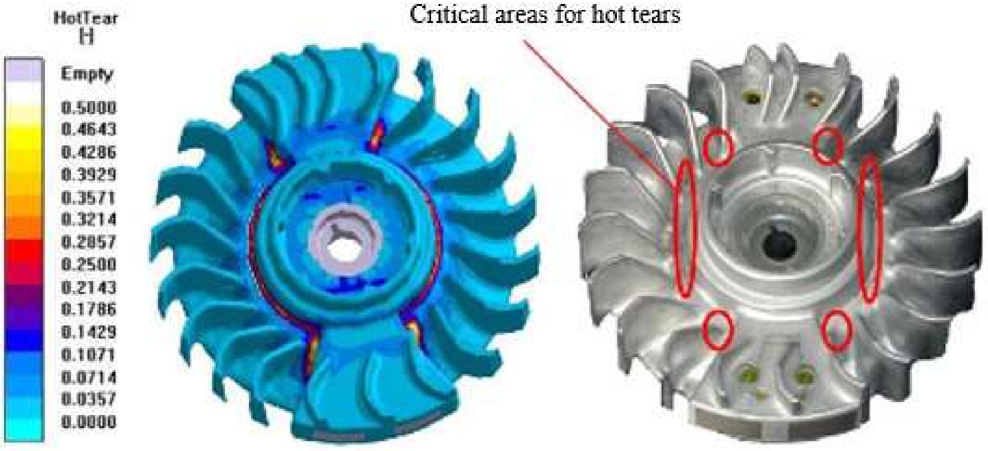

Figure 3.15 Prediction of hot tears in a flywheel casting using hot tear criterion [63]

Hartmann [64] studied the stress generation and distribution due to material combinations in light weight cast components. Engine blocks are one such application where the grey iron liners are set into the molds and preheated before pouring molten aluminum. The molten metal in contact with liner cools rapidly and solidifies quickly which sometimes results in incomplete filling of the mold. Certainly, residual stresses are generated due to a non-uniform temperature distribution in the cast part. Since, aluminum shrinks onto the iron liners, tensile stress is generated in aluminum whereas the liner experiences compressive stress, together with other internal stresses as shown in Figure 3.16. It is reported that the tensile residual stress observed in aluminum between the liners is high, however, any crack in this area does not affect the rigidity of cylinder block at operating temperature. For stress minimization, it was suggested to use the high pre-heat temperatures of the liners to decrease the tensile residual stress in the seam between liners.

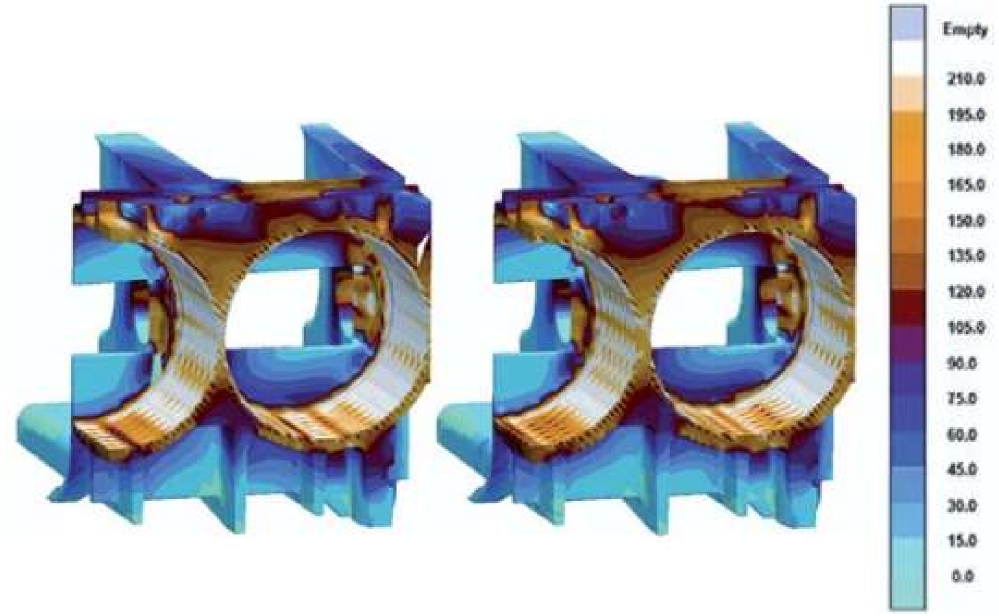

Figure 3.16 Internal stress in gap between two liners and uneven stress around the liner. High stress (left) in closer distances and low stress (right) in larger distances of the liners. [64]

3.5.4 CASTING SIMULATIONS INTEGRATED WITH MECHANICAL PERFORMANCE SIMULATIONS

In more recent years, casting simulations are combined with mechanical performance simulations to investigate the life of cast products in service. The effect of casting quality on service life is analyzed by taking the predictions of defects such as shrinkage and porosity from casting simulation results and map them with stress and fatigue life simulations.

Bordas et al. [71] studied the integration of foundry process simulations, non-destructive evaluation, stress analysis, and damage tolerance simulations to casting design as shown in Figure 3.17. Casting simulations are done to determine any porosity-related defects by using a radiographic inspection simulation tool (XRSIM). Failure caused by the predicted defects is determined by a fatigue crack growth simulation based on extended finite element method. This integrated approach enabled for an “accept or reject” criteria to be set at an early design stage and allows for damage tolerant design strategies. Dørum et al. [72] studied the effects of porosity and surface quality on structural behavior by mapping results of casting simulation by MAGMASOFT with a two-dimensional (shell element) finite element model developed in LS-DYNA. The study was primarily focused on mechanical performance of thin walled cast magnesium components subjected to quasi-static loading conditions. Olofsson et al. [73] presented software that incorporates the prediction of casting simulation software into a finite element method. The software is validated through a test case of ductile iron component.

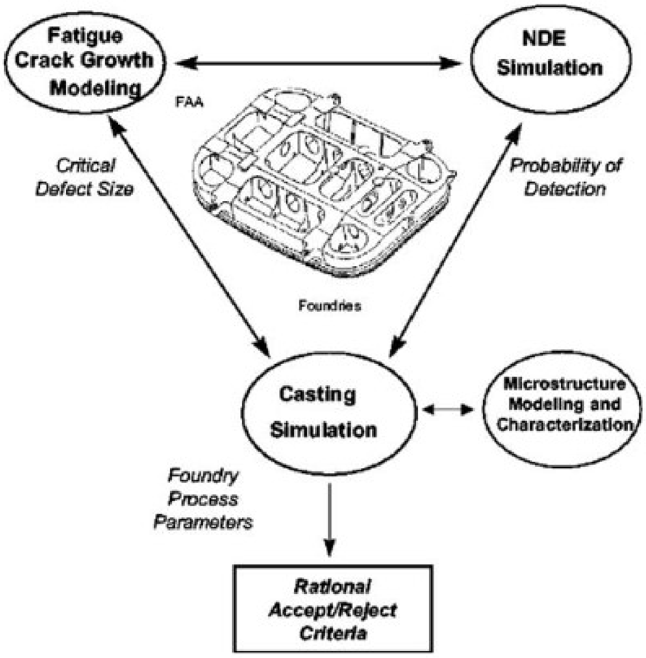

Figure 3.17 Integration of NDE simulation, casting modeling, and damage tolerance simulation [69]

The stress data from a finite element simulation is the input for the fatigue life estimation model. The linear elastic fracture mechanics (LEFM) and strain-life approaches can be used [74]. The strain-life prediction approach provided good agreement with measurements for micro porosity, but gave non-conservative results for macro porosity whereas linear elastic fracture mechanics (LEFM) method provided non-conservative estimates for both types of porosity [75]. The difficulty was to model the macro porosity due to their irregular shape and the fact that which of the specific macro pore was responsible for the failure [75]. Alternatively some commercial software for fatigue life predictions can be used [76].

In another study by Hardin et al. [77], the fatigue life of a cast steel component in service is predicted by utilizing the porosity predictions of MAGMASOFT in FE simulations. A block-diagram of the methodology used in the analysis is presented in Figure 3.18. This approach was first validated for a simple geometry of tensile test specimen by comparing experimentally obtained and the predicted crack initiation fatigue lives. The difference was reported to be within one decade that is thought to be very good for fatigue life prediction.

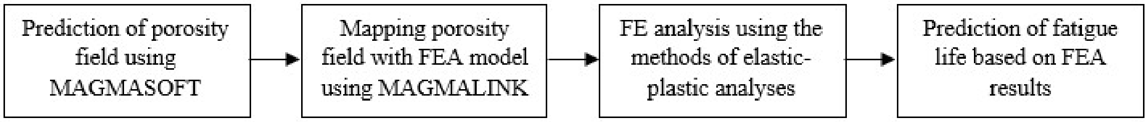

Figure 3.18 Integration of MAGMASOFT results in ABAQUS for fatigue life prediction

3.6 SUMMARY OF LITERATURE SURVEY

The case studies presented above provides details on how casting simulation tools are increasingly being utilized in modern foundries. A summary of literature survey for the current work is as follows.

- Literature review revealed that it is challenging to precisely model the boundary conditions and to validate the simulation results with the physical experiments.

- Casting simulations are capable of examining the effects of several casting parameters such as melt temperature, pouring time (velocity), gating and runner system design, riser design, mold configuration (single-cavity or multi-cavity) in producing sound castings.

- Most cast products are obtained with residual stresses. The accurate prediction of these residual stresses at design stage can greatly help in providing appropriate heat treatment strategies to reduce casting failures in service.
- Autonomous optimization method in casting simulation softwares must be fully utilized at its best to obtain good quality and defect free castings.
- There are recent attempts in literature to import the casting simulation results in FEM software to study the life of the part in service. This can lead to determine the reliability of parts in actual services where it is being used in dynamic loading of varying thermal and mechanical load cycles. This is a very promising direction and more rigorous work is needed in this area.

CHAPTER 4

CASTING SIMULATIONS USING MAGMASOFT

4.1 INTRODUCTION

Metal castings have always remained in question for their quality issues and uncertainty of service performance. Quality and performance issues arises due to casting defects, such as porosity, caused by shrinkage during solidification or formation of bubbles due to entrapped gases within the mold. Porosity can be minimized, if not eliminated, to improve casting quality and reliability. If such defects are ignored, then the castings are over-designed with exaggerated safety factors. This adds unnecessary weight to casting together with very little or no effect on the robustness of the design. A more realistic approach in pursuing a robust casting design could be utilizing casting simulations for prediction of porosity and incorporating it into the performance evaluation [76]–[79]. With integrated simulations, it is possible to achieve a casting design which is robust, porosity tolerant, and reliable.

In the present work, casting simulations are done using MAGMASoft for mold filling, solidification sequence, stresses and defects prediction in cast products. A common practice in analyzing the effect of porosity is to draw standard specimens from regions of interest in already cast plates, blocks, or even actual cast parts for testing and evaluation. Since, the objective of this work is to develop a methodology for simulation-based cradle to grave analysis of real castings, the standard specimens (tensile and fatigue) as shown in

Figure 4.1 are being considered as simple cast products for which a multi-cavity mold is designed, simulated and optimized based on the defects predicted in casting simulations. A multi-cavity mold is used for two reasons: (i) to produce more specimens for testing and (ii) to avoid or minimize the process related variabilities which are expected if each specimen is cast using a single cavity mold. The details of materials, casting simulation sequence in MAGMASoft, development of initial and optimized mold design, and casting simulation results are presented in the forthcoming sections.

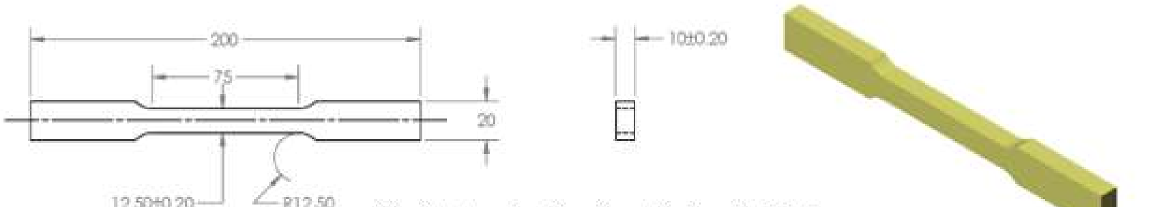

(a) Rectangular Specimen for Tensile Testing

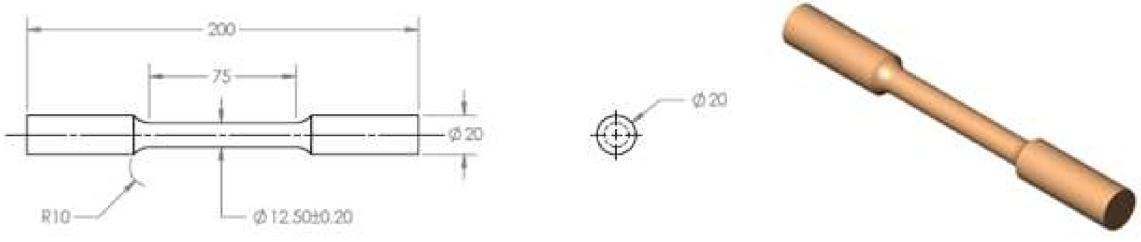

(b) Round Specimen for Fatigue Testing

Figure 4.1 a) Rectangular specimen for tensile testing (b) Round specimen for fatigue testing

4.2 MATERIALS

The selected materials for this study are widely used in foundries for casting variety of engineering applications. The first material is ASTM A216 WCB cast steel which provides a good combination of strength and ductility. The second material is GGG-40 ductile iron which provides a good combination of mechanical (high strength, ductility and wear resistance) and technological properties (low melting temperature, less shrinkage, and highest fluidity) [80]. The chemical composition and mechanical properties for selected grades of cast steel and ductile iron are presented in Table 4.1 and Table 4.2 respectively. Table 4.3 lists the properties of mold materials used in MAGMASoft simulations.

Table 4.1 ASTM A216 WCB Steel Material Specification

Chemical Composition (Wt. %)									
Fe	C	Mn	Si	P	S	Ni	Cr	Mo	Cu
96.2	0.3	1	0.6	0.035	0.35	0.5	0.5	0.2	0.3
Mechanical Properties (at room temperature as per ASTM A216)									
Yield Strength (MPa)			Tensile Strength (MPa)			Elongation (%)			
248			485			22			

Table 4.2 GGG-40 Ductile Iron Material Specification

Chemical Composition (Wt. %)			
Fe	C	Si	Mn
93.4	3.7	2.5	0.4
Mechanical Properties (at room temperature)			
Yield Strength (MPa)	Tensile Strength (MPa)	Elongation (%)	
250	400	15	

Table 4.3 Mold Material Specification

Cast Alloy	GGG-40 Ductile Iron	ASTM A216 WCB Steel
Mold Material	Green Sand	Furan
Base Materials	Silica Sand	Silica Sand
Binder	Bentonite	Furan
Water Content	3.50%	0%
Initial Temperature	40 °C	20 °C
Erosion Properties		
Reference Velocity	2.25 m/s	3 m/s
Reference Time	4.5 sec	6 sec
Sand Inclusion Parameters		
Sand grain diameter	240 µm	
Sand grain density	2650 kg/m^3	

4.3 CASTING SIMULATION SET UP IN MAGMASOFT

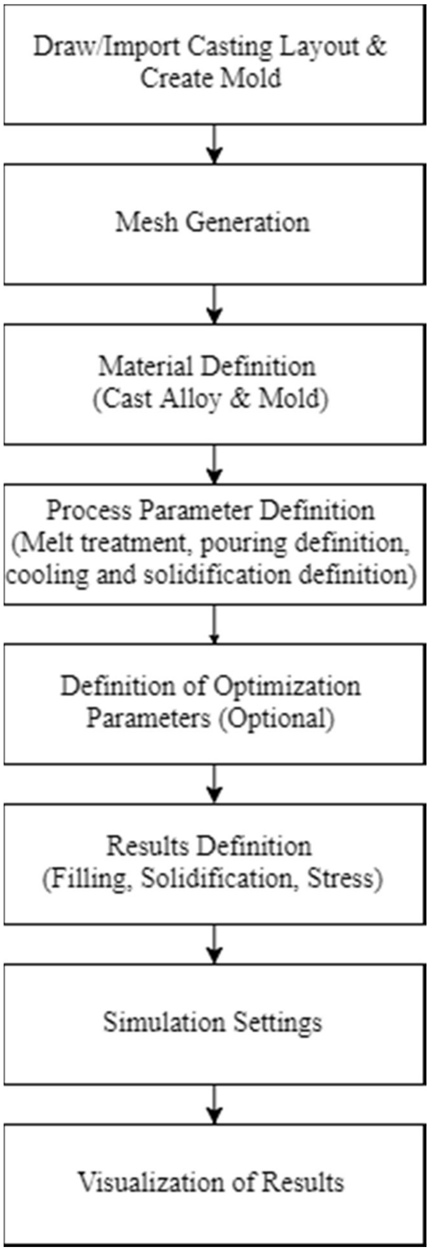

Figure 4.2 Simulation sequence in MAGMASoft

Casting simulations are set up in MAGMASoft using different perspectives within the software. To begin with, casting layout i.e. assembly of components such as pouring basin, sprue, runner, gates, casting, risers etc. is either drawn or imported from a CAD software in the *Geometry* perspective. A mold is also created in the same perspective. Next, the casting layout and mold is discretized using *Mesh* perspective. Following mesh generation, material (cast alloy and mold) properties and process parameters are defined using the *Definition* perspective. If needed, *Optimization* perspective can be used to set criteria for autonomous optimization of casting layout. The required results are defined and simulation settings are done using the *Simulation* perspective. At the end of simulation, the results are viewed in the *Results* perspective. A flow chart of simulation sequence in MAGMASoft is presented in Figure 4.2.

4.4 DEVELOPMENT OF OPTIMIZED MOLD DESIGN FOR CASTING STANDARD TEST SPECIMENS

The optimized mold designs for casting standard test specimens are developed as follows.

a) *Initial Mold Design:* The mold is initially designed using standards, foundry practices, and in-house mold design expertise of a foundry. In our case, we utilized the expertise of *Axles, Foundries & Spare Parts Factory - MASABIK* using their best design practices.
b) *Casting Simulation of Initial Mold Design:* Initial mold design is simulated for filling, solidification, stress distribution and porosity prediction in specimens using *MAGMASoft*.
c) *Optimized Mold Design:* Based on the results obtained in (b), casting layout of initial design is then optimized in virtual environment using MAGMASoft which offers multi-criteria optimization such as maximize yield, minimize defects (porosity, hotspots, cold shuts), avoid misruns, reduce velocities at gates etc. In present work, the casting design is optimized only to minimize the porosity.

The details of mold design optimization for tensile and fatigue test specimens of both materials under consideration are presented in the following sub-sections.

4.4.1 STEEL SPECIMENS FOR TENSILE TESTING

4.4.1.1 Initial Mold Design

The first step in casting simulation is the development of a CAD model of the casting layout in SOLIDWORKS (or any other CAD software) as shown in Figure 4.3. Sprue-runner configuration (single choke for multiple castings in a mold where it is impractical to choke the castings individually) is used to cast eight specimens at a time. Next, MAGMASoft is used to simulate the casting process using this initial mold design. The casting layout is discretized using a cubical mesh containing 1,961,750 volume elements. The materials properties, all modes of heat transfer i.e. conduction, convection, and radiation, and solvers used in simulations are already implemented/coded in the development of the software [81]. All properties such as heat transfer coefficients, density and kinematic viscosity at temperature of the melt, sand and core material properties are based on the embedded database in MAGMASoft. The initial temperature of the melt and the mold are 1630 °C and 20 °C respectively. The pouring time of the melt is specified to be 15 seconds and the feeding effectivity conservatively determined by the software is 30%. The mold design is simulated for filling and solidification behavior, generation and distribution of residual stresses, and to determine the location and magnitude of porosities within the cast specimens.

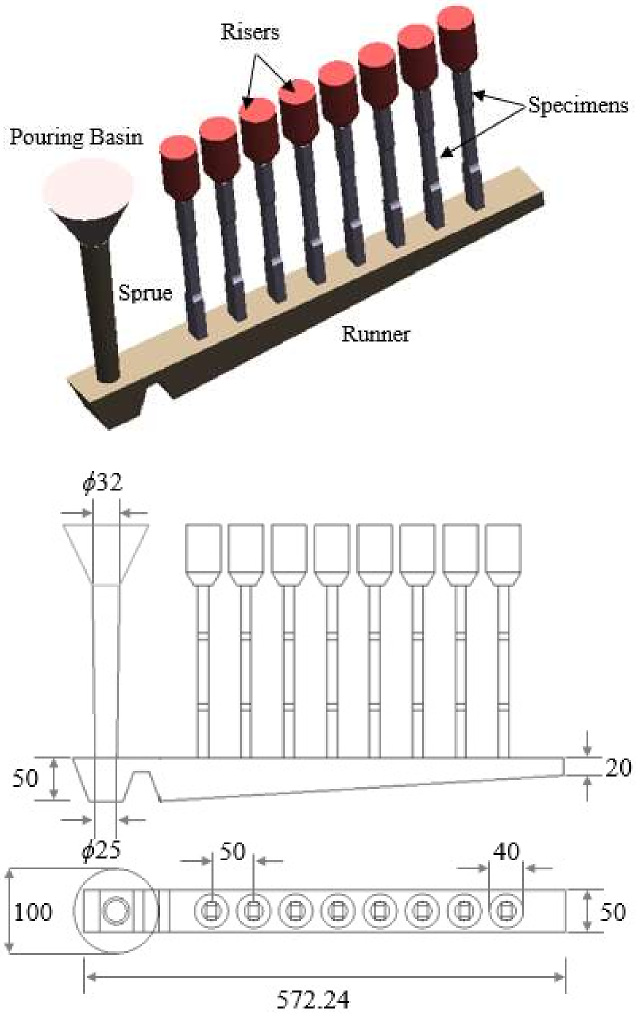

Figure 4.3 Initial casting layout for tensile specimens of steel

The temperature distribution within the mold after pouring (at 50% solidification) is presented in Figure 4.4 (a). The temperature distribution within the cast specimens is found to be non-uniform. Figure 4.4 (b) shows the solidification sequence (at 50% solidification) where the simulation confirmed that the last region to solidify will be sprue in the casting system. The whole casting system including the specimens, runner, risers and sprue took approximately 433 sec for complete solidification. Although the geometry of tensile specimen is fairly simple, the temperature gradient between different areas of specimen developed the residual stresses which are predicted as shown in Figure 4.4 (c) using stress simulation in MAGMASoft.

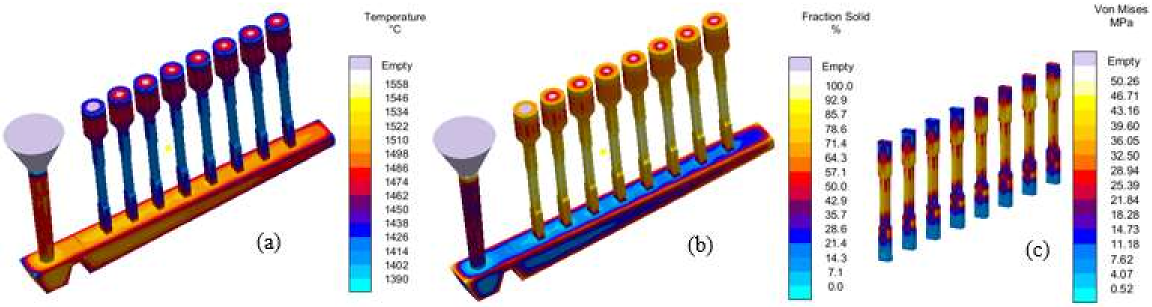

Figure 4.4 (a) Temperature profile within the mold at 50% solidification, (b) Percentage fraction solid at 50% solidification, and (c) Residual stresses in specimens at ejection

Figure 4.5 shows the X-ray views of simulated porosity, microporosity, and total porosity in the cast specimens. Six out of eight specimens resulted in almost no porosity as shown in Figure 4.5 (a), however, part of the specimens connected to runner contains significant porosity which needs to be minimized. Although the porosity in cast specimens 4 and 8 is predicted in the grip section as shown in Figure 4.5, it cannot be ignored because these specimens are considered as final cast products in this study. Hence, it is important to minimize/eliminate this porosity to produce all specimens with same quality. The distribution of microporosity in cast specimens is shown in Figure 4.5 (b). Figure 4.5 (c) shows the total porosity in the specimens where most of the porosity is internal, however, a closer observation also revealed porosity on the surface of some specimens. Although, the magnitude of total porosity is not too significant, it is decided to optimize the mold which can produce all of the specimens with more or less same level of porosity, microporosity, and total porosity.

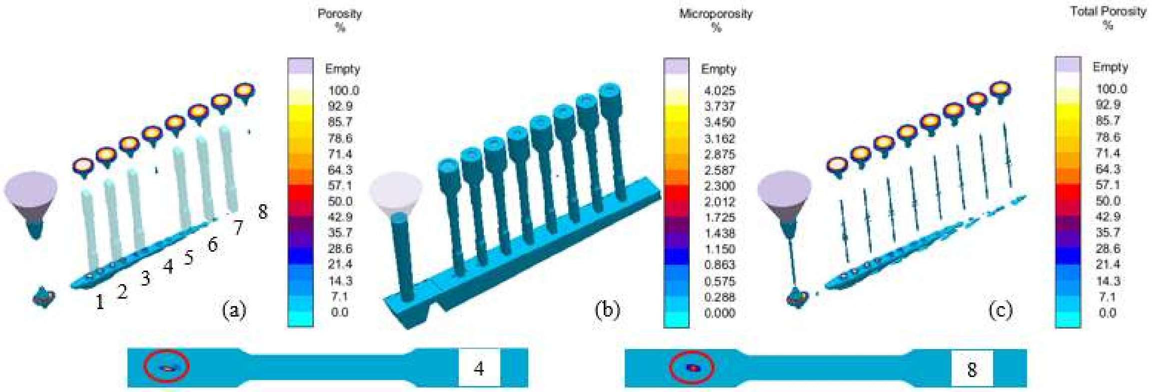

Figure 4.5 X-ray views of (a) porosity, (b) microporosity and (c) total porosity in simulated cast specimens using initial mold design

4.4.1.2 Optimized Mold Design

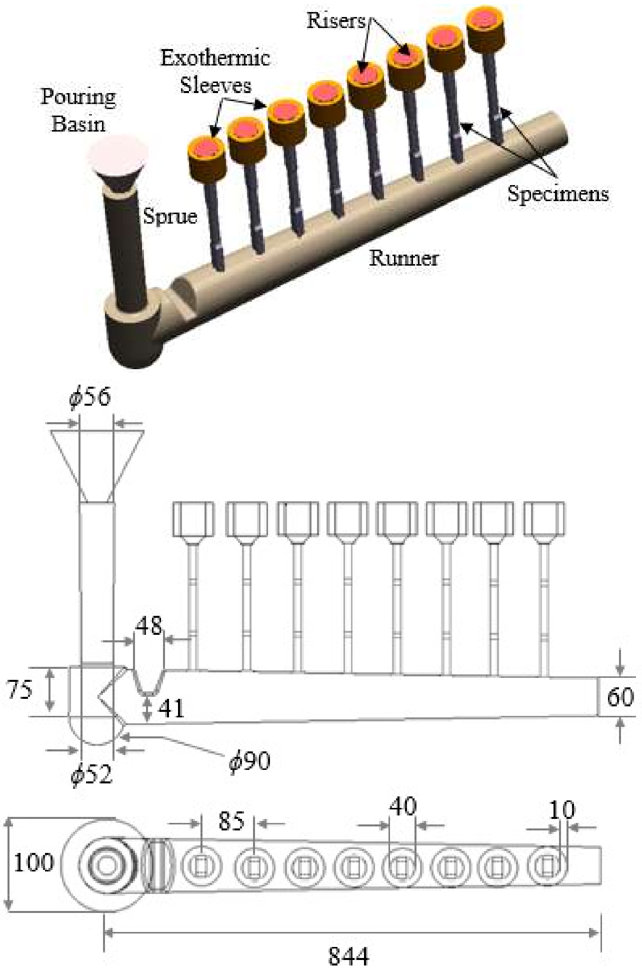

Figure 4.6 Optimized casting layout for tensile specimens of steel

The modification in casting layout of initial design began with modifying the elements of gating system as shown in Figure 4.6. Instead of providing a choke in sprue, a straight sprue is used in the mold and the choke is provided in the circular runner bar. A circular runner is used to avoid heat loss and to reduce friction in flow of the melt [82]. Exothermic sleeves, which delays the solidification in risers, are used to ensure no hotspots in cast specimens which is a common defect in steel castings [48]. This new casting layout is discretized into 1,960,287 volume elements. The simulation settings are kept same as already discussed in Section 4.4.1.1. Once again, simulation results indicated temperature gradient in cast specimens as shown in Figure 4.7 (a) and the last region to solidify is found to be sprue as shown in Figure 4.7 (b). The total solidification time is estimated to be 18 minutes. Residual stresses in cast specimens at ejection are shown in Figure 4.7 (c) and are reduced from ~50 MPa to ~40 MPa. Figure 4.8 shows the X-ray views of simulated porosity, microporosity, and total porosity in the cast specimens. It can be observed that same level of porosity is predicted in all eight specimens as shown in Figure 4.8 (a). No porosity is observed at the point where runner is connected to specimens. The distribution of microporosity in specimens is presented in Figure 4.8 (b). In terms of total porosity, no surface porosities are visible and the total porosity is confined to the test section (with reduced cross-sectional area) of specimens as shown in Figure 4.8 (c), which was previously noticed not only in the test section but also in the grips of specimens in Figure 4.5 (c).

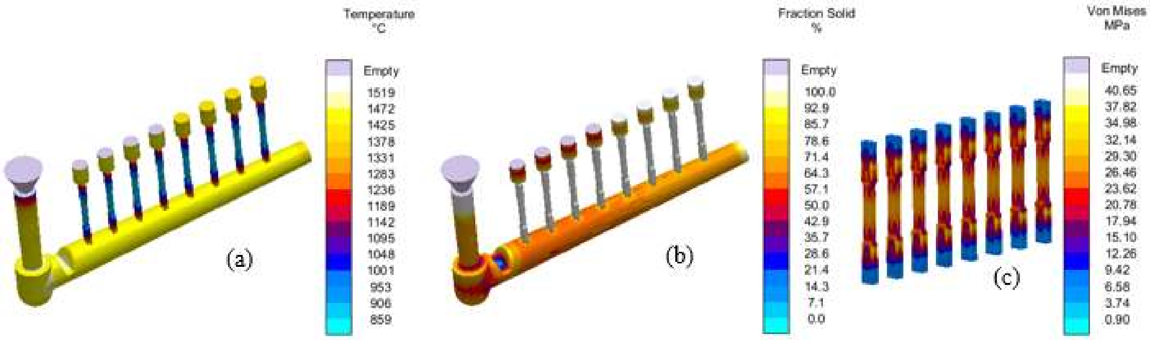

Figure 4.7 (a) Temperature profile within the mold at 50% solidification, (b) Percentage fraction solid at 50% solidification, and (c) Residual stresses in specimens at ejection

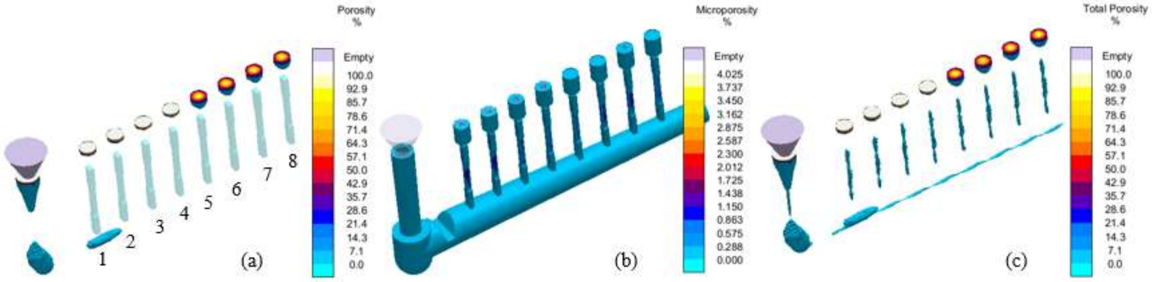

Figure 4.8 X-ray views of (a) porosity, (b) microporosity and (c) total porosity in simulated cast specimens using optimized mold design

4.4.2 IRON SPECIMENS FOR TENSILE TESTING

4.4.2.1 Initial Mold Design

The initial mold design for tensile specimens of iron is designed in a similar way to that of steel by using standards, foundry practices, in-house mold design expertise and formulae available in [83]. Figure 4.9 shows the casting layout for tensile specimens of iron which is imported to MAGMASoft for filling, solidification and stress simulations. The discretization of this layout using a cubical mesh resulted in 1,961,750 volume elements. The simulation settings are kept same as discussed earlier. The initial temperature of the melt and the mold are 1400 °C and 40 °C respectively. The pouring time of the melt is specified to be 15 seconds. Once again, the simulation is run for filling and solidification sequence, generation and distribution of residual stresses, and porosity in the test specimens.

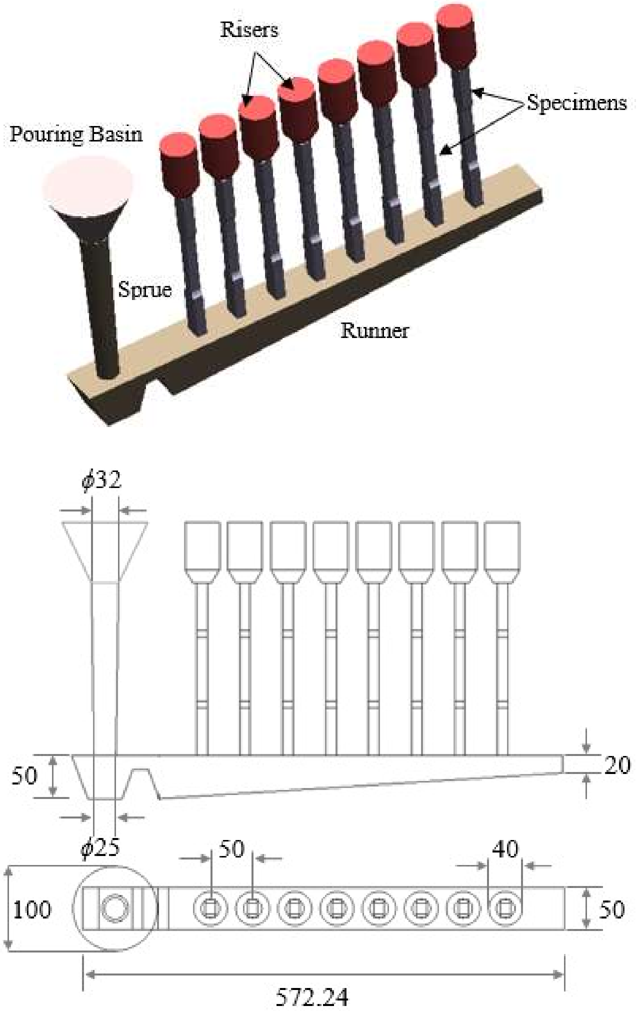

Figure 4.9 Initial casting layout for tensile specimens of iron

The temperature distribution within the mold after pouring is presented in Figure 4.10 (a). This temperature profile is presented at 50% solidification where it can be observed that the maximum pouring temperature i.e. 1400 °C is reduced to 1167 °C. A decrease in temperature profile is observed from grip to the test section of the specimens due to delayed solidification in risers and runner. This is also confirmed through solidification sequence in terms of percentage of fraction solid at 50% solidification as shown in Figure 4.10 (b).

Simulation confirmed that the last region to solidify will be runner in the gating system. The whole casting system including the specimens, runner, risers and sprue took approximately 43 min for complete solidification. The stress distribution in cast specimens at ejection is presented in Figure 4.10 (c) where most of the stresses concentration is mainly observed at the junction of test section and the grips of the specimens. Test section, on the other hand, is found to be free from any residual stresses in all specimens. The maximum stress in Figure 4.10 (c) is 6.5 MPa which is fairly less compared to typical stress of 20 to 50 MPa after casting [63], however, it could be further reduced using an optimized mold design.

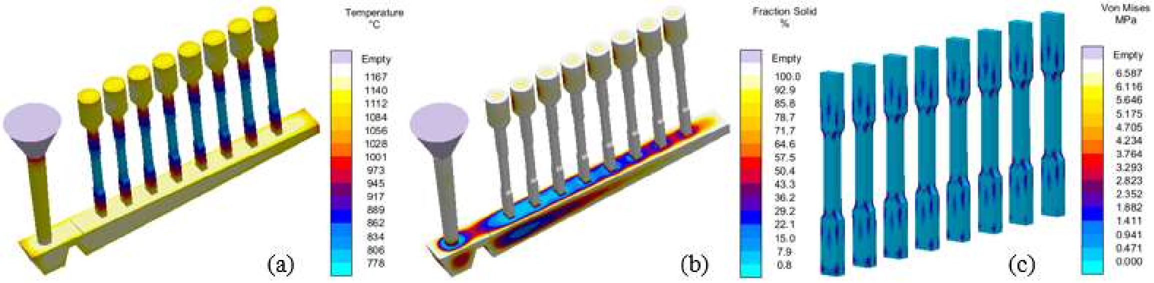

Figure 4.10 (a) Temperature profile within the mold at 50% solidification, (b) Percentage fraction solid at 50% solidification, and (c) Residual stresses in specimens at ejection

The solidification simulation also predicted the shrinkage related defects such as porosity in the cast specimens. MAGMASoft does not provide the results for microporosity and thus the total porosity for ductile iron. No surface porosity is observed in any specimens, however, some specimens are found with internal porosity. Figure 4.11 (a) depicts the cut-plane view of the porosity results which helps in visualizing the depth to which the casting is defected by porosity. Although the porosity in cast specimens 3, 5 and 7 is predicted in the grip section as shown in Figure 4.11 (b), it cannot be ignored because these specimens are considered as final cast products in this study. Hence it is decided to optimize the mold to minimize, if not eliminate, the porosity in all cast specimens.

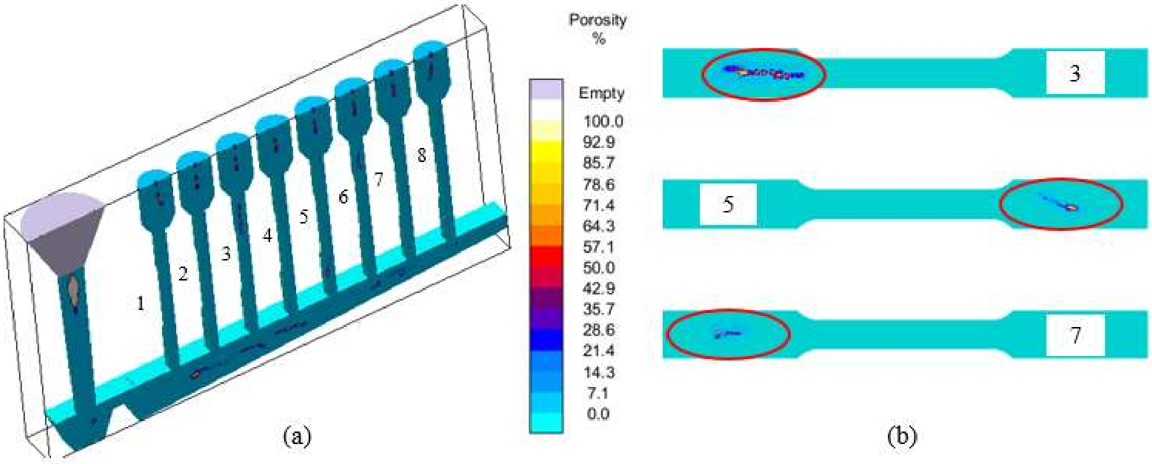

Figure 4.11 Simulated porosity in iron specimens using initial mold design (a) Cut-plane view and (b) Porous specimens

4.4.2.2 Optimized Mold Design

The initial casting layout is optimized in a similar manner to that of steel, however, exothermic sleeves are not used around the risers in this case as shown in Figure 4.12. This is due to using ductile iron for which the formation of hotspot defects is quite improbable. The modified casting layout is discretized into 1,986,864 volume elements using the cubical mesh. Simulation settings are kept same as already discussed previously. Once again, simulation results showed temperature gradient in cast specimens during solidification as shown in Figure 4.13 (a). The last region to solidify is found to be runner as shown in Figure 4.13 (b), whereas the total solidification time is estimated to be 28 minutes. Figure 4.13 (c) represents the stress distribution in cast specimens where no significant stresses are observed in the test section or in the grip areas. The maximum stress is reduced from 6.5 MPa to 3.97 MPa which confirms improved cooling and solidification. In terms of defects, the optimized mold design resulted in no porosity in the specimens.

Figure 4.14 (a) represents the cut-plane view of porosity results where some porosity is observed in risers, runner and sprue, however, all specimens are found to be pore-free. This is also confirmed through x-ray view of porosity results in MAGMASoft as shown in Figure 4.14 (b).

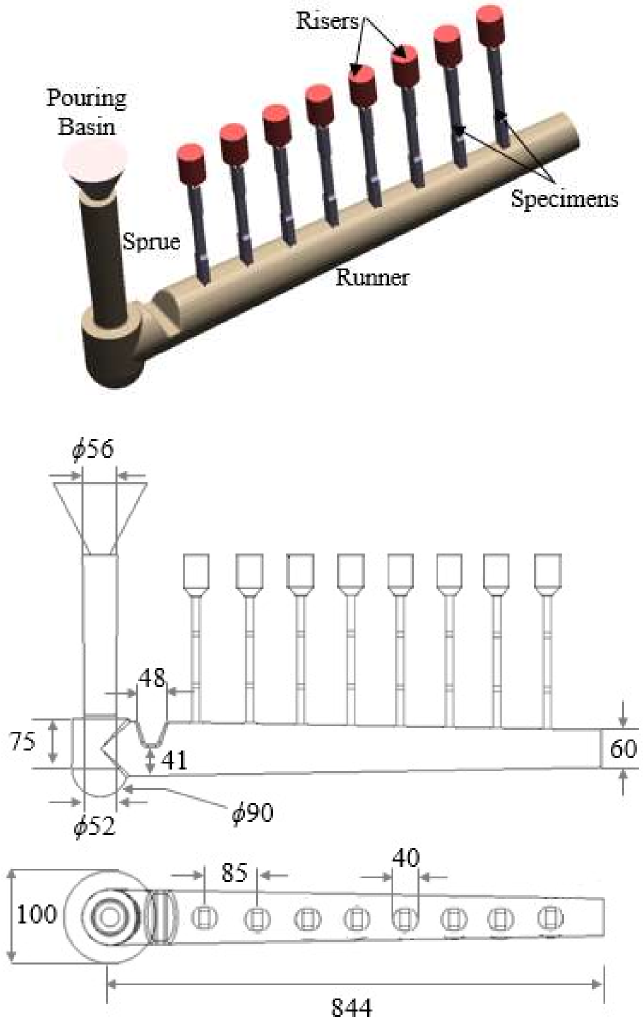

Figure 4.12 Optimized casting layout for tensile specimens of iron

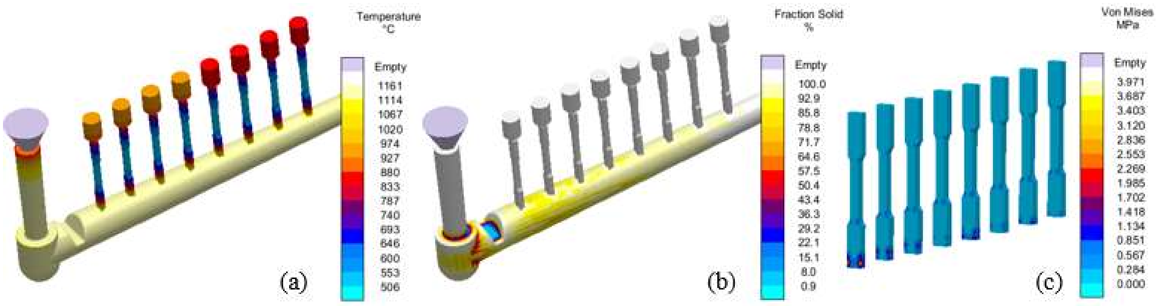

Figure 4.13 (a) Temperature profile within the mold at 50% solidification, (b) Percentage fraction solid at 50% solidification, and (c) Residual stresses in specimens at ejection

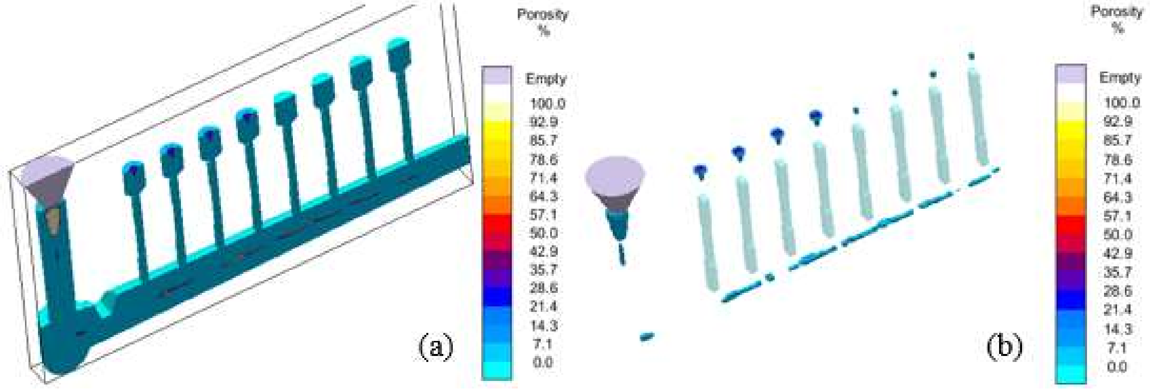

Figure 4.14 Simulated porosity using optimized mold for tensile specimens of iron (a) Cut-plane view and (b) X-ray view in MAGMASoft

4.4.3 STEEL SPECIMENS FOR FATIGUE TESTING

4.4.3.1 Initial Mold Design

The CAD model of initial casting layout for fatigue specimens is developed as shown in Figure 4.15. This layout is not much different from what is used for tensile specimens as shown in Figure 4.3. However, in this case, rectangular specimens are replaced by the round specimens. Similar sprue-runner configuration is used to cast right specimens at a time. This new casting layout is discretized in MAGMASoft using cubical mesh containing 1,975,320 volume elements. Since, same steel is used to cast fatigue specimens, material definition and simulation settings remained same as of simulation of tensile testing.

However, the pouring time in this case is set to be 15 seconds and the feeding effectivity determined by the software is 30%.

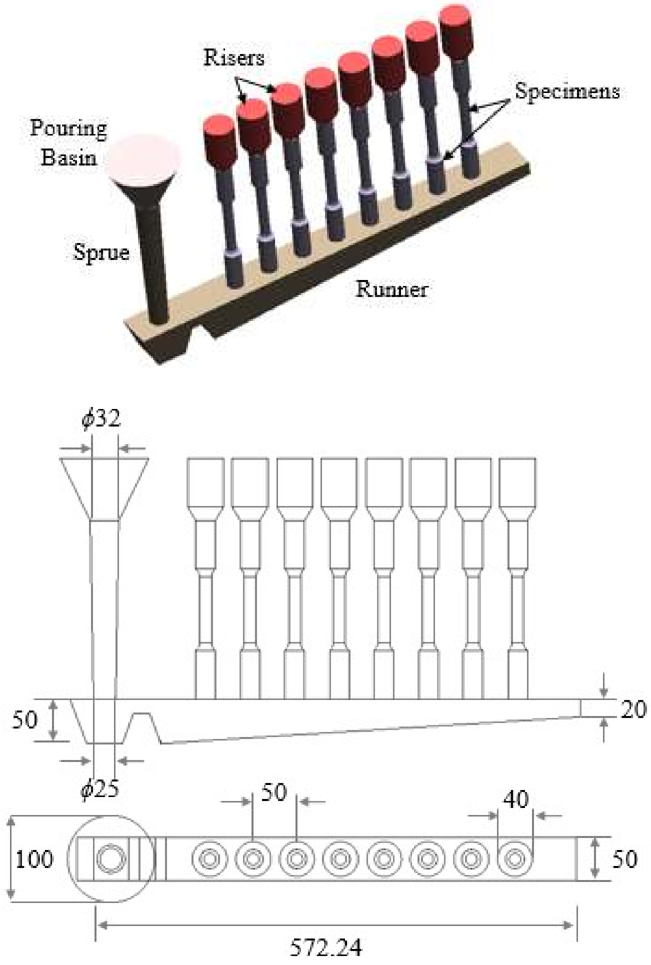

Figure 4.15 Initial casting layout for fatigue specimens of steel

The temperature distribution within the mold after pouring is presented in Figure 4.16 (a). It can be observed that the maximum temperature of the melt is dropped as the solidification progressed. The minimum temperature is found to be in test section of specimens suggesting the beginning of solidification from that region. At this stage i.e. 50% solidification, nearly all specimens are completely solidified as shown in Figure 4.16 (b). Simulation confirmed that the last region to solidify in casting layout are risers. The whole casting system including the specimens, runner, risers and sprue took approximately 8 minutes for complete solidification. The stress distribution in cast specimens at ejection is presented in Figure 4.16 (c) where stresses are found to be concentrated in the test section of the specimens. The maximum residual stress at ejection is about 50 MPa which is a typical magnitude of residual stress in steel castings [63].

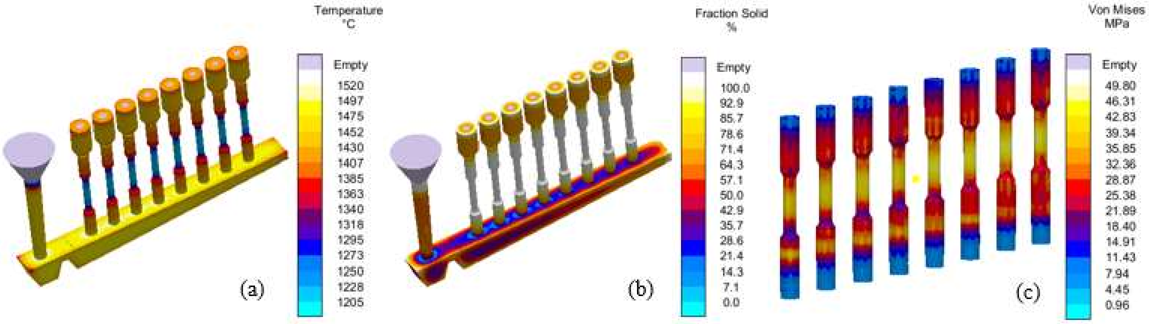

Figure 4.16 a) Temperature profile within the mold at 50% solidification, (b) Percentage fraction solid at 50% solidification, and (c) Residual stresses in specimens at ejection

In terms of porosity, the X-ray view shown in Figure 4.17 (a) revealed only one specimen to be pore-free. However, significant porosity is observed in specimens 4, 6, 7 and 8 as shown in Figure 4.17. Despite the porosity is observed in grips of test specimens, it had to be minimized for the reason that these specimens are simple cast products. Microporosity is distributed throughout the casting layout with a maximum microporosity to be ~4% as shown in Figure 4.17 (b). Figure 4.17 (c) shows the total porosity in the specimens which is found to be nearly same in all specimens and could be minimized with a better mold design.

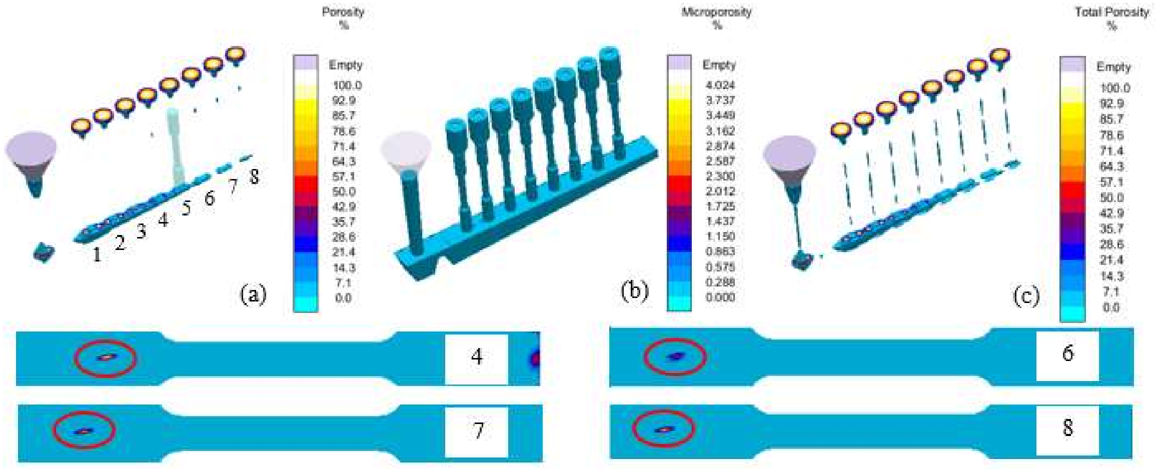

Figure 4.17 X-ray views of (a) porosity, (b) microporosity and (c) total porosity in simulated cast specimens using initial mold design

4.4.3.2 Optimized mold design

The optimized mold design for fatigue specimens of steel is essentially the same as of tensile specimens. The main changes are removal of choke from the sprue, choke at the beginning of runner bar, and use of exothermic sleeves. The new casting layout as shown in Figure 4.18 is discretized into 1,989,414 volume elements. The simulation settings are kept same as already discussed earlier. Once again, simulation results indicated temperature gradient in cast specimens as shown in Figure 4.19 (a) and the last region to solidify is found to be risers as shown in Figure 4.19 (b). The total solidification time is estimated to be 16 minutes. Residual stresses in cast specimens at ejection are shown in Figure 4.19 (c) and are reduced from ~40 MPa to ~30 MPa. Figure 4.20 shows the X-ray views of simulated porosity, microporosity, and total porosity in the cast specimens. It can be observed that same level of porosity is predicted in all eight specimens as shown in Figure 4.20 (a). No porosity is observed at the point where runner is connected to specimens. The distribution of microporosity in specimens is presented in Figure 4.20 (b).

Total porosity is found to be identical and reduced in all specimens as compared to the total porosity shown in Figure 4.17 (c).

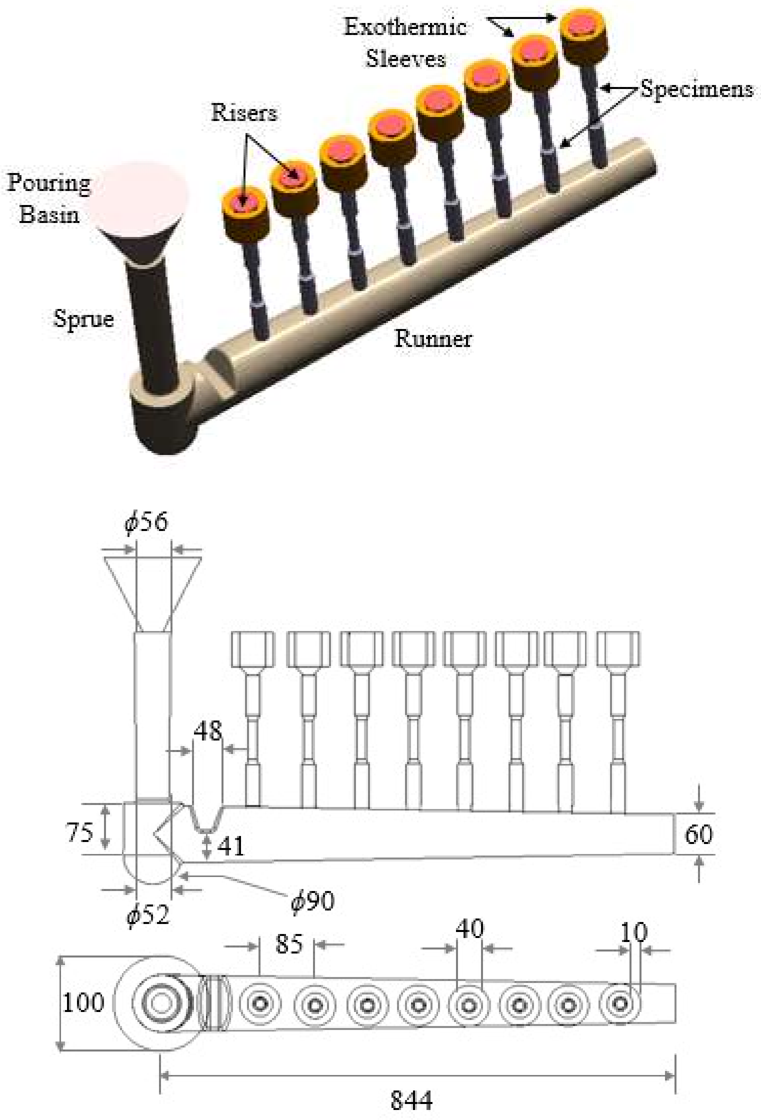

Figure 4.18 Optimized casting layout for fatigue specimens of steel

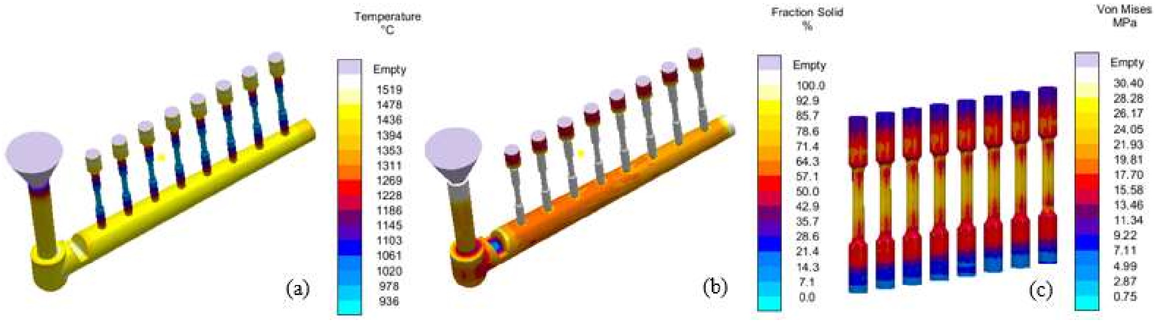

Figure 4.19 a) Temperature profile within the mold at 50% solidification, (b) Percentage fraction solid at 50% solidification, and (c) Residual stresses in specimens at ejection

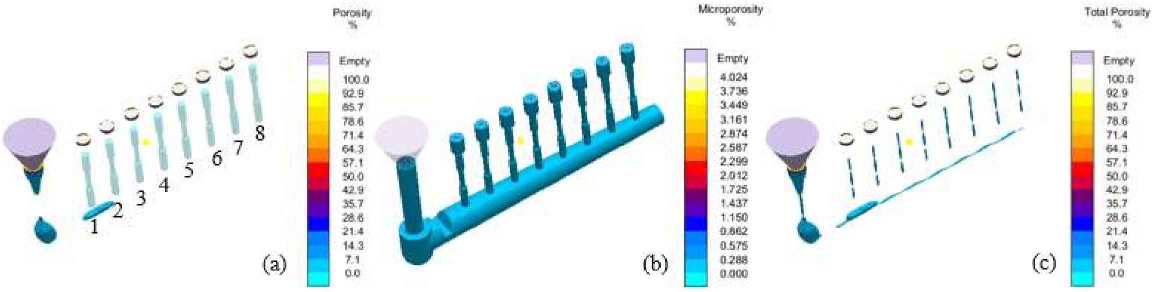

Figure 4.20 X-ray views of (a) porosity, (b) microporosity and (c) total porosity in simulated cast specimens using optimized mold design

4.4.4 IRON SPECIMENS FOR FATIGUE TESTING

4.4.4.1 Initial mold design

The initial mold design for fatigue specimens of iron is designed in a similar way to that of steel where rectangular specimens are replaced by the round specimens as shown in Figure 4.21. This casting layout is imported to MAGMASoft and discretized into 1,975,320 volume elements using cubical mesh. Since, same iron is used to cast fatigue specimens, material definition and simulation settings remained unchanged as of simulation of tensile specimens. However, the pouring time in this case is set to be 15 seconds.

The temperature distribution within the mold after pouring is presented in Figure 4.22 (a). It can be observed that the maximum temperature of the melt is dropped as the solidification progressed. The minimum temperature is found to be in test section of specimens suggesting the beginning of solidification from that region. At this stage i.e. 50% solidification, nearly all specimens are completely solidified as shown in Figure 4.22 (b). Simulation confirmed that the last region to solidify in casting layout is runner. The whole casting system including the specimens, runner, risers and sprue took approximately 11 minutes for complete solidification. The stress distribution in cast specimens at ejection is presented in Figure 4.22 (c). Residual stresses in most regions of the specimens are found to be in in range of ~4 MPa to ~7 MPa, however, the observed maximum stress as per the contour plot shown in Figure 4.22 (c) is ~20 MPa, which can be reduced further with an improved mold design.

The simulation results for porosity are presented in Figure 4.23 where no specimens are found with surface porosity. However, four out of eight specimens i.e. 2, 5, 7, and 8 resulted in internal porosity. Figure 4.23 (a) depicts the cut-plane view of the porosity results which helps in visualizing the depth to which the casting is defected by porosity. Simulated porosity is considered significant because the grips as well as test section of the specimens, particularly 2, 7 and 8, are affected as shown in Figure 4.23 (b). Hence, this porosity had to be minimized/eliminated through a better mold design.

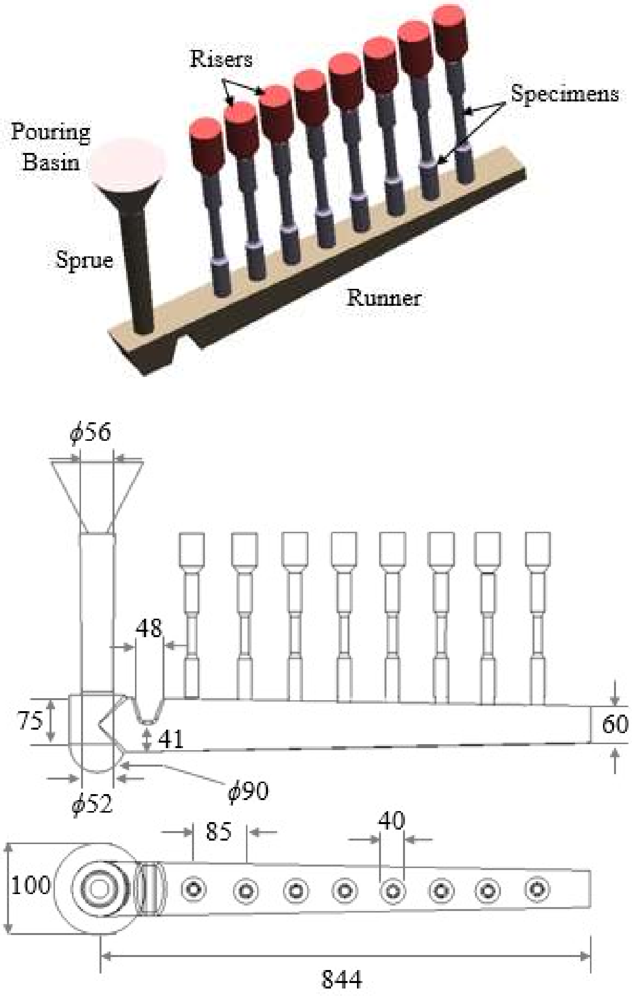

Figure 4.21 Initial casting layout for fatigue specimens of iron

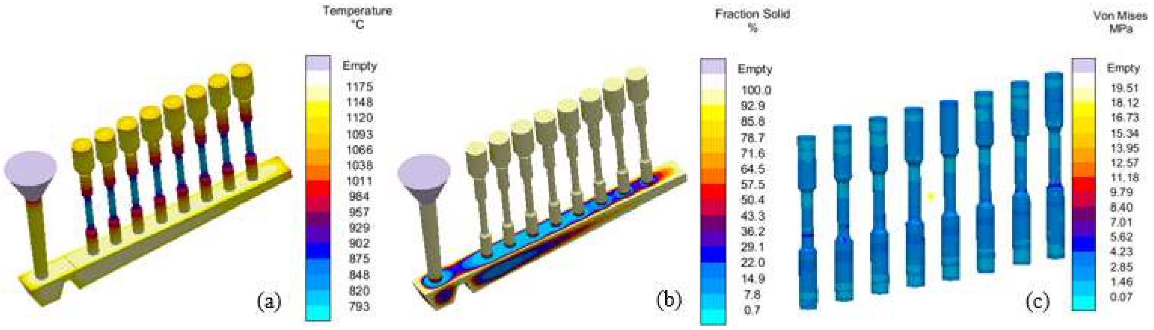

Figure 4.22 a) Temperature profile within the mold at 50% solidification, (b) Percentage fraction solid at 50% solidification, and (c) Residual stresses in specimens at ejection

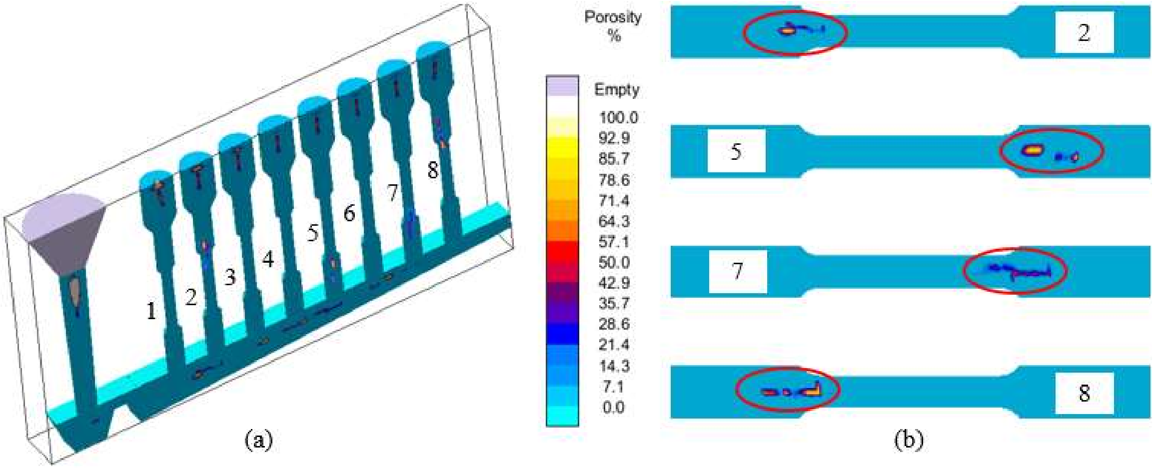

Figure 4.23 Simulated porosity in iron specimens using initial mold design (a) Cut-plane view and (b) Porous specimens

4.4.4.2 Optimized mold design

The initial mold design for casting fatigue specimens of iron is modified in a similar manner to that of steel, however, no exothermic are used in this case as shown in Figure 4.24. The modified casting layout is discretized into 1,950,480 volume elements using the cubical mesh. Simulation settings are kept same as already discussed previously. Once again, simulation results showed temperature gradient in cast specimens during solidification as shown in Figure 4.25 (a). The last region to solidify is found to be part of the runner connected to sprue as shown in Figure 4.25 (b), whereas the total solidification time is estimated to be 26 minutes. Figure 4.25 (c) represents the stress distribution in cast specimens where some residual stresses are found in the grips of the specimens. Nevertheless, the magnitude of observed residual stress in the grips is reduced to ~1 MPa to ~2.5 MPa with almost no residual stresses within the test section, thereby, suggesting improved cooling and solidification using the modified casting layout. In terms of defects, the optimized mold design resulted in no porosity in the specimens. Figure 4.26 (a) represents the cut-plane view of porosity results where some porosity is observed in risers, runner and sprue, however, all specimens are found to be pore-free. This is also confirmed through x-ray view of porosity results in MAGMASoft as shown in Figure 4.26 (b).

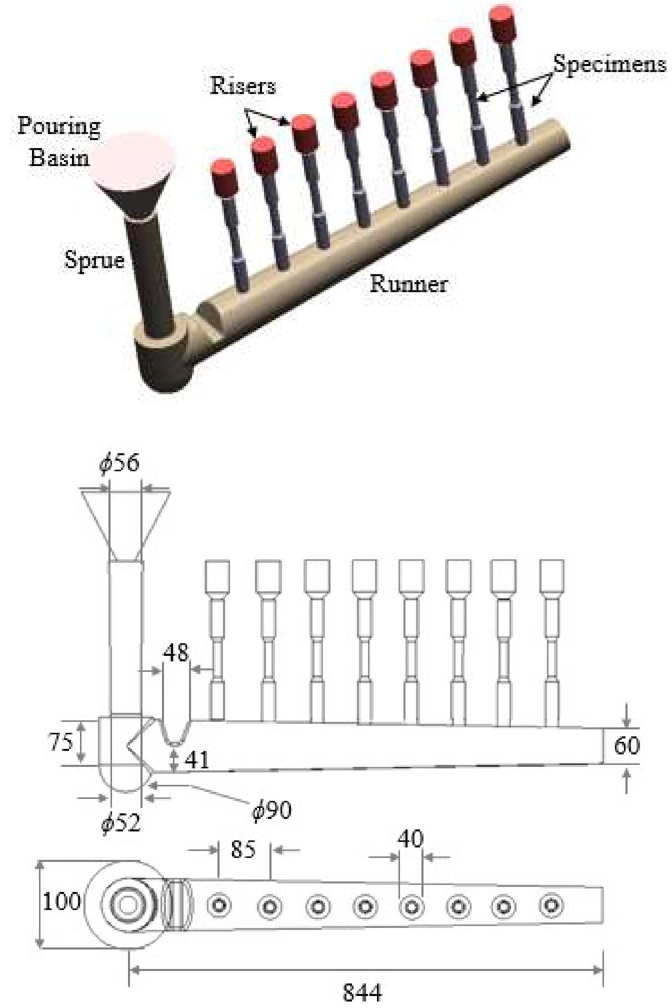

Figure 4.24 Optimized casting layout for fatigue specimens of iron

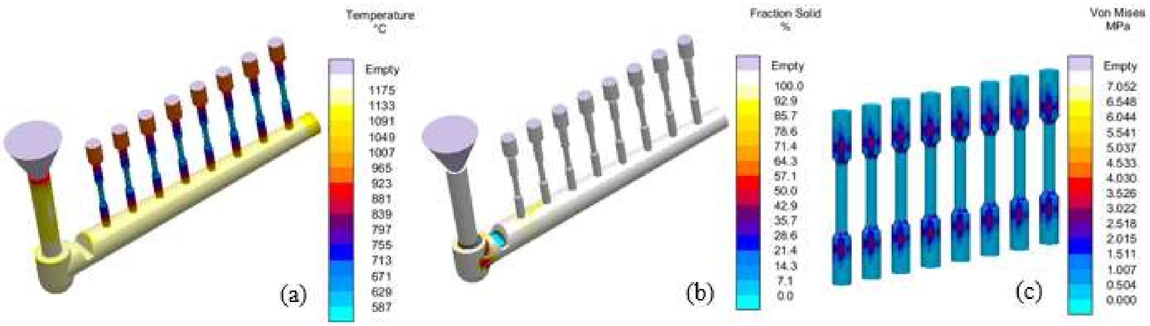

Figure 4.25 a) Temperature profile within the mold at 50% solidification, (b) Percentage fraction solid at 50% solidification, and (c) Residual stresses in specimens at ejection

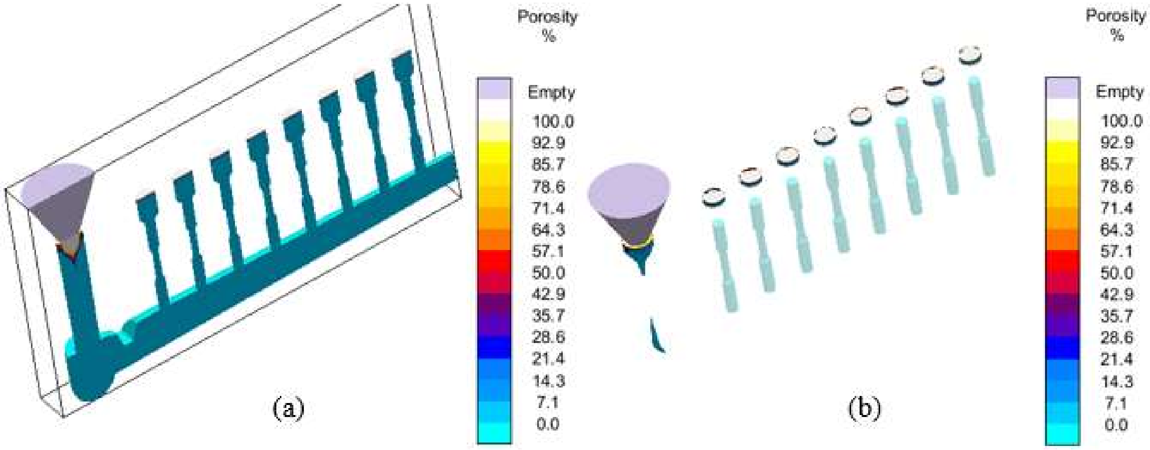

Figure 4.26 Simulated porosity using optimized mold for tensile specimens of iron (a) Cut-plane view and (b) X-ray view in MAGMASoft

4.5 CONCLUDING REMARKS

In this chapter, the optimized mold design for casting tensile and fatigue specimens of both materials are obtained using MAGMASoft simulations. It is observed that the modification in gating system and use of auxiliary products can significantly reduce the porosity in castings when compared with initial best practices based molds design in each case. With these optimized mold designs, it is expected to produce high quality pore-free specimens at MASABIK foundry.

CHAPTER 5

CASTING OF STANDARD TEST SPECIMENS AND MECHANICAL TESTING

5.1 INTRODUCTION

The actual casting process, subsequent to the development of an optimized mold design, involves a series of steps such as pattern and core making, mold preparation, melt preparation and treatment, pouring, cleaning and heat treatment etc. This chapter presents the details of casting standard test specimens at MASABIK foundry using optimized mold designs. Next, the cast specimens, after final machining, are subjected to mechanical testing. The details of experiments for tensile and fatigue testing of cast specimens and the results are presented in the forthcoming sections.

5.2 CASTING OF STANDARD TEST SPECIMENS

5.2.1 STEEL SPECIMENS FOR TENSILE AND FATIGUE TESTING

The casting of specimens began with making patterns based on the optimized mold designs for tensile and fatigue test specimens. In the present work, wooden patterns are used for mold preparation as shown in Figure 5.1. These patterns are then used to prepare furan sand molds. The mold halves for casting tensile and fatigue specimens are presented in

Figure 5.2. The mold is coated with Zirkofluid, a zirconium based coating to produce a dense layer for protection against penetrations and mold-metal reactions. The compression strength and scratch hardness of the mold are found to be 18 kg/cm^2 and 28-29 respectively. The molten metal is poured in to the mold at 1590-1600 °C at MASABIK foundry. It is tried to maintain the same physical conditions used in casting simulations. The resulting tree of cast specimens from the molds are shown in Figure 5.3. After removing pouring basin, sprue, runner bar, and risers, the final cast specimens are obtained as shown in Figure 5.4 which are subjected to heat treatment. The specimens are annealed at 920 °C, held for half an hour, and cooled in furnace. Specimens after heat treatment are machined to final dimensions for testing and evaluation.


(a) (b)

Figure 5.1 Wooden pattern for mold preparation (a) Tensile Specimens and (b) Fatigue Specimens

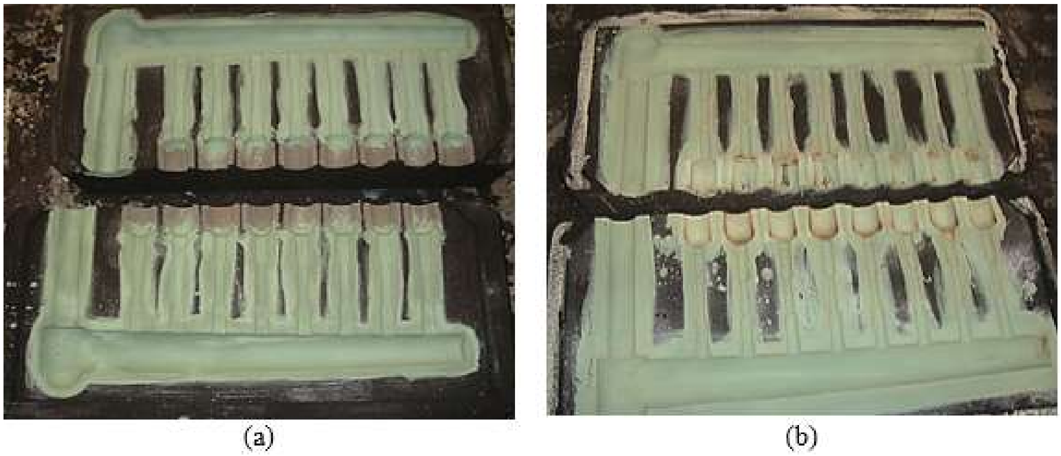
(a) (b)

Figure 5.2 Furan sand mold for casting steel specimens (a) Tensile and (b) Fatigue

Figure 5.3 Steel specimens before cleaning and finishing (a) Tensile and (b) Fatigue

Figure 5.4 Steel specimens before machining to standard dimensions (a) Tensile and (b) Fatigue

5.2.2 IRON SPECIMENS FOR TENSILE AND FATIGUE TESTING

The patterns shown in Figure 5.1 are used in mold preparation for casting tensile and fatigue specimens of ductile iron. In this case, mold is prepared using green sand. The mold halves for casting tensile and fatigue specimens are presented in Figure 5.5. Once again, the mold is coated with Zirkofluid to protect from melt penetrations and mold-metal reactions. The compression strength and scratch hardness of the mold are found to be 1.5-2 kg/cm^2 and 80-85 respectively. The melt is prepared and poured in the mold at 1420-1440 °C at MASABIK foundry. It is tried to maintain the same physical conditions used in casting simulations. The resulting tree of cast specimens from the molds are shown in Figure 5.6. After removing pouring basin, sprue, runner bar, and risers, the final cast specimens are obtained as shown in Figure 5.7 which are machined to final dimensions for testing and evaluation. No heat treatment is done for ductile iron specimens.

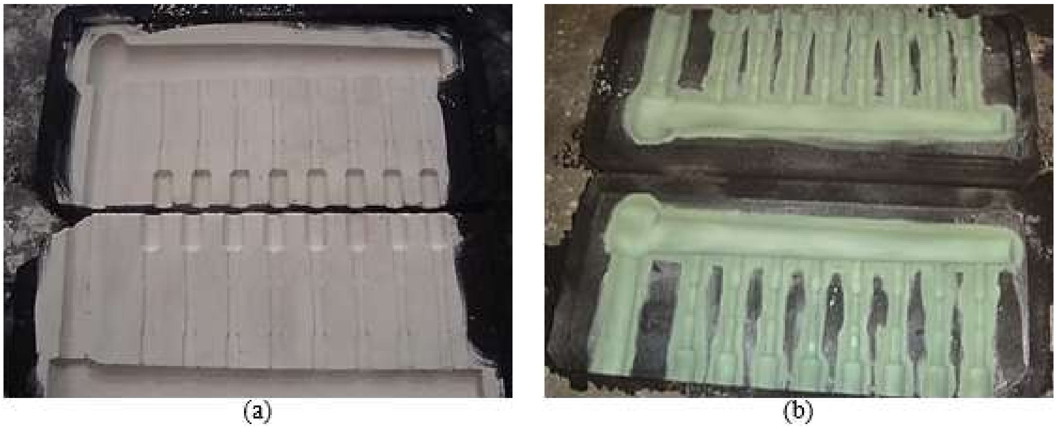

(a) (b)

Figure 5.5 Green sand mold for casting iron specimens (a) Tensile and (b) Fatigue

(a) (b)

Figure 5.6 Iron specimens before cleaning and finishing (a) Tensile and (b) Fatigue

(a) (b)

Figure 5.7 Iron specimens before machining to standard dimensions (a) Tensile and (b) Fatigue

The final dimensions of tensile and fatigue test specimens are determined from ASTM E 8 [84] and ASTM E 466 [85] standards respectively. The specimens are machined to dimensions shown in Figure 5.8. Since, the casting simulations resulted in nearly same quality of test specimens, therefore, five out of eight specimens of each material are selected for tensile testing. Tensile specimens are labelled with letter “S” and “I” for steel and iron respectively followed by number 1 through 5. In order to develop the Stress vs. Number of Cycles to Failure (S-N curve) from fatigue testing of cast specimens, it is decided to test six specimens for finite life and one for the infinite life (or the runout condition) from each material under consideration. Hence, fatigue specimens are labelled with letter “S” and “I” for steel and iron respectively followed by number 1' through 7'.

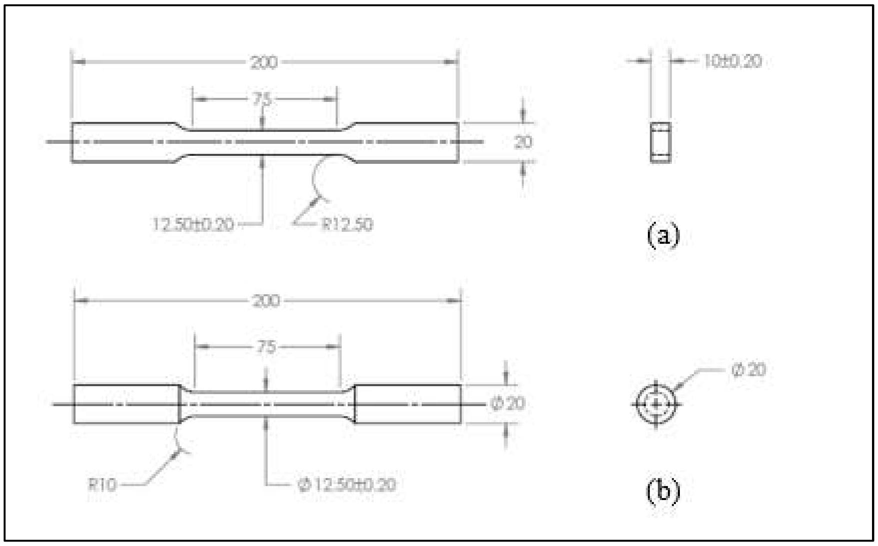

Figure 5.8 Standard dimensions of test specimens (a) Tensile and (b) Fatigue

5.3 HEAT TREATMENT OF CAST SPECIMENS

The recommended heat treatment for ASTM A216 WCB steel is either annealing (890-910 °C) or normalizing (910-920 °C). In the present study, only steel specimens produced after casting are subjected to heat treatment at MASABIK foundry. All tensile and fatigue specimens of steel are normalized. The specimens are heated to 910-920 °C, soaked for half an hour, and then cooled in still air.

5.4 RADIOGRAPHIC EXAMINATION OF CAST SPECIMENS

The quality of cast specimens is evaluated using radiographic examination. X-ray imaging of selected specimens for tensile and fatigue testing of each material is done prior to testing. The results of X-ray imaging are presented in Figure 5.9 to Figure 5.12. No apparent traces of any significant porosity are observed in tensile specimens of each material as shown in Figure 5.8 and Figure 5.9 which confirms high quality. For fatigue specimens, some porosity is revealed within the test section of steel specimens which is observed as difference in appearance of grips and the test section in the X-ray image as shown in Figure 5.11. However, the distribution of porosity from one specimen to another is not much different. Fatigue specimens cast from ductile iron showed no traces of porosity as shown in Figure 5.12 thereby confirming good quality of casting in this case.

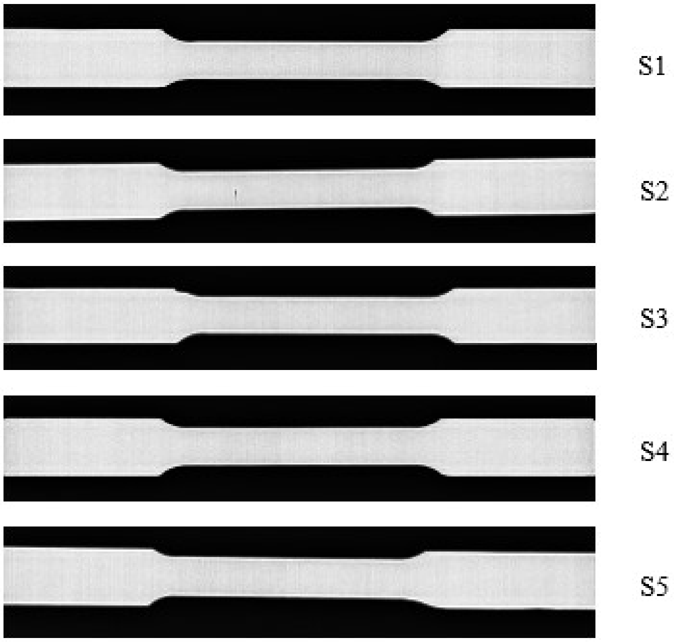

Figure 5.9 X-ray image of tensile specimens of cast steel

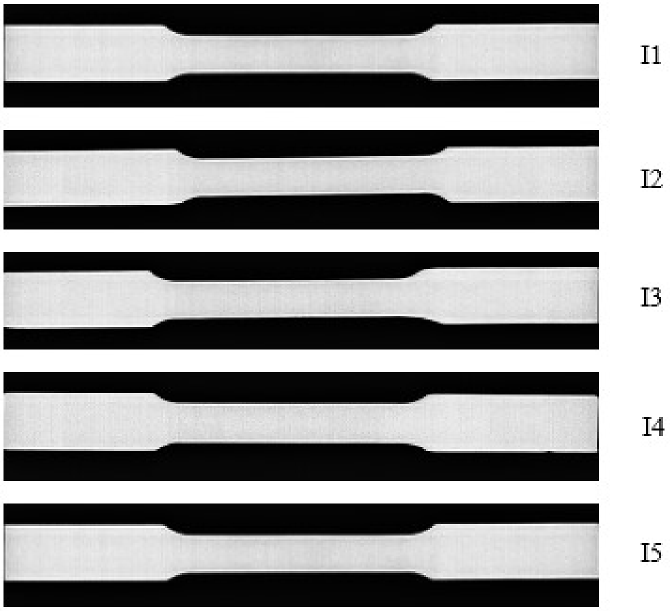

Figure 5.10 X-ray image of tensile specimens of ductile iron

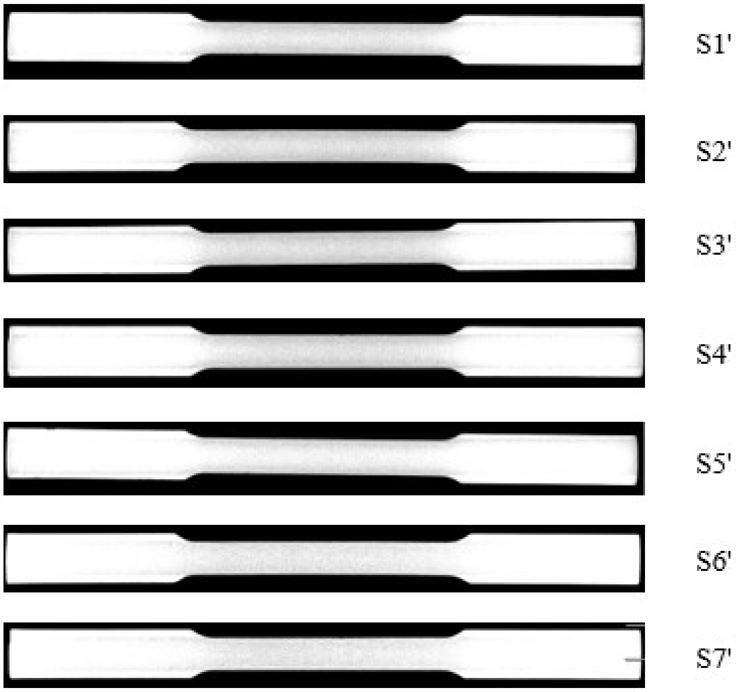

Figure 5.11 X-ray image of fatigue specimens of cast steel

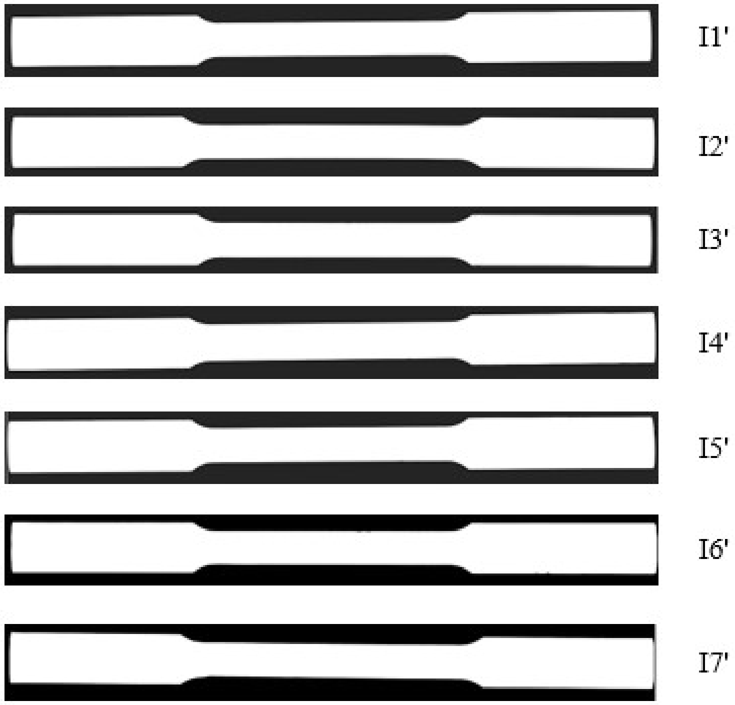

Figure 5.12 X-ray image of fatigue specimens of ductile iron

5.5 MECHANICAL TESTING

5.5.1 TENSILE TESTING

Figure 5.13 shows the tensile testing arrangement for test specimen where the position of extensometer is indicated. Tensile testing of sound steel and iron specimens are done at MASABIK foundry, whereas, for porous specimens (S1 to S5 and I1 to I5), the testing is done using in-house facilities. The sound specimens are prepared from rolled sheets of each material. A displacement rate of 1 mm/min is used throughout for testing each specimen.

Figure 5.13 Experimental setup for tensile testing of cast specimens

The results of tensile testing for sound and cast specimens of steel are presented in Figure 5.14. The cast specimens S1 through S5 are found to have reduced strength and ductility when compared to sound specimen. Moreover, Figure 5.14 indicates some differences in the stress-strain behavior of the tested specimens. Table 5.1 shows the summary of results obtained for tensile testing of steel specimens. These results demonstrated that in each specimen a complex stress field is generated upon loading which needs to be simulated in order to predict the accurate stress-strain behavior of a given specimen.

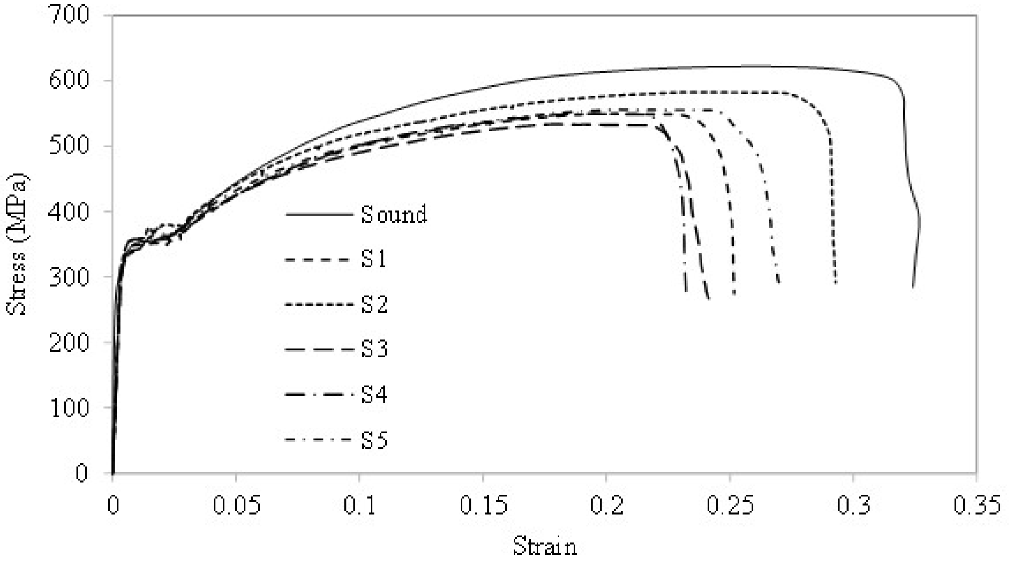

Figure 5.14 Results of tensile testing for sound and cast steel specimens

Table 5.1 Summary of tensile testing experiments of steel specimens

Specimen	Yield Strength (MPa)	Tensile Strength (MPa)	Elongation (%)	Modulus of Elasticity (GPa)	Fracture Strength (MPa)
Sound	355	620	32.5	198	293
S1	340	549	25.2	193	275
S2	355	583	29.3	196	292
S3	337	534	23.2	191	267
S4	356	549	23.2	196	275
S5	347	556	27.0	191	278

The results of tensile testing for sound and cast specimens of iron are presented in Figure 5.15. In terms of iron specimens, an excellent agreement is observed in the stress-strain behavior of the sound and cast specimens. The specimen I2 almost showed the stress-strain behavior of a sound specimen, thereby, confirms the effectiveness of casting simulations in obtaining the cast parts with nearly similar mechanical properties as in case of sound (pore-free) parts. Specimens I1, I3, I4, and I5 are found to have slightly reduced yield strength and ductility, however, the values obtained are above the standard minimum values of GGG-40 ductile iron already summarized above in Table 4.2. A summary of experimental results for tensile testing of iron specimens is presented in Table 5.2.

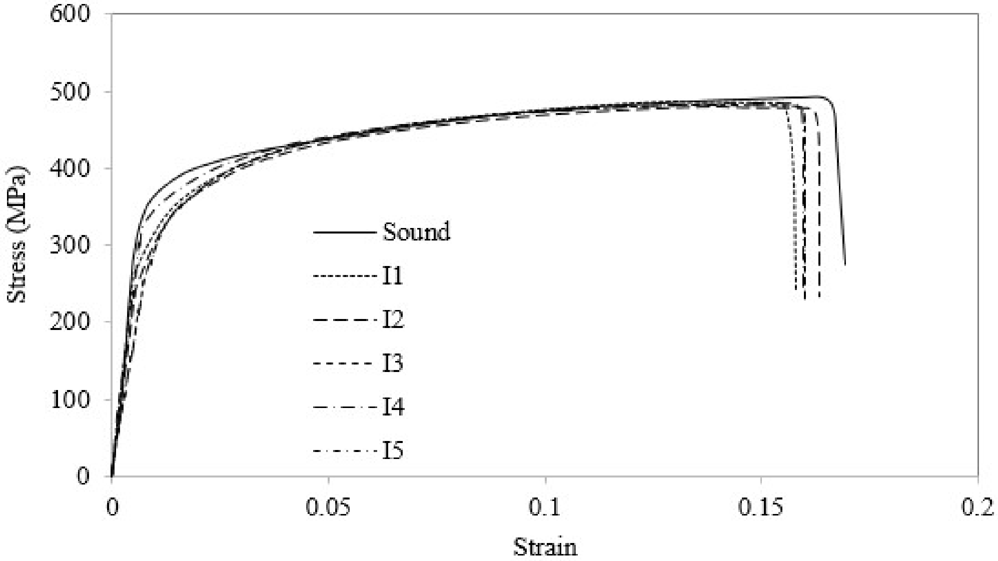

Figure 5.15 Results of tensile testing for sound and cast iron specimens

Table 5.2 Summary of tensile testing experiments of iron specimens

Specimen	Yield Strength (MPa)	Tensile Strength (MPa)	Elongation (%)	Modulus of Elasticity (GPa)	Fracture Strength (MPa)
Sound	280	492	16.9	167	275
I1	275	486	15.8	158	243
I2	278	480	16.3	165	234
I3	266	483	15.9	156	231
I4	279	485	15.9	160	234
I5	272	483	15.9	159	231

5.5.2 FATIGUE TESTING

The stress amplitudes to conduct fatigue testing are selected by constructing the theoretical S-N curve for sound steel and iron using analytical relationships. The fatigue failure which occurs for 1 to 1000 number of cycles is classified as low-cycle fatigue, whereas, above

1000 cycles the failure is termed as high-cycle fatigue. Moreover, the fatigue life below and above 10^6cycles are generally considered as finite and infinite life region for a specific material [86]. Each region i.e. low, high, and infinite can be represented by straight lines. The equation for low cycle region in a semi-log plot i.e. S-log (N) can be represented as follows [86].

$$S = S_{ut}N^{(log f)/3} \tag{5.1}$$

Where, S_{ut} is the ultimate tensile strength material, and f is the fatigue strength fraction defined as

$$f = \frac{S_{10^3}}{S_{ut}} \tag{5.2}$$

Equation 5.1 is valid for $10^0 \leq N \leq 10^3$ and $S_{ut} \geq S \geq S_{10^3}$. For high cycle region, the relationship between S and N is as follows [86].

$$S = aN^b \tag{5.3}$$

The a and b are computed as

$$a = \frac{(fS_{ut})^2}{S_e} \tag{5.4}$$

and

$$b = -\frac{1}{3}\log\left(\frac{fS_{ut}}{S_e}\right) \tag{5.5}$$

Equation 5.3 is valid for $10^3 \leq N \leq 10^6$ and $S_{10^3} \geq S \geq S_e$, where, S_e is the endurance limit of the material and could be obtained either through a laboratory experiment or using an approximate relationship [86] which is

$$S_{e'} = \begin{cases} 0.5\, S_{ut} & S_{ut} \leq 700MPa \\ 700MPa & S_{ut} \leq 1400MPa \end{cases} \tag{5.6}$$

The S_{ut} values for sound steel and iron and obtained from Table 5.1 and Table 5.2 respectively. Equation 5.5 is used to calculate S_e for each material. f can be estimated from Figure 5.16. Equations 5.1 to 5.6 indicates that analytical expression between S and N requires S_{ut}, S_e, and f values for a material. Table 5.3 lists the S_{ut}, S_e, and f values for sound steel and iron which are used to develop the theoretical S-N curves for sound steel and iron as shown in Figure 5.17 and Figure 5.18 respectively.

Table 5.3 S_{ut}, S_e, and f values for sound steel and iron

	Cast Steel	Ductile Iron
S_{ut} (MPa)	620	492
S_e (MPa)	310	246
f	0.855	0.89

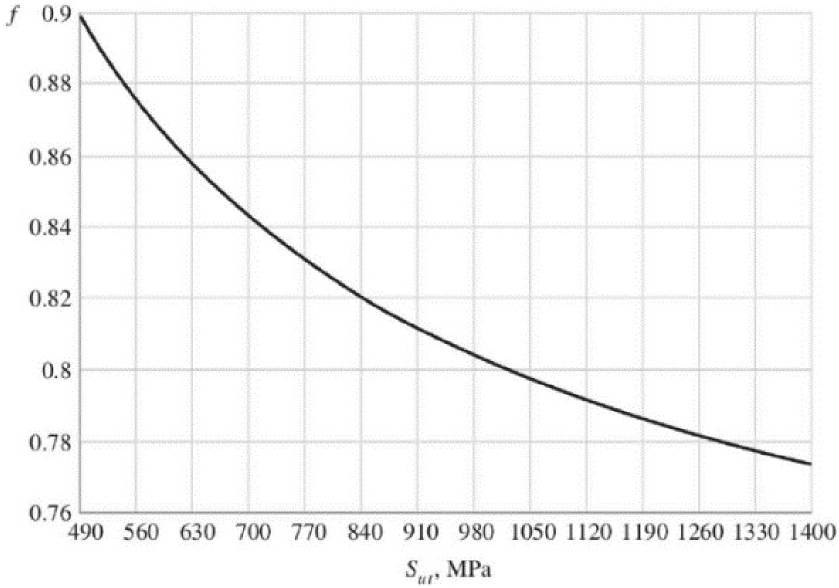

Figure 5.16 Fatigue strength fraction (f) of S_{ut} at 10^3 cycles [86]

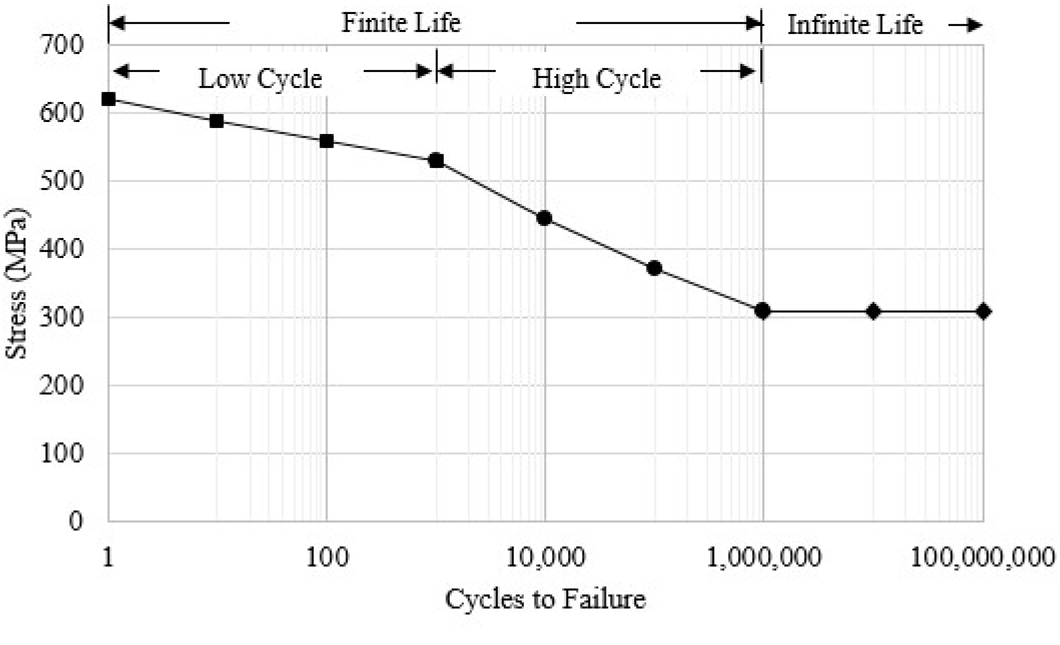

Figure 5.17 Theoretical S-N curve for sound steel

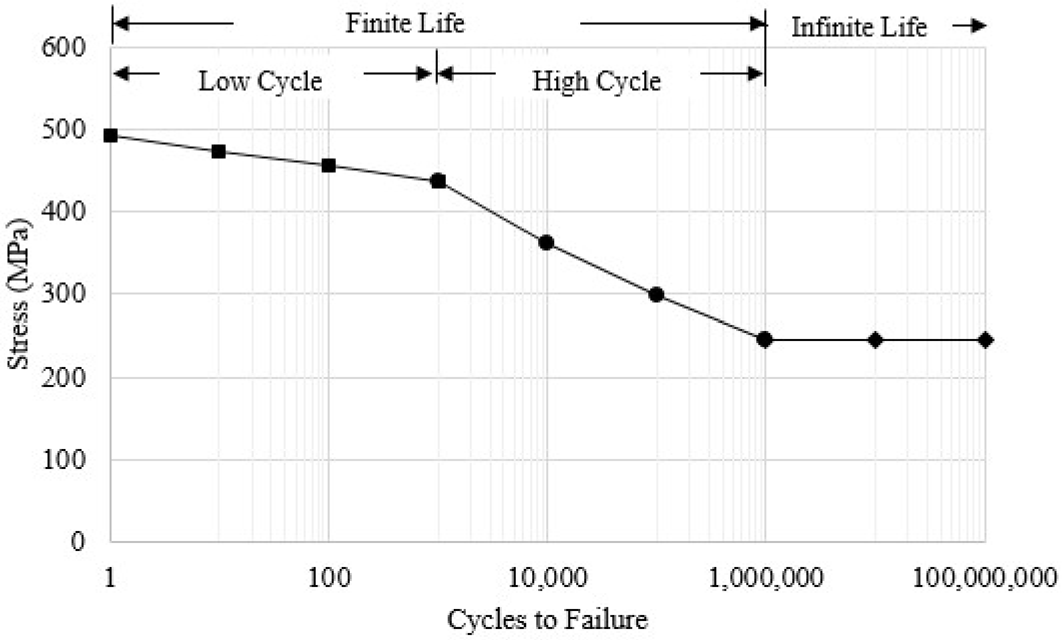

Figure 5.18 Theoretical S-N curve for sound iron

The specimen preparations and fatigue testing are done in accordance with ASTM E-466 standard [85]. Figure 5.19 shows the experimental setup used for fatigue testing of cast samples. All fatigue tests are performed under fully reversed i.e. R = -1, loading conditions. Load-controlled testing mode is used due to its faster testing capability. Depending upon the lower or higher amplitude of nominal stress for testing, the frequency of the test is set to 10 Hz or 5 Hz respectively. All specimens are subjected to cyclic loading until fracture and for infinite life the measured life is beyond the runout condition i.e. 1×10^6 cycles in the present work. The stress amplitude used for testing steel and iron specimens are carefully selected to test six specimens for finite and one for infinite life. The applied stress levels for testing are listed in Table 5.4 and Table 5.5 for steel and iron respectively along with the frequency of the test and number of cycles to failure in each case. The S-N curves developed as a result of fatigue testing of steel and iron specimens are shown in Figure 5.20 and Figure 5.21 respectively.

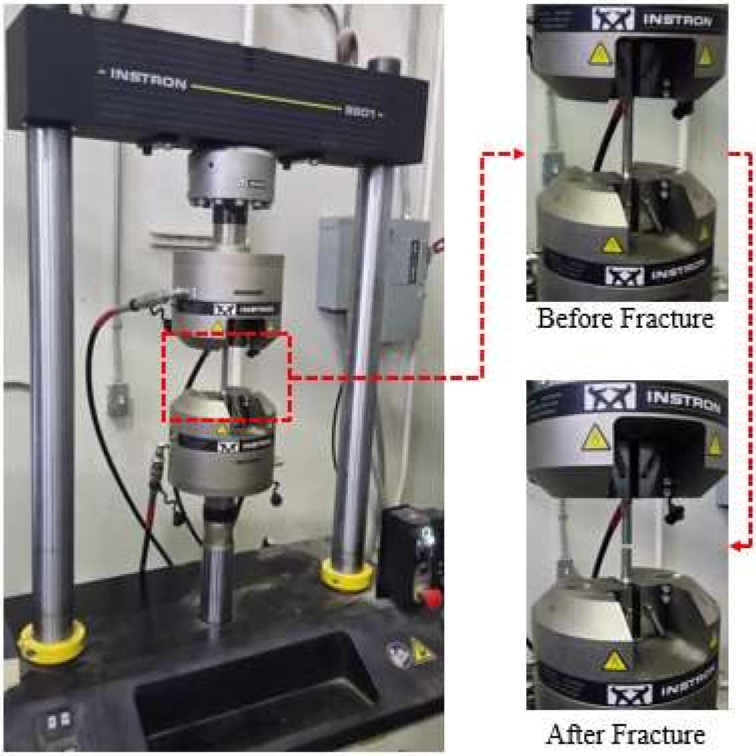

Figure 5.19 Experimental setup for fatigue testing of cast specimens

Table 5.4 Summary of results for fatigue testing of cast steel specimens

Specimen ID	Stress Applied for Test (MPa)	Frequency (Hz)	Fatigue Life (Cycles)
S1'	326	5	62
S2'	244	5	6,545
S3'	204	5	20,561
S4'	163	5	56,893
S5'	122	5	145,089
S6'	81	5	535,564
S7'	41	5	3,061,195

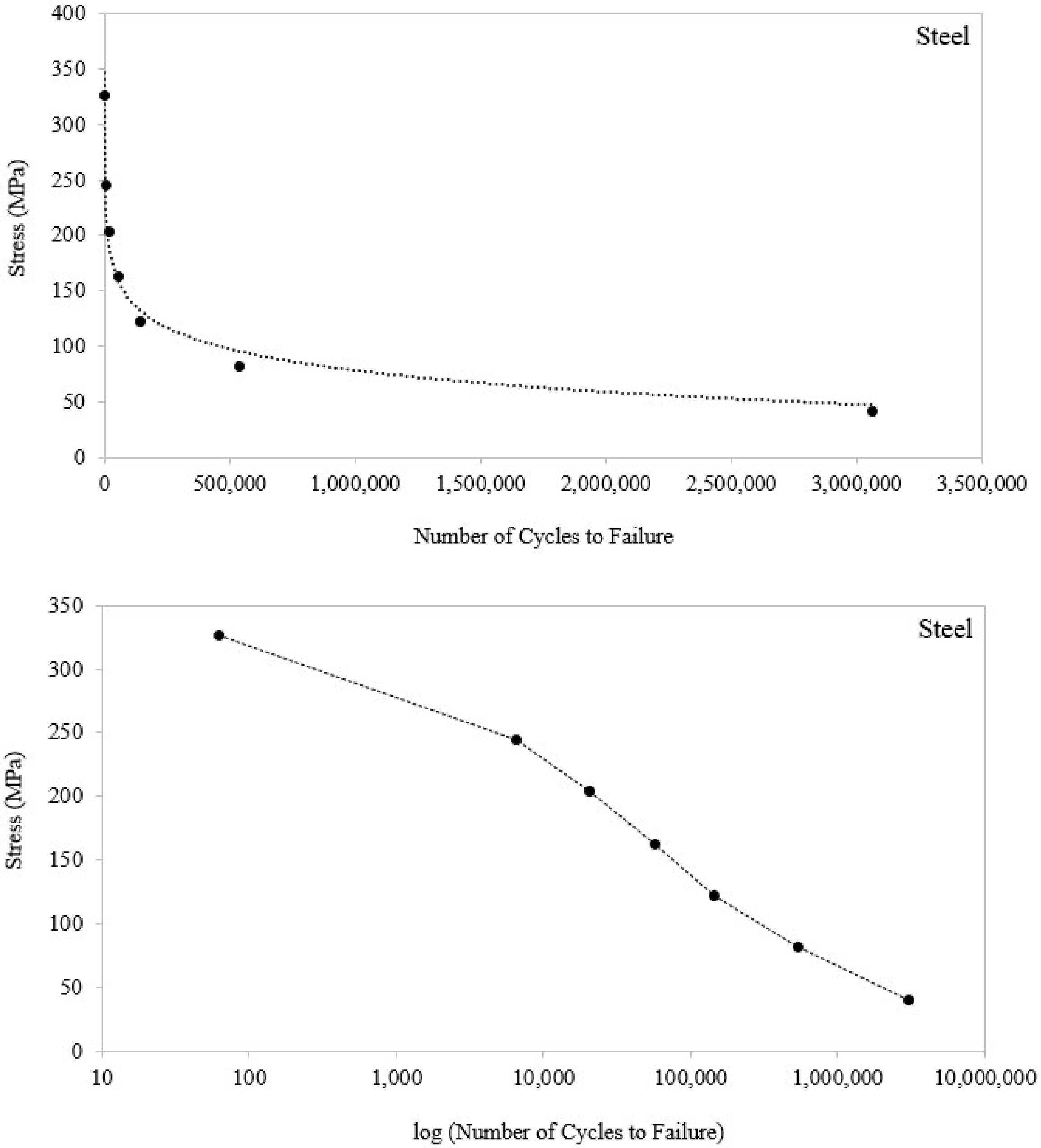

Figure 5.20 S-N curve for cast steel specimens

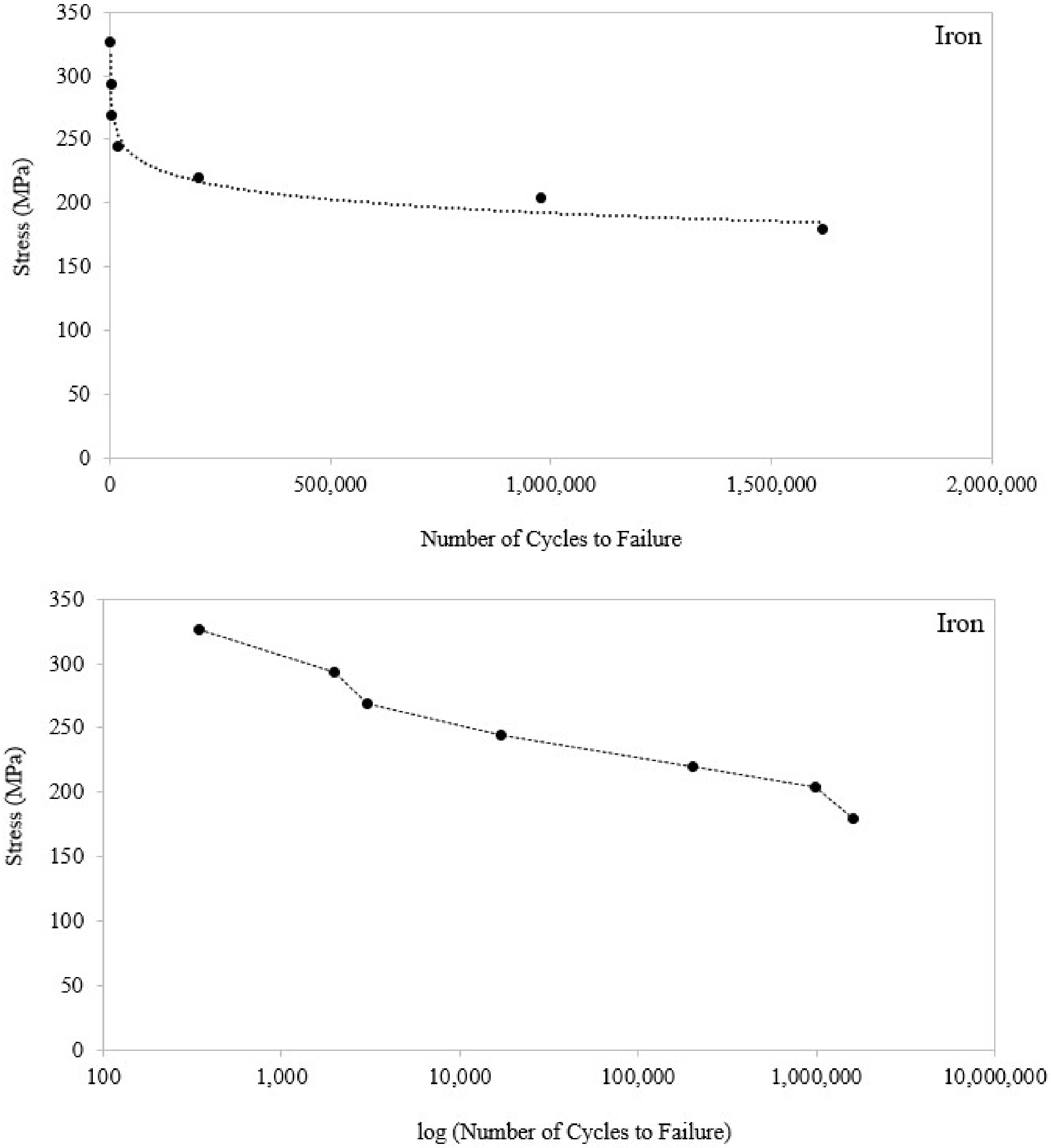

Figure 5.21 S-N curve for ductile iron specimens

Table 5.5 Summary of results for fatigue testing of ductile iron specimens

Specimen Number	Stress Applied for Test (MPa)	Frequency (Hz)	Fatigue Life (Cycles)
I1'	326	5	342
I2'	293	5	1,973
I3'	269	10	3,016
I4'	244	10	17,148
I5'	220	10	200,798
I6'	204	10	978,556
I7'	179	10	1,614,616

5.6 CONCLUDING REMARKS

The experimental work done as part of the current study is presented in this chapter. This includes casting of tensile and fatigue specimens of both materials under consideration and their mechanical testing under monotonic and cyclic loads. The overall results for tensile testing of steel specimens are encouraging, yet some differences are observed in the stress-strain behavior of the tested specimens. On the other hand, ductile iron specimens did not show much variation in results for tensile testing. In terms of fatigue testing, theoretical S-N curves suggested a higher endurance limit for steel as compared to iron. Conversely, the experiments demonstrated a higher endurance limit of iron than the steel. This could be attributed to the traces of porosity observed in the X-ray imaging of fatigue specimens of steel because such porosities adversely affects the fatigue life of steel.

CHAPTER 6

FINITE ELEMENT SIMULATIONS AND FATIGUE LIFE PREDICTION

6.1 INTRODUCTION

In this chapter, engineering approaches are utilized to simulate the deformation, damage, and fracture of specimens during tensile testing. Fatigue testing is simulated by doing (i) finite element elastic stress analysis corresponding to the load in experimental fatigue testing and (ii) fatigue life prediction using multi-axial strain-life approach using stress fields predicted in (i). These simulations are done using the porosity field predicted by MAGMASoft mapped to the FEA nodes. MAGMAlink module of MAGMASoft is used for porosity mapping. MAGMAlink enables users to import and export results to and from other softwares into and out of MAGMASoft. The translation and rotation of FEA mesh is possible to properly overlay the MAGMASoft model. FEA mesh is generated in ABAQUS before the stress simulation. The result generated from MAGMAlink contains the magnitude of nodal porosity which has to be integrated in ABAQUS. The node sets and nodal porosity data is included in the ABAQUS input file which contains all commands, boundary conditions, and properties required to run the stress simulation. Simulated and experimental results are compared to ensure models' competencies in predicting the fracture behavior and fatigue life prediction. Figure 6.1 shows the steps followed in the methodology used in this chapter.

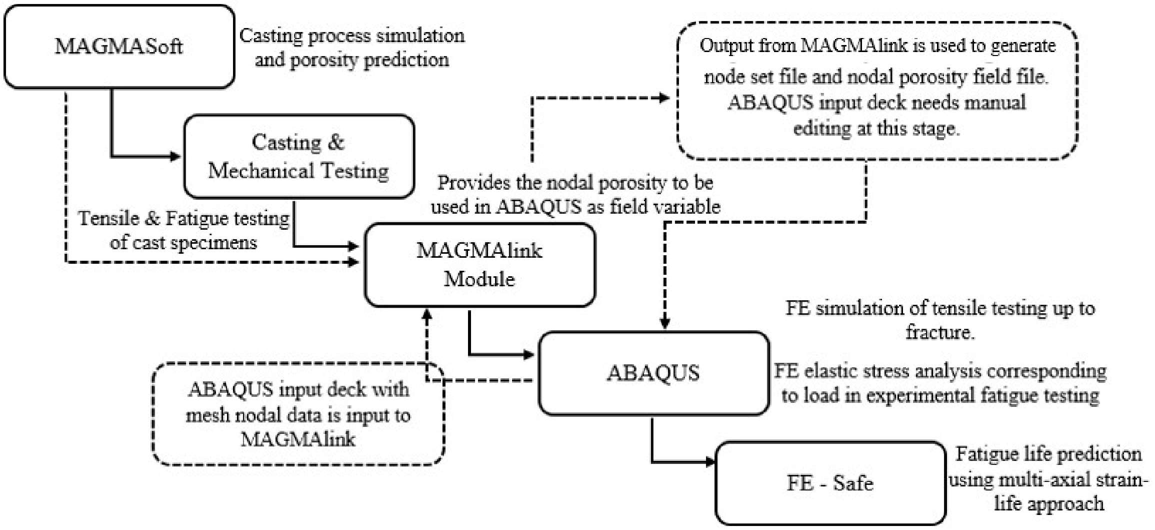

Figure 6.1 Steps to simulate mechanical testing and fatigue life prediction

6.2 FINITE ELEMENT SIMULATION OF TENSILE TESTING IN ABAQUS

On a microscopic scale, the fracture of ductile materials occurs though the mechanisms of void nucleation, growth, and coalescence [87]. Voids either exist as microporosity or nucleate from inclusions such as second phase particles. Once nucleated, the voids grow with increasing plastic strain. Consequently, the void (or porosity) volume fraction increases. The interaction of voids begins as at a critical porosity volume fraction. With increasing plastic strain, local necking and coalescence take place in the materials between voids and failure occurs through a connected chain of voids. Fracture of material occurs at a certain porosity fraction termed as failure porosity volume fraction.

6.2.1 MATERIAL AND FAILURE MODELS

The model used for this work is a standard material model available in the commercially available stress analysis program ABAQUS. The underlying assumption is the linear small strain theory which decomposes the total strain tensor ε into elastic ε^{el} and plastic ε^{pl} components so that $\varepsilon = \varepsilon^{el} + \varepsilon^{pl}$. The recoverable elastic strains of the material are determined from

$$\sigma = D^{el}\varepsilon^{el} \tag{6.1}$$

where, σ is the stress tensor, D^{el} is the fourth order elasticity tensor, and ε^{el} is the elastic strain tensor. For uniaxial tension, D^{el} becomes the elastic modulus E, and Equation 6.1 reverts to Hooke's law. The properties needed to define isotropic elasticity tensor D^{el} are elastic modulus E and Poisson ratio ν. In current study, these elastic properties are used as a function of porosity fraction f i.e. $= \frac{V_{pore}}{V_0}$, where V_{pore} is the volume of porosity and V_0 is the volume about a node in the sound material matrix [78]. At each node, the elastic modulus and porosity fraction are related using Equation (6.2), which was obtained by comparing excellent agreement between measured and predicted strains in test specimens with porosity [88],

$$E(f) = E_0(1 - f/0.5)^{2.5} \tag{6.2}$$

Where, E_0 is 198 GPa for A216 WCB Steel and 167 GPa for GGG-40 ductile iron. The Poisson ratio $'\nu'$ is dependent on f using Equation (6.3), which was developed through simulations of computer generated representative elemental volumes of porous structures [89],

$$\nu_f = \nu_S + \left(\frac{f}{f_\infty}\right)(\nu_\infty - \nu_S) \tag{6.3}$$

Where, $\nu_\infty = 0.14$, $f_\infty = 0.472$, and the Poisson ratio ν for sound steel and iron is 0.29 and 0.275 respectively.

The plasticity and failure is simulated using porous metal plasticity model in ABAQUS. A complete presentation of the model can be found in Gurson et al. [90]–[92], ABAQUS manual [93], and the numerical integration method used in the software is proposed by Aravas [94]. It is required to specify the hardening behavior using true stress-strain data obtained from tensile testing of sound (pore-free) steel. The yield condition employed by the model is

$$\phi = \left(\frac{q}{\sigma_y}\right)^2 + 2q_1 f cosh\left(-\frac{3}{2}\frac{q_2 p}{\sigma_y}\right) - (1 + q_3 f^2) = 0 \tag{6.4}$$

Where, f is the porosity fraction, q is the effective Von Mises stress, p is the hydrostatic stress, σ_y is the yield stress of the sound metal as a function of plastic strain, q_1, q_2, and q_3 are material parameters. Figure 6.2 (a) and (b) shows the plastic true stress-strain curves which are derived from the measured sound steel and iron tensile test data given in Figure 5.14 and Figure 5.14 respectively. It can be noted in Equation (6.4) that in case of zero porosity i.e. $f = 0$, the yield condition becomes equal to Von Mises yield condition i.e. $q = \sigma_y$. The hydrostatic stress, $p = -\left(\frac{1}{3}\right)\mathrm{\sigma}\colon \mathrm{I}$ and the Von Mises stress, $q = \sqrt{\left(\frac{3}{2}\right)\mathrm{S}\colon \mathrm{S}}$ are the two stress invariants where $'\mathrm{\sigma}'$ is the Cauchy stress tensor and $'\mathrm{S}'$ is the deviatoric stress tensor $\mathrm{S} = p\mathrm{I} + \mathrm{\sigma}$.

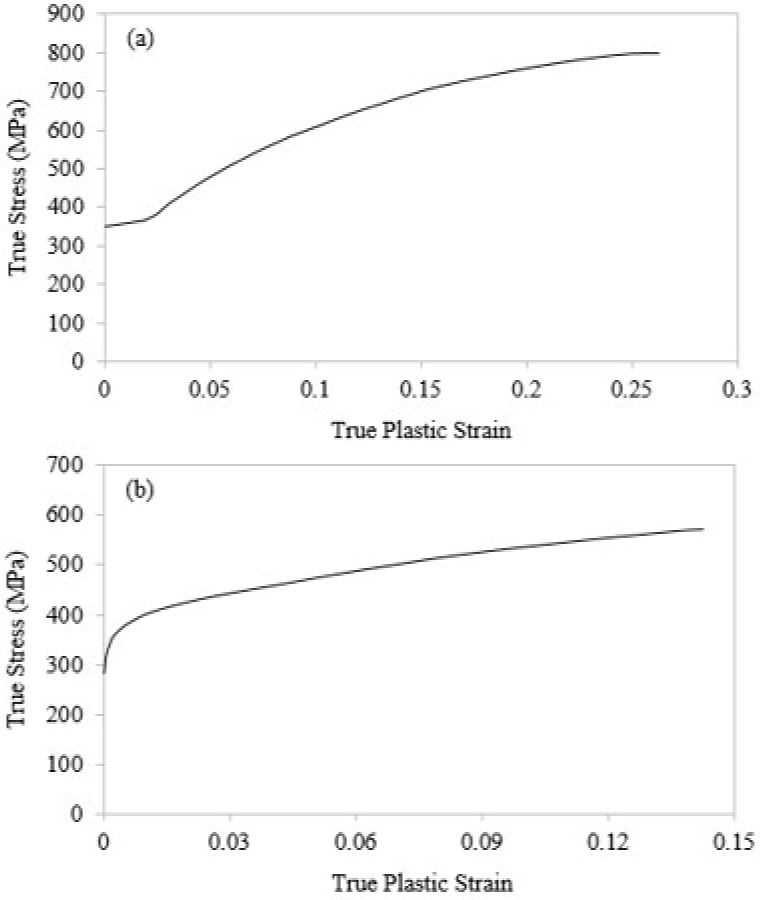

Figure 6.2 True plastic stress-strain curve for (a) Steel and (b) Iron without porosity

Material parameters q_1, q_2, and q_3 in Equation (6.4) are added to Gurson's model by Tvergaard [91] to consider the interactions between voids and to improve the accuracy of Gurson's model. The recommended values for ductile materials [93] are used in this study i.e. $q_1 = 1.5, q_2 = 1.0,$ and $q_3 = {q_1}^2 = 2.25$.

It is assumed that plastic flow is normal to the yield surface formed by Equation (6.4) for a given porosity fraction f. With this assumption, the yield condition in Equation (6.4) is used to determine the plastic strain to grow and nucleate porosity, starting from an initial porosity fraction. The flow rule for plastic strain rate is

$$\dot{\varepsilon}^{pl} = \dot{\lambda}\frac{\partial\phi}{\partial\sigma} = \dot{\lambda}\left(-\frac{1}{3}\frac{\partial\phi}{\partial p}\mathrm{I} + \frac{3}{2q}\frac{\partial\phi}{\partial q}\mathrm{S}\right) \tag{6.5}$$

Where, $\dot{\lambda}$ is a non-negative scalar constant of proportionality, a measure of the plastic flow rate. Void nucleation and growth take place as the plastic strain in Equation (6.5) increases. The rate of void change by nucleation and growth is described by

$$\dot{f} = (1 - f)\dot{\varepsilon}_{kk}^{pl} + A\dot{\varepsilon}_{m}^{pl} \tag{6.6}$$

Where, the first term on the right hand side represents the growth in existing voids from current void fraction f and $\dot{\varepsilon}_{kk}^{pl}$, the total plastic strain rate, and the second term represents the rate of change caused by nucleation. The plastic strain rate $\dot{\varepsilon}_{m}^{pl}$ in the nucleation term is multiplied by a scaling coefficient A which is

$$A = \frac{f_N}{S_N\sqrt{2\pi}} \exp\left[-\frac{1}{2}\left(\frac{\varepsilon_m^{pl} - \varepsilon_N}{S_N}\right)^2\right] \tag{6.7}$$

The nucleation function $\left(\frac{A}{f_N}\right)$ is assumed to follow a normal distribution depending on the plastic strain range about a mean value ε_N, a standard deviation S_N for a volume fraction of nucleated voids f_N. Typical values recommended for ductile metals are used in this study: $\varepsilon_N = 0.3$, $S_N = 0.1$, and $f_N = 0.03$. By using coalescence and failure criteria models [92], [93], the porosity fraction f in Equation (6.4) is replaced by f^*, an effective void volume fraction due to coalescence. If $f \le f_c$, f^* is simply considered as f since no coalescence had started yet. If $f > f_c$, f^* increases more rapidly due to coalescence. The material has no load carrying capacity if $f \ge f_F$, where f_F is the void volume fraction at failure. Mathematically, if f^* is used in Equation (6.4), it depends upon f as follows.

$$f^* = \begin{cases} f & if \quad f \le f_c \\ f_c + \dfrac{\bar{f}_F - f_c}{f_F - f_c}(f - f_c) & if\ f_c < f \le f_F \\ \bar{f}_F & if \quad f \ge f_F \end{cases} \tag{6.8}$$

The value of $\bar{f}_F$ is determined by material parameters q_1, q_2, and q_3 in porous metal plasticity model using

$$\bar{f}_F = \frac{q_1 + \sqrt{{q_1}^2 - q_3}}{q_3} \tag{6.9}$$

It is important to determine two additional parameters for using coalescence and failure model i.e. critical porosity fraction f_c and failure porosity fraction f_F. These values could be determined by fitting the model fracture curve to the experimental curve for sound steel. In the present study, the values giving the best agreement are $f_c = 0.05$ and $f_F = 0.2$. Initial porosity fraction f_0 for the sound steel and iron is set to 0.2% [77] and 0.3% [95] respectively, in addition to other porous metal plasticity model parameters determined above. A summary of all parameters used in porous metal plasticity model is given in Table 6.1. These values provided the best agreement between the measured and simulated tensile curves for steel and iron.

Table 6.1 Parameters for Porous Metal Plasticity Model for ABAQUS simulations

q_1	q_2	q_3	f_0 (Steel)	f_0 (Iron)	f_c	f_F	ε_N	S_N	f_N
1.5	1.0	2.25	0.002	0.003	0.05	0.2	0.3	0.1	0.03

6.2.2 FINITE ELEMENT MODELING

The tensile testing simulations are done with an encastre boundary condition at the bottom end of the specimen and a normal displacement applied to the top end of the specimen using a multi-point constraint as shown in Figure 6.3 (a). Figure 6.3 (b) shows the meshed test specimen with 1 mm node spacing as the mesh sensitivity analysis suggested no significant difference in results upon further mesh refinement i.e. 0.8 mm node spacing.

The FEA model developed to simulate tensile testing consists of 34,510 eight-node linear brick elements (C3D8R) elements, 40,393 nodes, and 121,776 total number of variables. In order to produce the simulated stress-strain curve, the stress is determined from the reaction force calculated at the node where the displacement boundary condition is applied and dividing it by the nominal area of the test section. The simulated strain is computed by the relevant displacement of node sets defined at the points where extensometer is attached to the test specimens. The simulations of sound steel specimens are considered as base case to determine all parameters of porous metal plasticity model presented in Table 6.1. The specimens with porosity are then simulated without changing the porous metal plasticity parameters.

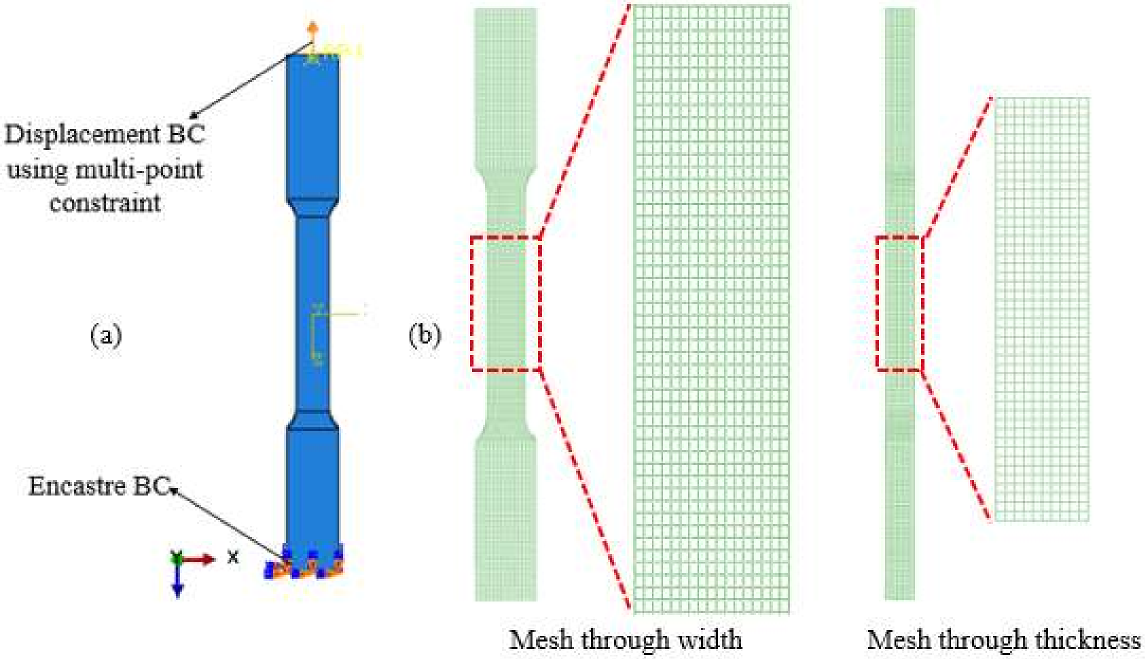

Figure 6.3 (a) Boundary conditions and (b) Meshed specimen with 1 mm node spacing

The failure criterion in porous metal plasticity model requires ABAQUS Explicit to simulate fracture. It is important to consider two aspects while using explicit procedure for simulating a quasi-static process such as tensile testing. The first is the time period of testing which could be on the order of a minute in the actual testing, however, it could be simulated using a much smaller time period without affecting the results. Second important consideration is the stable time increment which is determined by smallest characteristic element length L_e in the mesh and the dilatational wave speed of the material [79]. At first, stable time increment is adjusted to run the simulations in a reasonable time without compromising the accuracy of results. The wave speed C_d is given by $\sqrt{\frac{E}{\rho}}$ where E is the elastic modulus and ρ is the density. The largest stable time step Δt_{stable} for a dynamic explicit analysis is given by $\Delta t_{stable} = \frac{L_e}{C_d}$. The E values of 198 GPa and 167 GPa and ρ values of 7800 kg/m^3 and 7100 kg/m^3, for steel and iron respectively, are used to compute C_d for each material. The wave speed C_d in steel and iron are found to be ~5,000 m/s and 4,850 m/s respectively. For a minimum characteristic length of 1mm the largest stable time step is found to be around 2×10^{-7} sec in case of each material. With this time step, the simulation takes tens of millions of time steps which is definitely impractical. Alternatively, a practical time scale can be established by taking into account the time the stress wave transmits through the specimen and multiply it by a safety factor which is sufficiently large. In the present work, the length of specimen is 200 mm and therefore, time to transmit a stress wave through the specimen is approximately 4×10^{-5} sec. A safety factor of over 1000 times is used due to which the time period for tensile testing is set to 0.1 sec. Simulations with larger and smaller time periods confirmed that the results are insensitive to testing duration.

In order to check the rate of loading used in simulations, velocity of the displacement of the testing is compared with the wave speed. Since, the time period for tensile testing is set to be 0.1 sec, the specimen end displacement speed is about 0.25 m/s and 0.15 m/s in case of steel and iron respectively. Although this displacement speed is high, it is only about 0.005% of material’s wave speed. The final check on simulations is done as per the software guidelines i.e. the kinetic energy should not exceed approximately 5% of the internal energy for simulating a quasi-static process. During simulations, the kinetic and internal energies are stored and it is found that the kinetic energy did not exceed 0.006 % of the internal energy.

6.2.3 RESULTS OF TENSILE TESTING SIMULATIONS

Figure 6.4 to 6.9 shows the results of tensile testing simulations and their comparison with experimental results for steel specimens. Initially, the base case with no porosity is simulated using porous metal plasticity parameters already discussed in Table 6.1. The simulated and experimental results are found to be in good agreement as shown in Figure 6.4. Hence, the developed model is deemed sufficient to be utilized for integration of porosity predicted by MAGMASoft. After porosity integration in the simulations, it is observed that the reduction in ductility is the most noticeable effect, however, no significant change in strength is observed as shown in Figure 6.4 to Figure 6.9. Since, the predicted level of porosity from MAGMASoft for all specimens is nearly similar, the simulated elongation and strength in all specimens with porosity, S1 through S5, are not much different.

A summary of results for all tensile tests is presented in Table 6.2. Among all specimens, S2 shows an excellent agreement in the simulated and experimental results, whereas, in all other specimens i.e. S1, S3, S4, and S5, some discrepancy is observed between the simulated and experimental results. However, it is encouraging to obtain the elongation and strength in all specimens greater than 22% and 485 MPa respectively, which are the minimum values as per ASTM 216 standard steel (Table 4.1).

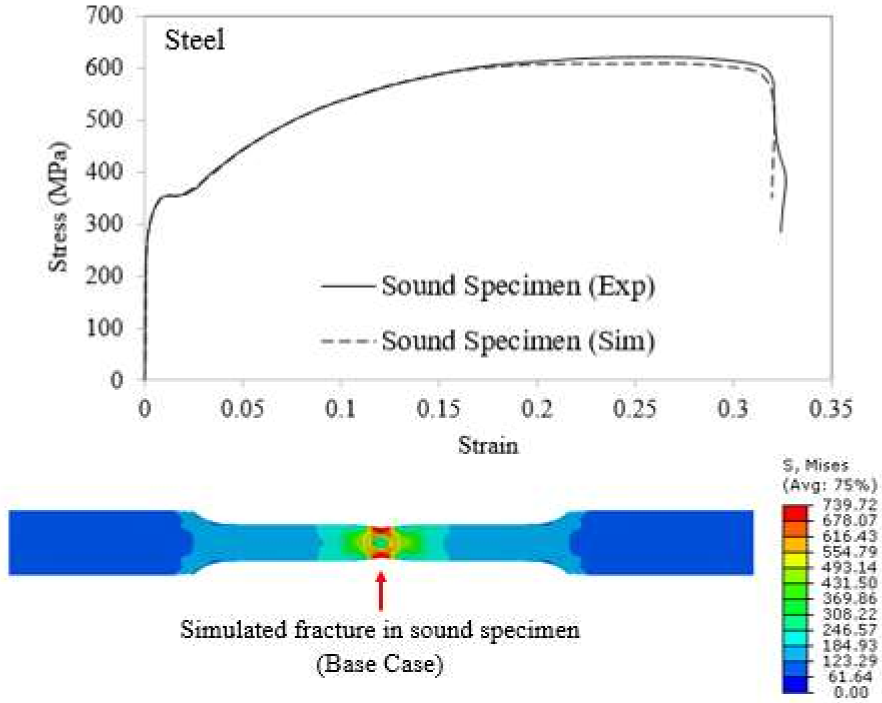

Figure 6.4 Simulated and experimental results of tensile testing for sound steel specimen

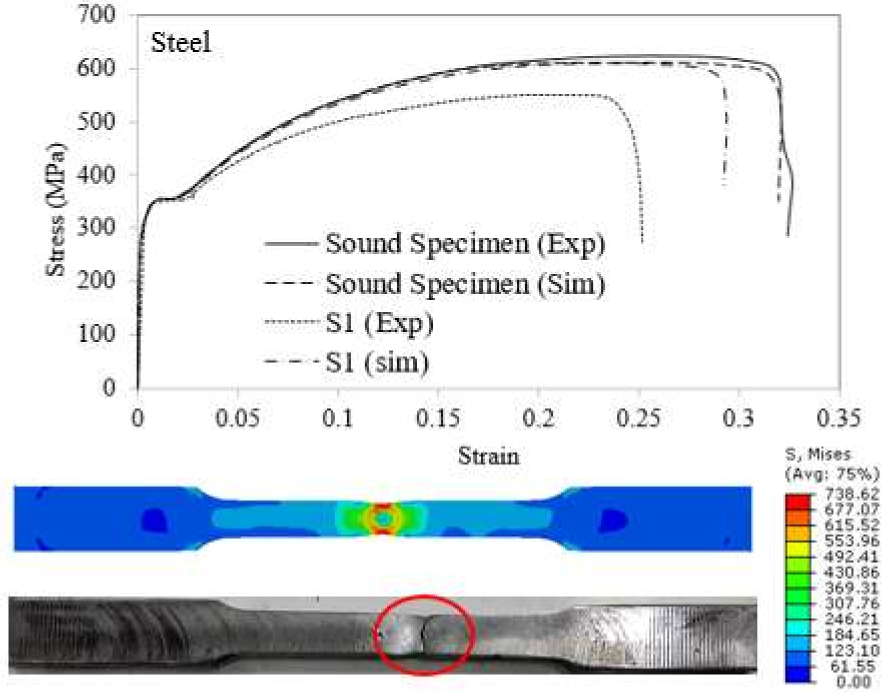

Figure 6.5 Simulated and experimental results of tensile testing for porous steel specimen ‘S1’

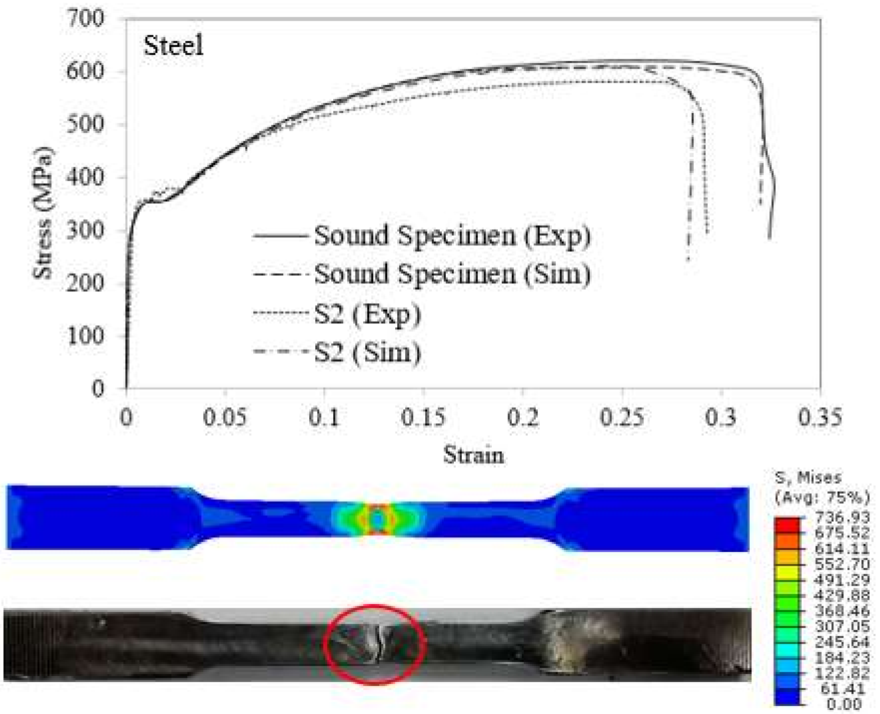

Figure 6.6 Simulated and experimental results of tensile testing for porous steel specimen ‘S2’

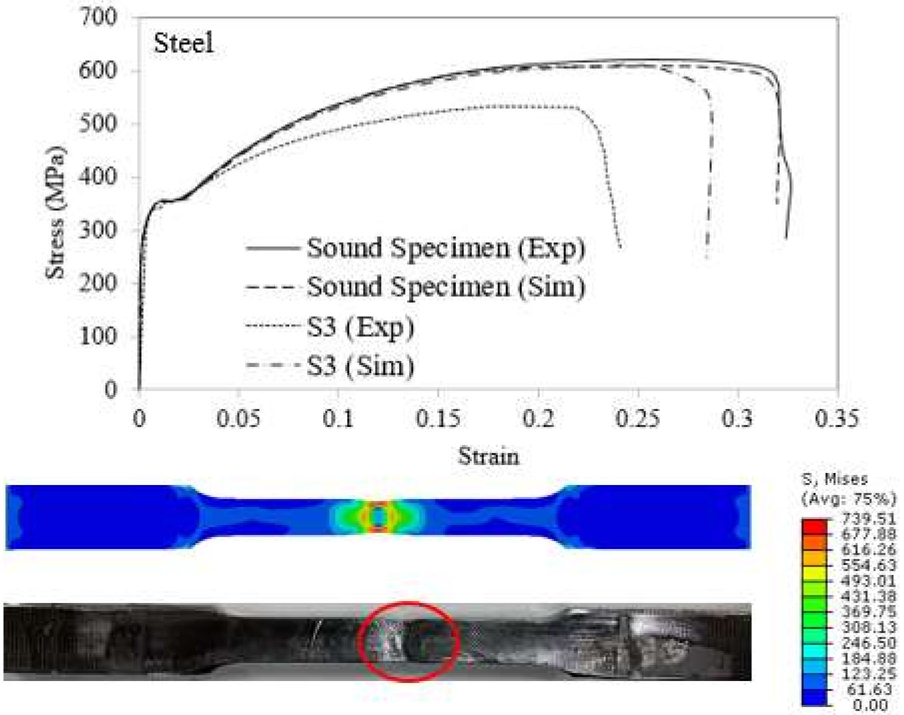

Figure 6.7 Simulated and experimental results of tensile testing for porous steel specimen ‘S3’

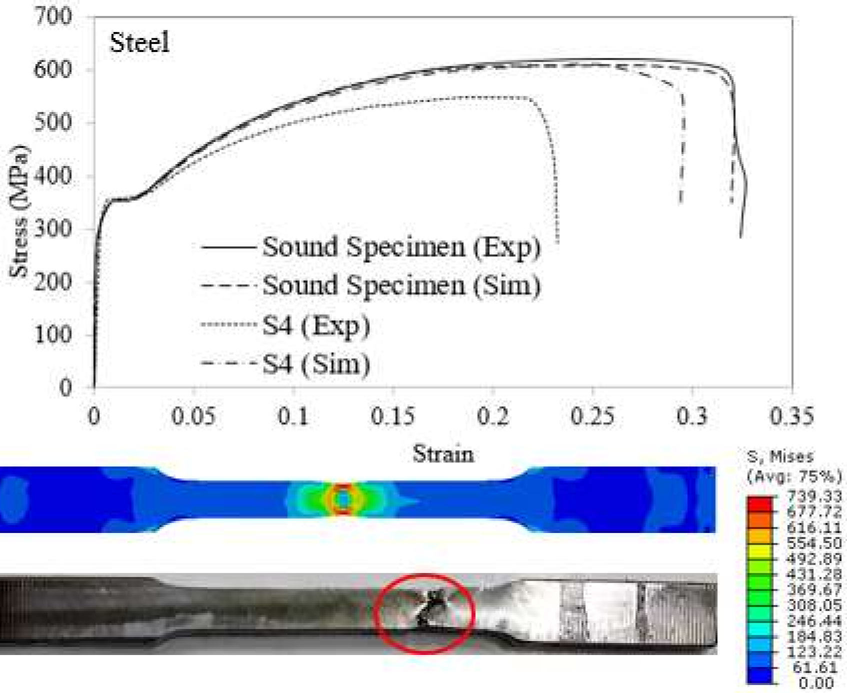

Figure 6.8 Simulated and experimental results of tensile testing for porous steel specimen 'S4'

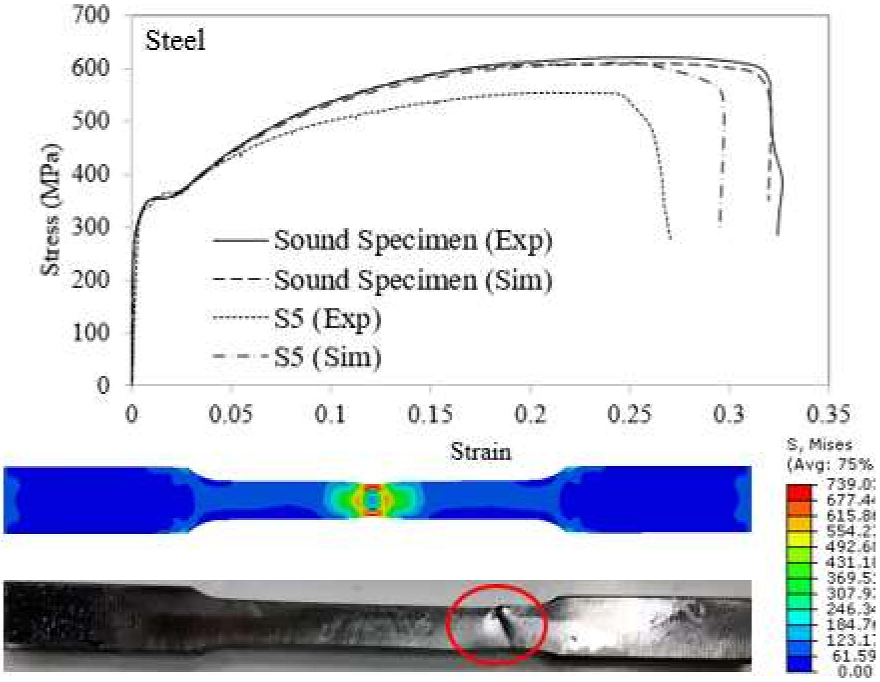

Figure 6.9 Simulated and experimental results of tensile testing for porous steel specimen 'S5'

Table 6.2 Summary of simulated and experimental results of tensile testing for steel specimens

Specimen	Yield Strength (MPa)		Tensile Strength (MPa)		Elongation (%)		Modulus of Elasticity (GPa)		Fracture Strength (MPa)	
	Exp	Sim	Exp	Sim	Exp	Sim	Exp	Sim	Exp	Sim
Sound	355	348	620	610	32.5	32.0	198	198	293	297
S1	340	320	549	608	25.2	29.4	193	197	275	380
S2	355	321	583	609	29.3	28.5	196	197	292	244
S3	337	320	534	609	23.2	29.3	191	198	267	248
S4	356	322	549	609	23.2	29.3	196	197	275	341
S5	347	323	556	609	27.0	29.5	191	197	278	298

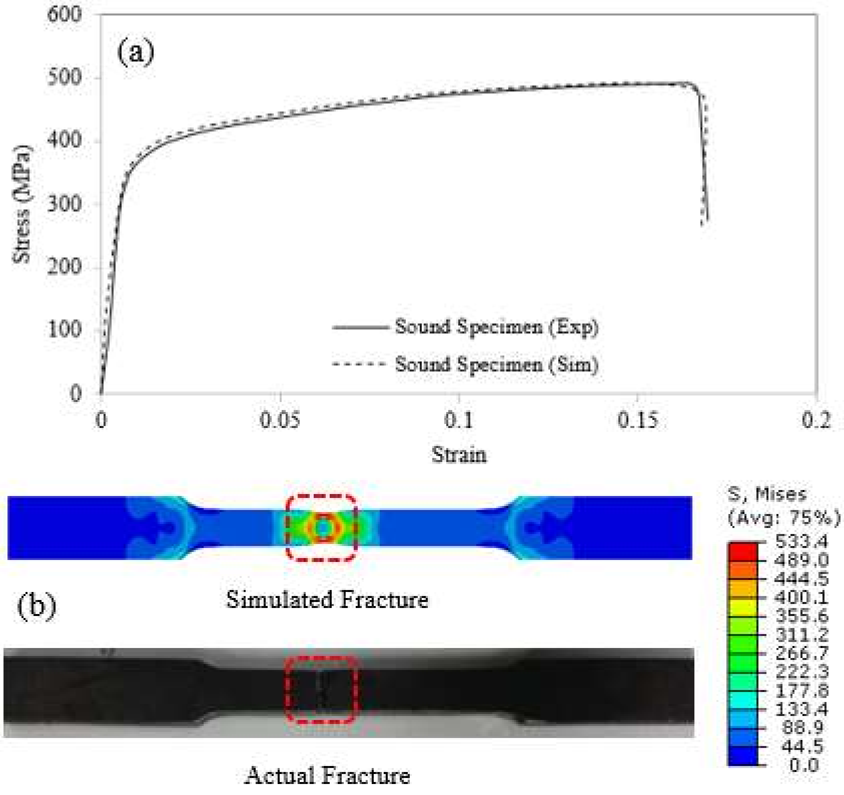

Figure 6.10 (a) Simulated and experimental stress-strain behavior of sound iron specimen (b) Simulated and actual fracture

Since, no porosity is predicted in MAGMASoft simulations for iron specimens, the base case with no porosity is simulated using the porous metal plasticity parameters already discussed in Table 6.1. The simulated and experimental results are found to be in good agreement as shown in Figure 6.10 (a). The contour plot for stress field along with simulated and actual fracture are presented in Figure 6.10 (b). It can be observed that all tensile properties such as yield and tensile strength, ductility and modulus of elasticity are perfectly matched in experiments and simulation. Since, the experimental and simulated results for sound iron specimen are found to be in excellent agreement, it allows the developed model to be used for integration of porosity, if observed, in simulations or experiments.

6.2.4 DISCUSSIONS

Although, casting simulations predicted same quality for all steel specimens, it is almost impossible to control the entire process perfectly in line with the simulations. It is most likely to have differences in either magnitude or distribution of simulated and actual porosity field within the specimens which causes such discrepancies. Therefore, it is important to quantify the simulated and actual porosities in the specimens. The nodal porosity exported from MAGMASoft to FEA mesh is transformed to total porosity using pore volume and bulk volume of the specimens. For actual cast specimens, the total porosity is obtained using bulk density method. Figure 6.11 shows the simulated and actual porosities in specimens, S1 through S5. The actual porosity in the cast specimens is found to be slightly more than simulated porosities, however, this cannot be considered solely responsible for reduction in ductility in specimens S1, S3, S4 and S5.

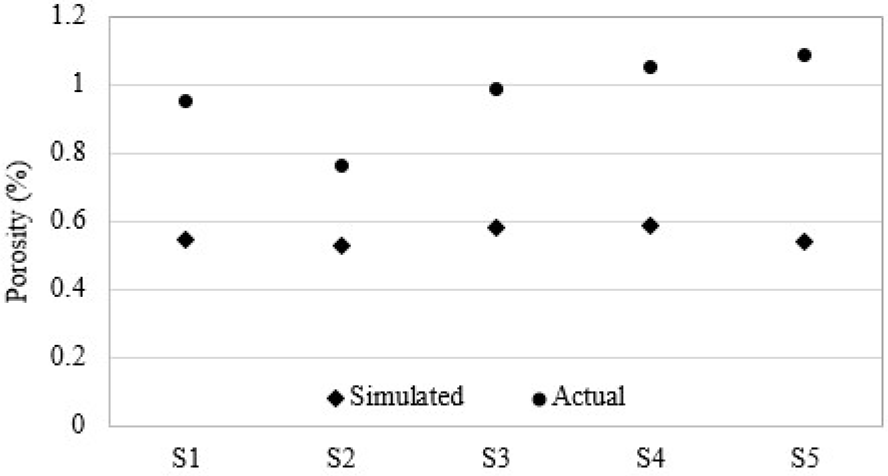

Figure 6.11 Simulated and actual porosity observed in tensile specimens of steel

Another reason of deviation in the simulated and experimental results could be post-casting treatment of specimens such as heat treatment and final machining operations. The hardness of all specimens, S1 through S5, is measured at ten different locations (both in test section and grip areas) to check if the heat treatment has effectively homogenized the properties in specimens. The results of hardness measurements are presented in Figure 6.12. It is observed that except S2, in all other specimens the hardness is found to be significantly varying at different regions of the specimen. This supports the closest agreement of simulation and experimental results in specimen S2. The average hardness of specimens is 90.5 HRB and the coefficient of variation (without considering S2) shows that the standard deviation is 5% of the mean, which indicates some non-uniformity in the hardness of specimens. Since, cooling in a multi-cavity mold often poses challenges in obtaining same quality of casting, it is common to homogenize the castings through heat treatment. However, it is possible to improve the finishing and heat treatment operations to ensure same quality and performance of castings produced using a multi-cavity mold. Although, all specimens are heat treated at nominally the same conditions, the variability in hardness within 5% of its average value shows some lack of control on heat treatment process which could be improved further.

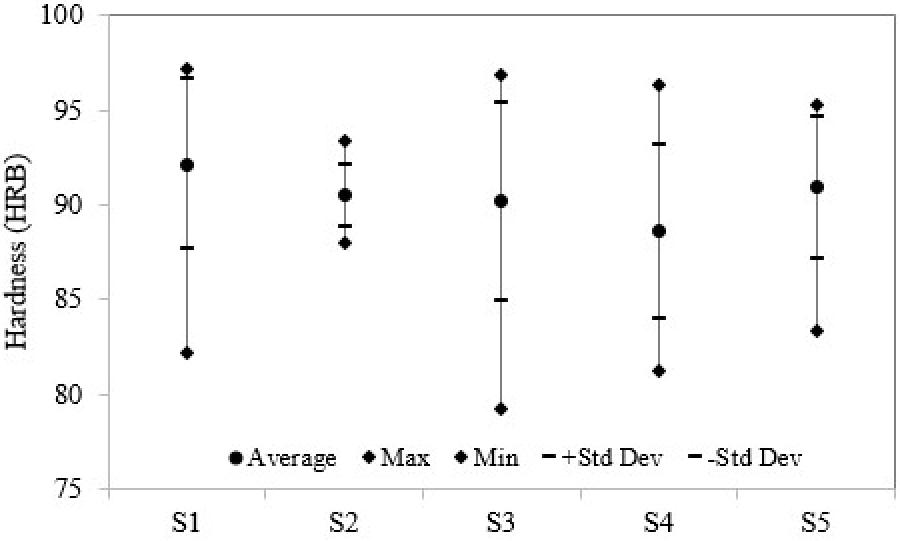

Figure 6.12 Hardness measurement in steel specimens with average, max, min, and standard deviation

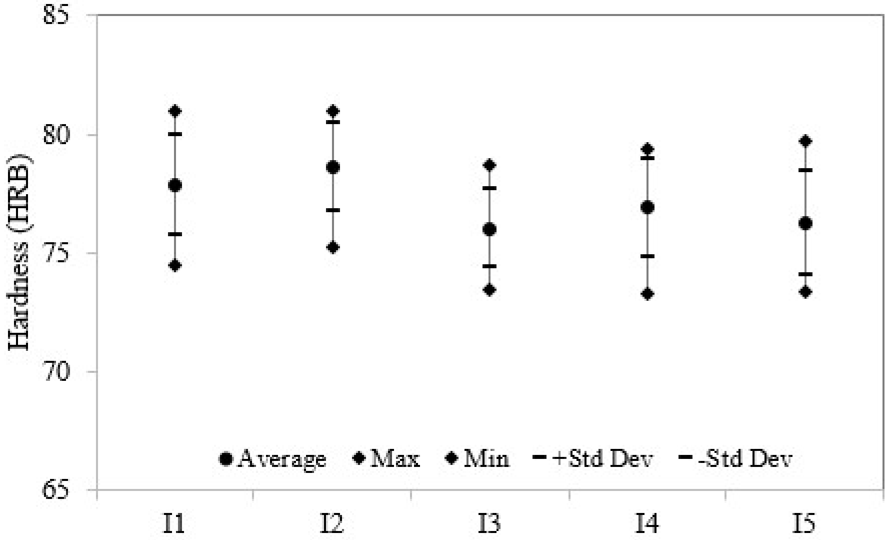

Figure 6.13 Hardness measurement in iron specimens with average, max, min, and standard deviation

In case of ductile iron specimens, no heat treatment is done. Hardness measurement is also done for these specimens as shown in Figure 6.13. It is observed that the hardness is not varying much, at different sections, within the same specimen which supports the nearly similar behavior of all ductile iron specimens during tensile testing experiments as reported earlier in Figure 5.15. The average hardness of specimens is 77 HRB and the coefficient of variation shows that standard deviation is only 1.4% of the mean, which is fairly reasonable to infer that each specimen has nearly uniform hardness.

6.3 FATIGUE LIFE PREDICTION

6.3.1 SIMULATION PROCEDURE

Fatigue life of test specimens is predicted by following a series of steps which are as follows.

a) The porosity field predicted by MAGMASoft is mapped onto the nodes of FEA mesh.
b) Elastic properties are degraded at each node as a function of porosity fraction f.
c) A finite element elastic stress analysis is performed for each specimen corresponding to the load used in fatigue testing.
d) The stress field obtained in (c) is imported corresponding to tension and compression into the life prediction software to conduct a multi-axial strain-life analysis.

The steps (a) and (b) of the methodology are already developed for tensile specimens and are repeated for the fatigue specimens. A mesh of the fatigue specimen is created in ABAQUS which is imported in MAGMASoft using MAGMAlink. Using MAGMAlink, the predicted porosity field is mapped to the nodes of FEA mesh. The elastic properties E and ν are defined at each node as a function of porosity fraction f using Equations (6.2) and (6.3) respectively. No significant plasticity is observed during fatigue testing of the specimens, hence, the plastic effects are ignored in the FEA simulations.

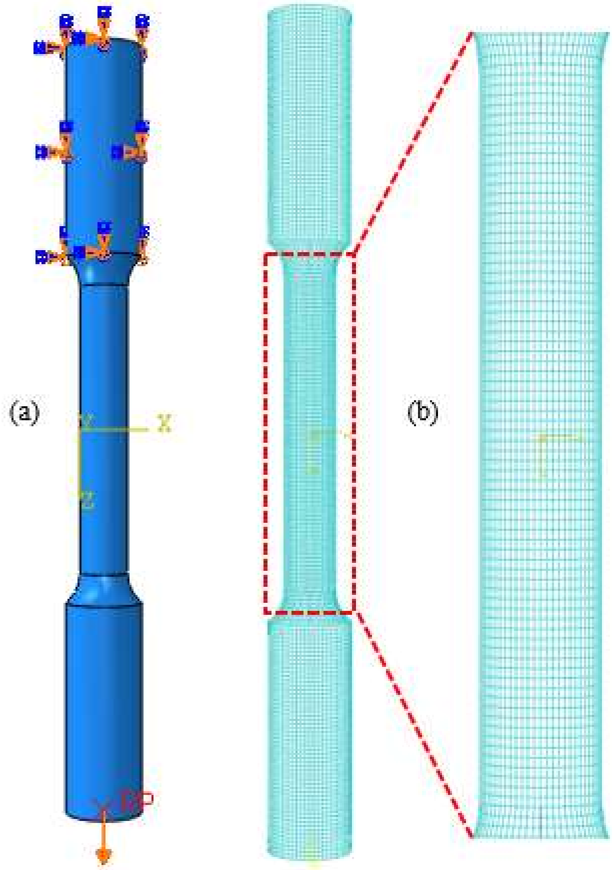

Figure 6.14 (a) Boundary conditions and (b) Meshed specimen with 1 mm node spacing

The specimens with porosity are simulated using eight-node linear brick elements (C3D8R) using ABAQUS/standard. The boundary conditions in simulations are carefully selected to closely match the experimental fatigue testing conditions. During actual testing, the upper end of the specimens is fixed, whereas, the load is applied to the lower end which is allowed to move vertically to apply alternating cycles of tension and compression. Therefore, the upper grip is constrained for no translation and rotation using encastre boundary condition, and, a uniformly distributed load corresponding to the testing condition for each specimen is applied to the face at the lower grip as shown in Figure 6.14 (a). A node spacing of 1 mm is used for all simulations and experimenting with further mesh refinement provided no significant change in the results. Figure 6.14 (b) shows the mesh used in these simulations. The FEA model developed to simulate stress field for fatigue life prediction consists of 83,433 eight-node linear brick elements (C3D8R) elements, 90,373 nodes, and 345,546 total number of variables.

Table 6.3 ASTM A216 WCB Steel Monotonic and Cyclic Properties

ASTM A216 WCB Monotonic Properties		
Ultimate Tensile Strength, σ_{UTS}	(MPa)	620
Yield Strength, σ_y	(MPa)	355
Modulus of Elasticity, E_0	(MPa)	198,000
Percentage Elongation, %EL	-	32.5
Fracture strength, σ_f	(MPa)	293
ASTM A216 WCB Cyclic Properties		
Fatigue Strength, S_f	(MPa)	141
S_f/σ_{UTS}		0.227
Cyclic Strain Hardening Coefficient, K'	(MPa)	1558
Cyclic Strain Hardening Exponent, n'		0.295
Fatigue Strength Coefficient, $\sigma_f{}'$	(MPa)	1015
Fatigue Strength Exponent, b		-0.136
Fatigue Ductility Coefficient, $\varepsilon_f{}'$		0.195
Fatigue Ductility Exponent, c		-0.435

Once, the simulations are done for each material and loading condition in ABAQUS, the resulting stress fields are imported as an ABAQUS .odb file to life prediction software corresponding to the tension and compression steps of the fully reversed loading (R = -1). Fe-safe life prediction software [96] is used in the present work to estimate the fatigue life of specimens. It is required by user to define the loading cycle and material properties. The material properties for sound steel and iron used in the analysis are summarized in Table 6.3 and Table 6.4 respectively.

Table 6.4 GGG-40 Ductile Iron Monotonic and Cyclic Properties

GGG-40 Monotonic Properties		
Ultimate Tensile Strength, σ_{UTS}	(MPa)	490
Yield Strength, σ_y	(MPa)	334
Modulus of Elasticity, E_0	(MPa)	167,000
Percentage Elongation, %EL	-	16.9
Fracture strength, σ_f	(MPa)	266
GGG-40 Cyclic Properties		
Fatigue Strength, S_f	(MPa)	197
S_f/σ_{UTS}		0.402
Cyclic Strain Hardening Coefficient, K'	(MPa)	877
Cyclic Strain Hardening Exponent, n'		0.14
Fatigue Strength Coefficient, $\sigma_f{}'$	(MPa)	585
Fatigue Strength Exponent, b		-0.075
Fatigue Ductility Coefficient, $\varepsilon_f{}'$		0.666
Fatigue Ductility Exponent, c		-0.751

Two approaches could be adapted in calculating the strain-life using fe-safe [97] which are as follows.

1. Using the strains from ABAQUS simulations run with E dependent on nodal porosity fraction f and then using the same variable E in fe-safe strain-life calculations.
2. Using the stress field resulted from ABAQUS simulations run with E dependent on nodal porosity fraction f and to generate the strains within fe-safe using E_0 for

sound material to perform conversion and then using the E_0 throughout the fe-safe strain-life calculations.

In the present work, the method in (2) is used due to its relative simplicity. The stress at FEA nodes resulting from ABAQUS simulations are converted to strains within the Fe-safe using elastic modulus of sound material. It is decided to use the algorithm for fatigue life predictions for each material as recommended by fe-safe. Therefore, for life prediction of cast steel specimens, Brown-Miller algorithm, and, for ductile-iron specimens, Maximum Principal-Strain algorithm are used both with Morrow mean stress correction [96].

6.3.1.1 Brown-Miller Analysis

The Brown-Miller algorithm is considered to be a conservative method for fatigue life prediction, using planes perpendicular to the surface and at 45 degree to the surface. It uses a critical plane analysis to estimate the fatigue life in reversals to failure, $2N_f$, by solving the following equation [96] at each node.

$$\frac{\Delta\gamma_{max}}{2}+\frac{\Delta\varepsilon_n}{2}=1.65\frac{\sigma'_f}{E}\left(2N_f\right)^b+1.75\varepsilon'_f\left(2N_f\right)^c \tag{6.10}$$

With Morrow mean stress correction, Equation (6.10) is modified to

$$\frac{\Delta\gamma_{max}}{2}+\frac{\Delta\varepsilon_n}{2}=1.65\frac{(\sigma'_f-\sigma_m)}{E}\left(2N_f\right)^b+1.75\varepsilon'_f\left(2N_f\right)^c \tag{6.11}$$

where, $\frac{\Delta\gamma_{max}}{2}$ is the maximum shear strain amplitude, $\frac{\Delta\varepsilon_n}{2}$ is the strain amplitude normal to the shear stress plane, σ_m is the mean stress, σ'_f is the fatigue strength coefficient, b is the fatigue strength exponent, ε'_f is the fatigue ductility coefficient, and c is the fatigue ductility exponent.

The underlying idea of a critical plane analysis is to compute the strain tensor at a FE node having three direct and three shear components. The strain tensor is then resolved onto a number of planes, where, at each place the damage associated with the strain is evaluated. The plane resulted with maximum damage is used in strain-life computations. For a Cartesian $x - y - z$ coordinate system, the unique planes can be defined by the orientation the normal of the plane surface makes with respect to the coordinate system [76]. This orientation can be defined by an angle from x-axis toward the y-axis, and another angle from the z-axis toward the $x - y$ plane [96]. fe-safe searched for the critical plane having worst damage in 10 degree increments over the 180 degree range of the first angle and 90 degree range of the second angle. The strains are projected to the calculation plane using direction cosines.

6.3.1.2 Maximum Principal Strain Analysis

The maximum principal strain algorithm only uses the planes perpendicular to the surface. It also uses a critical plane analysis to estimate the fatigue life in reversals to failure, $2N_f$, by solving the following equation [96] at each node.

$$\frac{\Delta\varepsilon}{2} = \frac{\sigma'_f}{E}\left(2N_f\right)^b + \varepsilon'_f\left(2N_f\right)^c \tag{6.12}$$

With Morrow mean stress correction, Equation (6.12) is modified to

$$\frac{\Delta\varepsilon}{2} = \frac{(\sigma'_f - \sigma_m)}{E}\left(2N_f\right)^b + \varepsilon'_f\left(2N_f\right)^c \tag{6.13}$$

where, $\frac{\Delta\varepsilon}{2}$ is the strain amplitude, σ_m is the mean stress, σ'_f is the fatigue strength coefficient, b is the fatigue strength exponent, ε'_f is the fatigue ductility coefficient, and c is the fatigue ductility exponent.

6.3.2 RESULTS OF FATIGUE LIFE SIMULATIONS

Figure 6.15 to Figure 6.21 represents a series of simulation results for steel specimens. Each of these figures shows the predicted stress field in porous specimens, S1' through S7', using ABAQUS and the fatigue life calculated by fe-safe. The scale used for fatigue life is Log10 life i.e. 1 million cycles are represented by 6 on this scale. As mentioned earlier, a node spacing of 1 mm is found to show good agreement between the measured and the predicted fatigue lives. A complex stress field is developed due to porosity upon loading each specimen. It is observed that the shortest lives are predicted in the regions of higher stress concentration. Moreover, in each specimen, the smallest number of cycles to failure is predicted on the surface of the specimen. This shortest life predicted at any node in fe-safe is considered to be the fatigue life for that specimen. A summary of simulated stress, measured and predicted fatigue life for each specimens in presented in Table 6.5.

A comparison of the experimental and simulated S-N curve for steel specimens in shown in Figure 6.22. Simulation results indicated two specimens to experience the infinite life where the predicted number of cycles to failure are beyond the runout condition i.e. 1×10^{6} cycles in the present work. For a better understanding of experimental and simulated results, the measured and predicted fatigue lives for all seven steel specimens are compared in Figure 6.23. A line of perfect correspondence is provided in the figure to determine if a prediction is non-conservative (above the line) or conservative (below the line). It can be observed that six out of seven specimens are within a factor of 10 of the test results, which can be considered as a good agreement in fatigue life prediction [77]. The specimen S1' is found to have a relatively bad agreement since the predicted fatigue life is slightly more than the factor of 10 of the test result. In general, the overall results for fatigue life prediction are encouraging, however, the overall nature of predictions are found to be non-conservative in steel specimens.

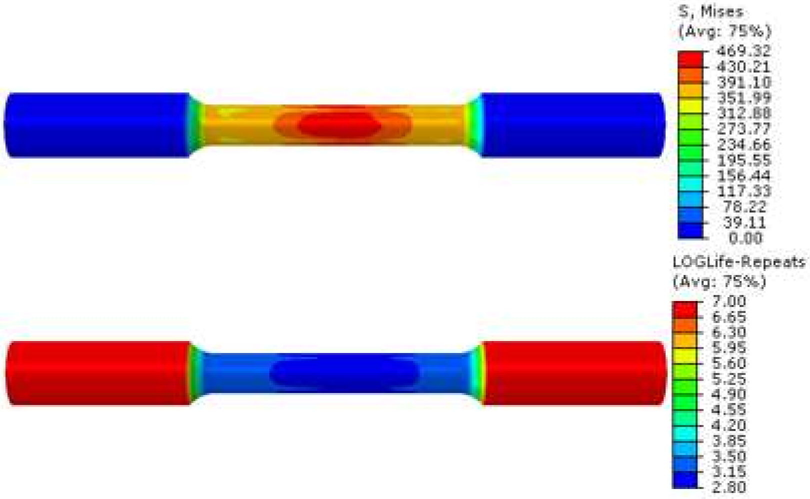

Figure 6.15 ABAQUS stress analysis and fatigue life prediction from fe-safe for specimen S1'

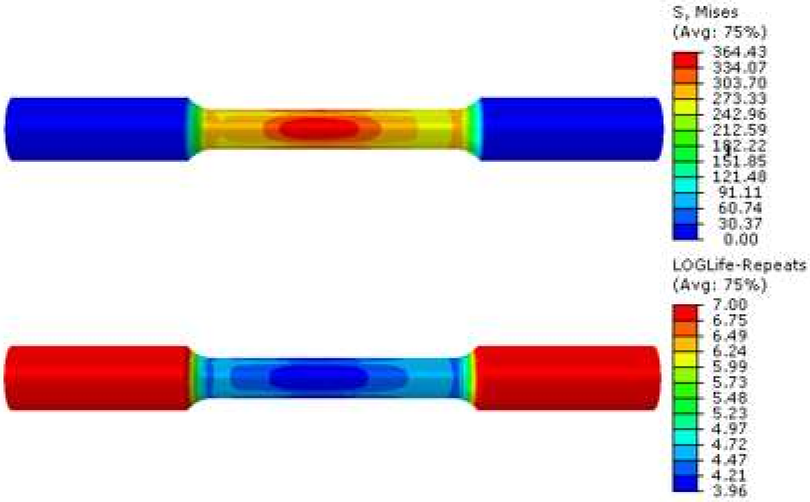

Figure 6.16 ABAQUS stress analysis and fatigue life prediction from fe-safe for specimen S2'

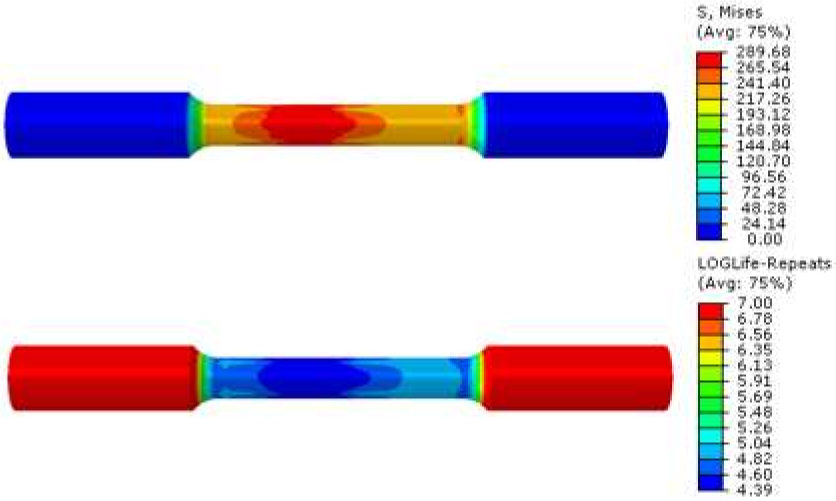

Figure 6.17 ABAQUS stress analysis and fatigue life prediction from fe-safe for specimen S3'

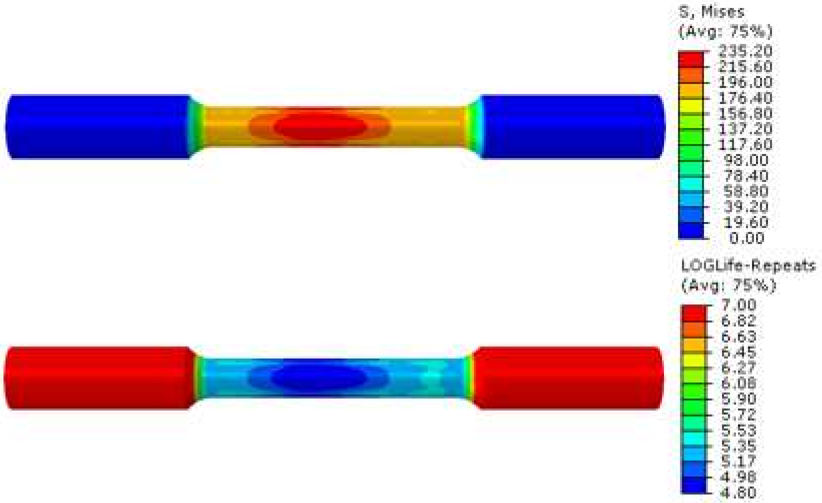

Figure 6.18 ABAQUS stress analysis and fatigue life prediction from fe-safe for specimen S4'

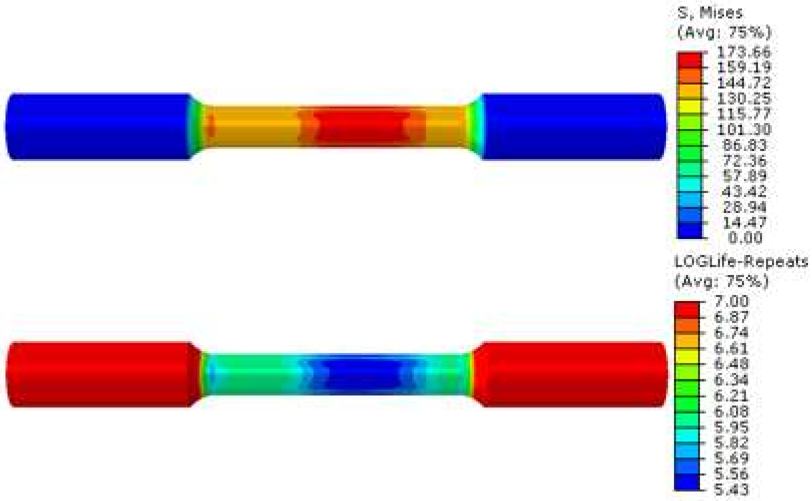

Figure 6.19 ABAQUS stress analysis and fatigue life prediction from fe-safe for specimen S5'

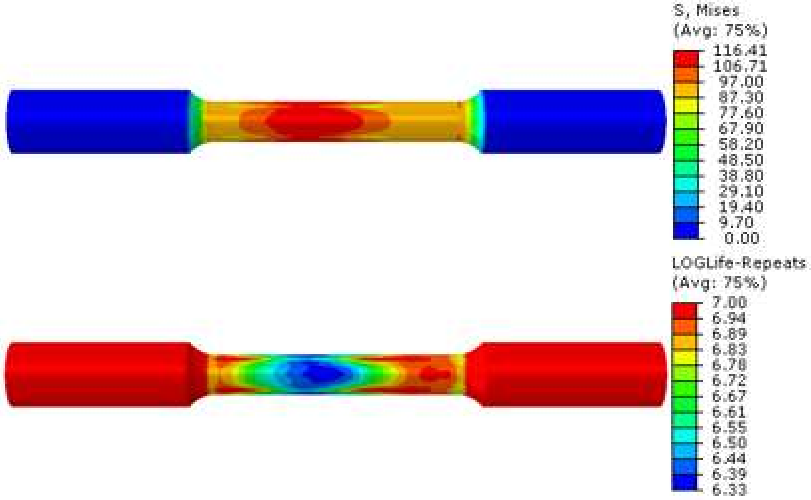

Figure 6.20 ABAQUS stress analysis and fatigue life prediction from fe-safe for specimen S6'

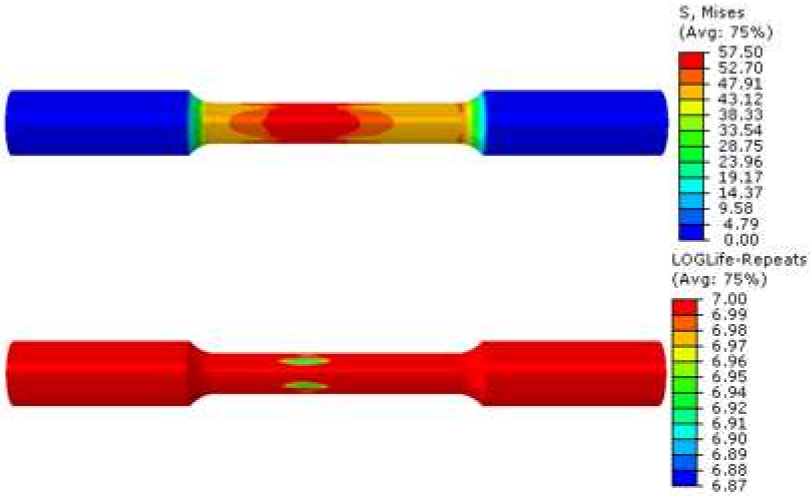

Figure 6.21 ABAQUS stress analysis and fatigue life prediction from fe-safe for specimen S7'

Table 6.5 Summary of simulated and experimental results of fatigue testing for steel specimens

Specimen ID	Simulated Stress (MPa)	Measured Fatigue Life (Cycles)	Simulated Fatigue Life (Cycle)
S1'	469.32	62	630
S2'	364.43	6,545	9,115
S3'	289.68	20,561	24,219
S4'	235.20	56,893	62,983
S5'	173.66	145,089	259,682
S6'	116.41	535,564	2,133,921
S7'	57.50	3,061,195	7,421,449

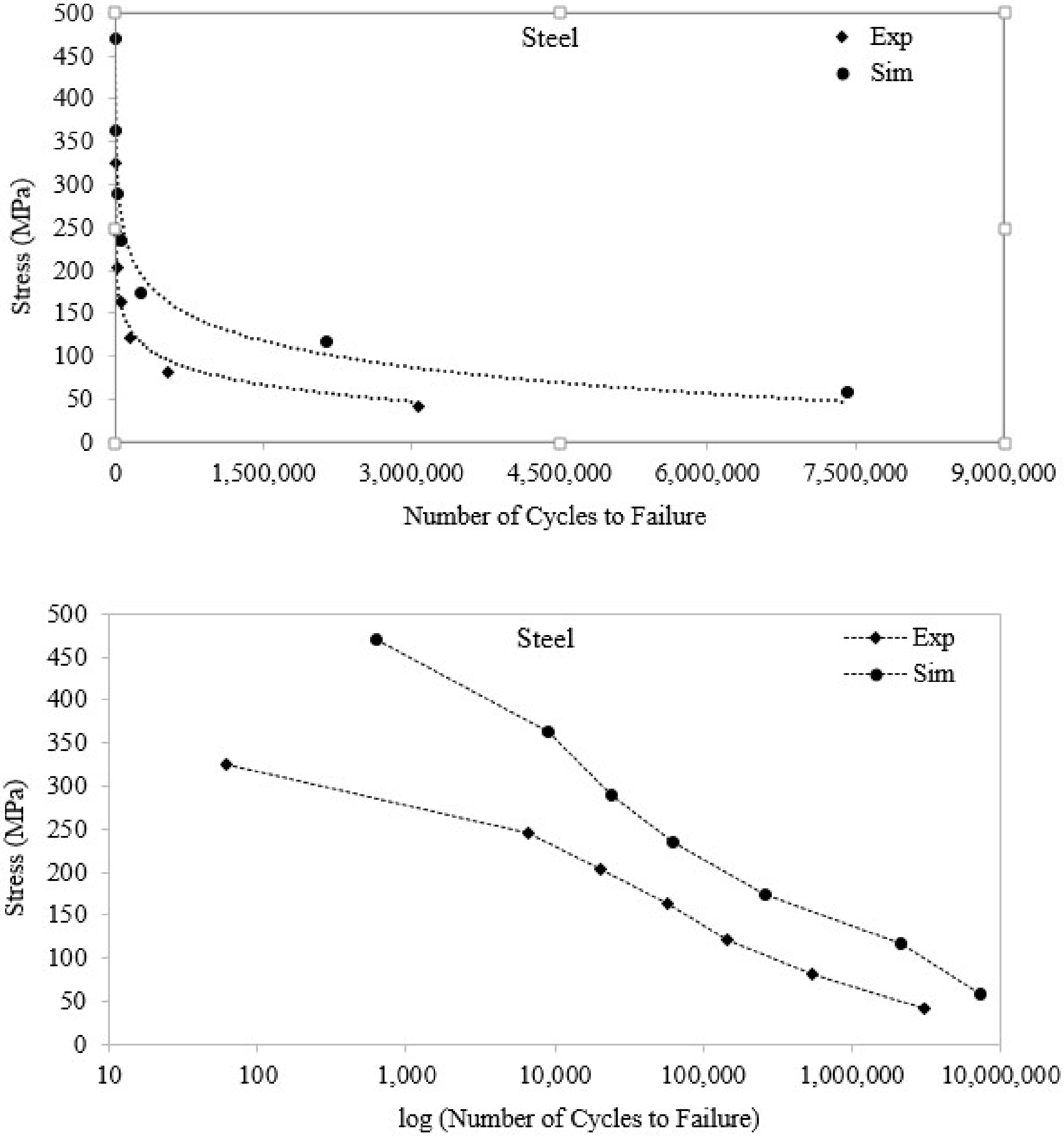

Figure 6.22 Simulated and experimental S-N curve for steel specimens

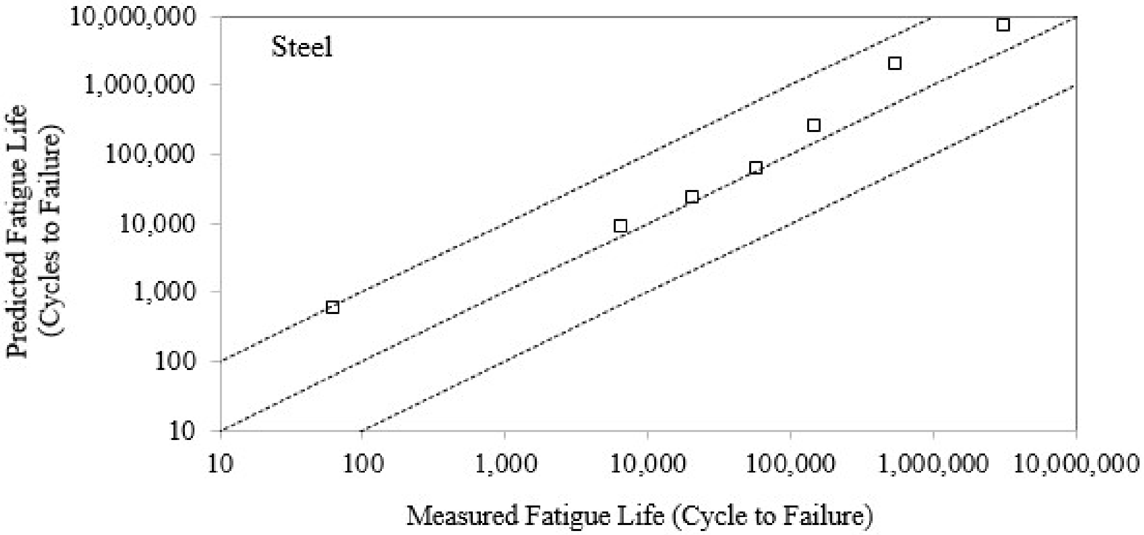

Figure 6.23 Comparison between measured and predicted fatigue lives of steel specimens

Figure 6.24 to Figure 6.30 represents a series of simulation results for iron specimens. Each of these figures shows the predicted stress field in specimens, I1' through I7', using ABAQUS and the fatigue life calculated by fe-safe. Since no porosity is predicted in iron specimens and microporosity cannot be predicted by MAGMASoft, the stress fields obtained are for sound specimens under different loading conditions. Here, the node spacing is similar to that of steel specimens i.e. 1 mm. Due to pore-free nature of specimens, the predicted stress fields in all iron specimens appears to be the same with only difference in the magnitude of stress. However, the shortest lives are predicted within the test section of specimens owing to high stress concentration in this region. Based on the methodology, discussed above, for fatigue life calculation using fe-safe, specimens I1', I2', and I3' are found to have shortest life anywhere within the test section, however, in specimens I4', I5', I6'and I7', the shortest life is predicted near to the grips of the specimens. This is due to the shortest life predicted at that particular nodes of FE mesh in fe-safe. A summary of simulated stress, measured and predicted fatigue life for each specimens in presented in Table 6.6.

A comparison of the experimental and simulated S-N curve for iron specimens is shown in Figure 6.31. Simulation results indicated six specimens with finite and one specimen with the infinite life beyond the runout condition i.e. 1×10^6 cycles in the present work. Once again, the measured and predicted fatigue lives for all seven iron specimens are compared in Figure 6.32. It can be observed that all seven specimens showed an excellent agreement between the predicted and measured fatigue lives. With such agreement for iron specimens, it cannot be inferred that the nature of predictions is non-conservative, however, the fatigue life prediction with microporosity, which is certainly present in the cast specimens (but not predicted in simulations) can lead to further refinement of results.

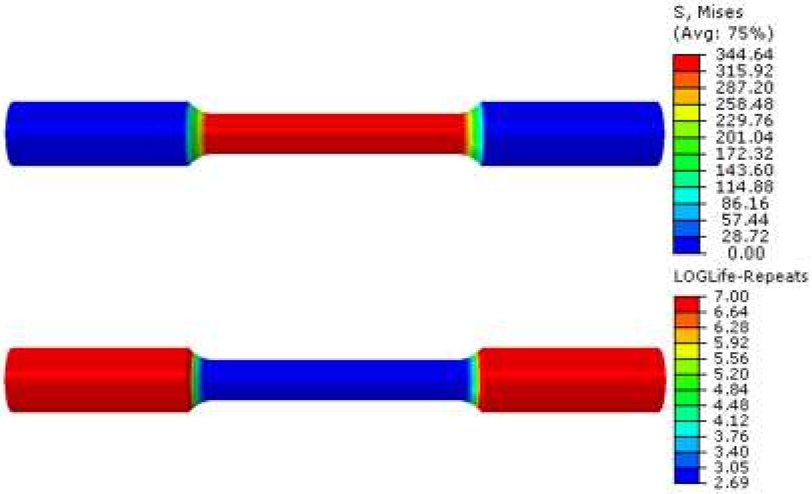

Figure 6.24 ABAQUS stress analysis and fatigue life prediction from fe-safe for specimen I1'

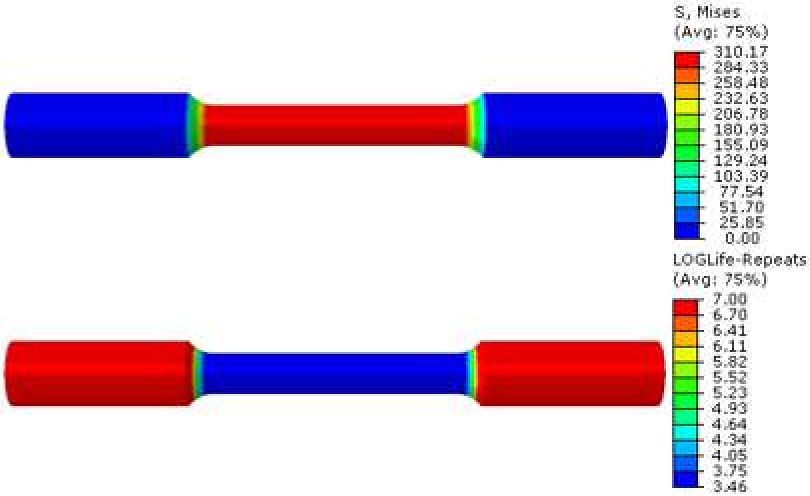

Figure 6.25 ABAQUS stress analysis and fatigue life prediction from fe-safe for specimen I2'

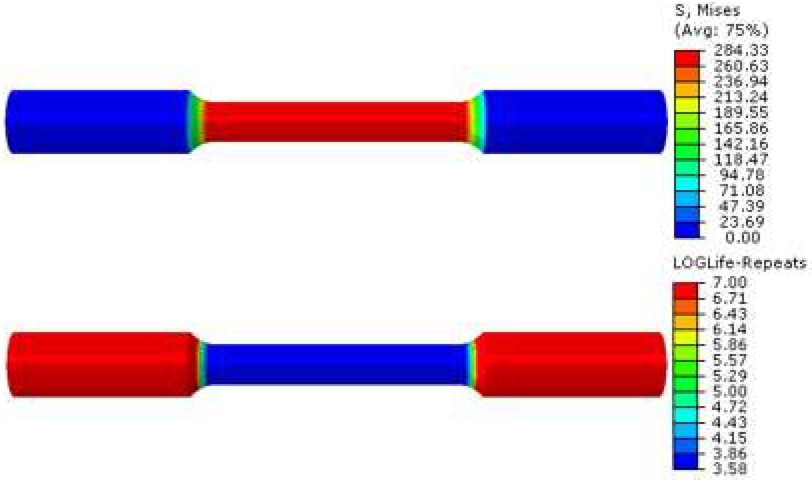

Figure 6.26 ABAQUS stress analysis and fatigue life prediction from fe-safe for specimen I3'

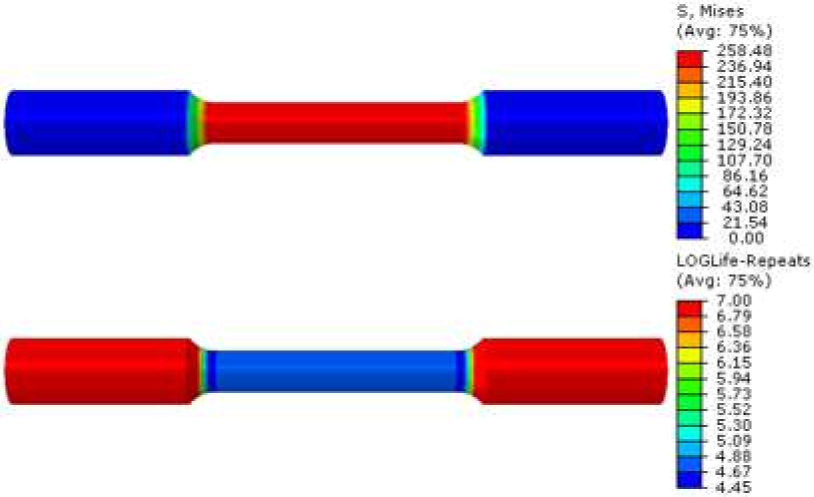

Figure 6.27 ABAQUS stress analysis and fatigue life prediction from fe-safe for specimen I4'

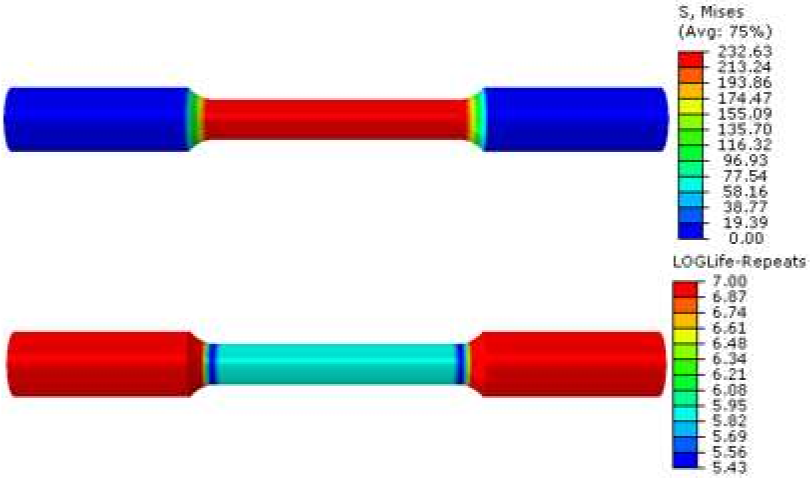

Figure 6.28 I ABAQUS stress analysis and fatigue life prediction from fe-safe for specimen I5'

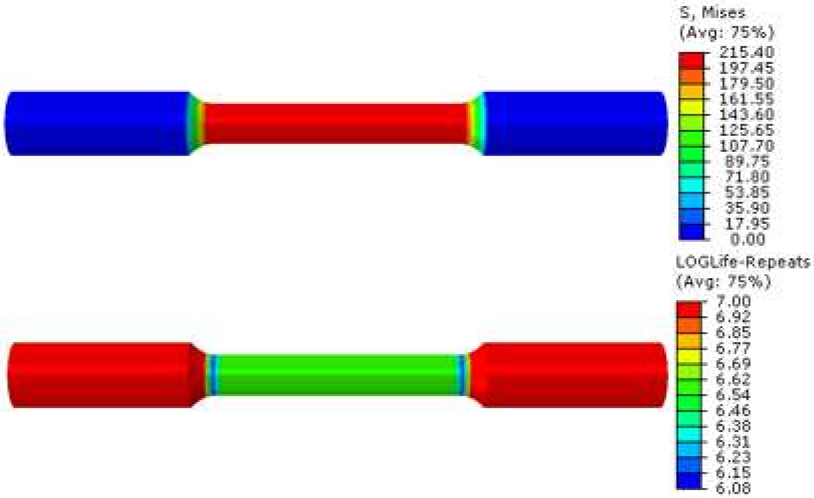

Figure 6.29 ABAQUS stress analysis and fatigue life prediction from fe-safe for specimen I6'

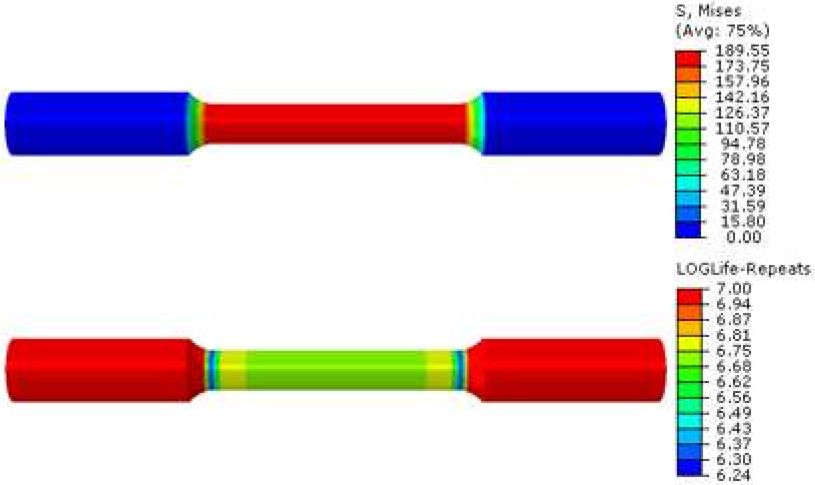

Figure 6.30 ABAQUS stress analysis and fatigue life prediction from fe-safe for specimen I7'

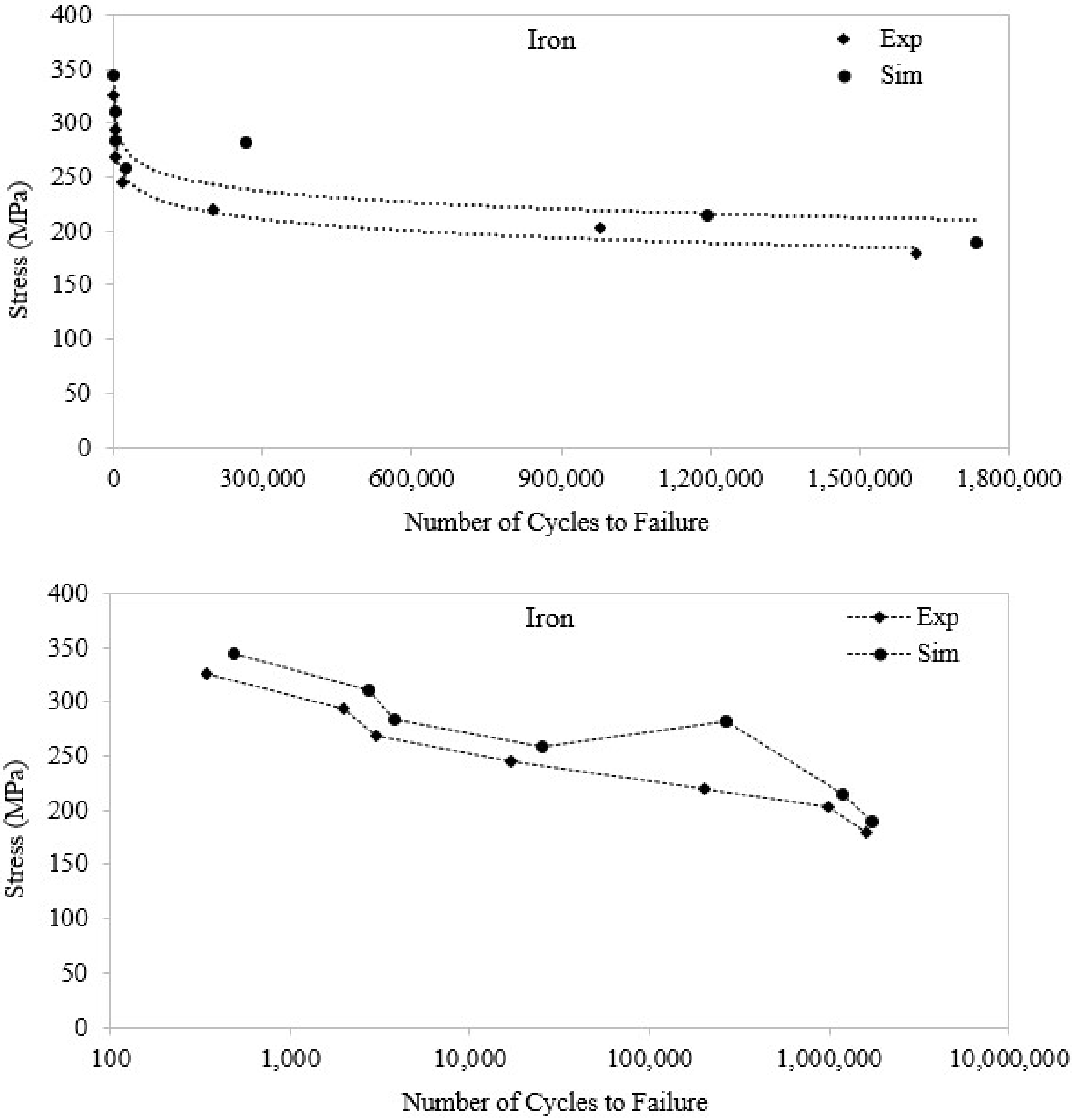

Figure 6.31 Simulated and experimental S-N curve for iron specimens

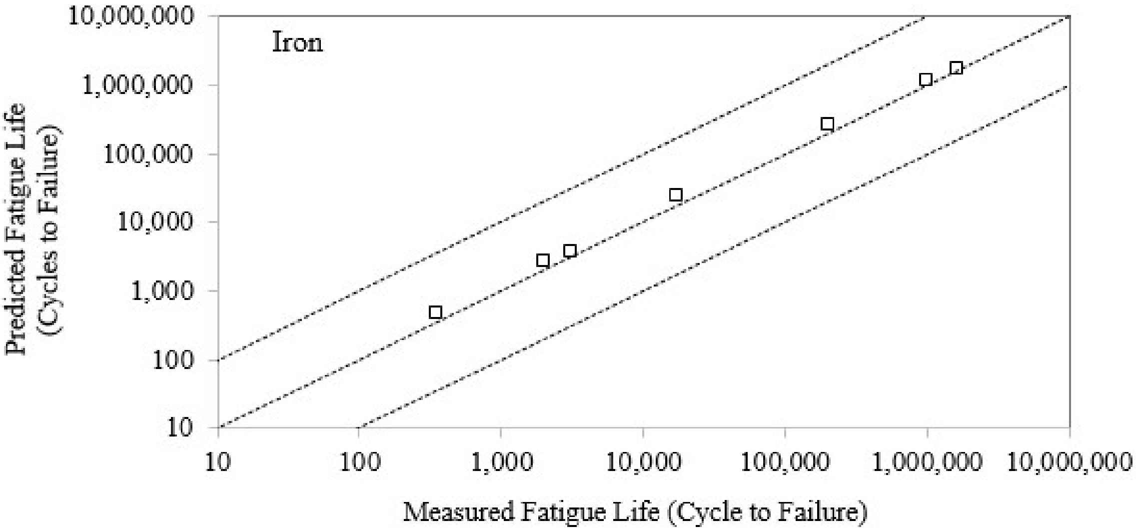

Figure 6.32 Comparison between measured and predicted fatigue lives of iron specimens

Table 6.6 Summary of simulated and experimental results of fatigue testing for steel specimens

Specimen ID	Simulated Stress (MPa)	Measured Fatigue Life (Cycles)	Simulated Fatigue Life (Cycle)
I1'	344.64	342	485
I2'	310.17	1,973	2,716
I3'	284.33	3,016	3,769
I4'	258.48	17,148	25,471
I5'	232.63	200,798	267,257
I6'	215.40	978,556	1,194,901
I7'	189.55	1,614,616	1,735,057

6.4 CONCLUDING REMARKS

The simulations of tensile testing and fatigue life prediction are presented in this chapter. In case of tensile testing of steel specimens, the comparison between simulated and experimental results is encouraging. The experimental tensile testing of specimens resulted in strength and elongation measurements greater than the minimum defined in ASTM standard for A216 WCB cast steel. The good quality of cast specimens is already confirmed through X-ray imaging prior to testing and by comparing the simulated and actual porosities. Some discrepancy in simulated and experimental results of tensile testing is observed but it cannot be solely attributed to porosity. Instead, the hardness measurement at different regions of the each specimen revealed significant variation which can be related to lack of control on heat treatment done to homogenize the cast parts produced using a multi-cavity mold. Hence, it can be concluded that the castings produced with optimized molds can result in high quality and performance with more controlled post-casting operations i.e. cleaning, finishing and heat treatment. For tensile specimens of ductile iron, the simulated and experimental results of tensile testing are compared only for the sound specimen and are found to be in good agreement.

Fatigue life predictions for steel specimens are found to be in good agreement with experimental results. It is known that fatigue life predictions are very sensitive to local stress concentrations [76]. The simulations done in this work rely on porosity fractions which are defined over a volume that is large compared to microscopic pore geometry. Therefore, it can be expected that further mesh refinement can resolve stress concentration around the small shrinkage pores. This can lead to an excellent agreement of measured and predicted fatigue lives, or, can even result in conservative nature of predictions.

CHAPTER 7

RELIABILITY ASSESSMENT

7.1 INTRODUCTION

The reliability of an engineering product deals with the undesirable events or failures during its service life. It can be precisely defined as the reliability of a part is the probability that, when operated under defined set of conditions, the part will perform its intended function adequately for a specified interval of time [98]. It is an established fact that apparently identical parts operating under similar conditions fail at different points in time. This brings about a need to describe failure phenomena in probabilistic terms and therefore, fundamental aspects of reliability heavily rely on concepts from probability. This chapter provides the methods for quantifying the reliability of cast parts produced as part of the present work.

7.2 RELIABILITY FUNCTION

The probability of failure is as a function of time is given by

$$P(\mathbf{t} \leq t) = F(t), \qquad t \geq 0 \tag{7.1}$$

where, $\mathbf{t}$ is a random variable denoting the time to failure. So, $F(t)$ is the probability that the system will fail by time . Alternatively, $F(t)$ is the failure distribution function (or the unreliability function). Then, the reliability of the part that it will perform the desired function at a certain time is given by

$$R(t) = 1 - F(t) = P(\mathbf{t} > t) \tag{7.2}$$

where, $R(t)$ is the reliability function. If the random variable i.e. time to failure $\mathbf{t}$ has a density function $f(t)$, then

$$R(t) = 1 - F(t) = 1 - \int_0^t f(\tau)d\tau = \int_t^\infty f(\tau)d\tau \tag{7.3}$$

If a particular failure density function or distribution function is known, the reliability function can be determined directly. Section 7.3 provide the reliability functions for some well-known distributions used in reliability computations.

7.3 RELIABILITY FUNCTION FOR WELL-KNOWN DISTRIBUTIONS

Some of the commonly used probability distributions in reliability are *Exponential Distribution, Normal Distribution, Log-Normal Distribution,* and *Weibull Distribution*. Each distribution has its unique reliability function which are presented in the following sub-sections.

7.3.1 EXPONENTIAL DISTRIBUTION

The exponential distribution is widely used in reliability computations. This distribution should not be used indiscriminately as there could be certain situations where it clearly does not apply. The failure density function for exponential distribution is given by

$$f(t) = \frac{1}{\theta} e^{-t/\theta}, \qquad t \geq 0 \tag{7.4}$$

where, θ is a parameter such that $\theta > 0$. The resulting reliability function is

$$R(t) = e^{-t/\theta}, \qquad t \geq 0 \tag{7.5}$$

The exponential density function is illustrated in Figure 7.1.

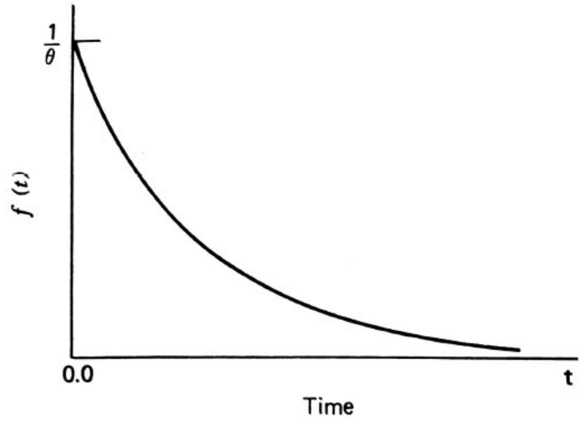

Figure 7.1 The exponential function [98]

7.3.2 NORMAL DISTRIBUTION

The normal distribution is represented by its well-known bell shape and is symmetrical about its mean value. The cumulative distribution is given by

$$F(t) = P[\mathbf{t} \leq t] = \int_{-\infty}^{t} \frac{1}{\sigma\sqrt{2\pi}} \exp\left[-\frac{1}{2}\left(\frac{\tau - \mu}{\sigma}\right)^2\right] d\tau \tag{7.6}$$

where, μ is the mean and σ is the standard deviation. The resulting reliability function is simply

$$R(t) = 1 - F(t) \tag{7.7}$$

The probability density function of a standard normal distribution is

$$\phi(z) = \frac{1}{\sqrt{2\pi}} \exp(-z^2/2), \qquad -\infty < z < \infty \tag{7.8}$$

The standard cumulative distribution function is

$$\Phi(z) = \int_{-\infty}^{z} \frac{1}{\sqrt{2\pi}} \exp(-\tau^2/2) d\tau \tag{7.9}$$

Then for a normally distributed random variable $\mathbf{t}$, with mean μ and standard deviation σ yields the following relationship.

$$P(\mathbf{t} \le t) = P\left(z \le \frac{t-\mu}{\sigma}\right) = \Phi\left(\frac{t-\mu}{\sigma}\right) \tag{7.10}$$

Figure 7.2 depicts the shape of reliability function for some normal random variables.

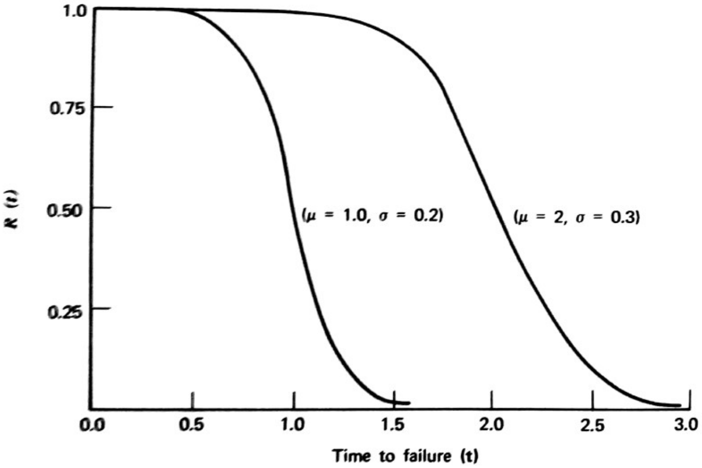

Figure 7.2 The normal reliability function [98]

7.3.3 LOG-NORMAL DISTRIBUTION

The log-normal density function is given by

$$f(t) = \frac{1}{\sigma\sqrt{2\pi}} \exp\left[-\frac{1}{2}\left(\frac{lnt-\mu}{\sigma}\right)^2\right], \qquad t \ge 0 \tag{7.11}$$

where, $-\infty < \mu < \infty$ and $\sigma > 0$. The cumulative distribution function for the log-normal distribution is

$$F(t) = \int_0^t \frac{1}{\tau\sigma\sqrt{2\pi}} \exp\left[-\frac{1}{2}\left(\frac{ln\tau-\mu}{\sigma}\right)^2\right] d\tau \tag{7.12}$$

and it can be related to standard normal deviate z by

$$F(t) = P[\mathbf{t} \leq t] = P\left[z \leq \frac{ln\tau - \mu}{\sigma}\right] \tag{7.13}$$

The resulting reliability function is given by

$$R(t) = P[\mathbf{t} > t] = P\left[z > \frac{ln\tau - \mu}{\sigma}\right] \tag{7.14}$$

The reliability function for various log-normal distributions is shown in Figure 7.3.

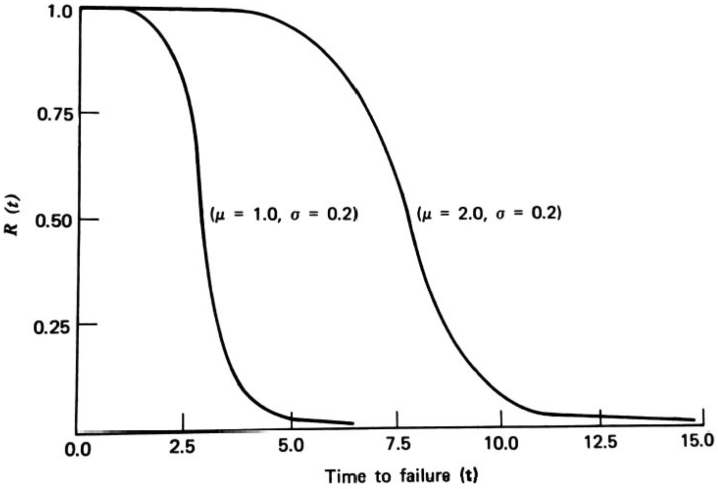

Figure 7.3 The log-normal reliability function [98]

7.3.4 WEIBULL DISTRIBUTION

The Weibull failure density function is given by

$$f(t) = \frac{\beta(t-\delta)^{\beta-1}}{(\theta-\delta)^{\beta}} \exp\left[-\left(\frac{t-\delta}{\theta-\delta}\right)^{\beta}\right], \qquad t \geq \delta \geq 0 \tag{7.15}$$

where, β is the shape parameter, and $(\theta - \delta)$ is the scale parameter, and both are always positive. For $t \geq \delta$

$$R(t) = 1 - F(t) = \exp\left[-\left(\frac{t-\delta}{\theta-\delta}\right)^{\beta}\right] \tag{7.16}$$

The introduction of parameter δ means that instead of assuming that the possibility of failure starts when t is zero, a period of zero probability of failure is allowed. If δ is taken as zero, Equation (7.15) becomes

$$R(t) = 1 - F(t) = \exp\left[-\left(\frac{t}{\theta}\right)^{\beta}\right] \tag{7.17}$$

The shapes of Weibull reliability function with varying β are presented in Figure 7.4. When $\beta < 1$, the Weibull distribution takes the form of a hyper-exponential distribution, for $\beta = 3.5$, the distribution becomes symmetric starting at δ, and for $\beta > 3.5$, the distribution moves away from δ along the t-axis and becomes negatively skewed.

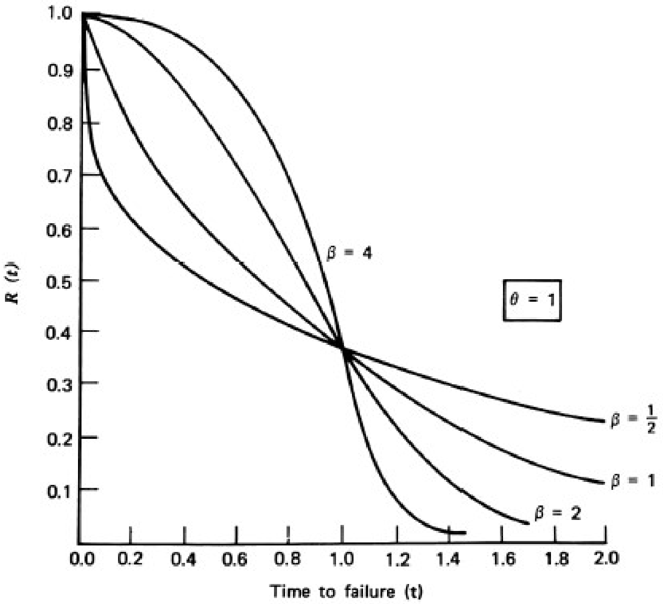

Figure 7.4 The Weibull reliability function [98]

7.4 INTERFERENCE THEORY AND RELIABILITY COMPUTATIONS

In a classical strength-limited design, once the criterial of failure is identified, the rule for an adequate design is

Strength > Stress

and to cover uncertainties

Strength > (design factor) Stress

The underlying idea behind the design factor is to keep mean strength and mean stress sufficiently separated to ensure the desired level of safety in design. However, there are issues in using the design factors. The inherent variability of strength and strength factors and of stress and stress factors leads to the idea of stress and strength distributions. If the distributions of strength and stress are known, the adequacy of a component can be estimated from the interference as shown in Figure 7.5. The curves in Figure 7.5 represents the interaction of stress and strength distributions when the mean strength exceeds the mean stress and it shows a finite incidence of failure, which is represented by the intersected region.

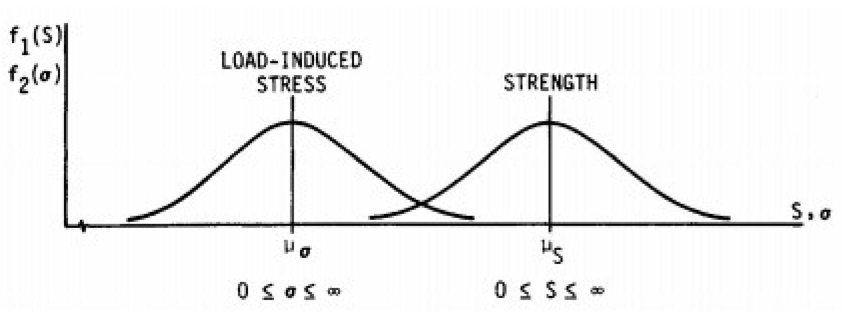

Figure 7.5 Stress and Strength interference when the mean strength exceeds the mean stress [99]

For a strength-limited design, let the density function for the strength is f_1 and that for stress is f_2, the reliability function will be a joint probability function, where

$$P(S > \sigma) = P[S - \sigma > 0] = R$$

$$R = \int_{-\infty}^{\infty} f_1\,(S) \left[\int_{S}^{\infty} f_2\,(\sigma) d\sigma \right] dS \tag{7.18}$$

where, S is the significant strength and σ is the significant load-induced stress. The task for a given design is to ensure that $S > \sigma$.

In a typical problem of reliability in fatigue analysis, the stress-strength model discussed above is applied as shown in Figure 7.6. The components are *safe* until the strength and stress distributions are separated with a *safety margin*, however, failure of components is expected when the two distributions starts to intersect as shown in the *unsafe* region. With this approach, the reliability assessment of the cast specimens produced as part of this study is done.

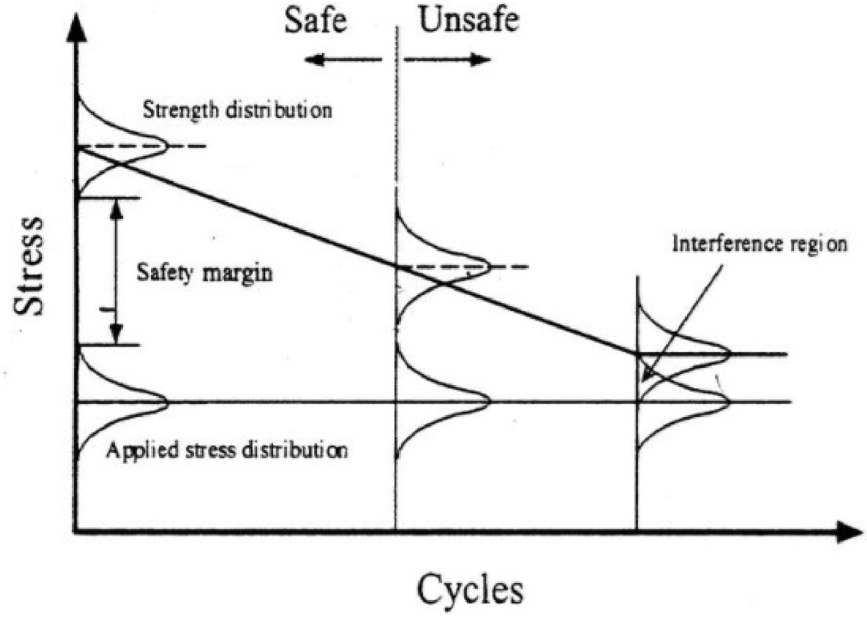

Figure 7.6 Applied fatigue stress-strength interference model [100]

7.5 RELIABILITY ASSESSMENT OF CAST SPECIMENS

The fatigue lives of test specimens is already determined in Chapter 6. Here, the reliability of test specimens is calculated for the already predicted fatigue lives at varying stress levels. The reliability analysis of the cast specimens subjected to cyclic loading can be classified as

a) Time Independent Load-Induced Stress – the stress applied on the component does not change with time
b) Time Dependent Load-Induced Stress – the stress applied on the component changes with time

7.5.1 RELIABILITY ANALYSIS WITH TIME INDEPENDENT LOAD-INDUCED STRESS

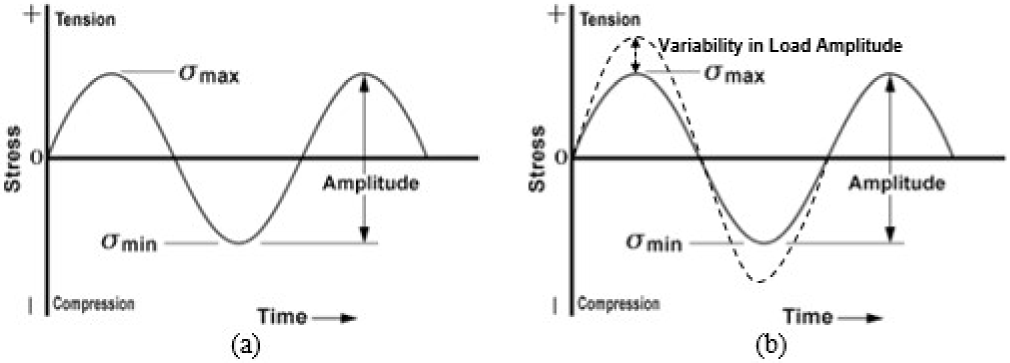

Figure 7.7 (a) No change in load-induced stress amplitude and (b) Variability in defined load-induced stress amplitude over time [101]

A typical loading pattern where the stress on a component does not vary with time is shown in Figure 7.7 (a). Figure 7.7 (b) represents a special case of this loading pattern when there is some variability in load amplitude relative to the amplitude defined. In order to estimate the reliability, four values of load-induced stresses are selected for each material based on the minimum and maximum load-induced stresses experienced by the actual cast parts produced using each material. The selected load induced stresses for steel are 79 MPa, 87 MPa, 96 MPa, and 104 MPa and for iron are 90 MPa, 150 MPa, 200 MPa, and 250 MPa. The reliability analysis with time independent load-induced stress for cast specimens is done using fe-safe. The analysis combines variability in material fatigue strength and variability in applied the applied loading (if any), to calculate the probability of failure for the life or lives specified. The reliability computations in this case is based on normally distributed stress and Weibull distributed strength. The failure rates are calculated as follows.

i. It is assumed that for failure rate analysis to be useful the component must fail in the elastic area of the strain-life curve.
ii. A normal or Gaussian distribution is applied to the variation in loading. The percentage standard deviation of the loading is defined, representing the variability of the load amplitude relative to the amplitude defined. For non-constant amplitude loading the code derives an equivalent constant amplitude loading.
iii. A Weibull distribution is applied to material strength. This is defined by three parameters:
    a. The Weibull Mean: This is the strength at which the life curve exceeds the target life. This value is derived from the material data and the specified target life. The Weibull distribution is centered on this value.
    b. The Weibull Slope, β: This is the shape parameter which varies the probability density. The effect of β on the shape of the distribution is already shown in Figure 7.4.

c. The Weibull Minimum Parameter: This determines the width of distribution and lies between 0 and 1. As the lower edge of the distribution tends towards zero amplitude, it tends towards 0, and as the distribution gets narrower, it tends towards 1.

iv. The overlap area of the normal distribution of loading and Weibull distribution of strength is calculated for each of the target lives. This represents the probability of failure as shown in Figure 7.8. The two distributions are plotted on a linear scale, whereas, the strain axis is shown plotted on a logarithmic scale.

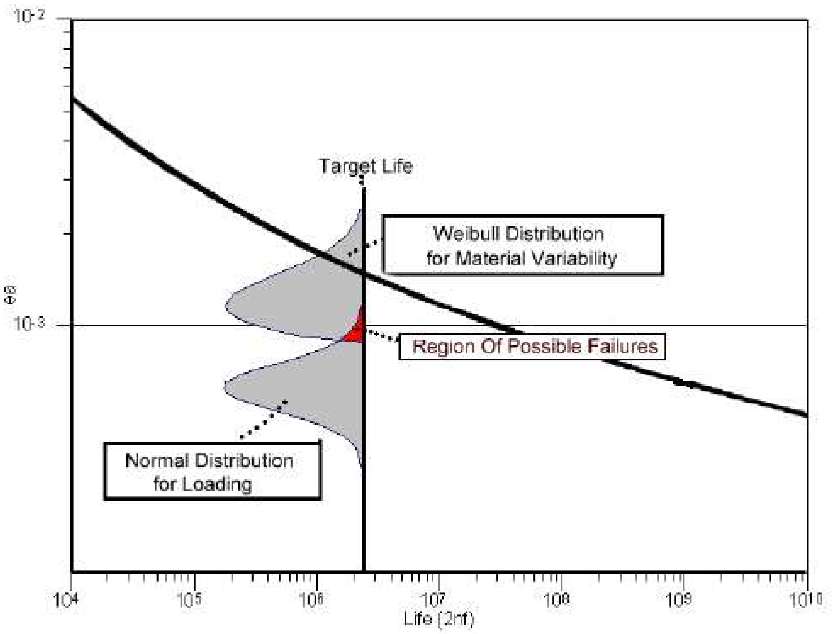

Figure 7.8 Determination of probability of failure using fe-safe [96]

7.5.2 RELIABILITY ANALYSIS WITH TIME DEPENDENT LOAD-INDUCED STRESS

The more realistic load-induced stress on a component varies with time as shown in Figure 7.9. Reliability predictions with such time dependent load-induced stresses results in more conservative estimates of component performance during service life. The strength-stress interference theory also applies to this analysis, however, the load-induced stress cannot be modeled through normal or Gaussian distribution. This limits the utilization of fe-safe in reliability analysis of components with time dependent load-induced stresses. Hence, analytical methods developed by Samar et al. [102] are used to estimate reliability in this case. The approach presented by Samar et al. [102] computes reliability using Weibull distributed stress and Weibull distributed strength. In this case the probability density functions of strength S and stress σ distributions are given by

$$f_1(S) = \frac{\beta_S}{\theta_S}\left(\frac{S}{\theta_S}\right)^{\beta_S - 1}.\exp\left(-\frac{S}{\theta_S}\right)^{\beta_S} \tag{7.19}$$

$$f_2(\sigma) = \frac{\beta_\sigma}{\theta_\sigma}\left(\frac{\sigma}{\theta_\sigma}\right)^{\beta_\sigma - 1}.\exp\left(-\frac{\sigma}{\theta_\sigma}\right)^{\beta_\sigma} \tag{7.20}$$

and the resulting reliability function is similar to Equation 7.18. The load-induced stress change on a component over time can be accurately modelled using Rayleigh distribution. A special case of Weibull distribution with the shape parameter β is equal to 2 represents the Rayleigh distribution. This suggests that, if the shape parameter of strength is twice to that of load-induced stress i.e. $\beta_S = 2\beta_\sigma$, then the reliability analysis is based on Weibull distributed strength and Rayleigh distributed load-induced stress. Using the results presented by Samar et al. [102] and with $\beta_S = 2\beta_\sigma$, the reliability function is given by

$$R = P(S > \sigma) = \frac{\theta_S}{\theta_\sigma}\sqrt{\pi}.\exp\left(\frac{1}{4}\left(\frac{\theta_S}{\theta_\sigma}\right)^2\right).\left\{1 - \phi\left[\frac{1}{\sqrt{2}}.\left(\frac{\theta_S}{\theta_\sigma}\right)\right]\right\} \tag{7.21}$$

Hence, the reliability can be estimated against the ratio of scale parameters i.e. $\frac{\theta_S}{\theta_\sigma}$ for the targeted lives. Here, the $\frac{\theta_S}{\theta_\sigma}$ ratio is approximated to be similar to that of the $\frac{S}{\sigma}$ ratios for the targeted lives.

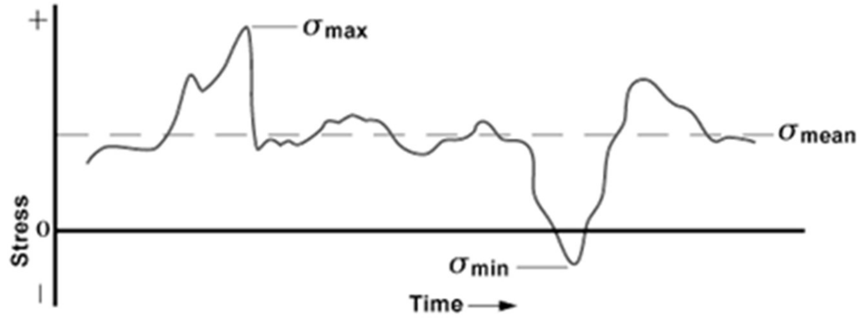

Figure 7.9 Stress changes on a component over time [101]

7.6 RELIABILITY RESULTS

7.6.1 TIME INDEPENDENT LOAD-INDUCED STRESS

Figure 7.10 to Figure 7.13 depicts the reliability curves for steel specimens with load-induced stress values 79 MPa, 87 MPa, 96 MPa, and 104 MPa. In each of these figures, the reliability of the cast parts is presented with a 0% and 5% variability in the load-induced stress. It can be observed that a 5% variability in load has not significantly affected the component's reliability. This could be due to the fact defined above that the software derives an equivalent loading for non-constant amplitude loading. However, the component's reliability for the same targeted life decreases with increasing load induced stress. Moreover, the effect of Weibull shape parameter β is also analyzed and presented. Previously, it is discussed that the coefficient of variation in hardness and strength of the specimens was very less, which suggests a higher value of β to be more realistic. Therefore, reliability is computed at various values of β i.e. 3, 4, 5, and 10. The higher the value of β, the components will be more reliable for the same targeted lives as shown in Figure 7.10 to Figure 7.13.

A summary of reliability computations for steel is presented in Figure 7.14. The plot indicates the reliability of components for the runout conditions used in fatigue life prediction i.e. 10^6 cycles against the load induced stress. A region of safe loading is defined based on how many component survive at a particular load. It is noted that, independent of β, more than 86% components survive for the infinite life at a load-induced stress of 85 MPa. However, this is a conservative estimate of safe loading on component to allow for possible variations in component strength, which is represented by β in reliability calculations. From experience, it is readily accepted that apparently same components fail at different points of time during service life. Therefore, in a strength-limited design, it is appropriate to consider such variations in reliability computations. Nevertheless, if such variations are assured to be at a minimum, the use of a higher value of β is more realistic, which in our case resulted in a reliability of more than 95% at a load induced stress of 95 MPa in Figure 7.14. Hence, with the optimized mold design and a higher $\beta = 10$, it is reasonable to infer a safe load-induced stress up to 95 MPa.

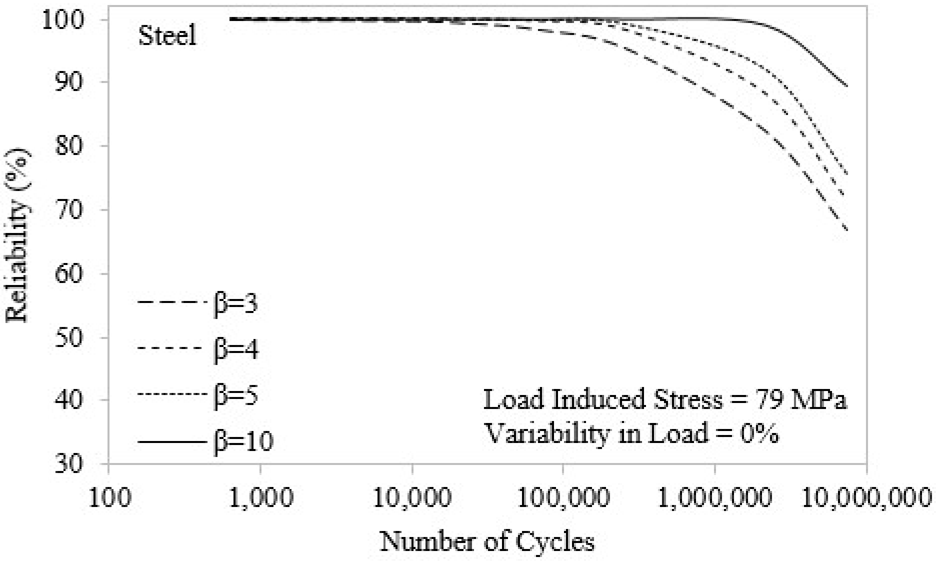

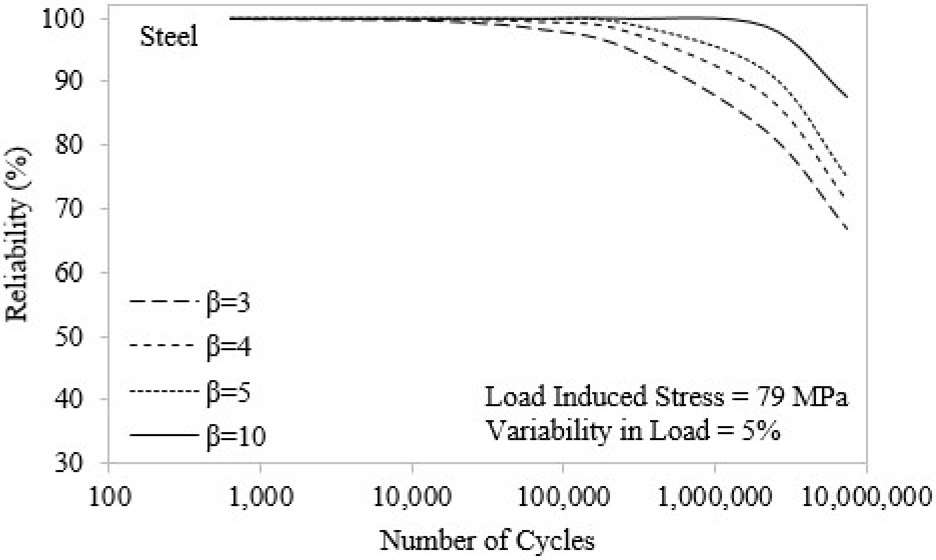

Figure 7.10 Reliability results with a load-induced stress of 79 MPa on cast steel

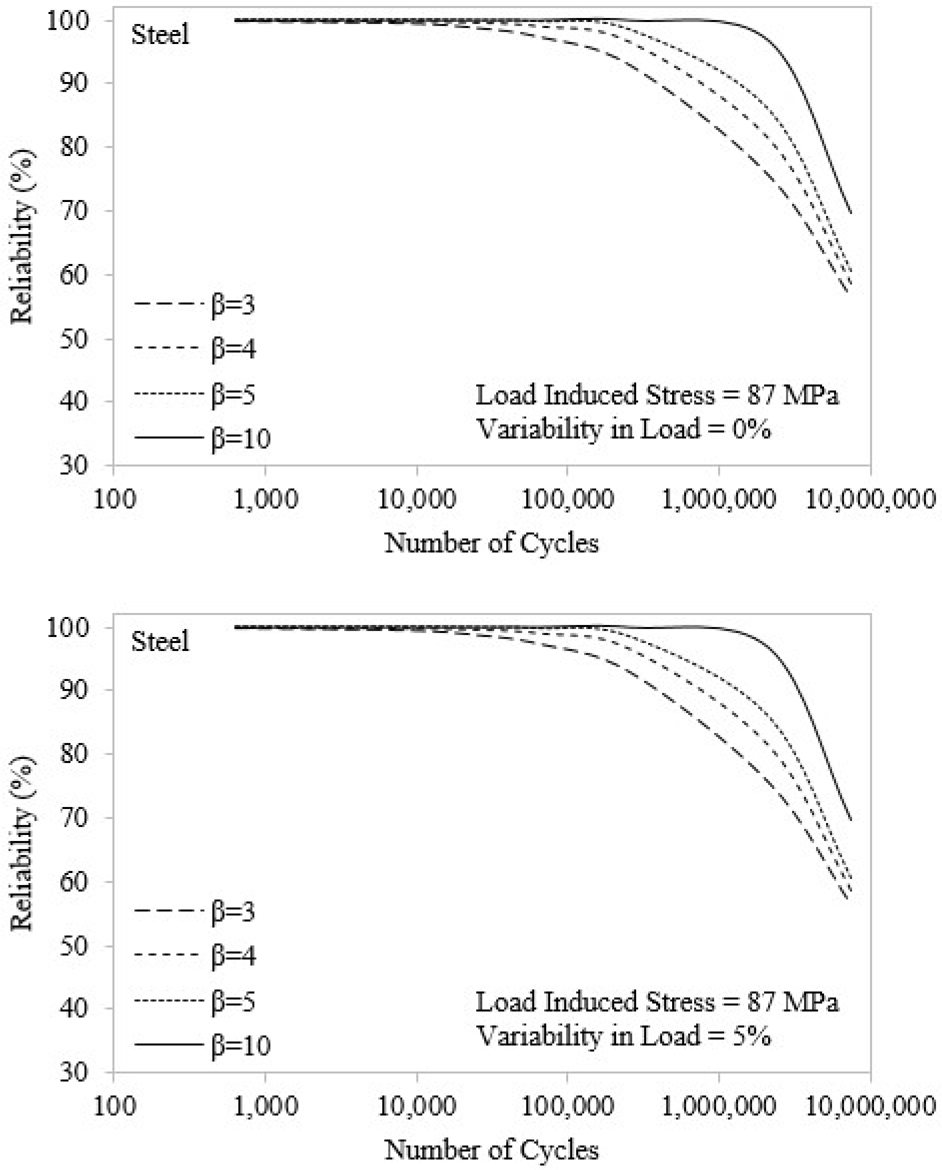

Figure 7.11 Reliability results with a load-induced stress of 87 MPa on cast steel

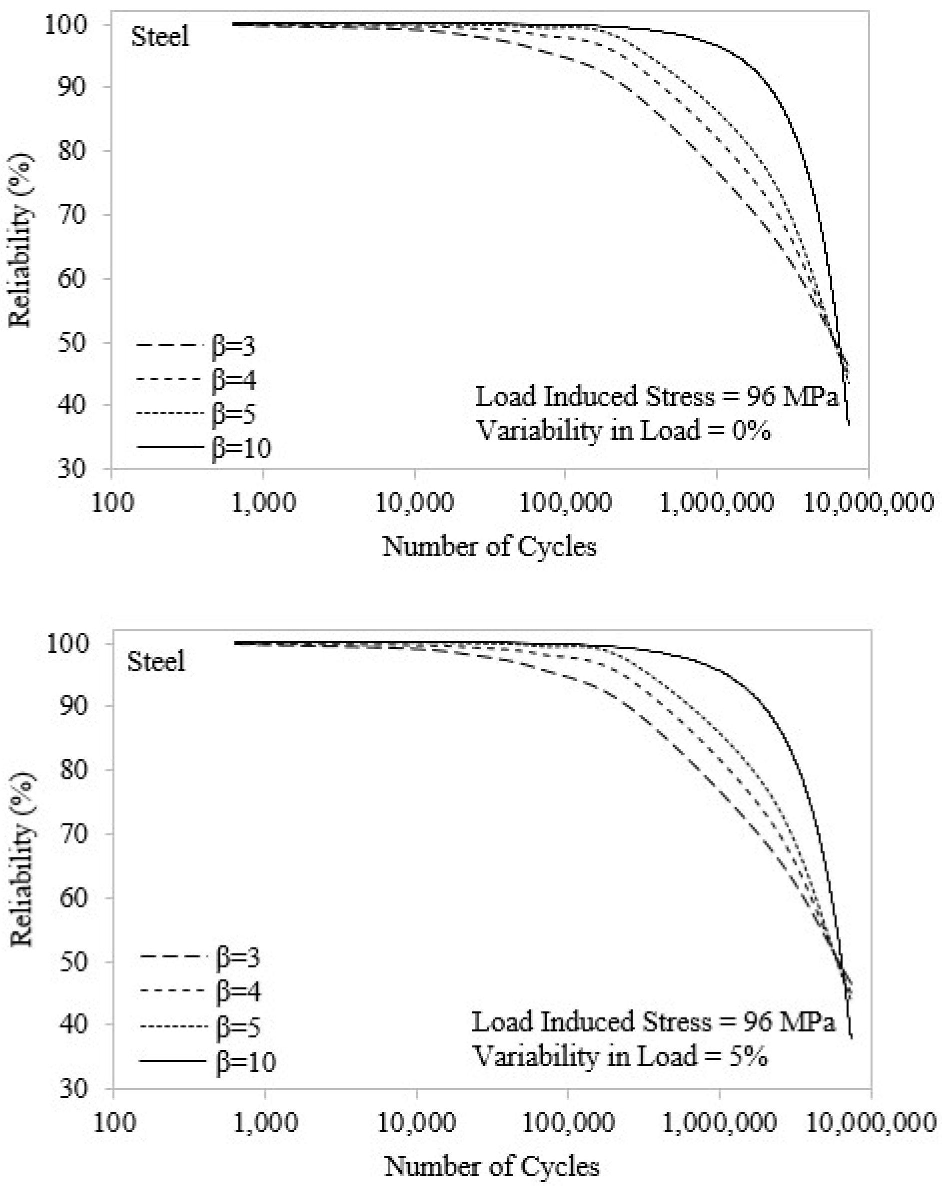

Figure 7.12 Reliability results with a load-induced stress of 96 MPa on cast steel

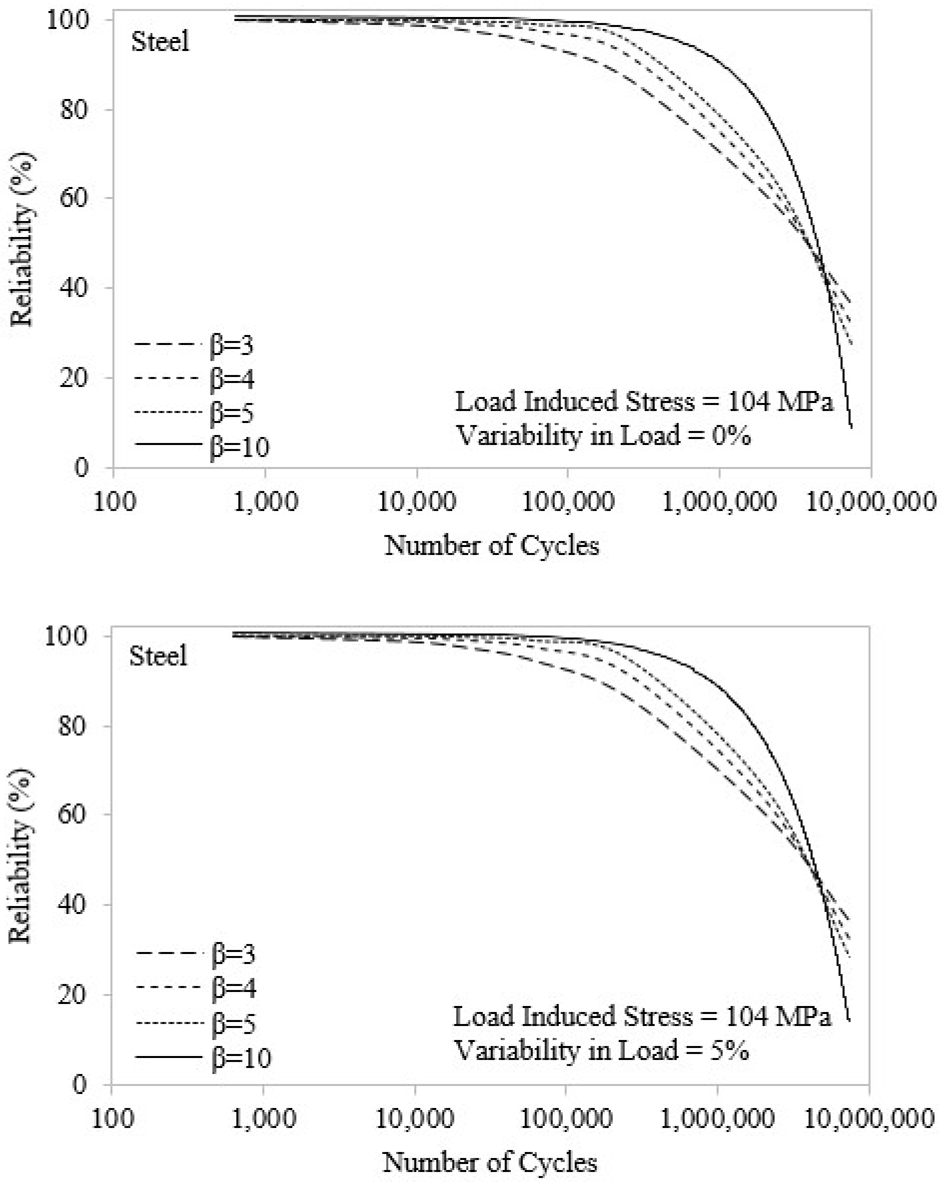

Figure 7.13 Reliability results with a load-induced stress of 104 MPa on cast steel

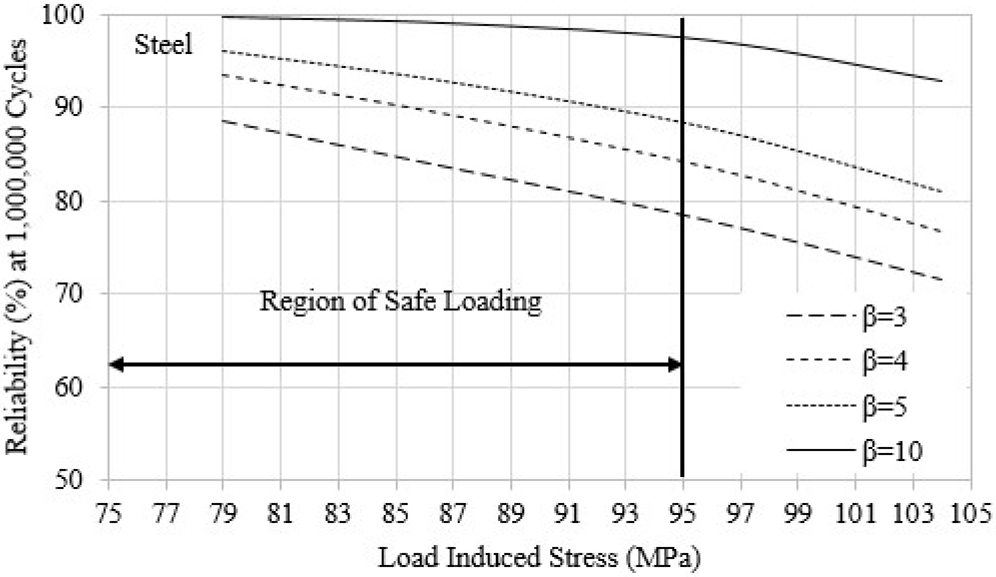

Figure 7.14 Summary of reliability results for cast steel

The reliability results for ductile iron are presented in Figure 7.15 to Figure 7.18. The load-induced stresses used in reliability computations for ductile iron are 90 MPa, 150 MPa, 200 MPa, and 250 MPa. Once again, no variability and 5% variability in the load-induced stress is considered. No significant effect of such variability is observed at lower load-induced stresses, however, for 200 MPa and 250 MPa, the effect of variability is observed in the infinite life region. In general, the overall pattern of reliability is found to be similar to that of steel such as the reliability of components for the same targeted lives is found to be decreasing with increasing load-induced stress and the higher values of β resulted in higher reliability.

A summary of reliability computations for iron is presented in Figure 7.19. The plot is similar to the one in Figure 7.14, however, a region of safe loading for ductile iron is determined this time. It is noted that, independent of β, more than 80% components survive for the infinite life at a load-induced stress of 140 MPa. Although this is a conservative estimate of reliability based on the reasons mentioned earlier, even with a higher value of

β, a maximum load-induced stress of 160 MPa results in nearly 95% survival of components for infinite life. Hence, it is appropriate to accept a safe load-induced stress up to 160 MPa to get infinite life of the ductile iron components. This is promising due to the loading scenario for moderately complex ductile iron cast part discussed in the next chapter as part of this work.

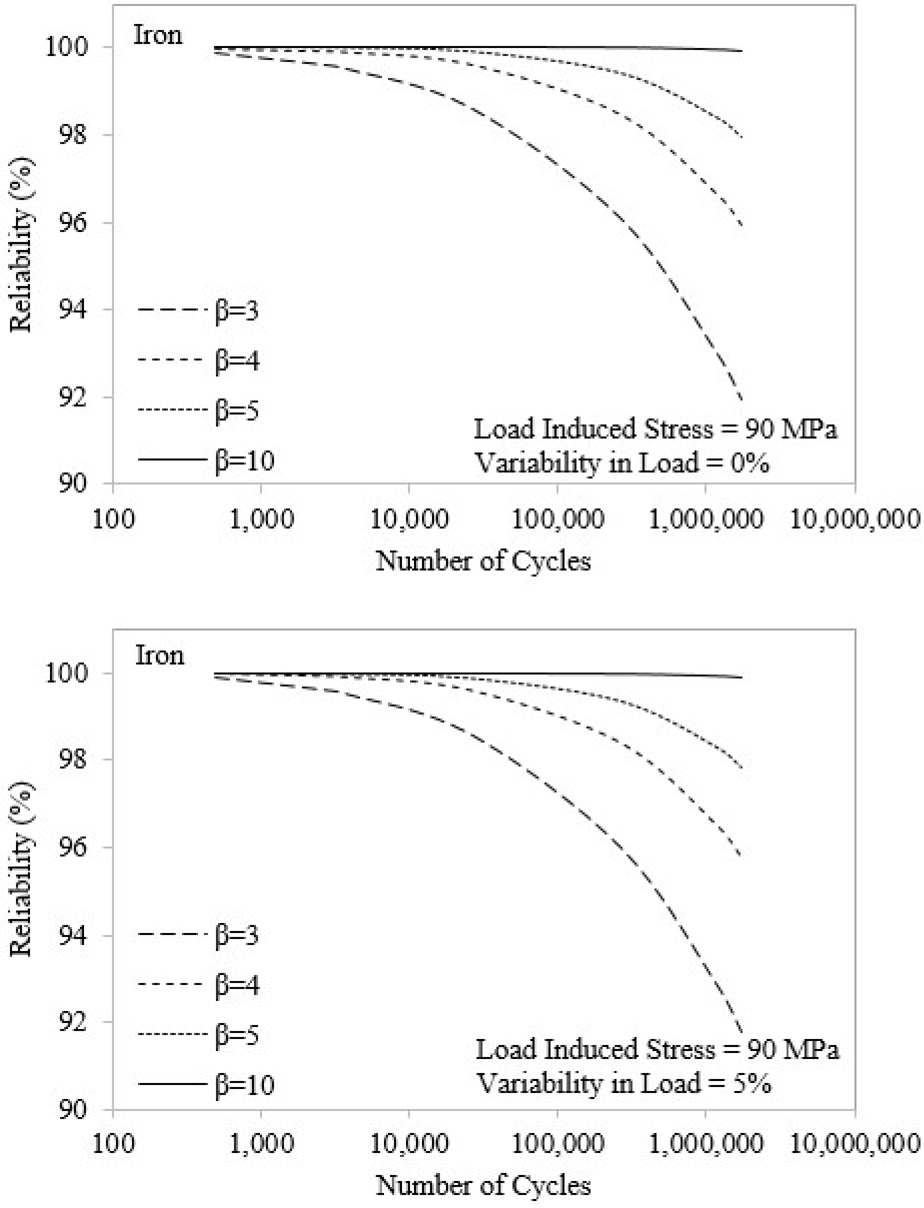

Figure 7.15 Reliability results with a load-induced stress of 90 MPa on ductile iron

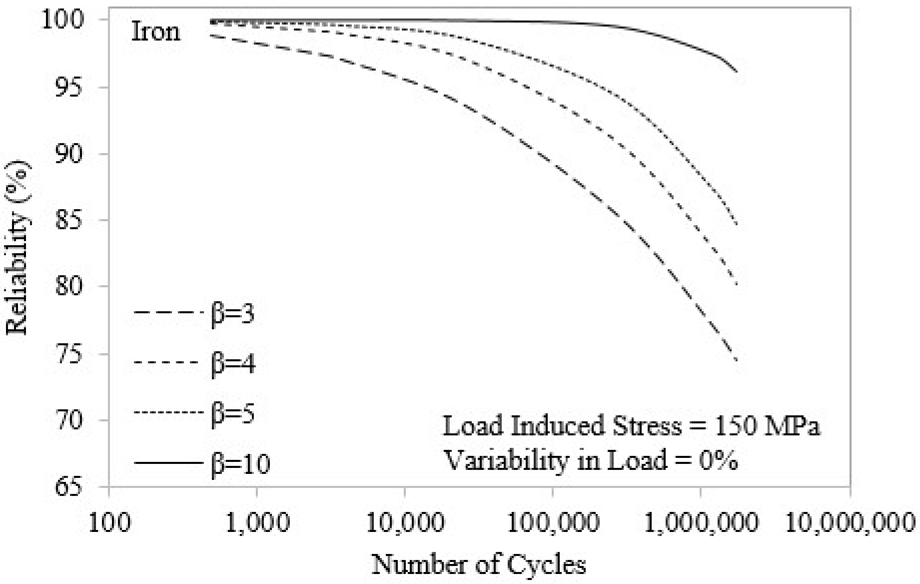

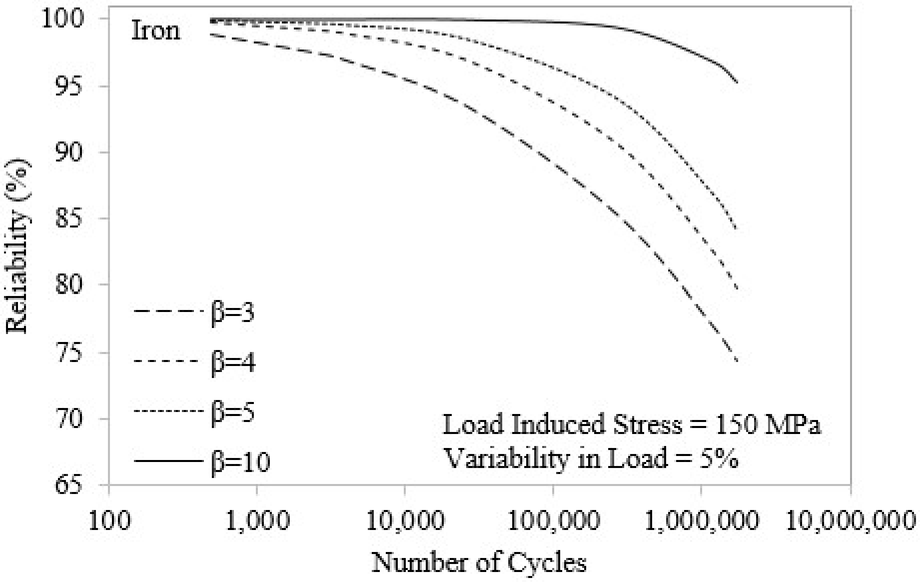

Figure 7.16 Reliability results with a load-induced stress of 150 MPa on ductile iron

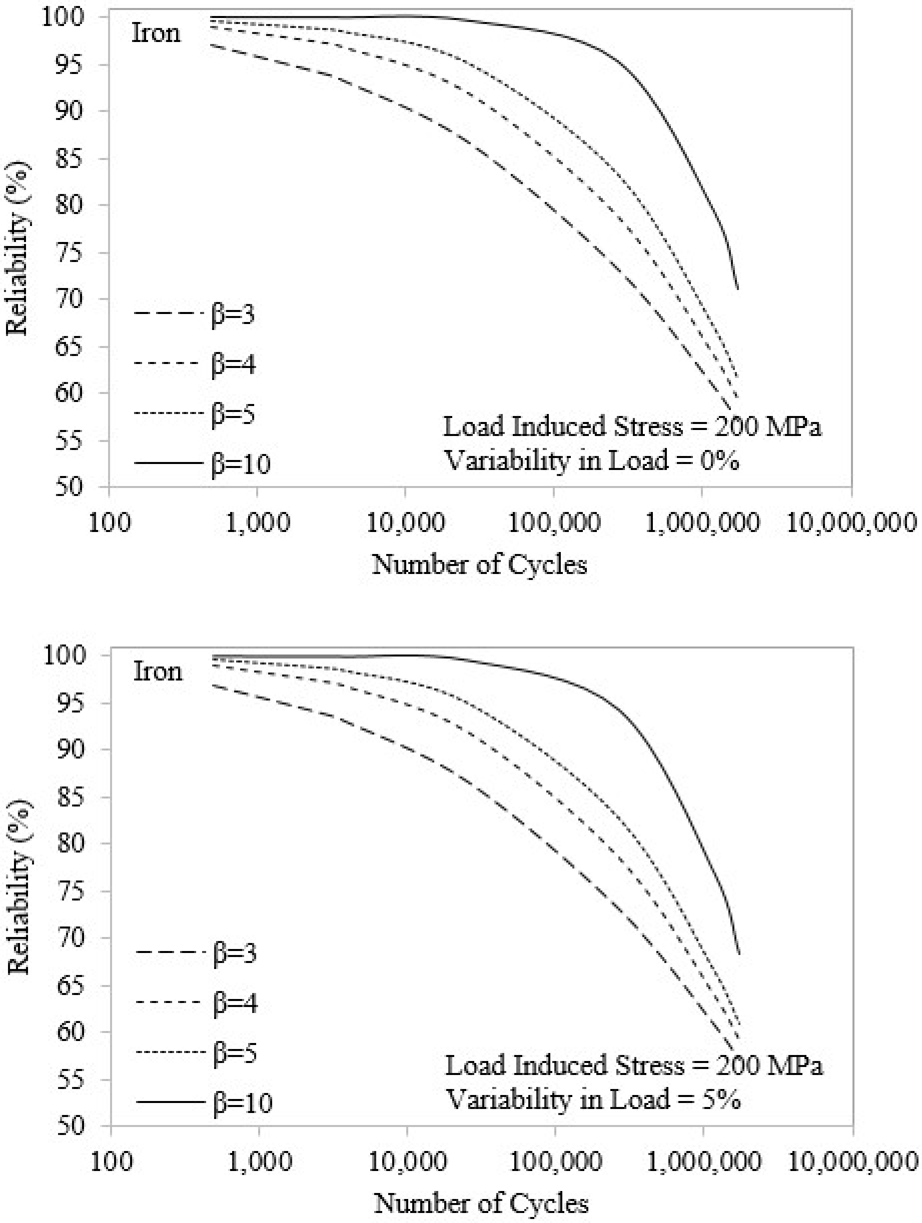

Figure 7.17 Reliability results with a load-induced stress of 200 MPa on ductile iron

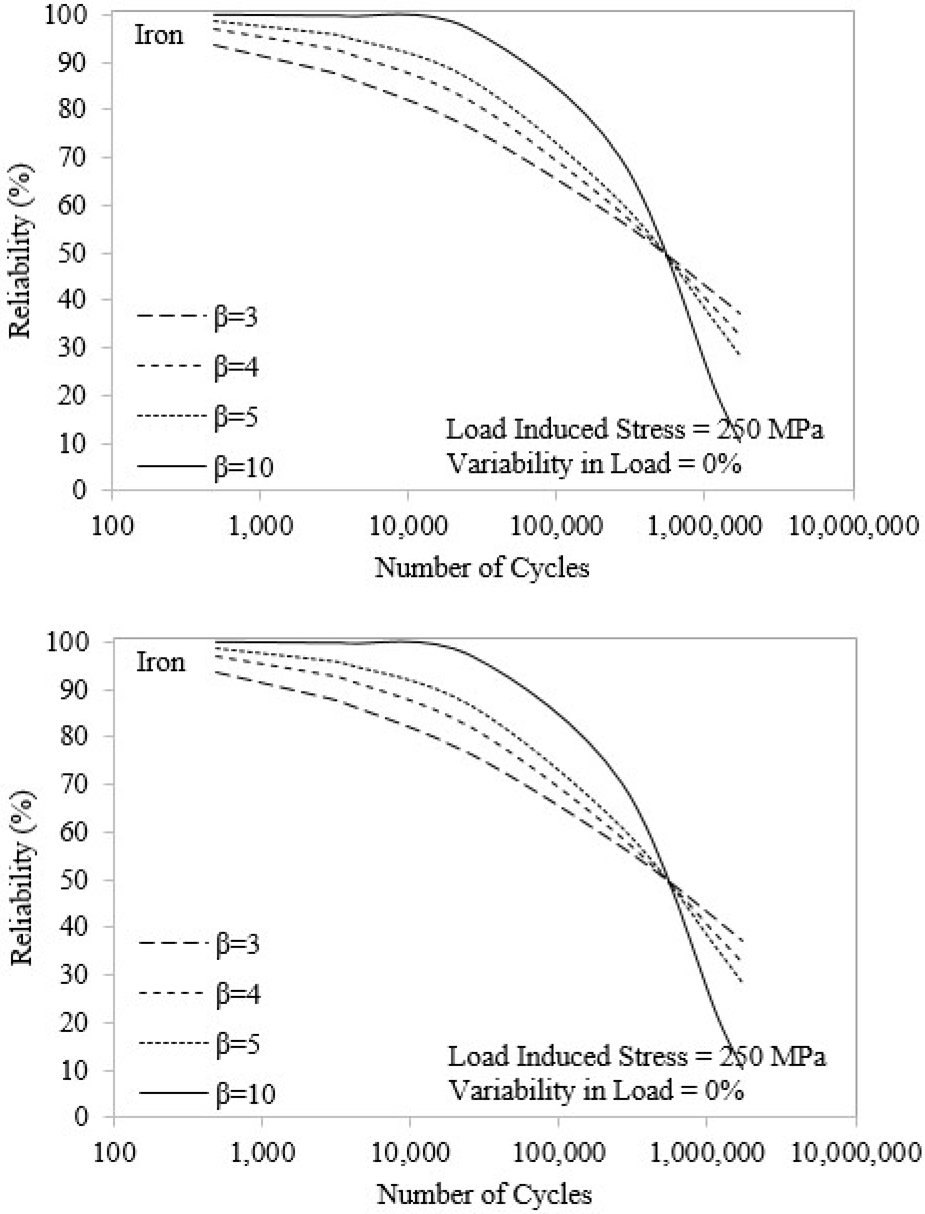

Figure 7.18 Reliability results with a load-induced stress of 250 MPa on ductile iron

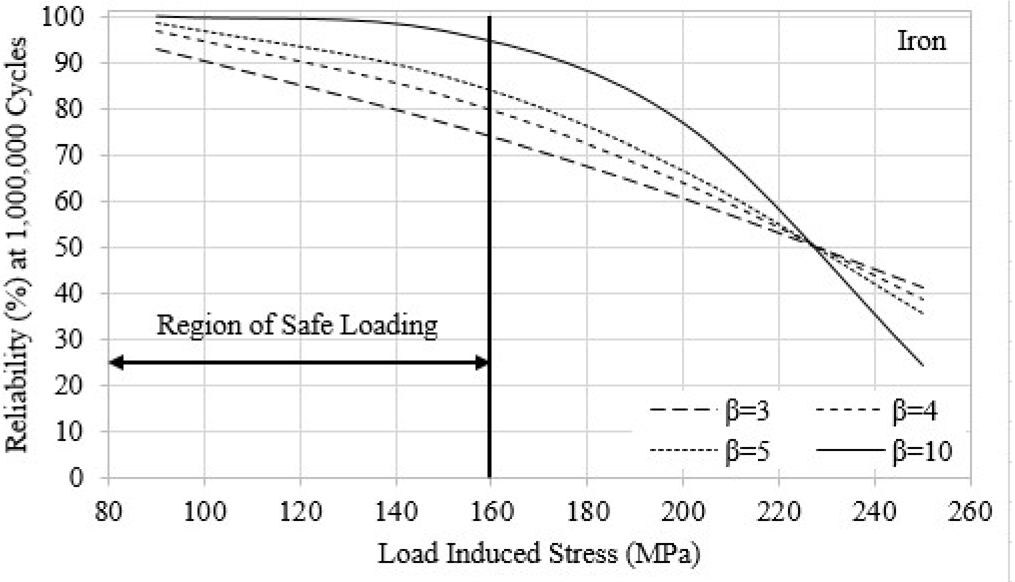

Figure 7.19 Summary of reliability results for ductile iron

7.6.2 TIME DEPENDENT LOAD-INDUCED STRESS

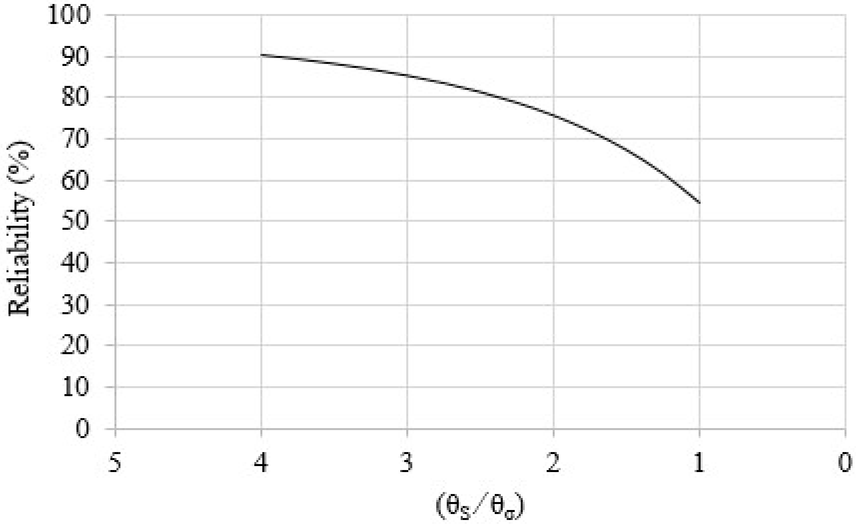

Figure 7.20 Reliability results for time-dependent load-induced stress

The result for time-dependent load induced stress is presented in Figure 7.20 which are based on Equation 7.21. Here the reliability of component is plotted against the ratio of scale parameters i.e. $\frac{\theta_S}{\theta_\sigma}$ in Weibull distribution. It can be observed that that the reliability of a component decreases with decreasing design factor. If material's strength S is assumed to be four times the mean load-induced stress σ, the components result in ~90% reliability which reduces to 54.5% in case of $S = \sigma$.

The results in Figure 7.20 are derived for $\beta_S = 2\beta_\sigma$ to reflect that the strength is Weibull distributed and load-induced stress is Rayleigh distributed. If we fix the parameters such that mean strength, S, is m times the mean stress, σ, then according to Samar et al. [102],

$$\theta_S{}^{\beta_\sigma}\Gamma\left(1+\frac{1}{2\beta_\sigma}\right)=\frac{m}{\theta_\sigma{}^{\beta_\sigma}}-\frac{1}{\beta_\sigma}\Gamma\left(1+\frac{1}{\beta_\sigma}\right) \tag{7.22}$$

for all β_σ and fixed m. Thin in turn implies that

$$\left(\frac{\theta_S}{\theta_\sigma}\right)^{\beta_\sigma{}^2}=\left[\frac{m\Gamma\left(1+\frac{1}{\beta_\sigma}\right)}{\Gamma\left(1+\frac{1}{2\beta_\sigma}\right)}\right]^{2\beta_\sigma} \tag{7.23}$$

For selected values of m and β_σ, the strength reliabilities are obtained as shown in Table 7.1. It should be noted that the value of $\Gamma\left[1+\left(\frac{x}{2}\right)\right]$ for $x = 0.00(0.001)^2$can be obtained from Mardia et al. [103] and the values of Φ. from Pearson et al. [104]. The following can be inferred from Table 7.1.

- For m = 1, the strength reliability decreases with increasing value of β_σ. This is because of the nature of the probability density function of Weibull curve i.e. the curve becomes narrower as β_σ increases. Hence, the inability of strength to meet a stress of equal mean value.

- An increase in the value of m increases the strength reliability. It also increases when both m and β_σ increased simultaneously, for example, $\beta_\sigma = 3$ (consequently β_σ = 6) and even for m = 2, the strength reliability is 0.98098.

Table 7.1 Strength reliability for $\boldsymbol{\beta_S = 2\beta_\sigma}$ and $\boldsymbol{S = m\sigma}$

β_σ/m	1	2	3	4
1	0.5906	0.7990	0.8868	0.9269
2	0.5254	0.8789	0.9669	
3	0.5096	0.9809		
5	0.4909			

7.7 DISTRIBUTIONS FITTING TO RELIABILITY ESTIMATES

The reliability results obtained in Section 7.6 represents the probability of survival at specified target lives. In order to determine the reliability models from these results, two probability distributions are fit to the reliability estimates: Log-Normal Distribution and Weibull Distribution. For distribution fitting, only the lowest load-induced stresses i.e. 79 MPa for steel and 90 MPa for iron with 5% variability in load are used

. The procedure to obtain the fitted models is as follows.

i. Linearize the reliability function.
ii. Plot the linearize reliability function.
iii. Estimate the distribution parameters.

7.7.1 LOG-NORMAL DISTRIBUTION

The reliability function for log-normal distribution is given by

$$R(t) = \phi\left[-\left(\frac{lnt - \mu}{\sigma}\right)\right]$$

or,

$$\phi^{-1}R(t) = -\frac{lnt}{\sigma} + \frac{\mu}{\sigma}$$

or,

$$\text{NormsInv}\, R(t) = -\frac{1}{\sigma} lnt + \frac{\mu}{\sigma} \tag{7.24}$$

Equation (7.24) is a linear equation with slope $m = -\frac{1}{\sigma}$ and intercept $b = \frac{\mu}{\sigma}$. These slope and intercept are used to estimate the log-normal distribution parameters μ and σ.The results for log-normal distribution fitted to reliability estimates for steel and iron are presented in Figure 7.21 and Figure 7.22 respectively. The equations of fitted models are shown which are used to determine distribution parameters. The distribution parameters are summarized in Table 7.2.

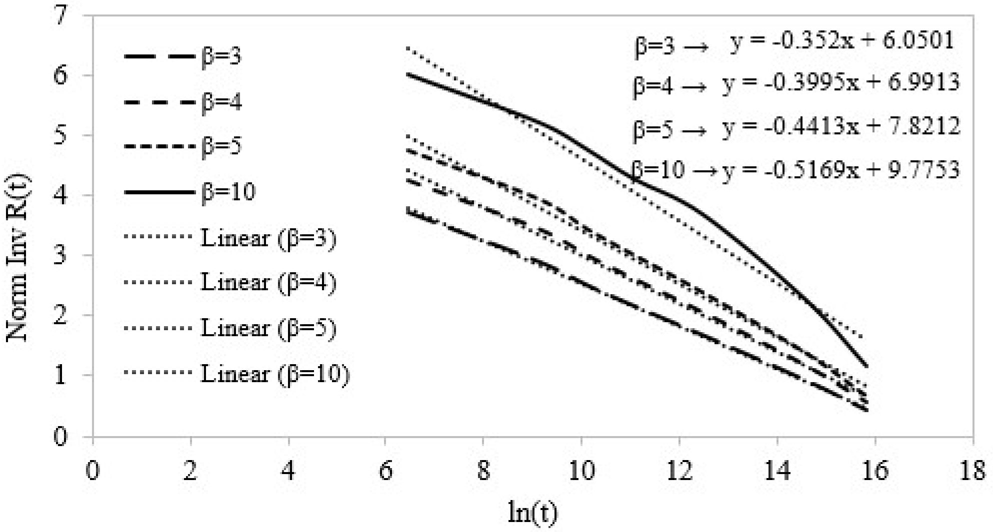

Figure 7.21 Log-Normal distribution fitted to reliability estimates of steel with load-induced stress 79 MPa

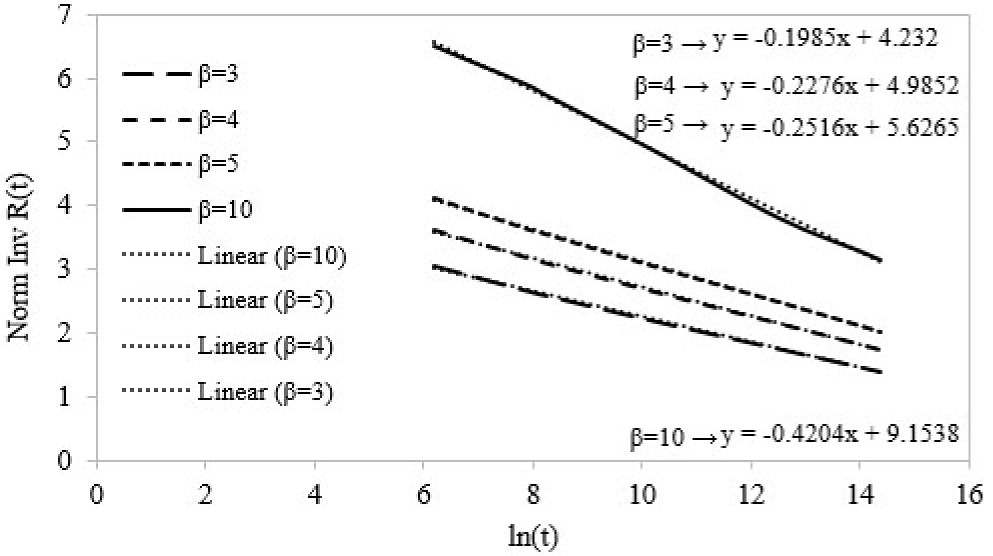

Figure 7.22 Log-Normal distribution fitted to reliability estimates of iron with load-induced stress 90 MPa

Table 7.2 Log-Normal distribution parameters fitted to reliability estimates of steel and iron

Weibull Shape Parameter for Reliability Estimate	Log-Normal Distribution Parameters			
	Cast Steel		Ductile Iron	
	μ	σ	μ	σ
β=3	17.19	2.84	21.32	5.04
β=4	17.50	2.50	21.90	4.39
β=5	17.72	2.27	22.36	3.97
β=10	18.91	1.93	21.77	2.38

7.7.2 WEIBULL DISTRIBUTION

The reliability function for Weibull distribution is given by

$$R(t) = \exp\left[-\left(\frac{t}{\theta}\right)^{\beta}\right]$$

The above equation can be linearized as follows.

$$\ln R(t) = -\left(\frac{t}{\theta}\right)^{\beta}$$

or

$$\ln\left[\ln\frac{1}{R(t)}\right] = \beta \ln\left(\frac{t}{\theta}\right)$$

or,

$$\ln\left[\ln\frac{1}{R(t)}\right] = \beta \ln t - \beta \ln \theta \qquad (7.25)$$

Equation (7.25) is a linear equation with slope $m = \beta$ and intercept $b = \beta \ln \theta$. These slope and intercept are used to estimate the Weibull distribution parameters β and θ.The results for Weibull distribution fitted to reliability estimates for steel and iron are presented in Figure 7.23 and Figure 7.24 respectively. The equations of fitted models are shown which are used to determine distribution parameters. The distribution parameters are summarized in Table 7.3.

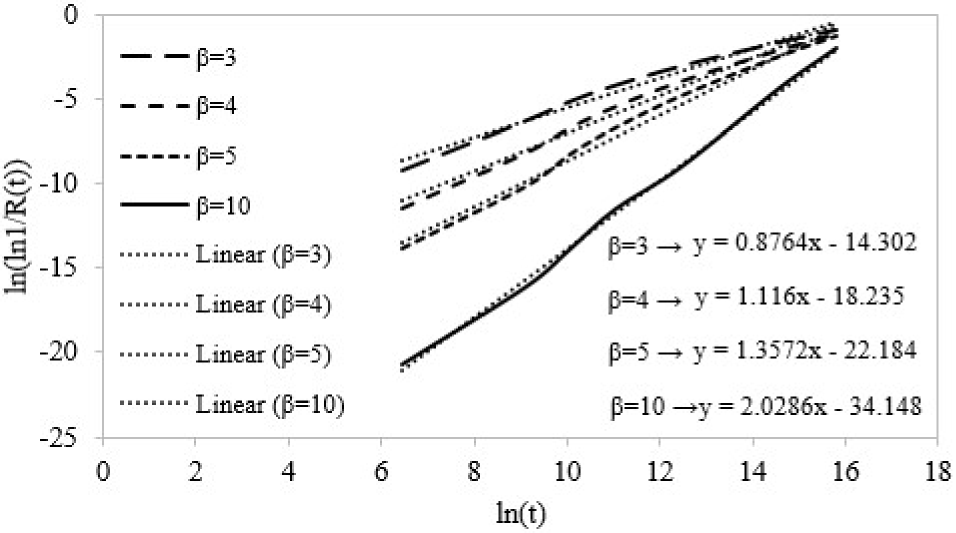

Figure 7.23 Weibull distribution fitted to reliability estimates of steel with load-induced stress 79 MPa

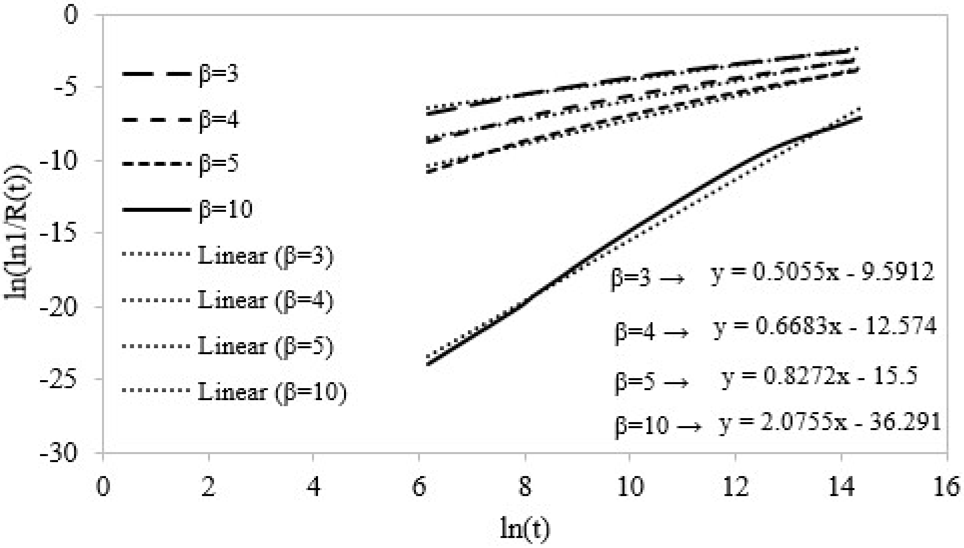

Figure 7.24 Weibull distribution fitted to reliability estimates of iron with load-induced stress 90 MPa

Table 7.3 Weibull distribution parameters fitted to reliability estimates of steel and iron

Weibull Shape Parameter for Reliability Estimate	Weibull Distribution Parameters			
	Cast Steel		Ductile Iron	
	β	θ	β	θ
β=3	0.876	15464922	0.5055	173847566
β=4	1.116	13564126	0.6683	148323089
β=5	1.357	12178806	0.8272	137331879
β=10	2.082	100931406	2.0755	39248555

7.8 CONCLUDING REMARKS

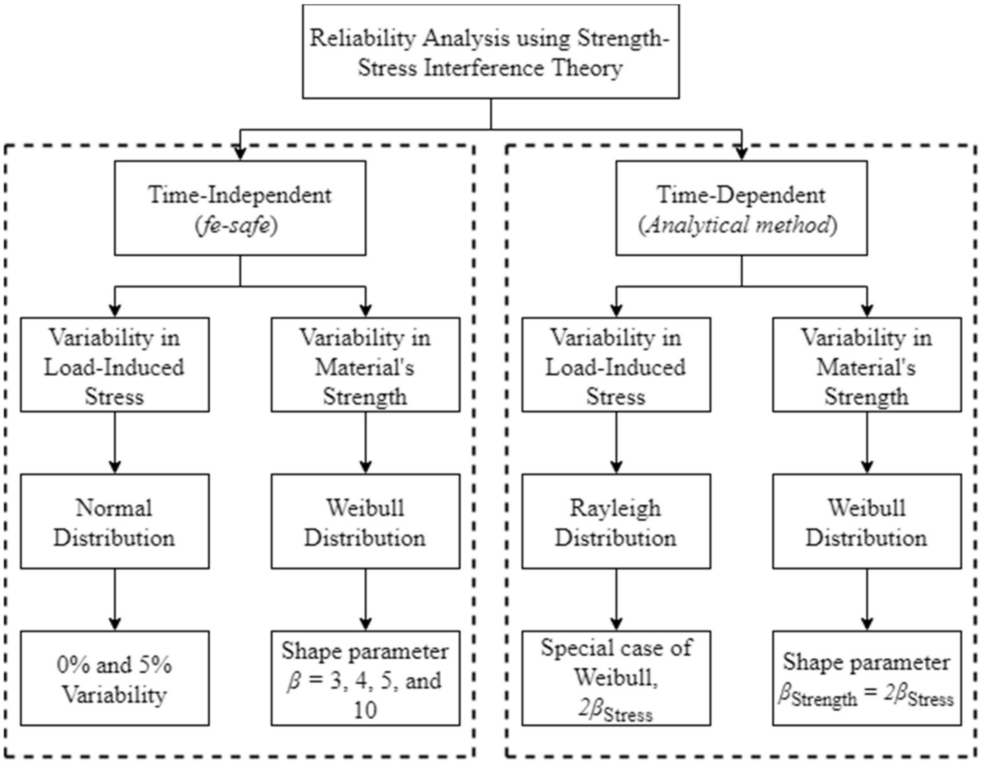

Figure 7.25 Graphical summary of reliability assessment

This chapter presents the reliability of steel and iron specimens under different scenarios. Strength-stress interference theory is used to determine the time-independent and time dependent reliability. Four load-induced stresses are used to determine reliability curves for each material in case of time-independent reliability analysis. Load-induced stress is modeled through normal distribution with zero and 5% variability, whereas, the variability in material’s strength is modeled using Weibull distribution. For time-dependent reliability analysis, the load-induced stress is modeled through Rayleigh distribution. It is observed that reliability of the components for infinite life drops down with increasing load-induced stresses. The overall results indicated a region of safe loading for each material i.e. 95 MPa for cast steel and 160 MPa for ductile iron. The reliability estimates are fitted to log-normal and Weibull distributions and the models are developed to estimate reliability at any life (number of cycles). A graphical summary of reliability assessment is presented in Figure 7.25.

CHAPTER 8

SIMULATION-BASED METHODOLOGY:

APPLICATION TO ACTUAL CAST PARTS

8.1 INTRODUCTION

This chapter presents the applications of the developed simulation based methodology from Chapter 4 to Chapter 7 on selected moderately complex cast parts. Since, the methodology is experimentally validated for simple cast parts, which are tensile and fatigue specimens in the present work, the forth coming analysis on actual parts is limited to simulations. Two real cast parts are selected for this study, one from the ASTM A216 WCB steel and the other from GGG-40 ductile iron. The details from mold design optimization to reliability assessment of the selected parts are presented in the following sections.

8.2 CASE STUDY # 1: SPRING FLAP

Spring flap is a component used in automotive suspension systems. The selected spring flap for this study is shown in Figure 8.1. This spring flap is originally produced by forging steel as it is subjected to higher loads while in service. The main objective is to determine the quality and performance of this spring flap if it is produced using casting process. Therefore, it is decided to use simulations for mold design and optimization, performance evaluation, and reliability assessment of this component.

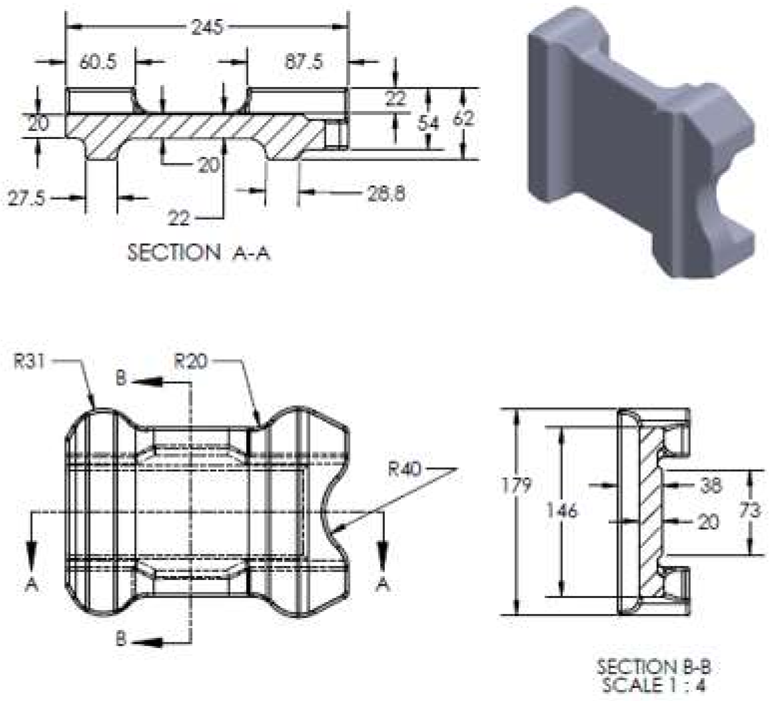

Figure 8.1 Spring Flap

8.2.1 MOLD DESIGN OPTIMIZATION USING MAGMASOFT

8.2.1.1 Initial Mold Design

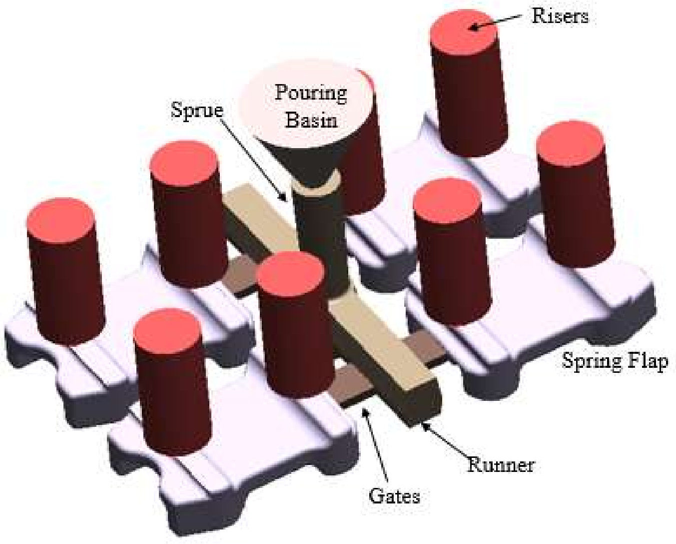

Figure 8.2 Initial casting layout for spring flap

The initial mold design for casting spring flap is prepared using the standards, in-house experience and the expertise of foundrymen. A multi-cavity mold is design to cast four flaps at the same time as shown in Figure 8.2. In this design, a gate-runner approach is used where each of the spring flap is choked by a separate gate. The initial design contains pouring basin, sprue with a well at the bottom, runner, gates, castings, and risers. Top-risers are used due to their high efficiency [105]. After preparing the initial casting layout in Solidworks, it is imported to MAGMASoft for casting simulation. The casting layout is discretized using a cubical mesh containing 1,962,156 volume elements. The materials properties for ASTM A216 WCB and mold material (Furan) are already presented in Table 4.1 and Table 4.3 respectively. The initial temperature of the melt and the mold are 1630 °C and 20 °C respectively. The pouring time of the melt is specified to be 20 seconds and the feeding effectivity determined by the software is 30%. The mold design is simulated for filling and solidification behavior, generation and distribution of residual stresses, and to determine the defects, particularly the location and magnitude of porosities.

The simulation results for initial mold design are presented in Figure 8.3 to Figure 8.7. Figure 8.3 shows the temperature profile within the mold at different stages of solidification. The temperature contour plots indicated that the solidification begins with the thin sections in the flap. This is also confirmed through results of percentage fraction solid shown in Figure 8.4. At 75% solidification as shown in Figure 8.4 (c), most of the regions in flap are solidified except the thicker sections. With initial mold design, the resulting residual stresses are quite higher i.e. ~182 MPa as shown in Figure 8.5. Moreover, these stresses are found to be concentrated in the load bearing region of the flap. Such high residual stresses brings about a need to improve the cooling and solidification sequence in cast spring flaps.

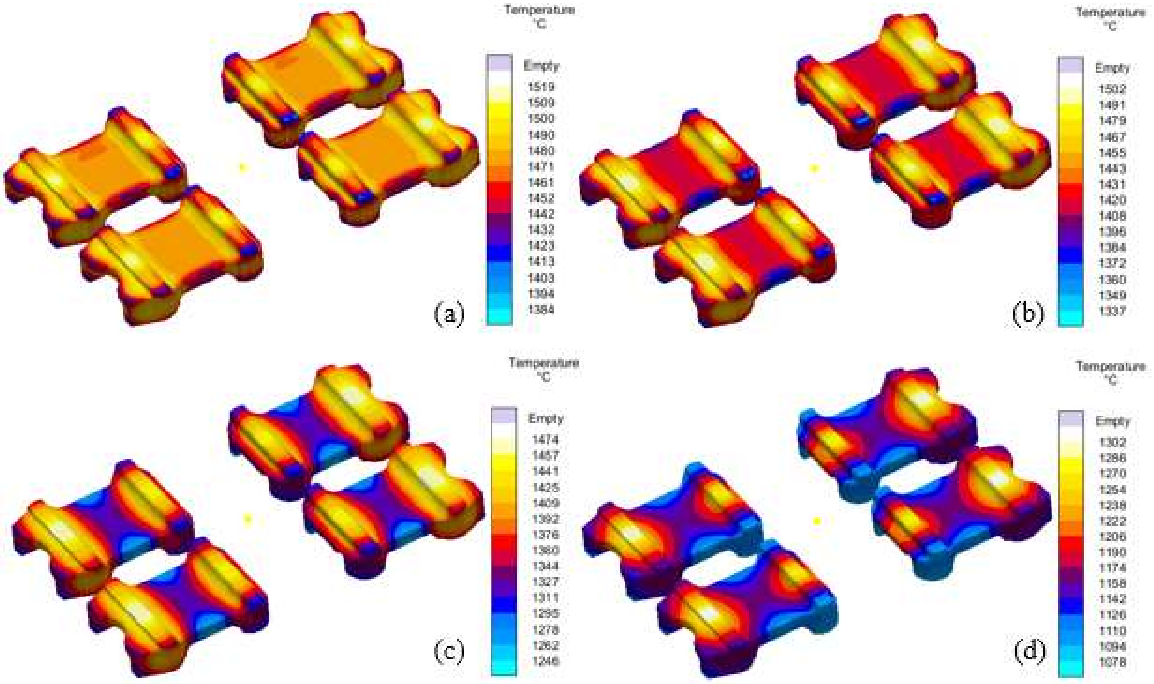

Figure 8.3 Temperature profile within the mold during solidification (a) 25%, (b) 50%, (c) 75% and (d) 100%

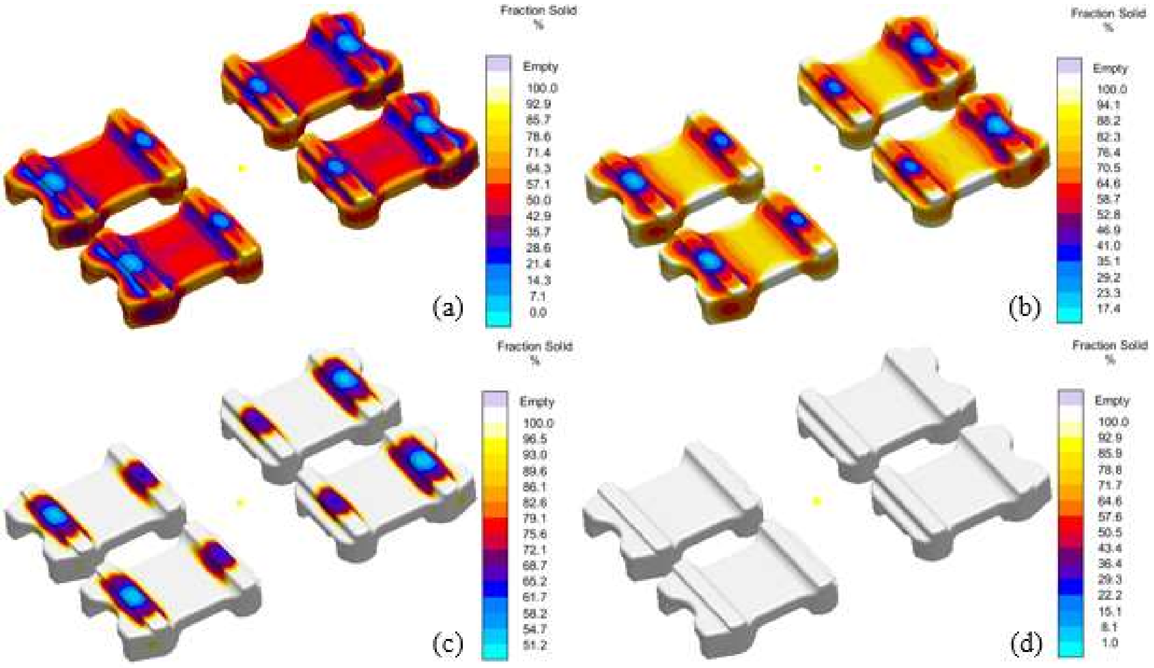

Figure 8.4 Solidification sequence (a) 25%, (b) 50%, (c) 75% and (d) 100%

In terms of defects, the first observation is the presence of hotspots as shown in Figure 8.6. These hotspots should be minimized or eliminated in order to avoid shrinkage porosities. Figure 8.7 shows the results of porosity predicted in casting simulations. Figure 8.7 (a) shows the surface porosity in spring flaps at different locations. Microporosity results are shown in Figure 8.7 (b) and it appears to be distributed over the entire casting region. The porosity is not only observed at the surface of castings, rather, there is also internal porosity in the slaps as revealed in the cut-plane view of total porosity as shown in Figure 8.7 (c). Therefore, it is decided to optimize the mold to minimize the residual stresses, hotspots and porosities in the cast spring flaps.

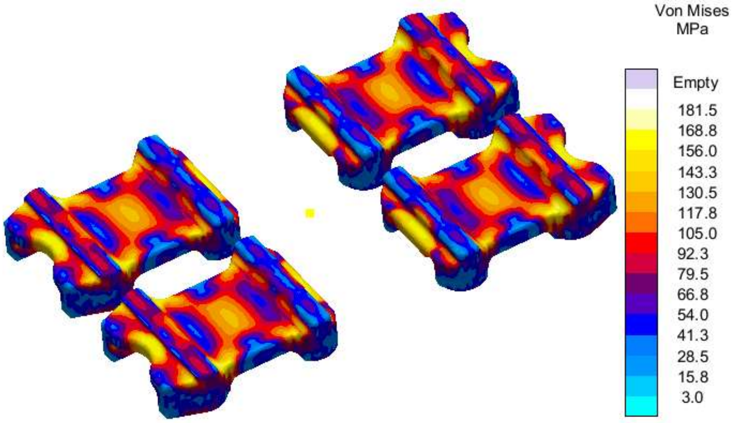

Figure 8.5 Residual stress distribution at ejection using initial mold design

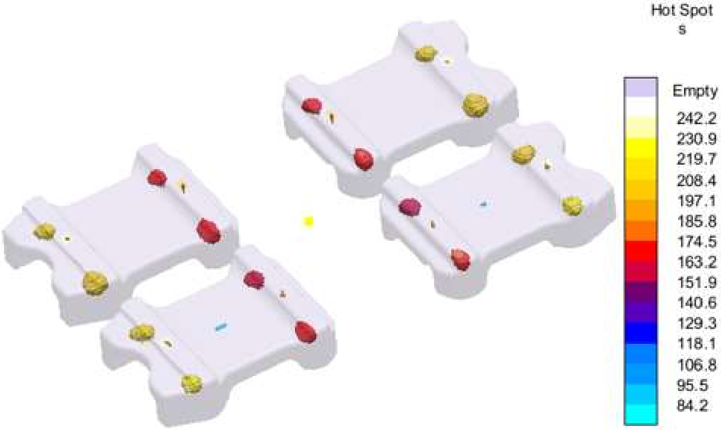

Figure 8.6 Hotspots in cast spring flaps using initial mold design

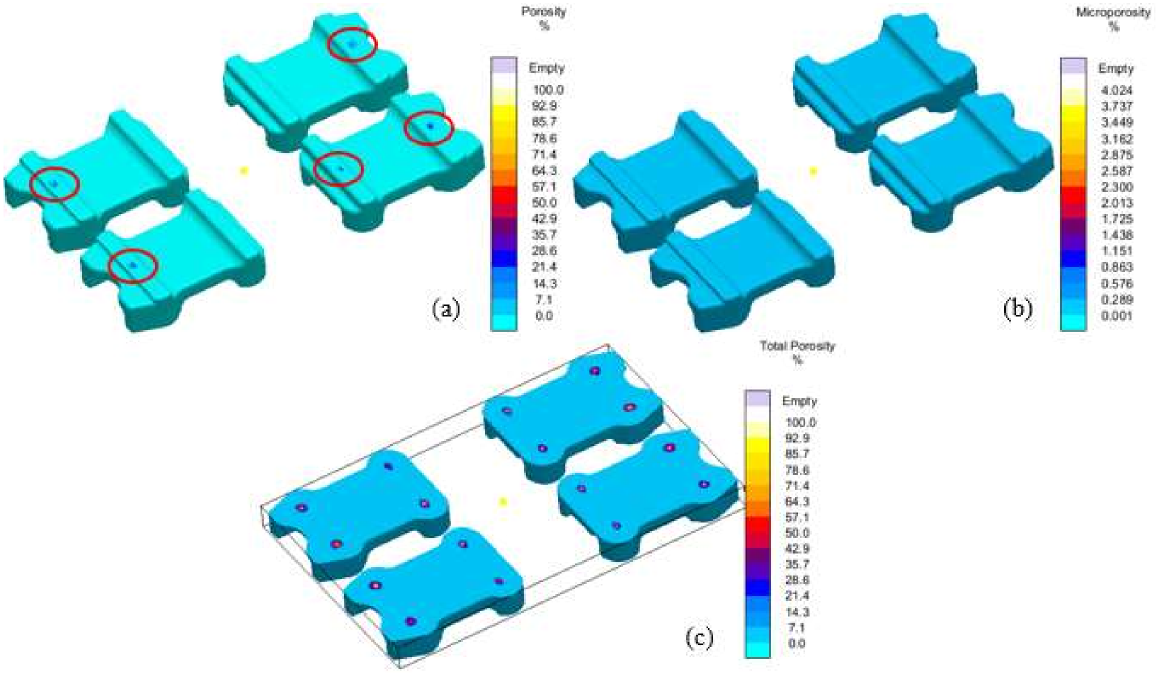

Figure 8.7 (a) Porosity, (b) Microporosity, and (c) Total porosity predictions using initial mold design

8.2.1.2 Optimized Mold Design

The mold design optimization started with improved cooling and directional solidification using chills in the mold. In total, 16 steel chills are used (4 for each spring flap) which are attached to positions such that the solidification starts from thick sections of the castings. With these chills it is expected to have improved cooling in the mold which can result in reduced residual stresses. The hotspots in castings can be reduced using exothermic sleeves around the riser, so that the solidification in riser could be delayed and shrinkage porosities can be minimized. A breaker core is used at the bottom end of the riser to avoid early freezing of riser neck and this also facilitates in removal of the riser from the casting during cleaning. The modified mold design with auxiliary components is shown in Figure 8.8. This modified casting layout is simulated using MAGMAsoft. The casting layout is discretized using a cubical mesh containing 2,011,764 volume elements. Similar material properties and process parameters are used as in the initial mold design. There is no change in pouring time as the overall weight of the casting remains unchanged. Once again, filling, solidification, and stress simulations are run to observe the filling and solidification sequence and to predict the defects such as hotspot and porosity.

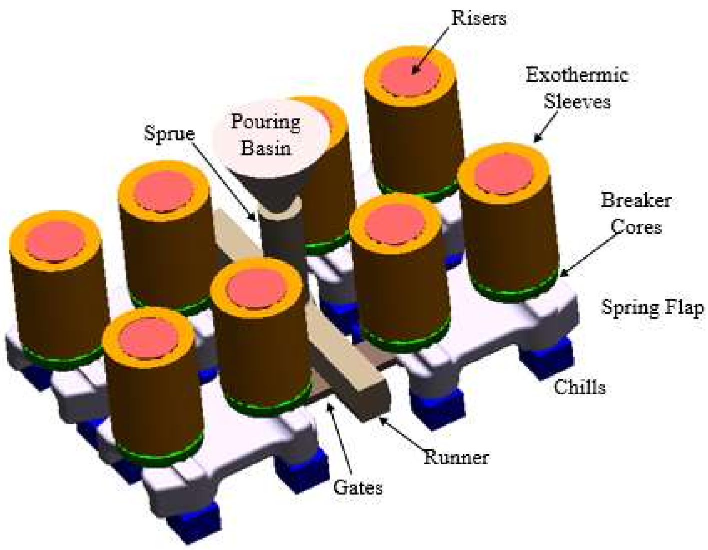

Figure 8.8 Optimized casting layout for spring flap

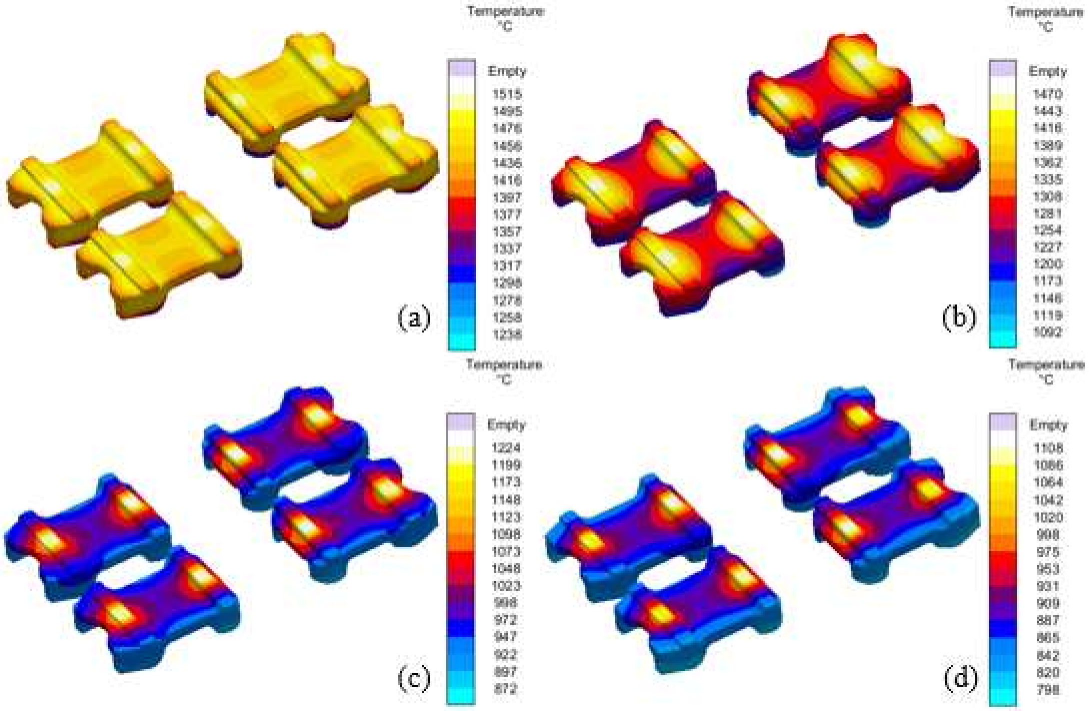

Figure 8.9 Temperature profile within the mold during solidification (a) 25%, (b) 50%, (c) 75% and (d) 100%

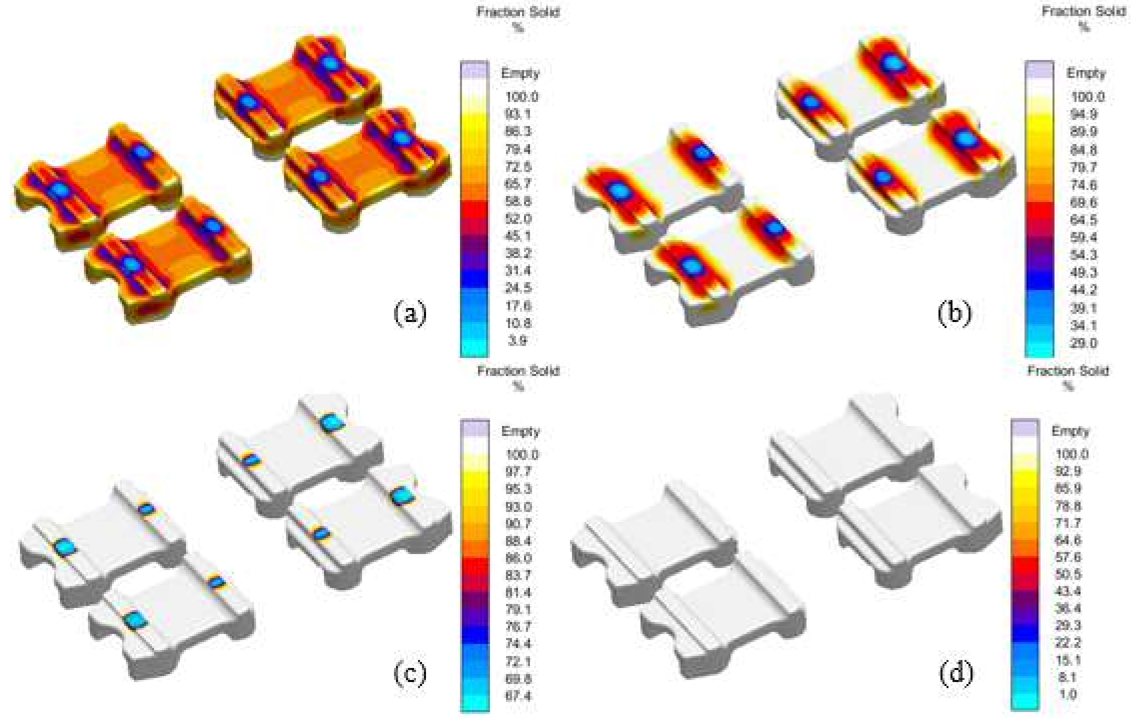

Figure 8.10 Solidification sequence (a) 25%, (b) 50%, (c) 75% and (d) 100%

The simulation results for optimized mold design are presented in Figure 8.9 to Figure 8.13. It can be observed the regions of the flap attached to chills have minimum temperature in Figure 8.9 (a) to (d). This suggests initiation of cooling and solidification from those regions. The solidification sequence in Figure 8.10 also confirmed the solidification began in the regions close to chills and most of the casting is solidified at around 75% solidification. The resulting residual stresses are reduced about 3 times when compared to initial mold design as shown in Figure 8.11. Moreover, the load bearing regions are found to be with minimum residual stresses. The use of exothermic sleeves with breaker cores in the optimized mold design completely eliminated the hotspots as shown in Figure 8.12. As a results of this, the porosity is also minimized as observed in Figure 8.13. The optimized mold design resulted in no surface porosity as shown in Figure 8.13 (a). Figure 8.13 (b) represents the microporosity, which is distributed over the entire casting but with a lower magnitude as compared to what is observed in the initial mold design. The total porosity results in Figure 8.13 (c) shows some traces of porosity within the flaps, however, the amount of porosity is fairly acceptable to consider this mold design for actual castings.

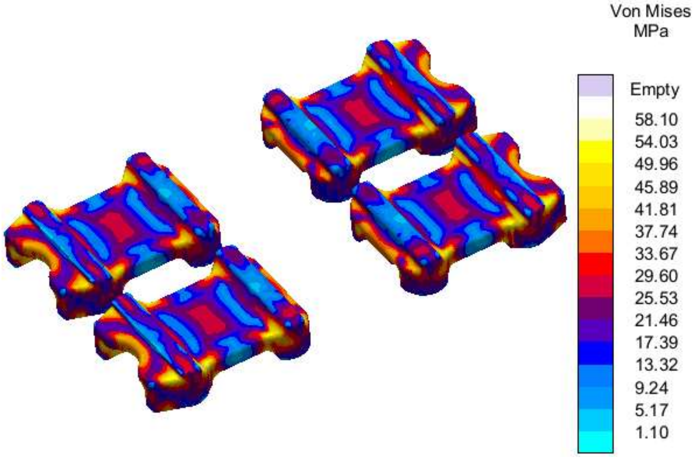

Figure 8.11 Residual stress distribution at ejection using optimized mold design

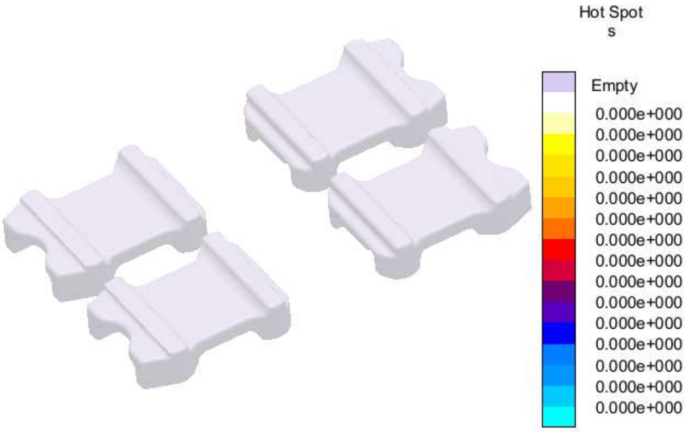

Figure 8.12 Hotspots in cast spring flaps using optimized mold design

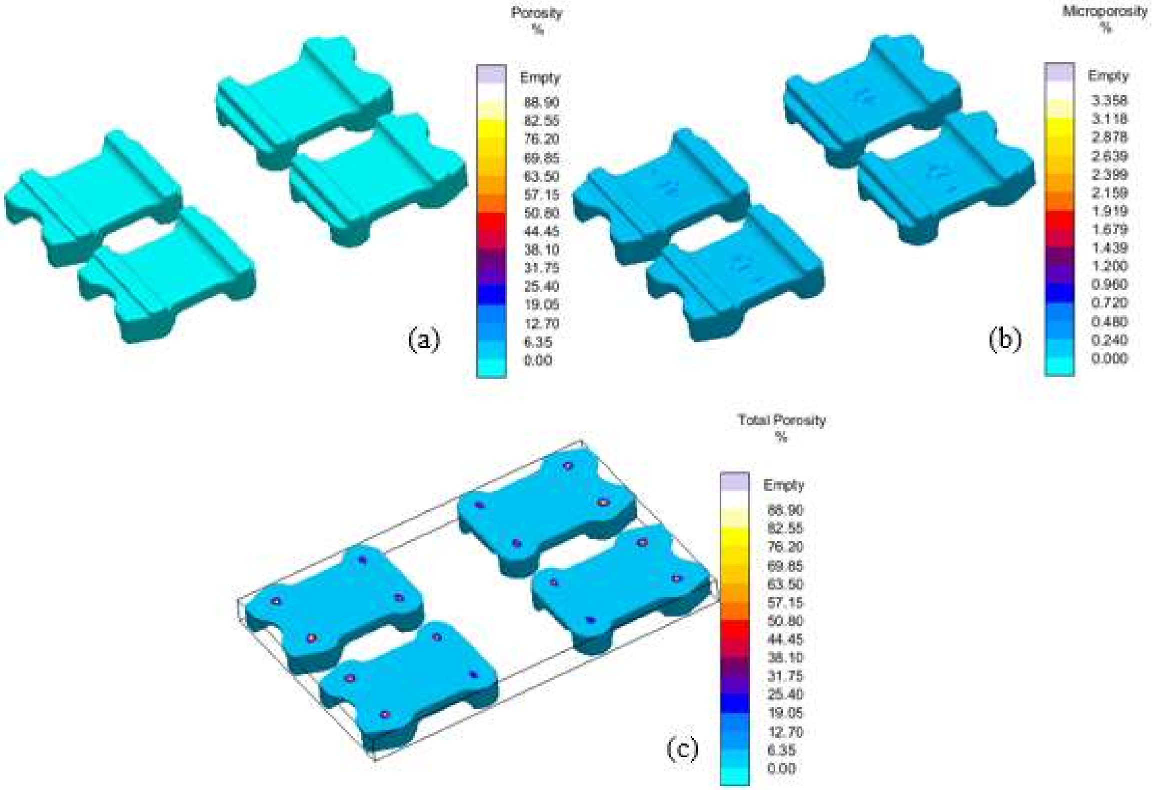

Figure 8.13 (a) Porosity, (b) Microporosity, and (c) Total porosity predictions using optimized mold design

8.2.2 FINITE ELEMENT MODELING AND FATIGUE LIFE PREDICTION

The finite element modeling of spring flap is done using ABAQUS standard. Since, a multi-cavity mold is designed and optimized to cast spring flap, it is decided to use one spring flap for FE analysis and subsequent life prediction. The optimized mold design contains some porosity in each spring flap which has to be included in FE analysis. The predicted porosity using optimized mold designed is incorporated to FE simulation using MAGMAlink. Spring flap geometry is imported to ABAQUS and discretized using a 10 node quadratic tetrahedron (C3D10) elements as shown in Figure 8.14. The resulting mesh contained 54,915 elements and 82,832 nodes, when a 6 mm spacing is used. Experimenting with further mesh refinement shows no significant changes in the results. The mesh shown in Figure 8.14 is then imported to MAGMASoft using MAGMAlink and the predicted porosity is mapped to FEA nodes. The nodal porosity is then exported and integrated to ABAQUS simulations using the same procedure described earlier in Section 6.3.

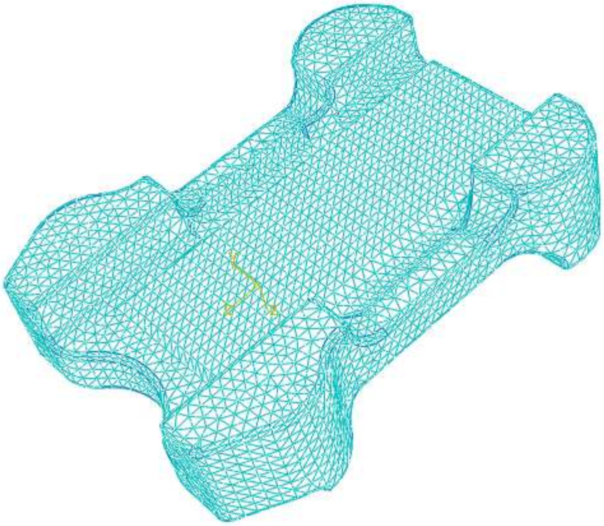

Figure 8.14 Spring flap mesh generated in ABAQUS

Next, the boundary conditions for FE simulations are carefully decided to replicate the actual conditions of spring flap in service. The boundary conditions are set in consultation with MASABIK foundry based upon the information provided by the end-user. As discussed earlier, the flap is used in suspension system where an axle rests on it due to which a load of ~70 kN is applied to the flap. The maximum load which can be applied to flap, as provided by the end-user, is ~90 kN. The thick sections of the flap are fixed using an encastre boundary condition, whereas, load is distributed over the surface where the axle and flap are in contact. Figure 8.15 shows the boundary conditions used in FE simulations.

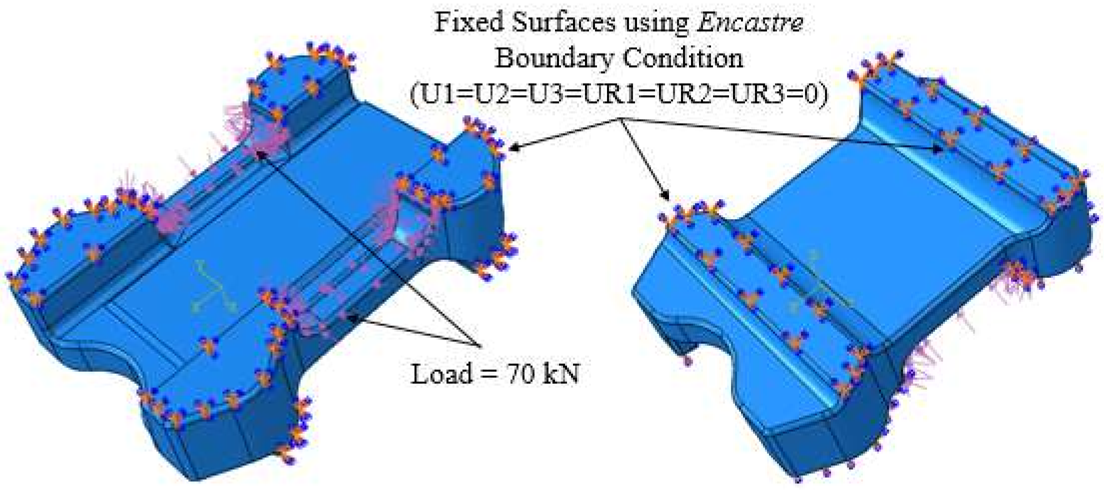

Figure 8.15 Boundary conditions for FE simulation of spring flap

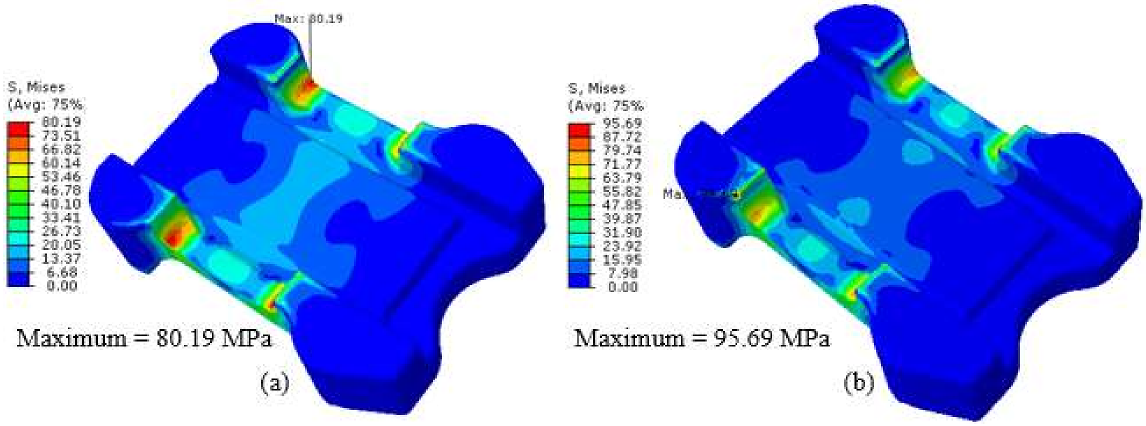

Figure 8.16 Von Mises stress results in spring flap (a) without porosity and (a) with porosity

The Von Mises stress results for the spring flap with the above boundary conditions are presented in Figure 8.16. Figure 8.16 (a) shows the stress field without porosity i.e. Sound spring flap. In this case, the maximum load induced-stress is found to be ~80MPa which gives a safety factor of 4.4 for steel with a yield strength of 355 MPa. With porosity, the load-induced stress is increased to ~96 MPa, thereby, resulting in a safety factor of 3.7. The location of maximum Von Mises stress is also shown in Figure 8.16 (a) and (b). Using the fatigue endurance limit of 141 MPa as given in Table 6.3, the factor of safety for the highest value of stress is ~1.5. The safety factors determined above are deterministic which involves no randomness in material's strength and load-induced stress. Therefore, probabilistic approach will be used here, similar to Chapter 7, to determine the reliability of the spring flap.

The next step in the analysis is to predict the fatigue life with and without porosity. The porosity will be of concern if it lowers the fatigue life below 10^6 cycles which is set as the runout condition in the present work. Fatigue life is predicted using fe-safe using the method discussed earlier in Section 6.3. The results of fatigue life prediction are presented in Figure 8.17 (a) and (b). The minimum fatigue life with and without porosity are found to be more than 10^6 cycles which suggests the survival of the part in these predictions. Hence, these results confirms the robustness of optimized mold design for spring flaps.

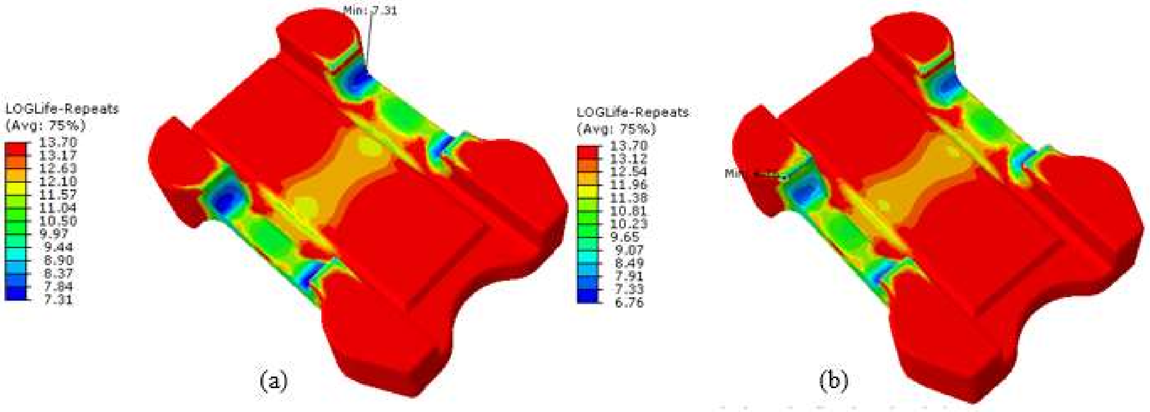

Figure 8.17 Fatigue life prediction using fe-safe (a) without porosity and (b) with porosity

8.2.3 RELIABILITY ASSESSMENT

The reliability of spring flap is estimated using the methodology described in Chapter 7. The strength-stress interference method is used to calculate the reliability at specified target lives. Two load-induced stresses are used for calculations as the normal load on the flap is 70kN and the maximum load capacity provided by MASABIK foundry and end-user is 90kN. Therefore, the flap with porosity is simulated for stresses at these two loading conditions. The resulting stress fields are presented in Figure 8.18. These stresses are then used in fe-safe for reliability computations. A 5% variability in load-induced stresses is considered and the material variability is represented by Weibull distribution with varying shape parameter β.

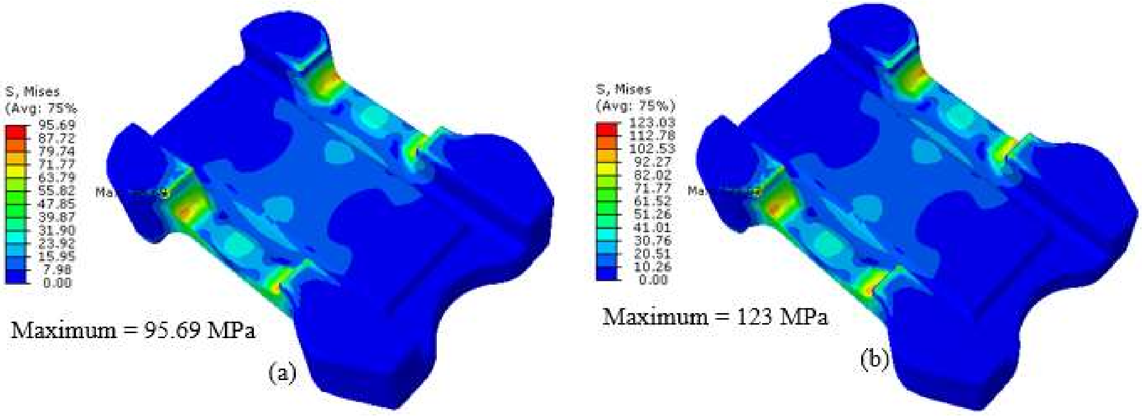

Figure 8.18 Von Mises stress in spring flap with porosity at (a) 70kN and (b) 90kN

The resulting reliability curves for both scenarios are presented in Figure 8.19. Figure 8.19 (a) shows the reliability results for a load of 70 kN on spring flap resulting in a load-induced stress of 96 MPa. It can be observed that the component shows nearly 95% reliability until 10^6 cycles with β =10. This higher β represents the actual scenario where the parts are produced using optimized mold with minimized porosity and variability in the product. If the parts are not produced using optimized mold it would result in reliability estimates using a lower β such as 3 or 4. In that case, 60-70% of the components survive until the infinite life. With maximum load of 90 kN and the corresponding load-induced stress of

123 MPa, the reliability is significantly compromised. It can be observed in Figure 8.19 (b) that even a higher value of β =10 resulted in ~65% of components which survive until the infinite life.

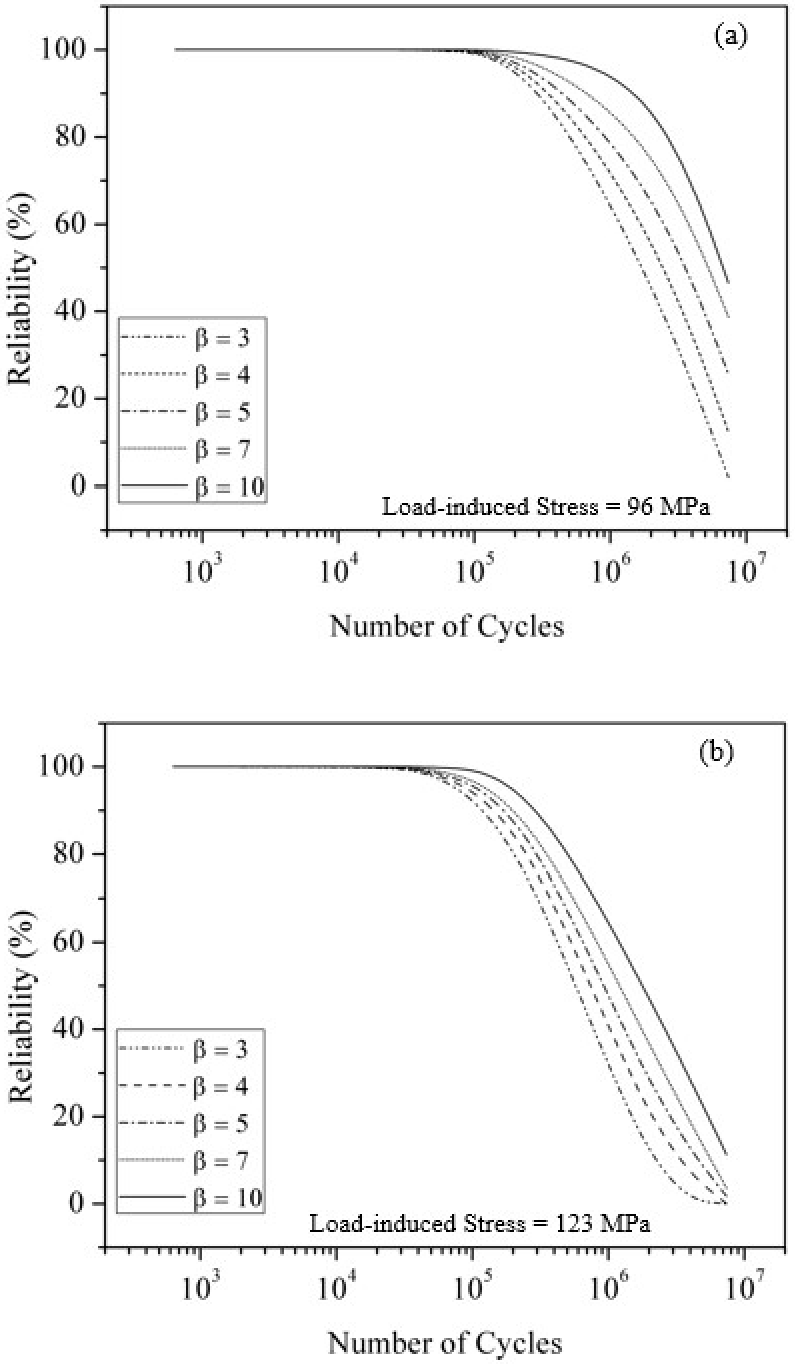

Figure 8.19 Reliability results with a load-induced stress of (a) 96 MPa and (b) 123 MPa on spring flap

8.3 CASE STUDY # 2: VALVE BODY

A ductile iron valve body is selected for second case study as shown in Figure 8.20. The details of mold design optimization using MAGMASoft, mechanical performance simulations using ABAQUS, and life prediction and reliability assessment using fe-safe are presented in the following sub-sections.

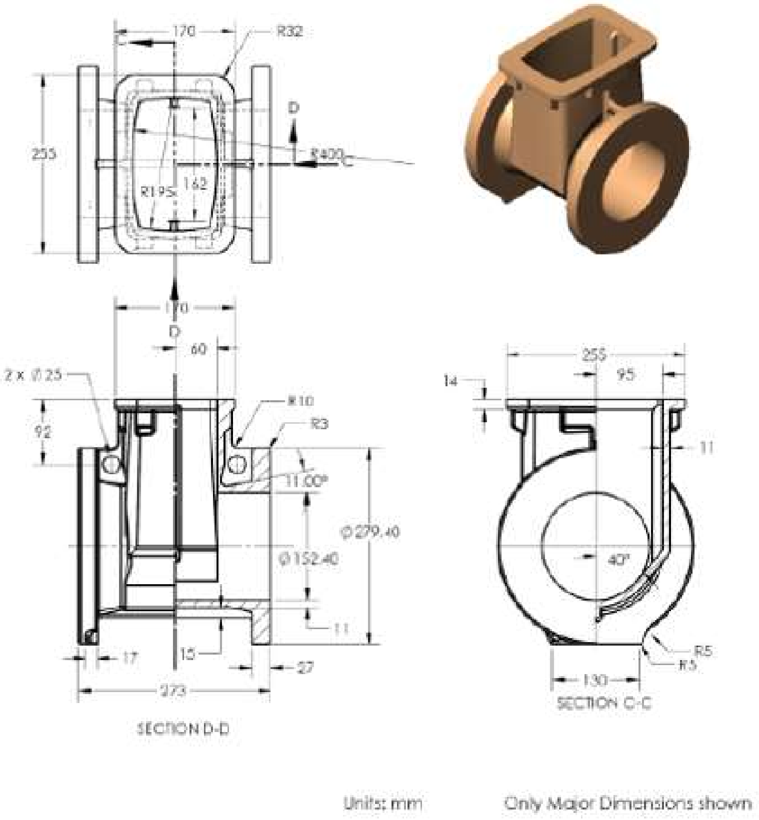

Units: mm

Only Major Dimensions shown

Figure 8.20 Ductile Iron Valve Body

8.3.1 MOLD DESIGN OPTIMIZATION USING MAGMASOFT

8.3.1.1 Initial Mold Design

The initial casting layout is prepared using standards, expertise of foundrymen and the mathematical formulations available in [83]. Due to geometry of the casting, two in-gates are used to supply the molten metal. Two-top risers are provided at those two ends of valve body which are connected to flanges during assembly. A core is used due to hollow nature of valve body. The initial casting layout for valve is shown in Figure 8.21. The initial casting layout is imported to MAGMASoft for filling, solidification and stress simulations. The casting layout is discretized into 2,927,232 elements using cubical mesh. Melt treatment is defined in the software in terms of inoculation method (Good), treatment yield (100%) and graphite precipitation. The pouring time is set to be 17 seconds. The materials properties for GGG-40 ductile iron and mold material (Green Sand) are already presented in Table 4.2 and Table 4.3 respectively. The initial temperature of the melt and the mold are 1400 °C and 40 °C respectively. Filling and solidification behavior, residual stresses and defects such as hotspot and porosities are predicted using simulations.

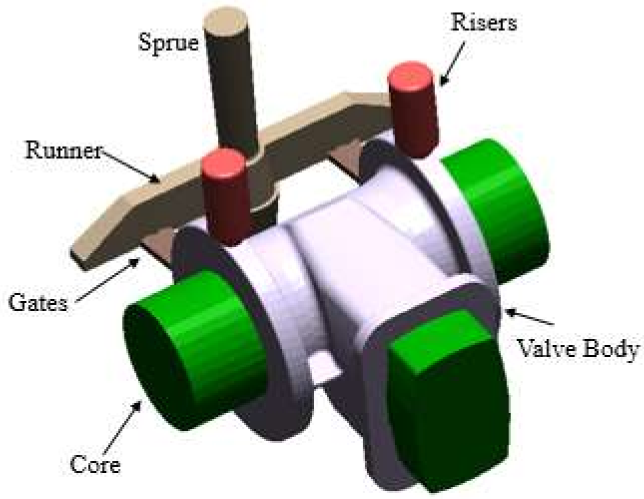

Figure 8.21 Initial casting layout for valve body

The results of casting simulations using initial mold design are presented in Figure 8.22 to Figure 8.26. The temperature distribution in the valve at different stages of solidification is shown in Figure 8.22. The temperature contour indicates the farthest point in casting with minimum temperature at 100% solidification which suggested the start of solidification from that point. This is also confirmed by percentage fraction solid results shown in Figure 8.23 (a) to (d). The residual stresses at ejection are ~60 MPa and the higher stresses are observed in thin sections of valve as shown in Figure 8.24. Figure 8.25 shows the presence of hotspots within the valve body. These hotspots should be minimized to avoid shrinkage related defects. The result of shrinkage porosities are presented in Figure 8.26 (a) to (f). No surface porosity is observed as shown in Figure 8.26 (a). Figure 8.26 (b) shows the X-ray view of the valve which shows internal porosity at various regions. The cut-plane view in Figure 8.26 (c) represents the depth to which the casting is affected with porosity. Figure 8.26 (d) to (f) indicates the regions with significant porosity which needs to be minimized to improve the overall quality of casting.

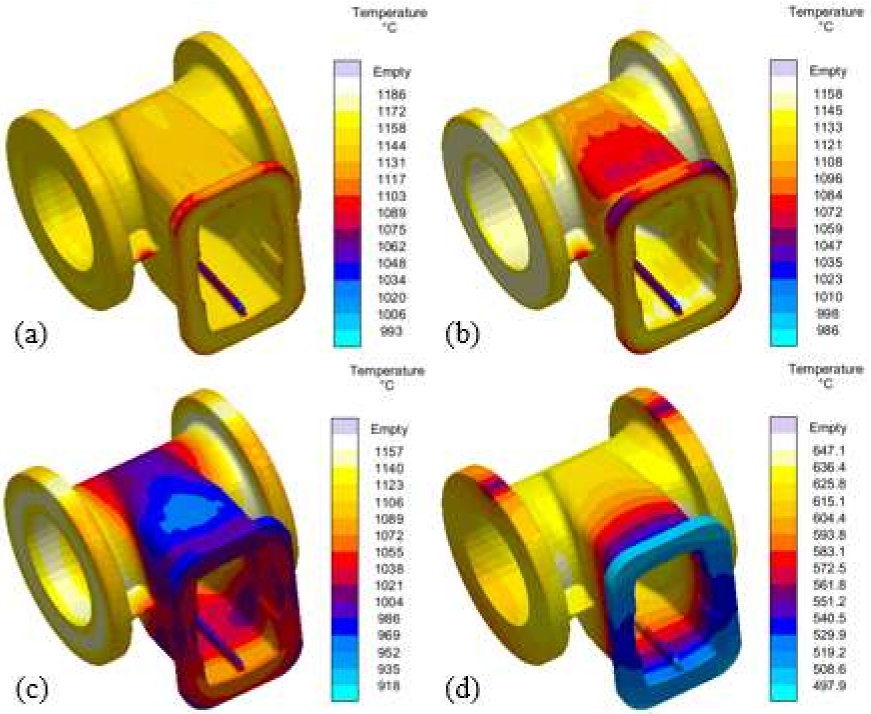

Figure 8.22 Temperature profile within the mold during solidification (a) 25%, (b) 50%, (c) 75% and (d) 100%

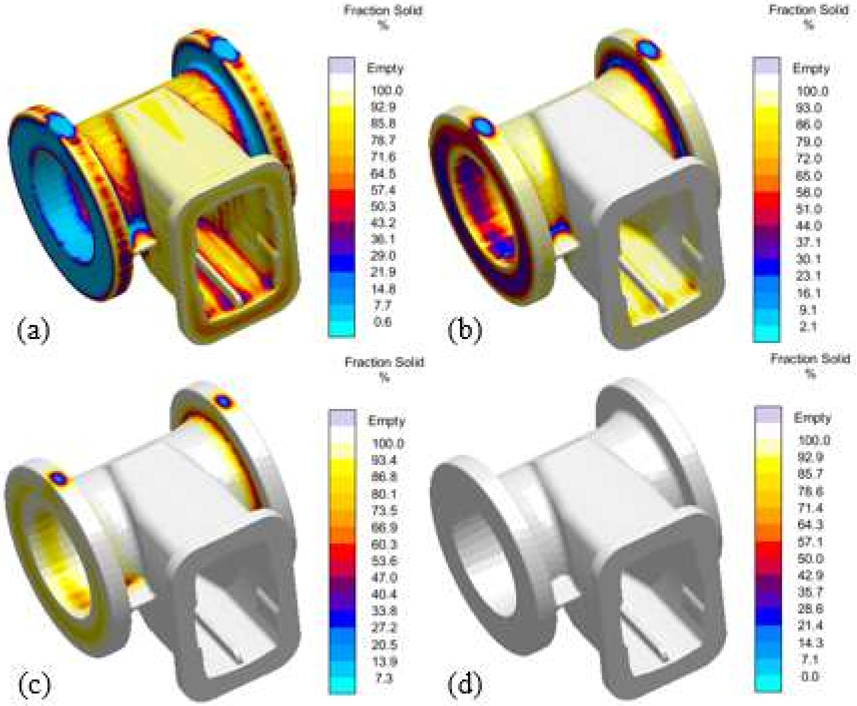

Figure 8.23 Solidification sequence (a) 25%, (b) 50%, (c) 75% and (d) 100%

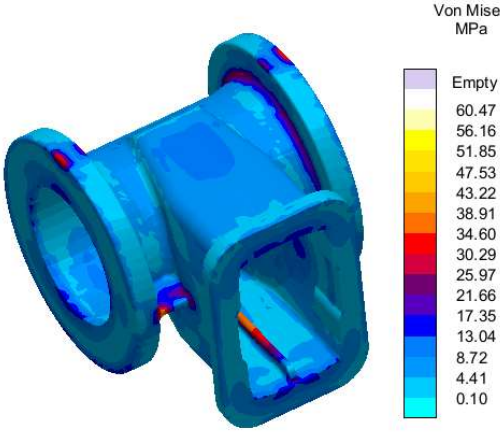

Figure 8.24 Residual stress distribution at ejection using initial mold design

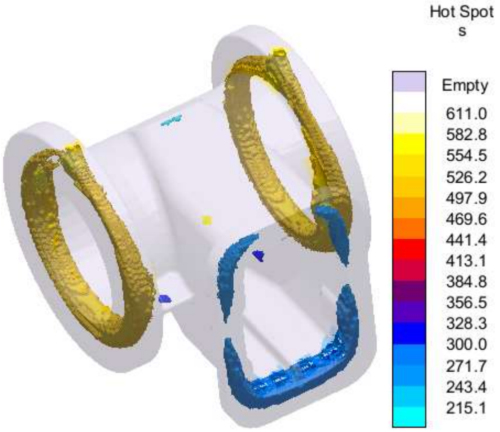

Figure 8.25 Hotspots in valve body using initial mold design

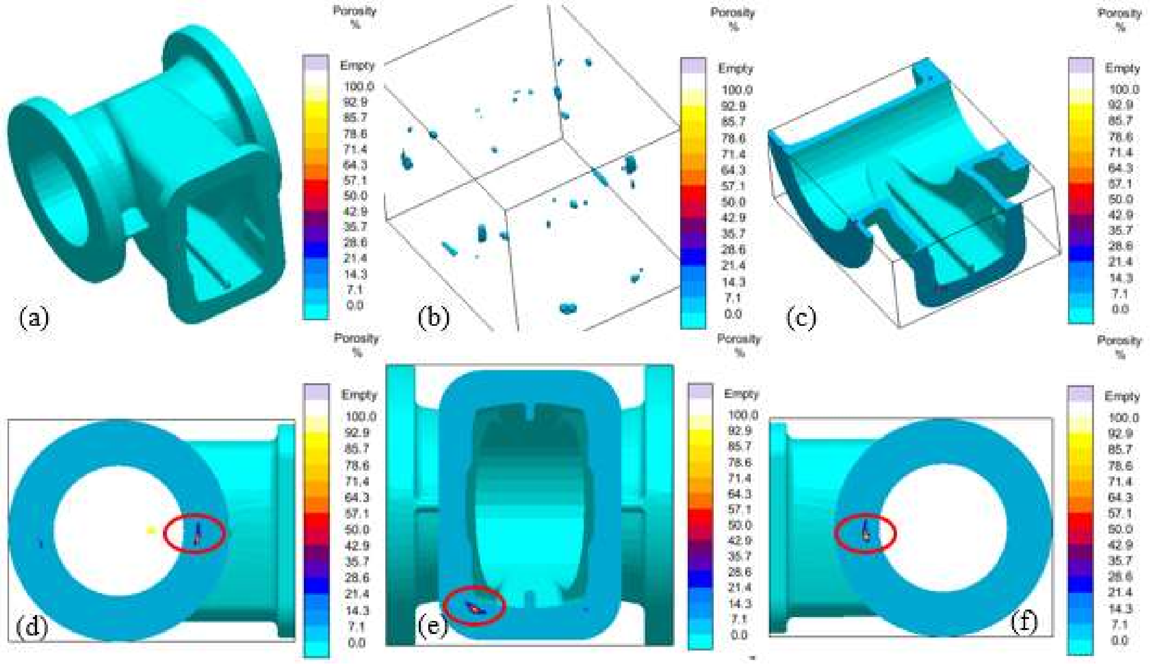

Figure 8.26 (a) Surface porosity, (b) X-ray view, (c) Cut-plane view, (d) to (f) porosity significant areas in valve body

8.3.1.2 Optimized Mold Design

Mold design optimization began with modifying the riser design. Top-risers are replace by side risers as shown in Figure 8.27. The casting is gated through the side riser for maximum efficiency. Moreover, the hemispherical bottom on the side riser prevent early freezing of the riser and casting junction [105]. In addition to this, vents are provided to permit the escape of entrapped gases within the cavity. The dimensions of the sprue and sprue well, runner and gates remained unchanged. The optimized casting layout is imported to MAGMASoft for simulation. A cubical mesh is used to discretize the modified casting layout in 3,051,620 elements. The material properties and process parameters are same as in the simulation of initial mold design. There is no change in pouring time as the overall weight of the casting is not much different. Once again, filling, solidification, and stress simulations are run to observe the filling and solidification sequence and to predict the defects such as hotspot and porosity.

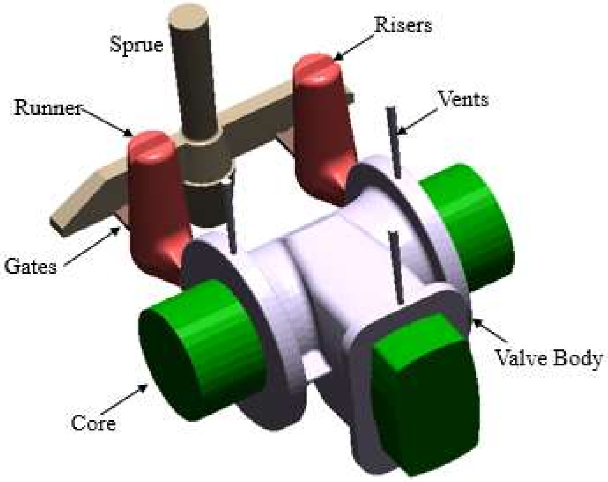

Figure 8.27 Modified casting layout for valve body

The simulation results for optimized mold design are presented in Figure 8.28 to Figure 8.32. The temperature contours in Figure 8.28 (a) to (d) depicts the start of solidification from the farthest point from pouring i.e. the end of the valve where bonnet is attached. This is also confirmed through percentage fraction solid results as shown in Figure 8.29. The residual stresses are significantly reduced from ~60 MPa to ~25 MPa with the optimized mold design as shown in Figure 8.30 which suggests improved cooling and solidification. The hotspots are not completely eliminated as shown in Figure 8.31, however, it is minimized when compared to the hotspot predicted in Figure 8.25. The overall porosity in the valve is significantly reduces as shown in Figure 8.32 (a) to (f). Figure 8.32 (a) shows no surface porosity in the valve. The X-ray view of valve in Figure 8.32 (b) shows the overall reduction in internal porosities. The cut-plane view in Figure 8.32 (c) shows the minor porosities at certain depths of casting. Figure 8.32 (d) to Figure 8.32 (f) shows areas of the valve where the porosity was significant in case of using initial mold design. It can be observed that the porosity is greatly reduced in all these areas. Although some porosity is observed in Figure 8.32 (d) to Figure 8.32 (f), however, the amount of porosity is fairly acceptable to consider this mold design for actual casting.

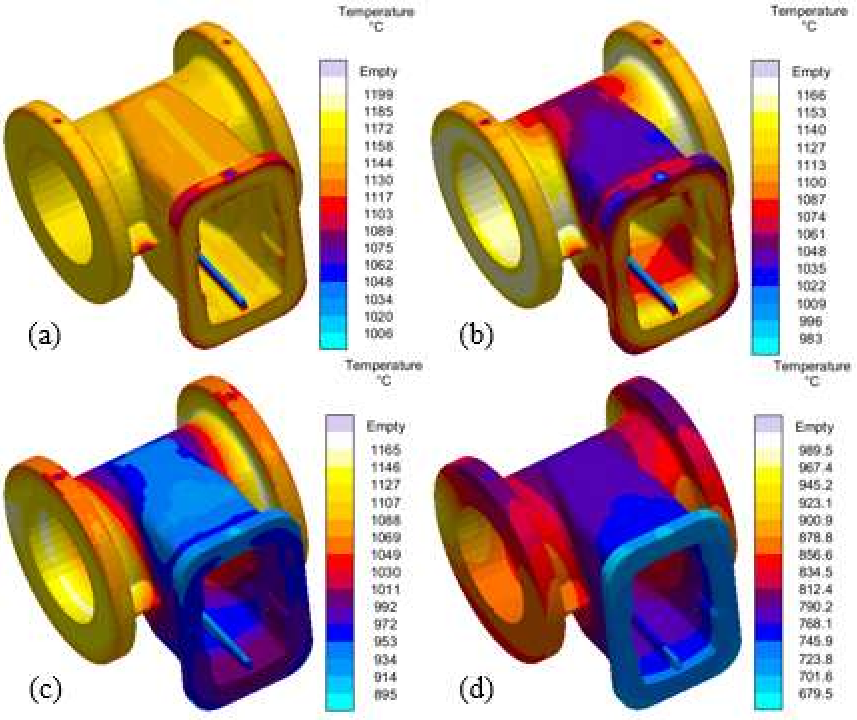

Figure 8.28 Temperature profile within the mold during solidification (a) 25%, (b) 50%, (c) 75% and (d) 100%

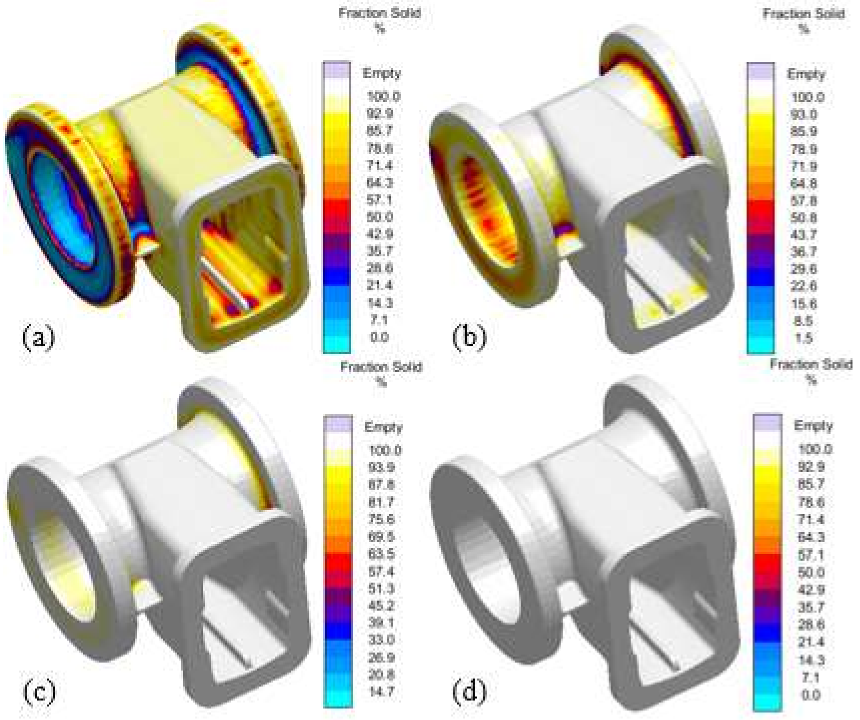

Figure 8.29 Solidification sequence (a) 25%, (b) 50%, (c) 75% and (d) 100%

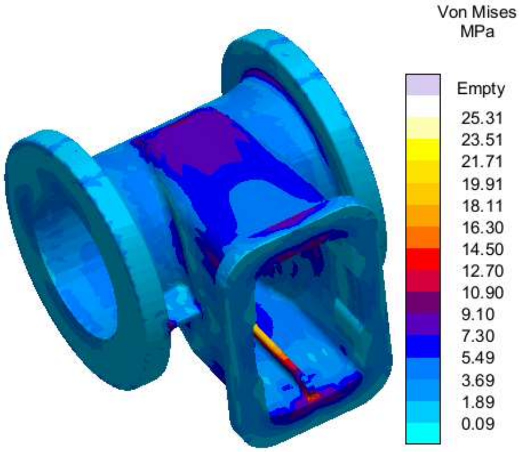

Figure 8.30 Residual stress distribution at ejection using optimized mold design

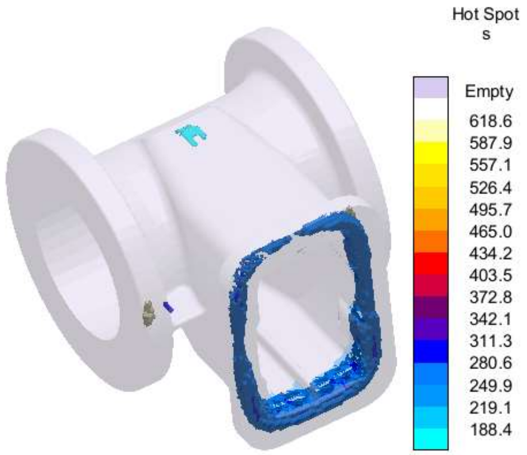

Figure 8.31 Hotspots in valve body using optimized mold design

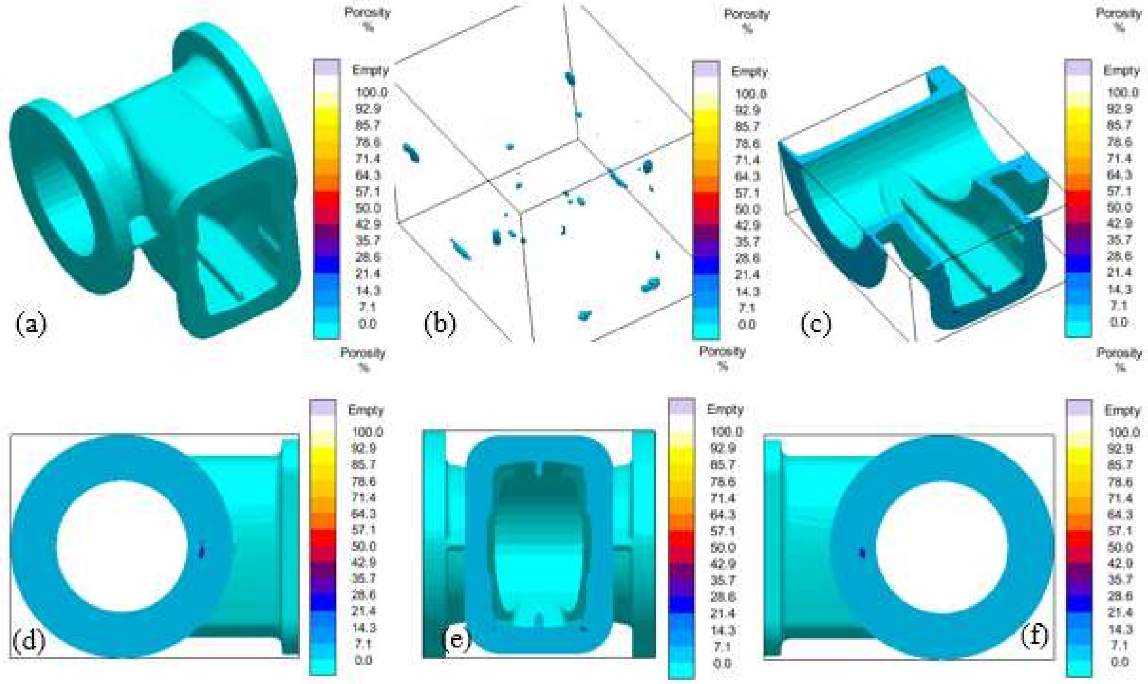

Figure 8.32 a) Surface porosity, (b) X-ray view, (c) Cut-plane view, (d) to (f) porosity significant areas in valve body

8.3.2 FINITE ELEMENT SIMULATION AND FATIGUE LIFE PREDICTION

The finite element modeling of valve body is done using ABAQUS standard. The optimized mold design contains some porosity in the valve body which has to be included in FE analysis. The predicted porosity is incorporated to FE simulation using

MAGMAlink. Valve geometry is imported to ABAQUS and discretized using a 10 node quadratic tetrahedron (C3D10) elements as shown in Figure 8.33. The resulting mesh contained 101,451 elements and 162,056 nodes, when a 8 mm spacing is used. Experimenting with further mesh refinement shows no significant changes in the results. The mesh shown in Figure 8.33 is then imported to MAGMASoft using MAGMAlink and the predicted porosity is mapped to FEA nodes. The nodal porosity is then exported and integrated to ABAQUS simulations using the same procedure described earlier in Section 6.3.

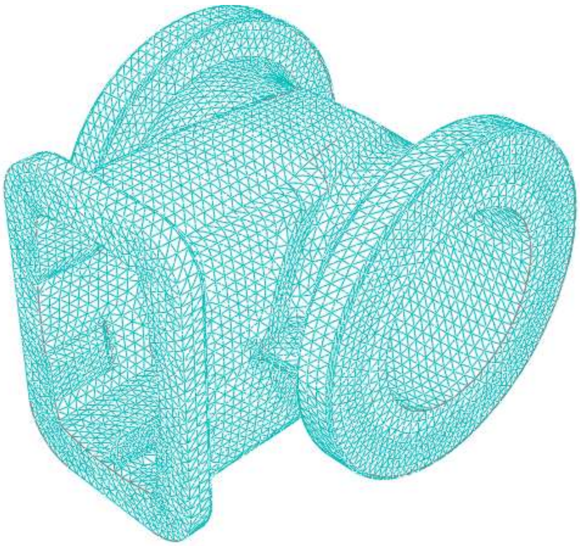

Figure 8.33 Valve body mesh generated in ABAQUS

Next, the boundary conditions for FE simulations are carefully decided to replicate the actual conditions of valve body in service. The boundary conditions are set in consultation with MASABIK foundry based upon the information provided by the end-user. The pressure applied to the valve body in normal operating conditions is 1 MPa, however, it is communicated that it can sustain a maximum pressure of 2.5 MPa. The ends of the valve connected to flange and bonnet are fixed using encastre boundary conditions, whereas, a pressure of 1 MPa is applied to the internal surface of the valve body. Figure 8.34 shows the boundary conditions used in FE simulations.

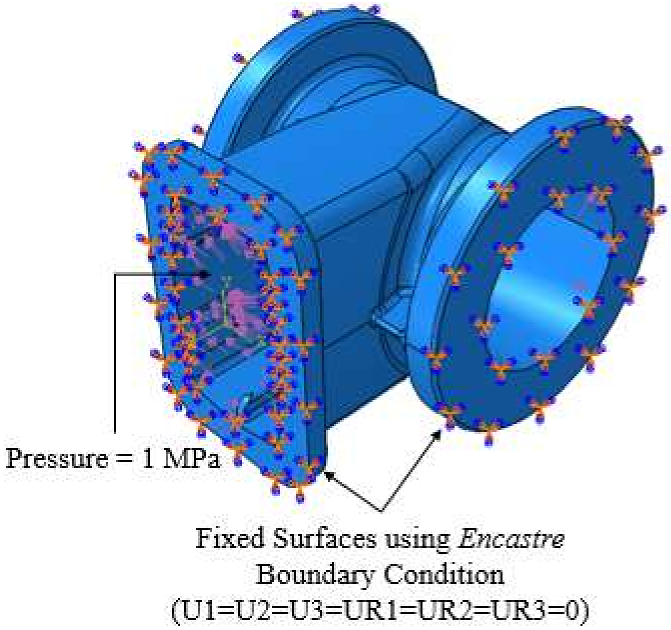

Figure 8.34 Boundary conditions for FE simulation of valve body

The Von Mises stress results for the valve body with the above boundary conditions are presented in Figure 8.35. Figure 8.35 (a) shows the stress field without porosity i.e. Sound valve body. In this case, the maximum load induced-stress is found to be ~99.17 MPa which gives a safety factor of 2.8 for iron with a yield strength of 280 MPa. With porosity, the load-induced stress is not significantly change i.e. ~99.24 MPa, thereby, resulting in same safety factor. The location of maximum Von Mises stress is also shown in Figure 8.35 (a) and (b). Using the factor of safety based on the fatigue endurance limit of 197 MPa as given in Table 6.4, the factor of safety for the highest value of stress is ~2. Once again, these values of safety factors are deterministic and the probabilistic reliability computations will be presented.

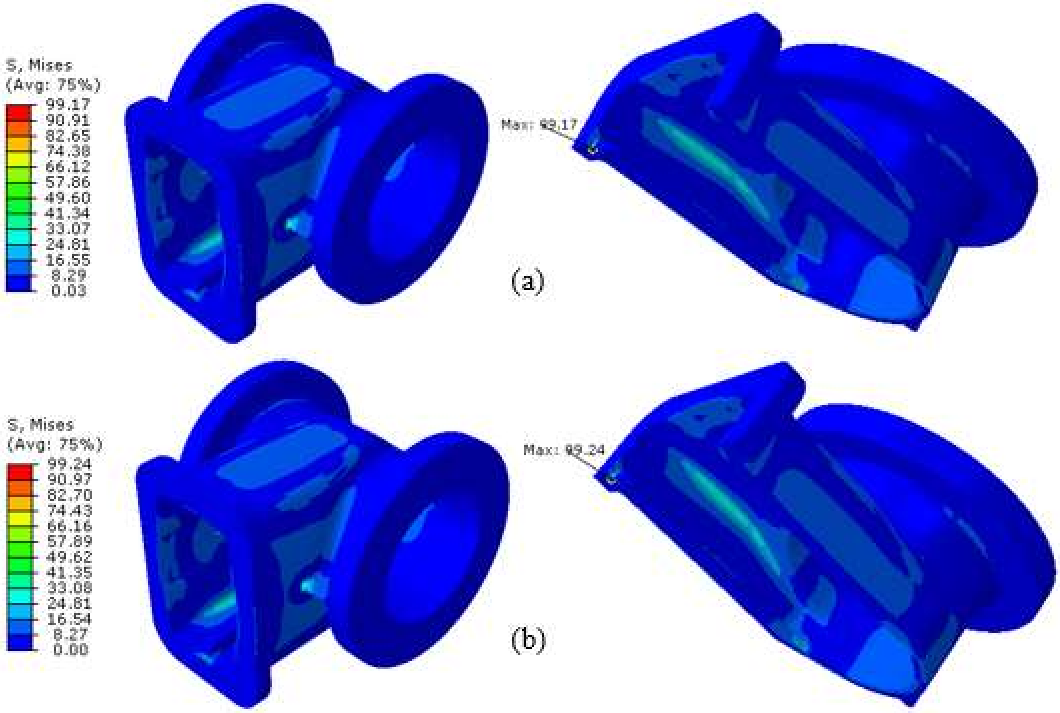

Figure 8.35 Von Mises stress results in spring flap (a) without porosity and (a) with porosity

The next step in the analysis is to predict the fatigue life with and without porosity. The porosity will be of concern if it lowers the fatigue life below 10^6 cycles which is set as the runout condition in the present work. Fatigue life is predicted using fe-safe using the method discussed earlier in Section 6.3. The results of fatigue life prediction are presented in Figure 8.36. The minimum fatigue life with and without porosity are found to be more than 10^9 cycles which suggests the survival of the part in these predictions. It is observed that the small porosities predicted using optimized mold design did not affect the life of valve body. Hence, these results confirms the robustness of optimized mold design for casting valve body.

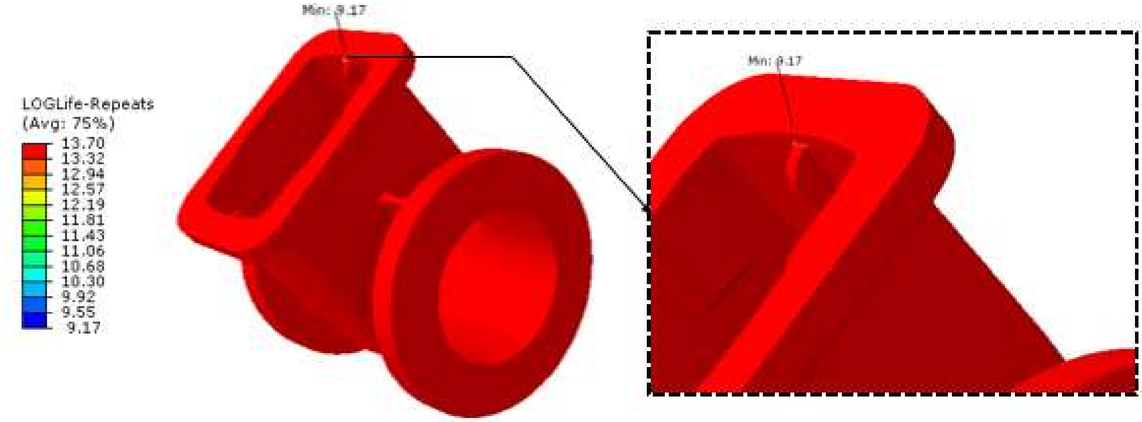

Figure 8.36 Fatigue life prediction using fe-safe

8.3.3 RELIABILITY ASSESSMENT

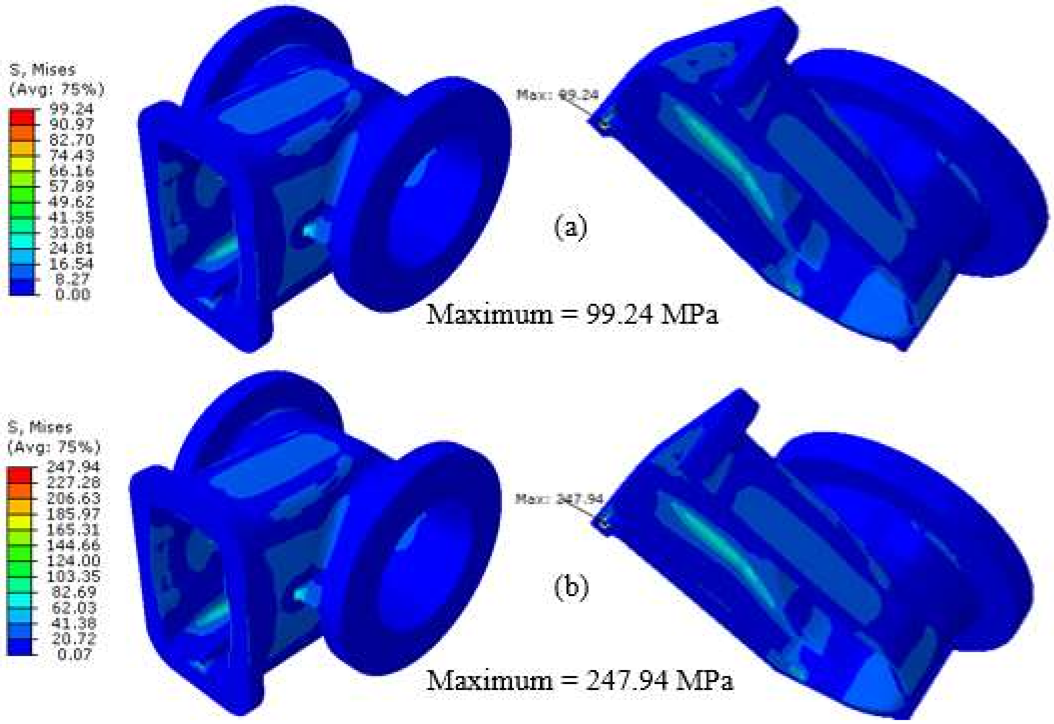

Figure 8.37 Von Mises stress in valve body with porosity at applied internal pressure (a) 1 MPa and (b) 2.5 MPa

In order to compute reliability of valve body, two load-induced stresses are used for calculations. The internal pressure applied to the valve under normal working conditions is 1 MPa, and maximum pressure that can be applied as provided by MASABIK foundry and end-user is 2.5 MPa. Therefore, the valve with porosity is simulated for stresses at these two loading conditions. The resulting stress fields are presented in Figure 8.37. These stresses are then used in fe-safe for reliability computations. A 5% variability in load-induced stresses is considered and the material variability is represented by Weibull distribution with varying shape parameter β.

The resulting reliability curves for both scenarios are presented in Figure 8.38. Figure 8.38 (a) shows the reliability results for an internal pressure of 1 MPa on valve resulting in a load-induced stress of 99 MPa. The component shows nearly 100% reliability until the infinite life i.e. 10^6 cycles when β = 10. As discussed earlier, a higher value of β shows less variability in the parts produced using the optimized mold design. At lower β values, the reliability dropped down to ~80%. With maximum pressure of 2.5 MPa and the corresponding load-induced stress of 248 MPa, the reliability is significantly compromised. It can be observed in Figure 8.38 (b) that reliability significantly dropped with increasing number of cycles. Even with a high value of β = 10, only 11% components resulted in an infinite life. Moreover, at lower β values, none of the component survives up to infinite life.

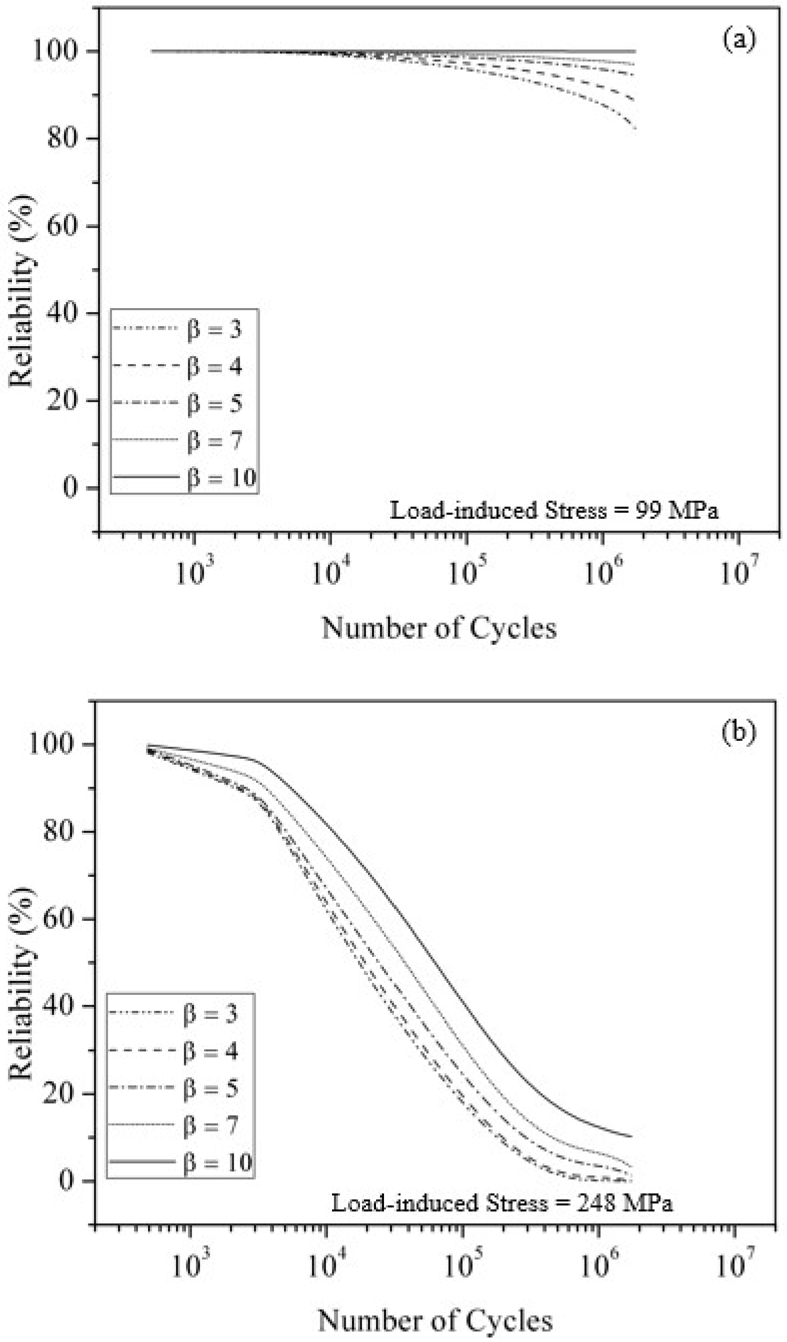

Figure 8.38 Reliability results with a load-induced stress of (a) 99 MPa and (b) 248 MPa on valve body

8.4 CONCLUDING REMARKS

The applications of the developed simulation based methodology are presented in this chapter. A steel spring flap and a ductile iron valve block is selected for this purpose. The optimized mold design for minimum porosities are obtained using MAGMASoft. Integration of predicted porosity to each component is done using MAGMAlink. The stress fields in components with porosity are obtained using ABAQUS which are then used to predict life and estimate reliability. The results of fatigue lives prediction at normal and maximum load conditions are encouraging since the life in each case is predicted to be more than 10^6 cycles (infinite life). In terms of reliability, it is observed that 95% of the steel spring flaps can survive until infinite life when subjected to normal loading conditions, however, the reliability is significantly compromised at maximum load conditions. Based on these results, it is promising to replace forged spring flap with the cast one, however, further improvements in casting design to reach nearly zero porosity can lead to ~100% reliability under normal loading conditions i.e. 70 kN in automotive suspension systems. The reliability results for valve under normal operating pressure i.e. 1MPa shows ~100% reliability for infinite life, however, under the maximum loading conditions, the reliability is significantly compromised. Therefore, ductile iron cast valves are suitable to be used under normal working conditions of up to 1 MPa pressure, whereas, the use of these cast valves at high pressures i.e. 2.5 MPa or more is not recommended. A safe load-induced stress on spring flap and valve body could be 95 MPa and 160 MPa respectively based on the reliability results obtained in Chapter 7.

CHAPTER 9

CONCLUSIONS AND FUTURE WORK

9.1 SUMMARY

The aim of the current works was to develop a simulation based methodology for cradle to grave analysis of metal castings in a virtual domain. In this regard, advanced simulation tools have been used to (i) design and optimize the molds for casting, (ii) evaluate the performance of cast parts with minimized porosity, and (iii) estimate the reliability of components during service life. The developed methodology has been validated through experiments conducted on sample cast products which are standard tensile and fatigue specimens casted in optimized molds. Applications of the developed methodology have been shown for some typical high value cast parts such as a cast steel spring flap and a ductile iron valve body.

- The methodology is developed and validated for two most widely used materials in metal casting industries. These are ASTM A216 WCB steel and GGG-40 ductile iron. Standard tensile and fatigue specimens are considered as simple cast products for which multi-cavity molds were designed, simulated, and optimized using high-end casting simulation software MAGMASoft. The main criteria of mold optimization in simulations was porosity minimization in castings. The main observations are

  - Casting simulations provided accurate and comprehensive insights on mold filling and solidification behavior, residual stresses and defects in cast parts.
  - The predicted defects, particularly porosity, were minimized through modification in mold design. These modifications were the geometric changes in the elements of gating and riser design and/or addition of auxiliary components such as exothermic sleeves, chills etc. within the mold.
  - An optimized mold design was obtained with minimal or nearly zero porosity using casting simulations for each materials and type of specimen.
- The castings of specimens using optimized mold design were done in MASABIK foundry. Some of the main casting features and observations are
  - Wooden patterns were used to prepare sand molds.
  - Furan sand mold and green sand mold were used for casting steel and iron respectively.
  - Casting of specimens was done in accordance with the process parameters used in casting simulations.
  - Heat treatment was done only on steel casting and not on ductile iron castings. Heat treatment done on sample specimens was same as done in high value cast parts which was analyzed in chapter 8 (spring flap and valve body).
- The cast specimens were machined to standard dimensions and tested under monotonic and cyclic loads. Prior to testing, radiographic examination of

specimens was done to determine the quality of castings. Following are the main observations from mechanical testing.

  - Results for tensile testing of cast steel specimens suggested some variability in the quality of cast specimens. However, ductile iron specimens did not show much variation in results for tensile testing.
  - In terms of fatigue testing, theoretical S-N curves suggested a higher endurance limit for steel as compared to iron. Conversely, the experiments demonstrated a higher endurance limit of iron than the steel. This could be attributed to the traces of porosity observed in the X-ray imaging of fatigue specimens of steel because such porosities adversely affects the fatigue life of steel.

- The simulations of mechanical testing were done with porosity integrated to specimens using MAGMAlink. Engineering approaches were utilized to simulate the deformation, damage, and fracture of specimens during tensile testing. Tensile testing was simulated using elastic-plastic material model and porous metal plasticity model in ABAQUS. Fatigue testing was simulated by doing finite element elastic stress analysis in ABAQUS corresponding to the load in experimental fatigue testing, followed by, fatigue life prediction in fe-safe using multi-axial strain-life approach. Some of the main observations are
  - In case of tensile testing of steel specimens, simulated and experimental results are found to be in good agreement since all specimens resulted in strength and elongation measurements greater than the minimum defined in ASTM standard for A216 WCB cast steel.

  - Some discrepancy is observed in simulated and experimental results of tensile testing of steel specimens which was investigated further. A comparison of simulated and actual porosities confirmed that although porosity played a major role in the discrepancy in these results but other factors also contributed.
  - The hardness measurement at different regions of each specimen revealed significant variation which can be related to lack of control on heat treatment done, specifically preheating, to homogenize the cast parts produced using a multi-cavity mold.
  - For tensile specimens of ductile iron, the simulated and experimental results of tensile testing are compared only for the sound specimen and are found to be in good agreement.
  - Fatigue life predictions for steel and iron specimens are found to be in good agreement with experimental results.
- The reliability of sample cast products was measured using strength-stress interference model. Both time-independent and time-dependent load-induced stresses were considered. For time-independent case, the stress was normal distributed and strength was Weibull distributed. Effects of variability in load-induced stress and shape parameter β of Weibull distribution were also presented. The time-dependent load-induced stress was modelled through Rayleigh distribution where strength variability was modeled using Weibull distribution. The main findings are

  - For time-independent load-induced stress, the reliability was computed at four different values of stresses for each material. It was observed that the rate of survival of components dropped down with increasing load-induced stresses.
  - A safe region of load-induced stress was determined for each material i.e. up to 95 MPa for cast steel and 160 MPa for ductile iron to have nearly 100% reliability of components until the infinite life (greater than 10^6 cycles).
  - For time-independent case, the reliability was computed against the ratio of scale parameters of Weibull distributions which are representative of ratio of median material's strength to median load-induced stress.
  - The reliability estimates were fitted to log-normal and Weibull distributions through linearization transforms of reliability functions. The parameters for each distributions were calculated to develop reliability models. The developed models can be used to estimate reliability at any targeted life.
- The application of developed simulation based methodology was presented for two value added moderately complex parts i.e. a cast steel spring flap used in automotive suspension systems and a ductile iron valve body (both used in industry).
  - Casting simulations provided the optimized mold with minimum porosity for each component.
  - With integrated porosity and under real-time loading conditions, the stress analysis was done and fatigue lives were predicted.

  - Reliability assessment for spring flap and valve body was done at normal and maximum operating conditions.
  - It was concluded that cast spring flap can be considered suitable for replacement of forged spring flap. This was due to reliability estimates of about 95% survival of the components for an infinite life under normal loading conditions. The reliability measurement under maximum loading condition dropped to 65%. So the threshold of maximum lading condition must be dropped to as shown in Figure 7.14.
  - The ductile iron valve body was found suitable under normal loading conditions with nearly 100% survival rate for infinite life. However, the cast valve body cannot be recommended for maximum loading condition communicated by MASABIK and end-user due to poor reliability results. Thus, the cast valve is highly reliable in a reduced window of loading as defined in the results shown in Figure 7.19.

9.2 CONCLUSIONS

The key conclusions drawn from this work are as follows.

- High end casting simulation software such as MAGMASoft are very capable of examining the effects of several factors such as temperature of molten metal, pouring time and velocity, gating and runner design, riser design, and mold configurations on the quality of castings. The results presented in this work emphasize the utilization of casting simulations to effectively design and optimize the casting process in a virtual domain before physically making the molds and parts.

- Residual stresses are critical in cast parts and can be significantly reduced using optimized mold design as presented in this study. The accurate prediction of these stresses at design stage greatly help in improved cooling and solidification and better heat treatment.
- Testing of cast standard specimens is a practical approach to validate the quality of castings produced using simulation-based optimized mold designs. Although, porosity is a major contributor to degradation in mechanical properties, there are other associated factors such as cleaning, finishing and heat treatment. Hence, besides porosity minimization, a more-controlled post casting treatment must be implemented to obtain excellent mechanical properties in cast parts.
- Fatigue life predictions are very sensitive to local stress concentrations. The simulations done in this work utilizes the porosity fractions which are defined over a volume that is large compared to microscopic pore geometry. The good agreement between measured and simulated fatigue lives confirms the adequate mesh used in life prediction with integrated porosity. Nevertheless, it can be expected that stress concentration around very small shrinkage pores can be modeled better with further mesh refinement, which consequently will require longer simulation time and more powerful computational facilities.
- Reliability assessment of cast parts provides the risk of failures associated with the parts during service life where it is expected to have variability in strength and load-induced stress. The variability in strength of material is modeled using Weibull

distribution in present work. The shape parameter β is the inverse of coefficient of variation in strength. Owing to less coefficient of variation in material's strength, a higher value of shape parameter β i.e. 10 is more realistic in reliability analysis of specimens and selected cast parts for this work. The lower values of parameter β (3 to 5) reflects greater dispersion and will adversely effect on part reliability.

- Simulation-based methodology developed and validated in this work can be applied to real cast parts. In addition to cast steel and ductile iron, this methodology can be applied to other cast alloys. Hence, the developed methodology is deemed robust in cradle to grave analysis of cast parts produced with almost any cast alloy.

9.3 RECOMMENDATIONS FOR FUTURE WORK

The developed simulation based methodology can be extended in a variety of directions. Below is a list of recommendations for possible future work based on this dissertation.

- The present study included mold design optimization only for porosity minimization. A holistic approach could be to optimize the mold design using autonomous optimization for more than one objectives such as porosity minimization, soundness, yield maximization, residual stress minimization etc. MAGMASoft can be explored further in this regard.
- Integration of porosity using MAGMAlink was challenging since it provides only nodal porosity corresponding to the nodes of FEA mesh. The output from MAGMAlink needs refinement to be integrated to FE analysis. A robust method for this integration could be introduced by developing the modules for refining the

output from MAGMAlink and direct integration to popular commercially available finite element packages.

- A comprehensive tool can be developed for cradle to grave analysis of castings by coupling casting simulations + mechanical performance simulation + reliability simulations. Although such integration is complex, it can greatly contribute to casting industry by reducing the product time, cost, and risks associated with performance during service life.

REFERENCES

[1] B. Ravi, *Metal casting: computer-aided design and analysis*. New Delhi: Prentice-Hall of India, 2005.

[2] M. W. Fu and M. S. Yong, “Simulation-enabled casting product defect prediction in die casting process,” *Int. J. Prod. Res.*, vol. 47, no. 18, pp. 5203–5216, Sep. 2009.

[3] B. Ravi, *Metal casting: computer-aided design and analysis*. New Delhi: Prentice-Hall of India, 2005.

[4] J. A. Schey, *Introduction to Manufacturing Processes*. McGraw-Hill, 1987.

[5] P. R. Beeley, *Foundry Technology*. Butterworth-Heinemann, 2001.

[6] *ASM Handbook Volume 15: Casting - ASM International*. .

[7] S. Kalpakjian and S. Schmid, *Manufacturing Engineering & Technology*, 7 edition. Prentice Hall, 2013.

[8] M. P. Groover, *Fundamentals of Modern Manufacturing: Materials, Processes, and Systems*. John Wiley & Sons, 2010.

[9] H. S. Bawa, *Manufacturing Processes - II*. Tata McGraw-Hill Education, 2004.

[10] M. Chhabra and R. Singh, “Experimental investigation of pattern-less casting solution using additive manufacturing technique,” *MIT Int. J. Mech. Eng.*, vol. 1, no. 1, pp. 17–25, 2011.

[11] C. Li, Z. Wei, W. Chenhong, J. Baochang, and X. Qingchun, “Application of digital pattern-less molding technology to produce art casting,” *Research and Development, China Foundary*, vol. 11, no. 06, Nov. 2014.

[12] V. Kostakis, V. Niaros, and C. Giotitsas, “Open source 3D printing as a means of learning: An educational experiment in two high schools in Greece,” *Telemat. Inform.*, vol. 32, no. 1, pp. 118–128, Feb. 2015.

[13] T. Wohlers, “Wohlers Report,” *State Ind. Annu. Worldw. Prog. Rep. Wohlers Assoc. Inc*, pp. 29–37, 2008.

[14] R. Singh and J. P. Singh, “Comparison of rapid casting solutions for lead and brass alloys using three-dimensional printing,” *Proc. Inst. Mech. Eng. Part C J. Mech. Eng. Sci.*, vol. 223, no. 9, pp. 2117–2123, Sep. 2009.

[15] T. J. Krouth, “Foundry Tooling and Metal Castings in Days,” in *roceedings from International Conference: Worldwide Advances in Rapid and High-Performance Tooling, EuroMold*, Frankfurt/M, Germany, 2002.

[16] J. P. Singh and R. Singh, “Investigations for a statistically controlled rapid casting solution of lead alloys using three-dimensional printing,” *Proc. Inst. Mech. Eng. Part C J. Mech. Eng. Sci.*, vol. 223, no. 9, pp. 2125–2134, Sep. 2009.

[17] R. Rajkolhe and J. G. Khan, “Defects, Causes and Their Remedies in Casting Process: A Review,” *Int. J. Res. Advent Technol.*, vol. 2, no. 3, pp. 2321–963, 2014.

[18] K. B. Rundman, “Metal casting,” *Dep. Mater. Sci. Eng. Mich. Technol. Univ. Michagan*, pp. 17–19, 2000.

[19] W. A. Buttler, “Melting and Holding Furnaces for Die Casting,” *Die Casting Engineer*, pp. 28–40, Mar-2006.

[20] W. M. A. Jadayil, “Studying the effects of varying the pouring rate on the casting defects using nondestructive testing techniques,” *Jordan J. OfMechanical Ind. Eng.*, vol. 5, pp. 521–526, 2011.

[21] J. Y. Kumar, K. S. Amirthagadeswaran, and S. Gowrishankar, “Casting process optimization for reducing the cold shut defect in castings using response surface methodology,” *IJEMS Vol222 April 2015*, Apr. 2015.

[22] A. Ghosh and A. K. Mallik, *Manufacturing science*. Ellis Horwood, 1986.

[23] V. Boljanovic, *Metal Shaping Processes: Casting and Molding, Particulate Processing, Deformation Processes, and Metal Removal*. Industrial Press Inc., 2009.

[24] K. B. Rundman, *Metal casting*. Department of Material Science and Engineering Michigan Technology University, Michagan, 2000.

[25] J. Beddoes and M. Bibby, *Principles of Metal Manufacturing Processes*. Butterworth-Heinemann, 1999.

[26] E. Niyama, T. Uchida, M. Morikawa, and S. Saito, “A Method of Shrinkage Prediction and its application to Steel Casting Practice,” *AFS Int. Cast Met. J.*, pp. 52–63, Sep. 1982.

[27] K. D. Carlson and C. Beckermann, “Use of the Niyama Criterion To Predict Shrinkage-Related Leaks in High-Nickel Steel and Nickel-Based Alloy Castings,” in *Proceedings of the 62nd SFSA Technical and Operating Conference*, 2008.

[28] B. Ravi, “Casting Simulation and Optimisation: Benefits, Bottlenecks, and Best Practices,” *Indian Foundry J. January*, no. Special Issue, 2008.

[29] B. Ravi, “Casting Simulation – Best Practices,” in *Transactions of 58th IFC*, Ahmedabad, India, 2010.

[30] M. Jolly, “Castings,” in *Comprehensive Structural Integrity*, vol. 1, Elsevier, 2003, pp. 377–466.

[31] M. Jolly, “Casting Simulation: How well do reality and virtual casting match? State of the art review,” *Int. J. Cast Met. Res.*, vol. 14, no. 5, pp. 303–314, Jan. 2002.

[32] L. D. Amin, S. Patel, P. Mishra, and D. Joshi, “Rapid Development of Industrial Castings Using Computer Simulation,” *Indian Foundry J.*, vol. 60, no. 8, Aug. 2014.

[33] B. Ravi, *Metal casting: computer-aided design and analysis*. New Delhi: Prentice-Hall of India, 2005.

[34] M. Sutaria and B. Ravi, “Computation of casting solidification feed-paths using gradient vector method with various boundary conditions,” *Int. J. Adv. Manuf. Technol.*, vol. 75, no. 1–4, pp. 209–223, Jul. 2014.

[35] M. Rappaz and M. Rettenmayr, “Simulation of solidification,” *Curr. Opin. Solid State Mater. Sci.*, vol. 3, no. 3, pp. 275–282, Jun. 1998.

[36] H.-M. Si, C. Cho, and S.-Y. Kwahk, “A hybrid method for casting process simulation by combining FDM and FEM with an efficient data conversion algorithm,” *J. Mater. Process. Technol.*, vol. 133, no. 3, pp. 311–321, Feb. 2003.

[37] B. H. Hu, K. K. Tong, X. P. Niu, and I. Pinwill, “Design and optimisation of runner and gating systems for the die casting of thin-walled magnesium telecommunication parts through numerical simulation,” *J. Mater. Process. Technol.*, vol. 105, no. 1–2, pp. 128–133, Sep. 2000.

[38] R. Seefeldt, J. C. Sturm, and A. Pawlowski, “Two for One–transferring proven filling characteristics from a single to a two cavity die casting die,” *Cast. Plant Technol.*, no. 3, 2007.

[39] Z. Sun, H. Hu, X. Chen, Q. Wang, and W. Yang, “Gating System Design for a Magnesium Alloy Casting,” *J. Mater. Sci. Technol.*, vol. 24, no. 1, pp. 93–95, 2008.

[40] I. Hahn and J. C. Sturm, “Autonomous optimization of casting processes and designs,” in *World Foundry Congress, Hangzhou, China October*, 2010, pp. 16–20.

[41] U. A. Dabade and R. C. Bhedasgaonkar, “Casting Defect Analysis using Design of Experiments (DoE) and Computer Aided Casting Simulation Technique,” *Procedia CIRP*, vol. 7, pp. 616–621, 2013.

[42] I. Hahn and G. Hartmann, “Automatic computerized optimization in die casting processes,” *Cast. Plant Technol.*, vol. 4, pp. 2–14, 2008.

[43] S. Sikorski, G. W. Dieckhues, and J. C. Sturm, “Systematic optimization of aluminum sand casting gating systems,” *Am. Foundry Soc.*, 2012.

[44] U. S. Khade and S. M. Sawant, “Gating Design Modification Using 3D CAD Modeling and Casting Simulation for Imrpoving the Casting Yield,” *Int. J. Adv. Mech. Eng.*, vol. 4, no. 7, pp. 813–820, 2014.

[45] T. Wang, S. Yao, and W. Shen, “A submerged-gate casting method,” *J. Mater. Process. Technol.*, vol. 222, pp. 21–26, Aug. 2015.

[46] W. Sequeira and R. R. Rosales, “Application of Casting Process Optimization Tools to a Structural Aluminum Part Made Via the Low Pressure Casting Process,” *Am. Foundry Soc.*, 2003.

[47] Y. Sun, J. Luo, G. F. Mi, and X. Lin, “Numerical simulation and defect elimination in the casting of truck rear axle using a nodular cast iron,” *Mater. Des.*, vol. 32, no. 3, pp. 1623–1629, Mar. 2011.

[48] C. M. Choudhari, B. E. Narkhede, and S. K. Mahajan, “Methoding and Simulation of LM 6 Sand Casting for Defect Minimization with its Experimental Validation,” *Procedia Eng.*, vol. 97, pp. 1145–1154, 2014.

[49] C. M. Choudhari, B. E. Narkhede, and S. K. Mahajan, “Casting Design and Simulation of Cover Plate Using AutoCAST-X Software for Defect Minimization with Experimental Validation,” *Procedia Mater. Sci.*, vol. 6, pp. 786–797, 2014.

[50] H. Bhatt, R. Barot, K. Bhatt, H. Beravala, and J. Shah, “Design Optimization of Feeding System and Solidification Simulation for Cast Iron,” *Procedia Technol.*, vol. 14, pp. 357–364, 2014.

[51] T. R. Vijayaram, S. Sulaiman, A. M. S. Hamouda, and M. H. M. Ahmad, “Numerical simulation of casting solidification in permanent metallic molds,” *J. Mater. Process. Technol.*, vol. 178, no. 1–3, pp. 29–33, Sep. 2006.

[52] X. J. Liu, S. H. Bhavnani, and R. A. Overfelt, “Simulation of EPS foam decomposition in the lost foam casting process,” *J. Mater. Process. Technol.*, vol. 182, no. 1–3, pp. 333–342, Feb. 2007.

[53] A. Kermanpur, S. Mahmoudi, and A. Hajipour, “Numerical simulation of metal flow and solidification in the multi-cavity casting moulds of automotive components,” *J. Mater. Process. Technol.*, vol. 206, no. 1–3, pp. 62–68, Sep. 2008.

[54] X. Yuwen, L. Chen, and Y. Han, “Numerical Simulation of Casting Filling Process Based on FLUENT,” *Energy Procedia*, vol. 17, Part B, pp. 1864–1871, 2012.

[55] G. Mi, X. Liu, K. Wang, and H. Fu, “Application of Numerical Simulation Technique to Casting Process of Valve Block,” *J. Iron Steel Res. Int.*, vol. 16, no. 4, pp. 12–17, Jul. 2009.

[56] D. Y. Maeng, J. H. Lee, C. W. Won, S. S. Cho, and B. S. Chun, “The effects of processing parameters on the microstructure and mechanical properties of modified B390 alloy in direct squeeze casting,” *J. Mater. Process. Technol.*, vol. 105, no. 1–2, pp. 196–203, Sep. 2000.

[57] G. O. Verran, R. P. K. Mendes, and M. A. Rossi, “Influence of injection parameters on defects formation in die casting Al12Si1,3Cu alloy: Experimental results and numeric simulation,” *J. Mater. Process. Technol.*, vol. 179, no. 1–3, pp. 190–195, Oct. 2006.

[58] A. Midea, M. Burns, M. Schneider, and I. Wagner, “Advanced thermo-physical data for casting process simulation –the importance of accurate sleeve properties,” *Int. Foundry Res.*, vol. 59, no. 1, pp. 34–43, 2007.

[59] S.-L. Lu, F.-R. Xiao, S.-J. Zhang, Y.-W. Mao, and B. Liao, “Simulation study on the centrifugal casting wet-type cylinder liner based on ProCAST,” *Appl. Therm. Eng.*, vol. 73, no. 1, pp. 512–521, Dec. 2014.

[60] Y.-L. Hsu and C.-C. Yu, “Computer Simulation of Casting Process of Aluminium Wheels - A Case Study,” *Proc. Inst. Mech. Eng. Part B J. Eng. Manuf.*, vol. 220, no. 2, pp. 203–211, Jun. 2006.

[61] G. Hartmann and U. Weiss, “Exploit the Casting - Optimized design processes by exploiting the full material performance: Computing local properties and residual stresses empowers engi ne casting development,” *Engine Technology*, p. 4, 2006.

[62] A. E. Walter, “Prediction of distortion in thin-walled die castings,” *Cast. PLANT Technol. Int.*, no. 1, pp. 24–29, 2007.

[63] A. Egner-Walter and M. Kothen, “Using stress simulation to tackle distortion and cracking in castings,” *Metall. Sci. Tecnol.*, vol. 24, no. 2, 2013.

[64] G. Hartmann, “Material combinations in light weight casting components,” *Cast. Plant Technol.*, vol. 4, pp. 32–37, 2013.

[65] H. Li, K. Chandrashekhara, S. Komaragiri, S. N. Lekakh, and V. L. Richards, "Crack prediction using nonlinear finite element analysis during pattern removal in investment casting process," *J. Mater. Process. Technol.*, vol. 214, no. 7, pp. 1418–1426, Jul. 2014.

[66] A. Schroth and D. Schemme, "Simulation in modern quality management systems-Simulation assists the implementation of quality management systems in foundries," *Cast. PLANT Technol. Int.*, vol. 19, no. 1, p. 8, 2003.

[67] I. Hahn and E. Hepp, "Improved ingot casting by using numerical simulation."

[68] I. Hahn, M. Schneider, J. Terhaar, J. Jarolimeck, and R. Sauermann, "Quality Prediction of Cast Ingots."

[69] S. L. Nimbulkar and R. S. Dalu, "Design optimization of gating and feeding system through simulation technique for sand casting of wear plate," *Perspect. Sci.*, vol. 8, pp. 39–42, Sep. 2016.

[70] C. Sturm and R. Seefeldt, "Two for One–transferring proven filling characteristics from a single to a two cavity die casting die," *Cast. Plant Technol.*, vol. 3, pp. 44–52, 2007.

[71] S. P. A. Bordas, J. G. Conley, B. Moran, J. Gray, and E. Nichols, "A simulation-based design paradigm for complex cast components," *Eng. Comput.*, vol. 23, no. 1, pp. 25–37, Aug. 2006.

[72] C. Dørum, O. S. Hopperstad, O.-G. Lademo, and M. Langseth, "Numerical modelling of the structural behaviour of thin-walled cast magnesium components using a through-process approach," *Mater. Des.*, vol. 28, no. 10, pp. 2619–2631, 2007.

[73] J. Olofsson and I. L. Svensson, "Incorporating predicted local mechanical behaviour of cast components into finite element simulations," *Mater. Des.*, vol. 34, pp. 494–500, Feb. 2012.

[74] R. Hardin and C. Beckermann, "Effect of Shrinkage on Service Performance of Steel Castings," in *56th Steel Founders' Society of America National Technical & Operating Conference, Chicago, Illinois*, 2002, pp. 7–9.

[75] K. M. Sigl, R. A. Hardin, R. I. Stephens, and C. Beckermann, "Fatigue of 8630 cast steel in the presence of porosity," *Int. J. Cast Met. Res.*, vol. 17, no. 3, pp. 130–146, Mar. 2004.

[76] R. A. Hardin and C. Beckermann, “Prediction of the Fatigue Life of Cast Steel Containing Shrinkage Porosity,” *Metall. Mater. Trans. A*, vol. 40, no. 3, pp. 581–597, Jan. 2009.

[77] R. A. Hardin and C. Beckermann, “Integrated design of castings: effect of porosity on mechanical performance,” *IOP Conf. Ser. Mater. Sci. Eng.*, vol. 33, no. 1, p. 012069, Jul. 2012.

[78] R. A. Hardin, R. K. Huff, and C. Beckermann, “Integrated design of steel castings for service performance,” in *Proceeding Of the 11th Int. Conf. On Modeling of Casting, Welding and Advanced Solidification Processes-XI*, 2006, pp. 653–660.

[79] R. A. Hardin and C. Beckermann, “Effect of Porosity on Deformation, Damage, and Fracture of Cast Steel,” *Metall. Mater. Trans. A*, vol. 44, no. 12, pp. 5316–5332, Dec. 2013.

[80] P. Ferro, P. Lazzarin, and F. Berto, “Fatigue properties of ductile cast iron containing chunky graphite,” *Mater. Sci. Eng. A*, vol. 554, pp. 122–128, Sep. 2012.

[81] J. Hattel, *Fundamentals of Numerical Modelling of Casting Processes*. Polyteknisk Forlag, 2005.

[82] P. N. Rao, *Manufacturing Technology*. Tata McGraw-Hill Education, 2013.

[83] Rio Tinto Iron and Titanium Inc., *Ductile Iron : the essentials of gating and risering system design*. QIT-Fer et Titane Incorporated, 1987.

[84] “ASTM E8 / E8M - 16a Standard Test Methods for Tension Testing of Metallic Materials.” ASTM International, West Conshohocken, PA, 2016.

[85] “ASTM E466 - 15 Standard Practice for Conducting Force Controlled Constant Amplitude Axial Fatigue Tests of Metallic Materials.” ASTM International, West Conshohocken, PA, 2015.

[86] R. Budynas and K. Nisbett, *Shigley’s Mechanical Engineering Design*. McGraw-Hill Education, 2010.

[87] T. L. Anderson and T. L. Anderson, *Fracture Mechanics: Fundamentals and Applications, Third Edition*. CRC Press, 2005.

[88] R. A. Hardin and C. Beckermann, “Effect of Porosity on the Stiffness of Cast Steel,” *Metall. Mater. Trans. A*, vol. 38, no. 12, pp. 2992–3006, Dec. 2007.

[89] A. P. Roberts and E. J. Garboczi, “Elastic Properties of Model Porous Ceramics,” *J. Am. Ceram. Soc.*, vol. 83, no. 12, pp. 3041–3048, Dec. 2000.

[90] A. L. Gurson, "Continuum theory of ductile rupture by void nucleation and growth: Part I—Yield criteria and flow rules for porous ductile media," *J. Eng. Mater. Technol.*, vol. 99, no. 1, pp. 2–15, 1977.

[91] V. Tvergaard, "Influence of voids on shear band instabilities under plane strain conditions," *Int. J. Fract.*, vol. 17, no. 4, pp. 389–407, Aug. 1981.

[92] A. Needleman and V. Tvergaard, "An analysis of ductile rupture in notched bars," *J. Mech. Phys. Solids*, vol. 32, no. 6, pp. 461–490, Jan. 1984.

[93] Dassault Syste`mes, "ABAQUS Theory Manual, Version 6.10, section 4.3.6 Porous Metal Plasticity," Providence, RI, 2010, pp. 1–7.

[94] N. Aravas, "On the numerical integration of a class of pressure-dependent plasticity models," *Int. J. Numer. Methods Eng.*, vol. 24, no. 7, pp. 1395–1416, Jul. 1987.

[95] W. A. Spitzig, "Effect of hydrostatic pressure on deformation, damage evolution, and fracture of iron with various initial porosities," *Acta Metall. Mater.*, vol. 38, no. 8, pp. 1445–1453, 1990.

[96] Dassault Systems UK Limited, "fe-safe User manual." 20-Aug-2015.

[97] R. A. Hardin and C. Beckermann, "Prediction of Fatigue Life of Cast Steel in the Presence of Porosity," in *Proceedings of the 61st Technical and Operating Conference*, Chicago, IL, 2007.

[98] K. C. Kapur and L. R. Lamberson, *Reliability in engineering design*. Wiley, 1977.

[99] J. E. Shigley and C. R. Mischke, *Standard Handbook of Machine Design*. McGraw-Hill, 1996.

[100] S. Woo, *Reliability Design of Mechanical Systems: A Guide for Mechanical and Civil Engineers*. Springer, 2017.

[101] NDT Resource Center, "Materials and Processes - Fatigue Properties." .

[102] S. Samar Ali and S. Kannan, "A diagnostic approach to Weibull-Weibull stress-strength model and its generalization," *Int. J. Qual. Reliab. Manag.*, vol. 28, no. 4, pp. 451–463, Apr. 2011.

[103] K. V. Mardia and P. J. Zemroch, *Tables of the F- and Related Distributions with Algorithms*. Academic Press, 1978.

[104] E. S. Pearson, K. Pearson, and H. O. Hartley, *Biometrika tables for statisticians*. Published for the Biometrika Trustees at the University Press, 1966.

[105] "Feeding & Risering Guidelines for Steel Castings." Steel Founders' Society of America, 2001.

Vitae

Name : Muhammad Azhar Ali Khan

Nationality : Pakistani

Date of Birth : 3/1/1988

Email : tanazhar88@hotmail.com

Address : B-12/423, Indus Mehran Town, Malir, 75080, Karachi, Pakistan

Educational Qualification:

M.S. (Sustainable Environment and Energy Systems)
July, 2013
Middle East Technical University, Turkey

B.E. (Mechanical Engineering)
Dec, 2009
NED University of Engineering and Technology

Publications

Book

1. M. A. A. Khan, A. K. Sheikh, and B. S. Al-Shaer, "Evolution of Metal Casting Technologies—A Historical Perspective," in SpringerBriefs in Applied Sciences and Technology, Springer International Publishing, 2017.

Journal Papers

1. M. A. A. Khan and A.K. Sheikh, "A Comparative Study of Simulation Software for Modelling Metal Casting Processes" International Journal of Simulation Modelling, Vol. 17, No. 2, June 2018.
2. M. A. A. Khan and A. K. Sheikh, "Virtual Casting: State of the Art in Metal Casting Simulation Tools" The Journal of Engineering Research, 2018.
3. M. A. A. Khan and A. K. Sheikh, "Simulation Tools in Enhancing Metal Casting Productivity and Quality – A Review" Proc. Inst. Mech. Eng. Part B J. Eng. Manuf., 2016.
4. M.A.A. Khan, A.K. Sheikh, "Mold Design Optimization and Quality Assessment of Steel Castings through Integrated Simulations and Experiments" *Submitted to Proc. Inst. Mech. Eng. Part B J. Eng. Manuf.*
5. M.A.A. Khan, A.K. Sheikh, "Mechanical Characterization and Quality of Iron Castings using Optimized Mold Design: Simulations and Experimental Validation" *Submitted to International Journal of Advanced Manufacturing Technology*

Conference Proceedings

1. M. A. A. Khan and A. K. Sheikh, "Recent Trends in Metal Casting Simulations". International Conference on Applied Mechanics and Industrial Systems, 2016, Muscat, Oman.